Ridge Segmentation, Tectonic Evolution and Rheology of Slow-Spreading Oceanic Crust

by

Javier Esteban Escartín Guiral

Licenciado en Geología Aplicada con grado, Universitat de Barcelona, Spain, 1990
Maitrise d'Océanologie Apliquée, Université de Perpignan, France, 1990

SUBMITTED IN THE PARTIAL FULFILLMENT OF THE REQUIREMENTS FOR THE DEGREE OF DOCTOR OF PHILOSOPHY IN OCEANOGRAPHY

at the
MASSACHUSETTS INSTITUTE OF TECHNOLOGY
and the
WOODS HOLE OCEANOGRAPHIC INSTITUTION

August, 1996

Signature of Author____
Joint Program in Oceanography, Massachusetts Institute of Technology and Woods Hole Oceanographic Institution, August 1996

Certified by_____
Dr. Jian Lin, Thesis Supervisor

Accepted by_____
Deborah K. Smith, Chair, Joint Committee for Marine Geology and Geophysics, Massachusetts Institute of Technology and Woods Hole Oceanographic Institution

RIDGE SEGMENTATION, TECTONIC EVOLUTION AND RHEOLOGY
OF SLOW-SPREADING OCEANIC CRUST

by

Javier Esteban Escartín Guiral

Submitted to the Department of Earth, Atmospheric, and Planetary Sciences
Massachusetts Institute of Technology
and
the Department of Geology and Geophysics, Woods Hole Oceanographic Institution, on
August 1996 in partial fulfillment of the requirements for the degree of

Doctor of Philosophy

ABSTRACT

Two-thirds of the Earth's surface is oceanic crust formed by magmatic and tectonic processes along mid-ocean ridges. Slow-spreading ridges, such as the Mid-Atlantic Ridge, are discontinuous and composed of ridge segments. Segments are thus fundamental units of magmatic accretion and tectonic deformation that control the evolution of the crust. The objective of this Thesis is to constrain the tectonic processes that occur at the scale of slow-spreading segments, to identify the factors controlling segment propagation, and to provide constraints on lithospheric strength with laboratory deformation experiments.

In chapter 2, bathymetry and gravity from various areas along the global mid-ocean ridge system are analyzed to quantify systematic variations at the scale of individual segments. There is a marked asymmetry in bathymetry and gravity in the vicinity of segment offsets. We develop a model of faulting to explain these observations. Low-angle faults appear to accommodate tectonic extension at the inside corners of ridge-offset intersections, and result in substantially uplifted terrain with thin crust with respect to that at the outside corners or centers of segments.

Results from Chapter 3 indicate that the crust magmatically emplaced on axis is not maintained off-axis. This transition is revealed by both statistical and spectral analyses of

bathymetry and gravity. Tectonic extension varies along the length of a segment, resulting in thinning and uplift of the crust at ridge-offset inside corners, and a decorrelation between bathymetry and gravity patterns. Tectonic deformation substantially reshapes the oceanic crust that is magmatically emplaced on-axis, and strongly controls the crustal structure and seafloor morphology off-axis.

Satellite gravity data over the Atlantic shown in Chapter 4 reveal a complex history of ridge segmentation, and provides constraints on the processes driving the propagation of segments. The pattern of segmentation is controlled mainly by the geometry of the ridge axis, and secondarily by hot spots. Segments migrate primarily down regional gradients associated with hot spot swells. However, the lack of correlation between gradients and propagation rate, and the propagation up gradient of some offsets, suggest that additional factors control propagation (e.g., variations in lithospheric strength). Most non-transform offsets are short-lived and migrating, while transform offsets are long-lived and stable.

Both the propagation of segments (Chapter 4) tectonism along a segment (Chapters 2 and 3) are controlled by the lithospheric rheology. In Chapter 5 I present results from laboratory deformation experiments on serpentinite. These experiments demonstrate that serpentinites are considerably weaker than peridotites or gabbros, display a non-dilatant style of brittle deformation, and strain is accommodated by shear cracking. Serpentinites may weaken the lithosphere, enhance strain localization along faults, and control the style of faulting.

Thesis supervisor: Jian Lin
Title: Associate Scientist, Woods Hole Oceanographic Institution

ACKNOWLEDGMENTS

Completing this Thesis has been possible thanks to numerous friends and my family, with whom I have shared the good moments and who have supported me during the times that were difficult over the last "few" years at WHOI. Jian Lin's advice, help, motivation, and support kept me on the track towards finishing and moving on, although this happened only after 6 instead of 5 academic years. Greg Hirth supervised an important part of the work presented, always with highly contagious enthusiasm and endless energy (that was not contagious, unfortunately!). To both I am indebted for their effort, time invested, and infinite patience. Apart from the advice of Jian and Greg, the work presented here has evolved, improved and been influenced by a large number of people through discussions, comments and suggestions from Alan Chave, Bob Detrick, Henry Dick, Brian Evans, Kip Hodges, Hans Schouten, Peter Shaw, Deborah Smith, Brian Tucholke, and Elazar Uchupi, and of course my fellow students; I will get to them later on, though. The Geodynamics seminar, conducted by Henry Dick, has been an important source of motivation, information, and geological field trips (*remember Canarias, Henry?*). Dave Aubrey guided me on my first steps in Woods Hole, after coming here with a fellowship from "La Caixa" to work on coastal processes; the only reason I got accepted at WHOI is that I had my own money, at least that's what I've overheard (*verdad, El?*). I haven't given yet the final title of my thesis to the grant managers of that bank yet. Finally, thanks to the members of my Thesis Committee, Jian Lin, Greg Hirth, Deborah Smith, Brian Tucholke, Kip Hodges, and the chair, Greg Ravizza, for their effort and time. Careful and thoughtful comments by Brian Tucholke are gratly appreciated. Deborah made sure I keept my priorities straight, in all senses. I finally got the handshake, and I can hit the lecture circuit well equipped now, Bob. Greg made me apprciate some of the best aspects of this world at 6:00AM in Providence, ready for a 29 hour day ahead; hard but great. Elazar made sure I was "making good progress" and "doing good work" at least three times a day, always with all that energy that I much needed (dinner in Madrid is still pending).

The unconditional support of the Education Office throughout these years has also been instrumental to the completion of this Thesis. Apart from the administrative support, they provided financial help to support my participation in different meetings, and to cover my

salary. And above all they provided a human environent and a friendship face to overcome some of the hardships of being here. I hope that this aspect is not totally lost for the future students, though. The warmest thanks to Jake Pierson, Abbie Jackson, Julia Westwater and Dacia Tucholke for everything. Pam Foster, Janet Jackson and Roy Smith made my stay at WHOI possible providing support and help for all those things needed to facilitate my stay here, and get my stuff done. Despite all my lack of organization, they showed infinite patience.

Six years is not a short time. Friends have left behind and new ones have come into life. Their friendship has been as important, if not more, than all the scientific input received. What is coming here is a short and fast account of flashbacks that go through my mind; the long version I leave it for another time. Joe Lacasce and Connie Hart were my first american "home" in Boston (*are you sure you want to sleep on the couch, Gary?)*, after I scaped the Spanish tribes in MIT. Joe always had a positive attitude and sense of humour that helped me through in many cases, specially when we lived together (*is the phone cold?*). He also provided me with a second family in this part of the world. Although he insisted and convinced me not to dislike Jazz, I never got him to appreciate the wonderful sounds Spanish Rocanrol. From Barb I begun to learn what is the balance between important matters and the rest, but I am not handling that well yet; I keep a lot from those times together (*sorry, but Miguelon did not make it this year*). Connie's stontoreous and contagious laughs (some for more than 45 minutes!) have cheered many of us during all these years (*nyigo nyigo; gloup gloup*), and hopefully you'll finish Platero, and you'll feed one of those in the Pirineos soon. Gary Jaroslow and Emilie Hooft have been with me in numerous trips to meetings, the field, cruises, and some "occasional" vacation. These have been many years of shared good experiences, amazing spots in the world, and happy moments (*I've got a esniker!*). By the way, Gary, you have to learn how to strech you arm better. Garret Ito had always a positive attitude towards things, and energy that I obviously lacked, which helped to get through problems coolheaded (*the SGI screen is broken, did you see it?*). He also provided us with an exotic and multicultural touch that Woods Hole lacks: the polynesian/punk crowds filled his house once a year. At least I'll get to see Hege and Dan (with the babies) soon in Europe, together with Cecilie, Joe and Johannes . Beverly Saylor and Meg Coleman gave MIT a much needed human aspect, specially during my first years up there in the big city.

With Thomas Ehrendorfer, my first officemate in Woods Hole, I learned how to spend whole afternoons well spent in endless and fascinating conversations (non-work related, of course!) about every imaginable aspect of life; the tradition was followed with Carl Wolfteich; the terminals are still there, mostly. Miguel, Kathleen and Isabel became my second home away from home in Woods Hole; great dinners, great parties, great times that won't be forgotten. Gorka and Miguel (*Carajillo rules!*) made me recover my rusty spanish behavioral patterns on these never too numerous nor too long parties and diners, substantially improving my Spanglish. Gorka helped me sharpen it while living together (*Caponazo!*). Ahora hay que buscar un arroyico cerca de una destileria pequeñica para el próximo verano. Chris, Melissa and the rest of the family are always there if anything, I mean anything, is needed. Alberto (*Ay quilombo!*) Maia and Sonso, Gaspar, Carlos and Mari Carmen, Xavi first, and Juan Pablo lately substantially contributed to the demise of my english, while keeping the place jumping and running. Pascal provided the wild edge at all times, and Yong-Yu perfected it in a rather subtle manner. Let's see how those *R*s sound like in two years. Margie and Ken, together with Emilie, allowed me to stay in their house for my last homeless summer... that was hard, with all that ocean right near by, and those great parties happening rather often. Soccer became as important (or more?) than work, although my skills were (are) worse than pathetic; however, those games under the rain covered in mud (*ah! it isn't raining too much, is it?*) were real fun and will be missed.

Muchas otras personas quedaron en el otro lado del mar, desafortunadamente. A pesar del tiempo y las distancias, Encarna Busquets y especialmente Marta Figueras (*mala herba...*), han mantenido un contacto casi semanal que ha mantenido mi mundo de alla un poco más cerca. Aún queda pendiente la excursion en Jeep al Pirineo de hace 4 años, pero... *no planifiquem, no*. Kiku, Batis, Ana Rosa, y Gloria siempre han encontrado tiempo para una larga comida o cena durante mis viajes relámpago de vuelta a casa. Ahora Kiku y Gloria saben lo que es el invierno de verdad. Sergio, Antonia y Xavi Carolina, y Nina, a pesar de comunicaciones esporádicas e inconsistentes, siempre han estado allí. El próximo encuentro será en menos de 5 años, eso seguro. Espero que a partir de ahora los contactos sean más cotidianos, y las cenas más frecuentes.

Los últimos meses han sido superados con la ayuda, paciencia y cariño de Emilie. Ha sido una amistad de varios años, que espero que continue siempre. Por mucho que lo intente, no hay agradecimientos que hagan honor a lo que me has dado todo este tiempo. Han sido muchos momentos de alegría a recordar y no tan alegrías ya superadas. Ya sabes donde me tienes, y con suerte dentro de poco estaremos en el Mediterráneo.

Finalmente, mi familia. Gracias a ellos he continuado en la "escuela" hasta tan avanzada edad. Mi abuela Ascensión siempre se preocupó (y con razón) de mi alimentación en estas tierras de Dios; nos dejó mientras estaba fuera de casa, pero continúa dentro de nosotros. El nervio y empeño de mi abuela María han sido ejemplos de tenacidad y insistencia a seguir. Sus continuos ánimos me han ayudado a superar todos los escollos encontrados. Lo que es seguro es que la que más ha sufrido ha sido mi madre, incluso después del fin de la tesis (y seguramente siempre). A mi padre, Esteban, mi madre, María Pilar, mis hermanas Eva y Elena, y especialmente al recién llegado a la familia, Javier, el hijo de Eva y Gonzalo, dedico este trabajo. Han sido muchos años fuera, y afortunadamente el siguiente escalón cae menos lejos de casa.

A fellowship from *Caixa de Pensions "La Caixa"* in Barcelona provided me with all the required financial support to come to WHOI. The work presented in this thesis was also supported by the National Science Foundation grants OCE-9012576, OCE-930078, OCE-9313812, and Office of Naval Research grant N00014-91-J-1433.

Caminante son tus huellas,
el camino y nada más;
caminante, no hay camino,
se hace camino al andar.
al andar se hace camino,
y al volver la vista atrás
se ve la senda que nunca
se ha de volver a pisar.
Caminante, no hay camino,
sino estelas en la mar

Antonio Machado
Campos de Castilla
(1907-1917)

VITA

Born September 9, 1967, Huesca, Spain

1990	Licenciatura de Geología Aplicada (BSc.), Universitat de Barcelona, Spain
1990	Maitrise d'Océnologie Apliquée (BSc.), Université de Perpignan, France
1990-1996	PhD., Department of Geology and Geophysics, Woods Hole Oceanographic Institution/Massachusetts Institute of Technology Joint Program, Woods Hole, Massachusetts

Publications:

Escartín, J. and J. Lin, Tectonic modification of axial crustal structure: Evidence from spectral analyses of bathymetry and gravity from the Mid-Atlantic Ridge flanks (25.5-27.5°N), *Earth, Planet. Sci. Lett.*, in prep., 1996.

Escartín, J., G. Hirth, and B. Evans, Non-dilatant brittle deformation of serpentinites: Implications for Mohr-Coulomb theory and the strength of faults, *Journal of Geophysical Research*, accepted, 1996.

Teide Group, Morphometric interpretation of the northwest and southeast slopes of Tenerife, Canary Islands, *Journal of Geophysical Research*, submitted, 1996.

Cann, J. R., D. K. Blackman, D. K., Smith, E. McAllister, B. Jassen, S. Mello, E. Avgerinos, A. R., Pascoe and J. Escartín, Corrugated slip surfaces at ridge-transform intersections of the Mid-Atlantic Ridge, *Nature*, accepted, 1996.

Escartín, J. and J. Lin, Ridge offsets, normal faulting, and gravity anomalies of slow spreading ridges, *J. Geophys. Res.*, 100, 6136-6177, 1995.

Escartín, J. and D. Aubrey, Flow structure and dispersion within algal mats, *Estuar. Coastal Shelf Sci.*, 40, 451-472, 1995.

Escartín, J. and J. Lin, Morfoestructura de la dorsal Medio-Atlántica entre 24°N y 30°N (*Morphostructure of the Mid-Atlantic Ridge between 24°N and 30°N*), *Acta Geològica Hispànica*, 27, 33-49, 1992.

Canals, M., J. Acosta, E. Gracia, J. Escartín, J. and ORCA group, Caracterización de la región de enlace entre la cuenca de Bransfield y la Dorsal Sur de Scotia (Antártida) (*Characterization of the linking region between the Bransfield basin and the South Scotia Ridge*). *Acta Geològica Hispànica*, 27, 89-110, 1992.

Abstracts:

Escartín, J. and J. Lin, Transforms and non-transform offsets of the central and northern Atlantic ocean crust, FARA-InterRidge Symposium, Reykjavik, Iceland, June 1996.

Escartín, J. and J. Lin, Segmentation, tectonism, and strength of oceanic lithosphere on the west flank of the Mid-Atlantic Ridge (25° - 27°10'N) inferred from coherence

between bathymetry and gravity, FARA-InterRidge Symposium, Reykjavik, Iceland, June 1996.

Searle, R. C., N. C. Mitchell, J. Escartín, P. Slootweg, S. Russell, P. A. Cowie, S. Allerton, C. J. MacLeod, T. Tanaka, C. Flewellen and I. Rousse, High-resolution TOBI study of Broken Spur segment, Mid-Atlantic Ridge, 29°N, FARA-InterRidge Symposium, Reykjavik, Iceland, June 1996.

Searle, R. C., C. Mitchell, J. Escartín, A. P. Slootweg, S. Russell, P. A. Cowie, S. Allerton, C. J McLeod, T. Tanaka, F. Flewellen and I. Russell, High resolution TOBI study of the Broken Spur segment, Mid-Atlantic Ridge, 29°N, ODP-InteRidge-IAVCEI Workshop "The oceanic lithosphere and Scientific Drilling into the 21st century", Woods Hole, USA, May 1996, p. 102.

Escartín, J. and J. Lin, Systematics of ridge segment propagation in the central and northern Atlantic Ocean Basin, *EOS, Transactions of the American Geophysical Union*, 77, May 1996 (AGU Spring'96, Baltimore, USA).

TEIDE Group, Evidence for episodic massive landslides off Tenerife, Canary Islands, *Proc. 2nd Workshop on the European Laboratory Volacanoes*, Santorini, Greece, 1996.

Acosta, J., C. Palomo, A. Muñoz, P. Herranz, J. L. Sanz, E. Uchupi and J. Escartín, Morphology and seismic character of northwest and southeast slopes of Tenerife Island. TEIDE-95. *Proc. 2nd Workshop on the European Laboratory Volcanoes*, Santorini, Greece, 1996.

Palomo, C., J. Acosta, J., A. Muñoz, P. Herranz, J. L. Sanz, E. Uchupi and J. Escartín, The Tenerife Island margin. Seismic, gravity, geomagnetic and bathymetric investigations. TEIDE Laboratory Volcano Project. *Proc. 2nd Workshop on the European Laboratory Volcanoes*, Santorini, Greece, 1996.

Escartín, J., G. Hirth, and B. Evans, 1995, Non-dilatant brittle deformation of serpentinites, *EOS, Transactions of the American Geophysical Union*, 76, 560, 1995 (AGU Fall'95, San Francisco, USA).

Lin, J., B. T. Tucholke, M. C. Kleinrock, and J. Escartín, 1995, Contrasting inside- vs. outside-corner crustal structure on the flanks of a slow-spreading ridge, *EOS, Transactions of the American Geophysical Union*, 76, 554, (AGU Fall'95, San Francisco, USA), 1995.

Escartín, J., G. Hirth, and B. Evans, Effects of serpentinization on the rheology of the oceanic lithosphere, (Fourth Ridge Theoretical Institute, Lake Tahoe, California, USA), 1995.

Escartín, J., G. Hirth, and B. Evans, Effects of serpentinization on the rheology and tectonics of the oceanic lithosphere, *Terra Nova*, 7, Abstract supplement 1, 147, 1995 (EUG 8, April 1995, Strasbourg, France), 1995.

Hirth, G., J. Escartín and B. Evans, The brittle-ductile transition in serpentinites, *Terra Nova*, 7, Abstract supplement 1, 51, 1995 (EUG 8, April 1995, Strasbourg, France), 1995.

Escartín, J., G. Hirth and B. Evans, Experimental constraints on the strength of serpentine: Implications for Mid-Ocean Ridge tectonics, *EOS, Transactions of the American Geophysical Union*, 75, 650, (AGU Fall'94, San Francisco), 1994.

Escartín, J. and Lin, J., Effects of transform and non-transform offsets on normal faulting and crustal structure of slow-spreading ridges, *EOS, Transactions of the American Geophysical Union*, 74, 664-665, (AGU Fall'93, San Francisco), 1993.

TABLE OF CONTENTS

Chapter 1

INTRODUCTION

Mid-ocean ridges extend over more than 75,000 km of the surface of the Earth. Magmatic, tectonic and hydrothermal processes concentrate along this narrow zone to produce the oceanic crust that covers roughly two-thirds of the surface of the planet. With the acquisition of geological and geophysical data our understanding of the mid-ocean ridge system has improved substantially with time. The original view of mid-ocean ridges as a linear feature dissected locally by large fracture zones [e.g., *Heezen*, 1960] has evolved to that of a ridge segmented at scales of 10-100 km [*Schouten et al.*, 1985]. At slow-spreading ridges, such as the Mid-Atlantic Ridge, these segments are characterized by systematic variations in bathymetry, gravity structure, and fault patterns [e.g., *Macdonald et al.*, 1988; *Kuo and Forsyth*, 1988; *Shaw*, 1992]. These systematic variations strongly suggest that segments are not only a morphologic feature of the seafloor, but also the units of magmatic accretion and tectonic deformation that construct and control the evolution of the oceanic crust.

Bathymetry data along the ridge axis and over the rift valley flanks reveal that segments are not stable features, but in numerous cases migrate along the ridge axis [e.g., *Johnson and Vogt*, 1973]. The combined effect of the systematic variations in tectonism and magmatism at the scale of individual ridge segments, together with the temporal evolution of these segments, are responsible for the final structure of the oceanic crust and morphology of the seafloor. The physical properties of the lithosphere and the composition of the crust also change along the length of a segment as a result of the inferred focused magmatic accretion under individual ridge segments [e.g., *Crane*, 1985; *Lin et al.*, 1990]. The objective of this Thesis is to constrain the tectonic processes that occur at the scale of individual ridge segments at slow-spreading centres, to determine which are the primary factors controlling the history of ridge segmentation in the Atlantic basin, and to provide mechanical data on serpentinites to better constrain the strength of the oceanic lithosphere and, ultimately, its tectonic evolution.

Information on seafloor morphology can be obtained from detailed bathymetric surveys, and sub-seafloor density structure can be obtained from a combination of gravity and bathymetry data. In chapter 2, both bathymetry and gravity from various areas along the global mid-ocean ridge system are analyzed to quantify systematic variations at the scale of individual segments. There is a marked asymmetry in bathymetry and gravity in the vicinity of segment offsets. We develop a model of faulting to explain these observations. Low-angle faults appear to accommodate tectonic extension at the inside corners of ridge-offset intersections, and result in substantially uplifted terrain with thin crust with respect to that at the outside corners or centers of segments.

The tectonic model proposed in Chapter 2 is further developed in Chapter 3 to explain the changes in bathymetry and gravity from on axis to off axis along the Mid-Atlantic Ridge. The thickest and shallowest crust along the ridge axis is observed at the center of segments, and has been interpreted to result from focused magmatic accretion [e.g., *Lin et al.*, 1990]. This structure is not maintained off-axis, however, and instead the shallowest terrain is found at inside-corner crust, not at the center of segments. This transition is characterized by both statistical and spectral analyses of the bathymetry and gravity. These results demonstrate that, at slow-spreading ridges, tectonic deformation reshapes the oceanic crust that is magmatically emplaced on axis, and strongly controls the crustal structure and seafloor morphology away from the ridge axis.

On a broader scale, analysis of satellite-derived free air anomaly maps over the Atlantic basin, in Chapter 4, reveals a complex history of ridge segmentation, and provides constraints on the processes driving the propagation of ridge segments. Satellite gravity is used to determine the geometry of ridge segmentation at the ridge axis, the traces of ridge segment discontinuities off-axis, and to measure several tectonic parameters (e.g., regional gravity gradients, segment and offset length, migration rate of discontinuities). These

parameters are used to evaluate several models that have been proposed to explain the propagation of segments, and to determine the relative importance of each process.

Both the propagation of individual segments documented in Chapter 4 and the variation of tectonism along a single ridge segment in Chapters 2 and 3 are controlled by the mechanical properties of the oceanic lithosphere. Our knowledge of the rheology and deformation style of rocks is limited mainly to olivine, while the mechanical properties of diabase are still poorly understood. Other rocks, such as the alteration products of gabbro, diabase and peridotites, have mechanical properties that are relatively unknown, but that could strongly influence the strength of the oceanic lithosphere and the tectonic evolution of the oceanic crust. In Chapter 5 we present results from deformation experiments on serpentinite. Serpentinites are ubiquitous in the oceanic lithosphere, particularly near discontinuities along the strike of the ridge axis [e.g., *Cannat et al.*, 1995]. Serpentinites are considerably weaker than peridotites or gabbros, and display a mode of brittle deformation that has not been described previously. These mechanical properties have several implications for Mohr-Coulomb theory, rheology of faults, and the strength of the oceanic lithosphere, particularly at slow-spreading ridges.

In Chapter 6 the main conclusions of Chapters 2 through 5 are summarized and put in the context of the segmentation of slow-spreading ridges. The variations in tectonic style along the length of a segment can be explained by changes in lithospheric rheology at the same scale. It is likely that these variations in rheology are caused by compositional changes within the lithosphere, and may be tied to the preferential presence of serpentinites at the end of segments. The along-axis propagation of segments is also strongly influenced by the rheology of the oceanic lithosphere.

The research presented in Chapter 2 has been published in the *Journal of Geophysical Research* in 1995, with Jian Lin as a co-author. Chapters 3 is being prepared for submission to *Earth and Planetary Science Letters*, with Jian Lin as a co-author. Chapter 4

will be submitted shortly to the *Geophysical Journal International*, with Jian Lin as a co-author. Chapter 5 has been accepted by the *Journal of Geophysical Research* for publication, with Greg Hirth and Brian Evans as co-authors.

References

Cannat, M., Emplacement of mantle rocks in the seafloor at mid-ocean ridges, *J. Geophys. Res.*, 98, 4163-4172, 1993.

Cannat, M., C. Mével, M. Maia, C. Deplus et al., Thin crust, ultramafic exposures, and rugged faulting patterns at the Mid-Atlantic Ridge (22°-24°N), *Geology*, 23, 49-52, 1995.

Heezen, B. C., The rift in the ocean floor, *Sci. Amer.*, 98-110, 1960.

Johnson, G. L. and P. R. Vogt, Mid-Atlantic Ridge from 47°N to 51°N, *Geol. Soc. Amer. Bull.*, 84, 3443-3462., 1973.

Kuo, B. Y. and D. W. Forsyth, Gravity anomalies of the ridge-transform system in the South Atlantic between 31 and 33°S: Upwelling centers and variations in crustal thickness, *Mar. Geophys. Res.* , 10, 205-232, 1988.

Lin, J., G. M. Purdy, H. Schouten, J. C. Sempere and C. Zervas, Evidence from gravity data for focused magmatic accretion along the Mid-Atlantic Ridge, *Nature*, 344, 627-632, 1990.

Macdonald, K. C., P. J. Fox, L. J. Perram, M. F. Eisen, R. M. Haymon, S. P. Miller, S. M. Carbotte, M.-H. Cormier and A. N. Shor, A new view of the mid-ocean ridge from the behavior of ridge-axis discontinuities, *Nature*, 335, 217-225, 1988.

Schouten, H., K. D. Klitgord and J. A. Whitehead, Segmentation of mid-ocean ridges, *Nature*, 317, 225-229, 1985.

Shaw, P. R., Ridge segmentation, faulting and crustal thickness in the Atlantic Ocean, *Nature*, 358, 490-493, 1992.

Chapter 2

RIDGE OFFSETS, NORMAL FAULTING, AND GRAVITY ANOMALIES OF SLOW-SPREADING RIDGES

Javier Escartín and J. Lin
Journal of Geophysical Research, 100 (B4), 6163-6177, 1995

JOURNAL OF GEOPHYSICAL RESEARCH, VOL. 100, NO. B4, PAGES 6163–6177, APRIL 10, 1995

Ridge offsets, normal faulting, and gravity anomalies of slow spreading ridges

Javier Escartín[1] and Jian Lin

Department of Geology and Geophysics, Woods Hole Oceanographic Institution, Woods Hole, Massachusetts

Abstract. We develop a model relating mid-ocean ridge normal faulting and crustal structure by examining recently available high-resolution gravity and multibeam bathymetric data of the Mid-Atlantic Ridge and other spreading centers. Results of the analysis reveal a consistent pattern of positive residual gravity anomalies along the crust paralleling all major Atlantic offsets studied, especially along the inside corner side of the offsets. Individual residual gravity anomaly spikes (local peaks), which have amplitudes of up to 20 mGal and typical across-axis spacing of 10-30 km, often coincide with individual major fault scarps, suggesting crust thinned by normal faulting. Theoretical calculations indicate that the amplitude and spacing of the observed residual gravity spikes are consistent with the presence of successive, ridge-parallel low-angle faults that originate episodically at inside corners of ridge offset intersections. Fault scarp heights and the amounts of crustal thinning (as inferred from gravity anomalies) are consistently larger at inside corners than at outside corners, supporting a model in which tectonic extension near ridge offsets is asymmetric with low-angle faults occurring preferentially at inside corners. These results on spatial variations in seafloor morphology and gravity anomalies further support a three-dimensional tectonic faulting model at oceanic spreading centers with three major characteristics: (1) Low-angle faults form preferentially at inside corners, where the mantle lithosphere is the strongest and the lithospheric plates are sufficiently decoupled across ridge axis offsets; (2) low-angle faults decrease in throw toward midpoints of long ridge segments, where large low-angle faults may not be sustained by a weak lithosphere; and (3) the residual gravity peaks are statistically larger at transform than near nontransform offsets, indicating that the length of a ridge offset and its tectonic style control the development of low-angle faults.

Introduction

Recent multibeam bathymetric and gravity mapping along mid-ocean ridges have provided detailed constraints on the architecture of the oceanic crust at ridge segment scale. The existence of distinctive lows in mantle Bouguer gravity anomalies (MBA) at the Mid-Atlantic Ridge (MAR) (Figure 1) indicate that the crust is thicker and the upper mantle is hotter at segment centers than at distal ends [*Kuo and Forsyth*, 1988; *Lin et al.*, 1990; *Blackman and Forsyth*, 1991; *Morris and Detrick*, 1991; *Detrick et al.*, 1995]. These residual gravity lows suggest that magmatic accretion occurs in the form of discrete, buoyancy-driven upwelling centers [*Kuo and Forsyth*, 1988; *Lin et al.*, 1990], thus supporting earlier hypotheses on the existence of melt or buoyant mantle diapirs in the underlying asthenosphere [e.g., *Rabinowicz et al.*, 1984; *Whitehead et al.*, 1984; *Crane*, 1985; *Schouten et al.*, 1985].

The "bull's eye" gravity lows, however, are of lesser amplitude at segments of fast-spreading ridges such as the East Pacific Rise (EPR) [*Madsen et al.*, 1990; *Lin and Phipps Morgan*, 1992; *Wang and Cochran*, 1993; *Cormier et al.*, 1995]. Results from numerical experiments on upper mantle convection [*Parmentier and Phipps Morgan*, 1990; *Sparks et al.*, 1993] suggest a transition from three-dimensional plumelike mantle upwelling to two-dimensional sheetlike upwelling with increasing spreading rate which is consistent with the observed spreading rate dependence of ridge axis gravity structure [*Lin and Phipps Morgan*, 1992]. The range of MBA amplitudes decreases with increasing spreading rate (Figure 2).

Estimates of gravity-derived crustal thickness along the MAR are in general agreement with results from limited seismic experiments, which also indicate thicker crust at segment centers than at segment ends [*Sinha and Louden*, 1983; *Tolstoy et al.*, 1993]. The observed reduction in seismic crustal thickness toward ridge offsets corresponds mainly to the thinning of layer 3 (cumulate gabbros), whereas the thickness of layer 2 (basalt and diabase) remains essentially constant, as interpreted by *Tolstoy et al.* [1993]. This seismic interpretation of crustal structure is consistent with the model of focused mantle upwelling, as the increased availability of melt at the segment center would result in a greater rate of crustal emplacement and a thicker section of gabbros (layer 3) than at distal ends, where the melt supply would be reduced. Alternatively, the variations in the seismic structure could be interpreted in terms of compositional variations of the crust [*Cannat*, 1993]. The limited seismic refraction and tomography study by *Tolstoy et al.* [1993] suggests that gravity-derived models may underestimate, rather than overestimate, the amplitude of seismic crustal thickness variations, and theoretical calculations indicate that mantle density may contribute only a

[1]Also at MIT/WHOI Joint Program in Oceanography, Woods Hole Oceanographic Institution, Woods Hole, Massachusetts.

Paper number 94JB03267.
0148-0227/95/94JB-03267$05.00

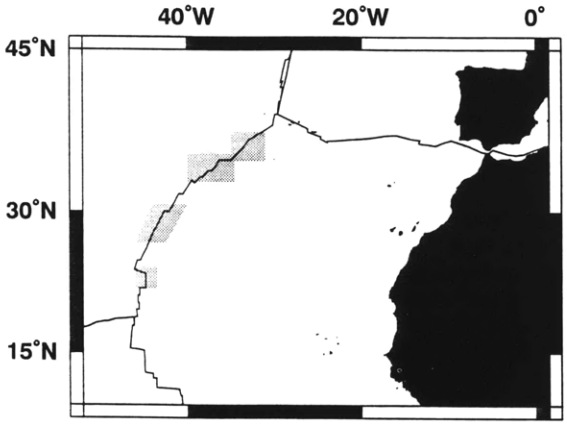

Figure 1. Location map of study areas (light shading) at the Mid-Atlantic Ridge where multibeam bathymetric and residual gravity data are available. Sources for individual data sets are listed in Table 1. Location of plate boundary is indicated by thin lines.

small amount to the observed residual gravity anomalies [*Lin and Phipps Morgan*, 1992; *Sparks et al.*, 1993].

The interpreted focused mantle upwelling and the resultant along-axis variations in crustal thickness may also have important effects on the thermo-mechanical properties of the oceanic lithosphere at the ridge axis [*Neumann and Forsyth*, 1993; *Shaw and Lin*, 1993]. Theoretical models of *Shaw and Lin* [1994] suggest that the decoupling of the upper crust from the mantle by a weak lower crust may occur only at segment centers ("pita pocket" structure), resulting in a thin, weak lithosphere at segment centers and a thick, strong lithosphere at distal ends. The thin lithosphere over the weak lower crust will favor the formation of small and closely spaced faults at the segment centers [e.g., *Shaw and Lin*, 1993]. This model is consistent with several lines of observations: (1) the clustering of teleseismic earthquakes in the proximity of ridge offsets [*Huang and Solomon*, 1988; *Lin and Bergman*, 1990], where the mantle lithosphere is the strongest; (2) the systematic deepening of axial seafloor depth toward segment ends [*Sempéré et al.*, 1993]; and (3) the occurrence of smaller, more closely spaced scarps inferred to be faults at segment centers than at distal ends [*Shaw*, 1992; *Shaw and Lin*, 1993] (Plates 1a and 1b). These fault scarps tend to be axis parallel at segment centers and to become oblique near offsets [*Escartín and Lin*, 1992], probably as a result of the interaction of far- and near-field stresses in the vicinity of ridge offsets [e.g., *Fujita and Sleep*, 1978; *Pollard and Aydin*, 1984].

The tectonic interaction of the ridge axis and offsets at slow- and intermediate-spreading centers is most evident in the remarkable contrast between elevated crust at ridge offset inside corners (ICs) and depressed seafloor at conjugate outside corners (OCs) (Plate 1) [e.g., *Searle and Laughton*, 1977; *Karson and Dick*, 1983; *Kuo et al.*, 1984; *Collette*, 1986; *Severinghaus and Macdonald*, 1988; *Blackman and Forsyth*, 1989; *Mutter and Karson*, 1992]. Significant differences in lithology between IC and OC crust have also been found in dredged rock samples. Upper mantle and lower crustal rocks are frequently dredged at IC crust, suggesting that low-angle faults may locally expose the lower crust and upper mantle there [*Karson and Dick*, 1983, 1984; *Dick*, 1989; *Dick et al.*, 1991; *Mével et al.*, 1991; *Tucholke and Lin*, 1994]. In contrast, mantle and lower crustal rocks were rarely found at OC crust or at segment centers [*Tucholke and Lin*, 1994]. Higher values of residual gravity anomalies similarly indicate greater amount of crustal thinning at IC crust than at OC crust (Plates 1c and 1d). Recent studies of micro-earthquakes at the MAR further documented strong clustering of seismic events at ICs and little activity at OCs, indicating that IC crust is seismically more active [*Barclay et al.*, 1993; *Wolfe et al.*, Microearthquake characteristics and crustal velocity structure at 29°N on the Mid Atlantic Ridge: The architecture of a slow-spreading segment, submitted to *Journal of Geophysical Research*, 1995]. In addition, significant differences in tectonic style exist between transform and nontransform offsets. Transform offsets are characterized by a well-defined strike-slip fault running within a transform valley, while nontransform often lack a well-defined transform fault and tend to have smaller lateral ridge offsets [*Macdonald et al.*, 1991].

In this paper we analyze high-resolution gravity and bathymetry data collected over several ridge offset intersections along the MAR (Figure 1) and other spreading centers to better understand the processes responsible for tectonic differences between IC and OC crust. We then analyze these anomalies in terms of the structure of individual faults and study the

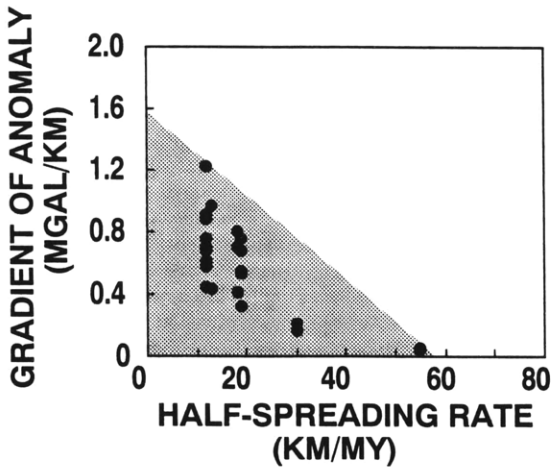

Figure 2. Along-axis gradients in mantle Bouguer gravity plotted against spreading rate (modified from *Lin and Phipps Morgan* [1992]). Note that both the gradient and its variation decrease with spreading rate (fan-shaped shaded area).

Plate 1. Oblique projection of shaded relief maps of (a) the Atlantis Fracture Zone (F. Z.) and (b) a ridge segment bounded by two nontransform offsets at the Mid-Atlantic Ridge (~29°N). Note that inside corners near both transforms and nontransform offsets are elevated and show large abyssal hill relief, which we interpret as due to large throw faults. In contrast, outside corners are depressed and show closely spaced fault scarps with smaller throws. Color residual gravity anomaly plotted on top of 3-D bathymetric meshes for (c) a segment north of the Atlantis F. Z. and (d) a segment bounded by two nontransform offsets. Note that inside corners are often associated with high residual gravity anomalies, indicating thinned crust. IC; inside corner; OC; outside corner.

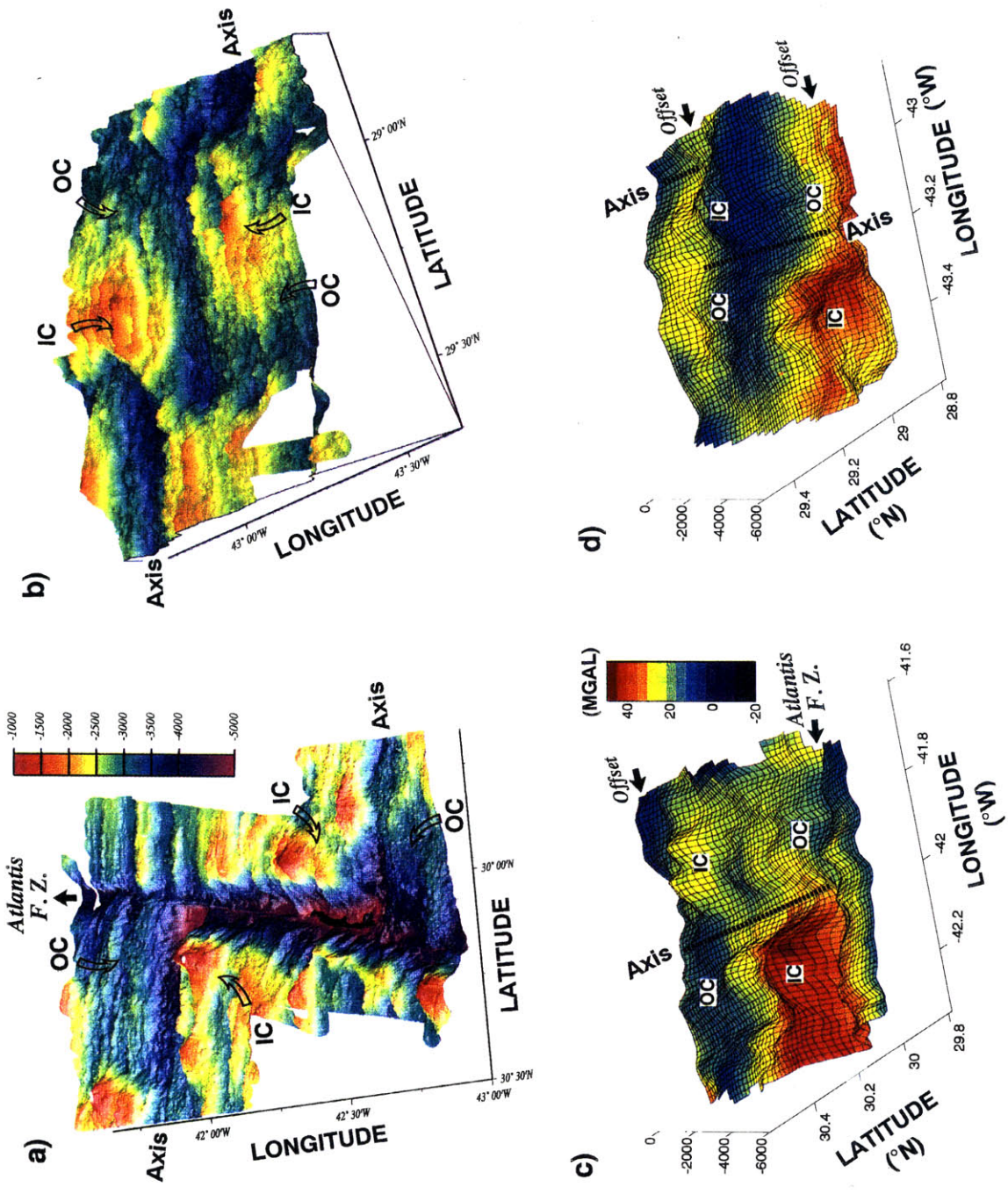
a)
b)
c)
d)
Axis
OC
IC
Atlantis F.Z.
Offset
LONGITUDE
LATITUDE
(MGAL)
-1000
-1500
-2000
-2500
-3000
-3500
-4000
-5000
42° 00'W
42° 30'W
43° 00'W
43° 30'W
30° 00'N
30° 30'N
29° 00'N
29° 30'N
40
20
0
-20
-41.6
-41.8
-42
-42.2
-43
-43.2
-43.4
30
30.2
30.4
29
29.2
29.4
28.8
29.8
-2000
-4000
-6000

relationship between these anomalies, offset styles, and crustal accretion variables of spreading rate, ridge offset length, and axial valley relief. Finally, we compare the data with synthetic results of two-dimensional kinematic models of crustal faulting. Through these analyses, we attempt to develop a three-dimensional tectonic model for the formation of IC and OC crust in relation to transform and nontransform ridge offsets.

Data Analysis

We examine digital multibeam bathymetric and residual gravity data collected over four areas of the slow-spreading MAR [*Purdy et al.*, 1990; *Lin et al*, 1990; *Morris and Detrick*, 1991; *Detrick et al.*, 1995] (Figure 1), two areas of the fast-spreading EPR between 7°-9°30'S [*Wang and Cochran*, 1993] and 8°50'-9°50°N [*Madsen et al.*, 1990], and the very slow-spreading Southwest Indian Ridge (SWIR) near the Atlantis II Transform [*Dick et al.*, 1991; *Dick*, unpublished data, 1990]. These data sets encompass a total of 8 transforms and 14 nontransform offsets with age offsets from 0.1 to 23 Ma and half-spreading rates from 0.8 to 7.7 cm/yr. Additional data from the southern MAR [*Kuo and Forsyth*, 1988; *Blackman and Forsyth*, 1991; *Neumann and Forsyth*, 1993] show similar IC/OC asymmetry but were not included in this study due to less dense coverage of the IC and OC areas. In each data set studied, residual mantle Bouguer anomalies (RMBA) are derived by subtracting from the free-air anomaly the following predictive components: (1) the effects of water-crust and crust-mantle interfaces assuming a reference 6-km-thick crust and water, crust and mantle densities of 1030, 2700 and 3300 kg/m^3, respectively; and (2) the effects of mantle density changes due to lithospheric cooling [*Kuo and Forsyth*, 1988; *Lin et al.*, 1990] based on a three-dimensional model of passive mantle upwelling [*Phipps Morgan and Forsyth*, 1988]. We infer crustal thickness variations primarily from the RMBA data since little seismic refraction data are currently available at either IC or OC crust along slow spreading centers [cf. *Detrick et al.*, 1993].

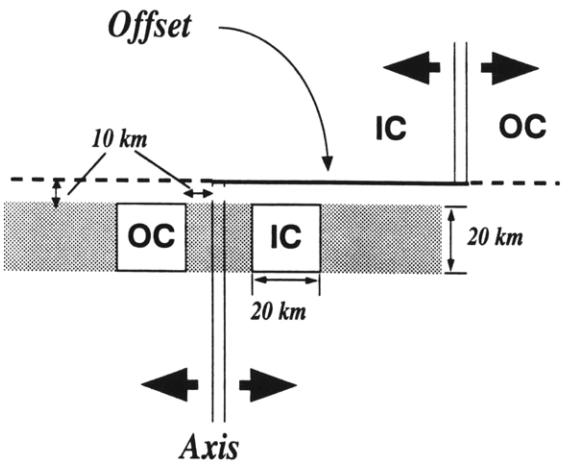

Figure 3. Method of defining the differences between IC and OC crust. Average across-axis profiles in bathymetry and gravity are calculated by stacking and averaging several profiles along each corridor (shaded area). To define an average IC/OC asymmetry we subtract the average depth in the conjugate IC and OC boxes (20 km x 20 km each), following the method of *Severinghaus and Macdonald* [1988].

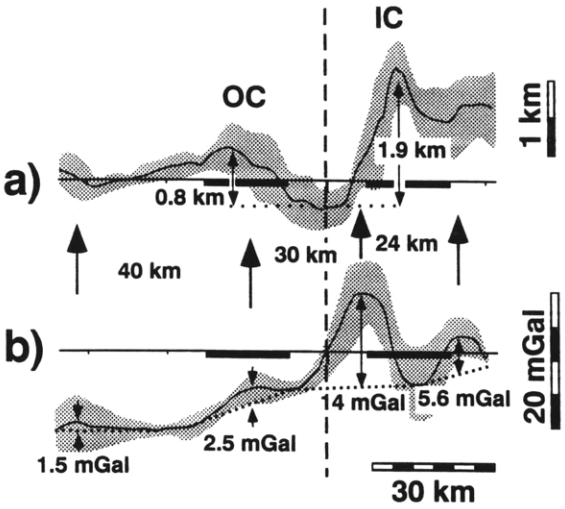

Figure 4. Examples illustrating methodology in measuring (a)individual fault scarps and (b) gravity spikes. (Data from the Oceanographer F. Z. in Figure 5.) The average profiles are marked by solid lines, and 1σ deviations are denoted by shaded regions. Thick bars on horizontal axis marks the location of the small IC and OC boxes shown in Figure 3. Location of local gravity peaks, which are interpreted as fault related, is marked by single-headed arrows; the spacing between successive relative gravity peaks is given in kilometers. Vertical relief on a fault scarp is measured from the axial valley floor. Amplitudes of individual gravity peaks (double-headed arrows) are calculated from a chosen baseline (dotted line) that connects points between low values. Since the choice of the baseline is somewhat subjective, maximum and minimum amplitudes are estimated for each gravity peak using different baselines.

In each study area we define a 20-km-wide corridor that lies parallel to the trace of a ridge offset crossing the spreading axis (shaded area in Figure 3). This corridor is located ~10 km away from the offset to avoid inclusion of transform fault valleys or nontransform basins. For those segments with along-axis length of less than 40 km, the corridor width is reduced to less than 20 km in order to prevent overlapping between corridors at two ends of a common segment. Bathymetric and RMBA profiles were calculated for each corridor (Figure 4). From these profiles we then identified and measured the location of individual gravity spikes (local peaks), the spacing between the peaks, the relative amplitudes of the peaks, and the vertical relief of the associated fault scarps (Figure 4).

The bathymetry and residual gravity profiles from both transforms (Figure 5) and nontransform offsets (Figure 6) reveal several systematic patterns. The residual gravity profiles are characterized by a succession of relative gravity peaks spaced 10 to 50 km (Figures 5 and 6), with average spacing of 16 km between off-axis peaks and 27 km for the nearest peaks abutting the ridge axis (Figure 7). The first pair of gravity peaks on either side of the ridge axis are consistently associated with fault scarps bounding the inner valley floor (e.g., profile 6, Figure 5; profile 18, Figure 6), although some profiles are too short to characterize the full shape of a peak (e.g., profile 16, Figure 6). The amplitude of the gravity peaks can reach 20 mGal and tends to increase with increasing relief on the corresponding fault scarps

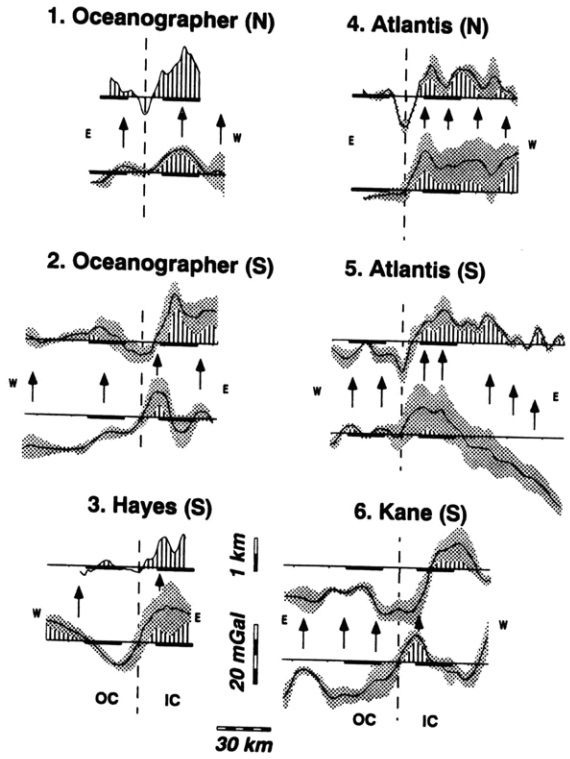

Figure 5. Averaged across-axis profiles in bathymetry and residual gravity for the transform offsets listed in Table 1. For each transform the upper profile corresponds to bathymetry and the lower profile to gravity. E and W mark east and west, respectively. Arrows indicate the location of local gravity peaks.

(Figure 8). Furthermore, larger fault scarps and gravity peaks are consistently associated with IC crust.

To define a value of across-axis asymmetry, values of bathymetry and gravity were averaged over a conjugate pair of 20 km x 20 km boxes at IC and OC crust, following the method of *Severinghaus and Macdonald* [1988]. The difference in the averaged values between the IC and OC boxes is then defined as the average asymmetry. For each site we also define a maximum asymmetry, which represents the largest difference between axis-parallel profiles that are located 15-25 km on opposite sides of the ridge axis and run over the highest IC topography [*Severinghaus and Macdonald*, 1988]. In our discussion, however, we refer primarily to the average asymmetry since it is a lesser subjective measurement. We also measured rift valley relief and ridge offset length using *Severinghaus and Macdonald*'s [1988] method (Table 1).

Results in Table 1 show that the average IC/OC asymmetries are significantly larger near transforms than nontransform offsets: the bathymetric asymmetry of individual transforms ranges from 0.4 to 1.0 km with a mean of 0.8 km. In contrast, the asymmetry of nontransform offsets ranges from 0.0 to 0.8 km with a mean of 0.4 km. Similarly, the gravity asymmetry of transforms ranges from 4.4 to 17.6 mGal with a mean of 10 mGal, whereas asymmetry of nontransform offsets ranges from -0.3 to 14.2 mGal with a mean of 5.7 mGal. These data suggest that although the crust is more elevated and thinner at all ICs, the anomalies are greater at transforms than at nontransform offsets.

The average asymmetry data also reflect fundamental differences in gross morphology between fast and slow spreading ridges (Table 1 and Figure 9). The fast spreading EPR (5.5-7.7 cm/yr half rate) is characterized by an axial high and more symmetrical IC and OC crust (Figures 9a and 9d). This is in contrast to the large variabilities in average asymmetry values for the slow spreading MAR and SWIR (0.8-1.4 cm/yr half rate). Within the slow spreading ridges, however, there is little correlation between average asymmetry and axial valley relief (correlation factor $r^2<0.1$ in all cases) (Figures 9c and 9f). *Severinghaus and Macdonald* [1988] suggested a linear relationship between these two parameters (dotted line in Figure 9c) that was not resolved by our limited data set. Consistent with the results from individual fault scarps (Figure 8), the average asymmetry is in general greater near transform than nontransform offsets (Figures 9b and 9e).

Crustal Thinning Models

To investigate possible contributions of normal faults to the observed gravity anomaly spikes, we examine in detail two-dimensional, axis-perpendicular kinematic models of crustal faulting. Using these models we calculate gravity anomalies associated with single and multiple faults, study the sensitivity of gravity anomalies to changes in fault geometry and crustal thickness, and compare theoretical results with the observed MAR data. We interpret the data using an end-member model of normal faulting. Other factors such as crustal density and thickness variations may also affect the gravity structure but are not the focus of this study.

Kinematic Models

Our model assumes a faulted elastic lithospheric layer overlying an inviscid, ductile mantle [*King et al.*, 1988; *Stein et al.*, 1988; *Weissel and Karner*, 1989; *Lin and Parmentier*, 1990]. The flexural response of the lithosphere is calculated for given combinations of fault geometry, effective elastic thickness (T_e), and density structure (Figure 10).

We examined both planar and listric fault geometries (Figure 11). In the case of a planar fault, dip angle (α) and downdip slip (s) are two critical parameters (Figures 11c and 11d). In the case of a listric fault, we define a detachment depth (where the fault becomes horizontal) and a dip angle at the seafloor; the fault curvature corresponds to an arc circle (Figures 11a and 11b). Displacement along the fault is imposed using a constant heave model [e.g., *Gibbs*, 1983] that assumes constant horizontal displacement [*Dula*, 1991]. Submersible observations show that fault scarps on the seafloor have slopes from less than 30° to 60° [*Macdonald and Luyendyk*, 1977; *Karson and Dick*, 1983, 1984; *Mével et al.*, 1991]; however, slopes derived from multibeam data rarely exceed 40° [*Escartín and Lin*, 1992]. In addition to deteriorating effects from mass wasting [*Tucholke*, 1992], talus accumulation, and sedimentation, the low apparent slopes in multibeam data may be largely due to inability of multibeam systems (footprint size of ~150 m x 150 m) to accurately resolve individual fault scarps. Thus good constraints on the dip angle of fault scarps cannot be accurately measured from available multibeam bathymetric data. Studies in ophiolites [e.g., *Alexander and Harper*, 1992; *Alexander et al.*, 1993] suggest that faults can be low-angle and propagate into the mantle and that the

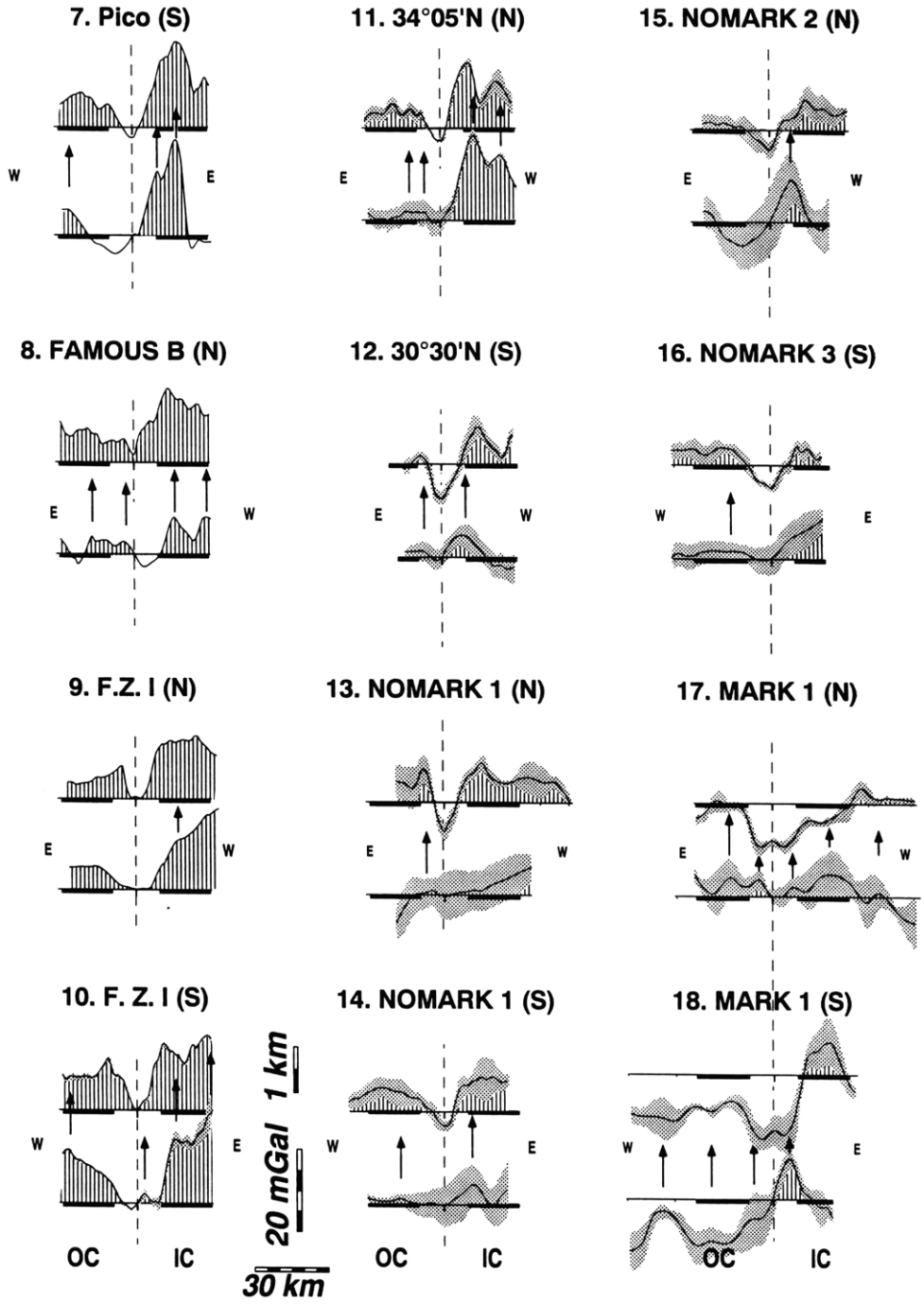

Figure 6. Averaged across-axis profiles in bathymetry and residual gravity for nontransform offsets listed in Table 1. See Figure 5 for explanations.

existence of a ductile layer in the lower crust or upper mantle could favor the formation of listric faults [*Harper*, 1985]. Such low-angle faults would exhumate mantle rocks at ICs of ridge offsets [e.g., *Karson*, 1990; *Mével et al.*, 1991; *Tucholke and Lin*, 1994] and their dip could be rotated to lower angles [*Buck*, 1993].

Estimates of the effective elastic thickness in the vicinity of slow-spreading ridge axes range from 2 to 13 km [*McKenzie and Bowin*, 1976; *Cochran*, 1979; *Louden and Forsyth*, 1982; *Blackman and Forsyth*, 1991; *Neumann and Forsyth*, 1993]. As the gravity anomaly is insensitive to the assumed T_e (Figure 10c),

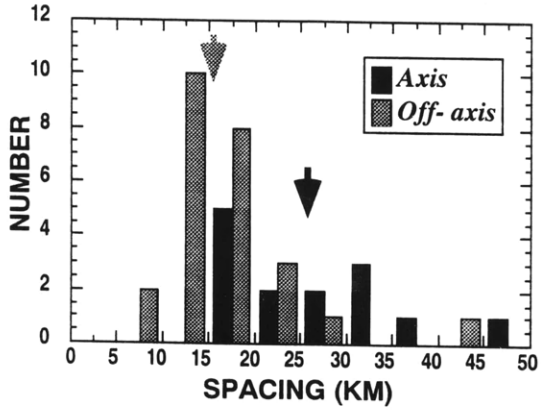

Figure 7. Histogram of measured spacings between successive gravity peaks from the profiles shown in Figures 5 and 6. We have separated the spacing values measured between peaks abutting the ridge axis (axis, black bars), and those measured between peaks off axis (off-axis, shaded bars). Arrows indicate the averages for each population (16 km for the off-axis data and 27 km for the axis data).

for the rest of our calculations we adopt T_e = 3 km, which is the average value reported for the MAR between the Kane and Atlantis transforms [*Ruppel and Shaw*, 1992] and appropriately fits the observed topography.

We assume densities of 1030 and 3300 kg/m^3 for the water and upper mantle, respectively, and an average crustal density of 2750 kg/m^3. The results of residual gravity anomaly for a three-layer or a five-layer crust with density increasing from 2600 at surface to 2900 kg/m^3 right above the Moho are practically identical to each other; they differ only slightly from the single-layer crust model with an uniform density of 2750 kg/m^3 (Figure 10b). We thus use the three-layer crust model in our discussion. The gravitational effects of various density interfaces were calculated using the upward continuation method of *Parker* [1973].

Sensitivity to Fault Parameters

Given the lack of good, direct constraints on fault configurations at depth, we examined a range of planar and listric fault geometries with different dip angles and detachment depths. These models allow us to predict the sensitivity of gravity anomalies to changes in model fault parameters, and the theoretical results can be used to compare with the observed RMBA.

Examples of two listric and two planar faults with vertical relief of 2 km each are shown in Figure 11. In the cases of listric faults, the dip angle at the seafloor is 45° and detachment depths are 7 km (Figure 11a) and 3 km (Figure 11b), respectively. For planar faults we examined cases with dip angle of 45° (Figure 11c) and 30° (Figure 11d), respectively. Although all four configurations have a very similar surficial expression, the predicted gravity anomalies vary from ~6 to ~18 mGal. The predicted anomaly is largest (~18 mGal) for the low-angle planar fault that propagates into the mantle (case d), and smallest (~6 mGal) for the listric fault confined to the crust (case b). When propagating into the mantle, both the listric (case a) and high-angle planar fault (case c) yield anomalies of ~10 mGal. These results suggest that large gravity anomalies may be found only where faults propagate deep enough to disturb the crust-mantle interface, whereas if faults are restricted to within the crust the anomalies will be small. Since the noise level of sea surface gravity data is between 2 and 5 mGal, only those faults with relatively large vertical throws are detectable. The model also indicates that the gravity anomaly is located at the base of the fault scarp (Figures 11 and 12) at a distance that will depend on the fault angle and slip as well as the crustal thickness. Such a relationship between the gravity peak and the fault scarp can be observed in many of the profiles in Figures 5 and 6. For cases in which such correlation does not hold (e.g., profiles 10 and 11, Figure 6), the gravity anomaly might be caused by off-axis variations in density or crustal thickness not associated with faulting.

Tectonic extension of the oceanic crust through normal faulting is thought to be between 10% and 20% of the total seafloor spreading for slow spreading ridges [*Macdonald and Luyendyk*, 1977; *Solomon et al.*, 1988]. In the simplest case of multiple faults with identical dip angles and displacements, we

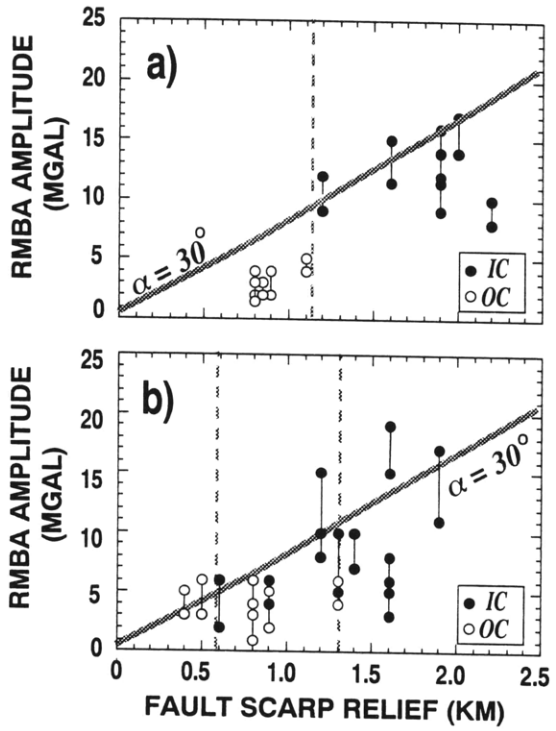

Figure 8. Measured amplitude of RMBA peaks plotted as a function of fault scarp relief for profiles parallel to (a) transforms and (b) nontransform offsets. Only the first gravity peaks on each side of the ridge axis are considered, and the estimated maximum and minimum values are shown (connected dots). Note that fault scarps associated with IC crust (solid circles) have larger relief and associated RMBA than those of OC crust (open circles). The transition between IC and OC crust in terms of relief on fault scarps occurs at ~1.5 km for transforms (Figure 8a) and 0.6-1.3 km for nontransform offsets (dashed lines). Inclined gray lines mark a theoretical relationship between gravity anomaly and fault throw for a 30° dipping fault that is separated 50 km from the nearest faults (See Figure 13 for further explanation).

Table 1. Measured Asymmetry Between Inside- and Outside-Corner Crust

Offset	Name	Side	Latitude	HSR*, cm/yr	Rift Relief, km	Offset, km	Offset, m.y.	Bathymetric Asymmetry+ Avg., km	Bathymetric Asymmetry+ Max., km	Bathymetric Asymmetry+ s.d., km	Gravity Asymmetry Avg., mGal	Gravity Asymmetry Max., mGal	Gravity Asymmetry s.d., mGal	References
Mid-Atlantic Ridge Transform Offsets														
‡ 1	Oceanographer	N	35°00'N	1.1	0.7	128	11.6	0.4	1.5	0.8	8.2	9.5	3.6	1
‡ 2	Oceanographer	S	35°00'N	1.1	0.8	128	11.6	0.6	1.5	0.5	6.7	20.3	7.0	1
3	Hayes	S	34°00'N	1.1	0.5	85	7.7	0.4	1.6	0.8	9.3	15.5	6.7	1
4	Atlantis	N	30°40'N	1.2	1.3	65	5.4	0.9	1.9	0.5	17.6	22.6	4.7	2, 3
5	Atlantis	S	30°40'N	1.2	0.5	65	5.4	1.0	1.8	0.5	4.4	19.0	9.6	2, 3
6	Kane	S	23°40'N	1.4	1.4	150	10.7	1.0	1.1	0.3	7.3	25.4	7.1	4
Mid-Atlantic Ridge Nontransform Offsets														
‡ 7	Pico Offset	S	37°40'N	1.0	0.7	45	4.5	0.7	1.0	0.5	9.3	10.2	7.4	1
‡ 8	FAMOUS B	N	36°35'N	1.0	1.0	22	2.2	0.8	1.1	0.4	5.4	9.3	4.6	1
‡ 9	FZ I	N	34°30'N	1.1	0.8	39	3.5	0.8	1.0	0.4	10.3	13.5	4.6	1
‡ 10	FZ I	S	34°30'N	1.1	1.4	39	3.5	0.6	1.0	0.5	5.9	7.7	2.3	1
‡ 11	34°05'N	N	34°05'N	1.1	1.4	36	3.3	0.6	1.4	0.3	14.2	24.0	2.8	1
12	30°30'N	S	30°30'N	1.2	1.3	4	0.3	0.5	1.5	0.3	2.7	11.6	4.6	2, 3
13	NOMARK 1	N	29°23'N	1.3	1.6	15	1.2	0.2	0.7	0.4	9.2	13.0	9.7	2, 3
14	NOMARK 1	S	29°23'N	1.3	0.9	15	1.2	0.5	0.9	0.4	-0.2	3.9	6.3	2, 3
‡ 15	NOMARK 2	N	28°51'N	1.3	0.9	11	0.8	0.2	0.9	0.4	7.5	9.7	8.6	2, 3
16	NOMARK 3	S	28°42'N	1.3	0.6	3	0.2	0.1	0.5	0.3	3.6	3.9	5.8	2, 3
17	MARK 1	N	23°08'N	1.4	1.0	5	0.4	0.0	1.1	0.5	0.6	4.2	6.1	4
18	MARK 1	S	23°08'N	1.4	0.8	5	0.4	0.3	0.7	0.4	-0.3	5.6	4.0	4
East Pacific Rise Transform Offsets														
19	Wilkes	N	8°05'S	7.7	-0.3	150	1.9	0.1	0.2	0.3	-0.8	2.0	3.1	5
East Pacific Rise Nontransform Offsets														
20	9°03'N OSC	N	9°03'N	5.5	-0.3	8	0.2	0.0	0.1	0.1	-0.4	1.0	2.9	6
21	7°12'S OSC	S	7°12'S	7.7	-0.3	8	0.1	0.1	0.3	0.4	2.0	2.5	2.4	5
Southwest Indian Ridge Transform Offsets														
‡ 22	Atlantis II	E	32°30'S	0.8	0.8	201	23.1	1.2	1.8	0.5	16.6	38.6	13.6	7, 8

References: 1, *Detrick et al.* [1995; 2, *Purdy et al.* [1990]; 3, *Lin et al.* [1990]; 4, *Morris and Detrick* [1991]; 5, *Wang and Cochran* [1993]; 6, *Madsen et al.* [1990]; 7, *Dick et al.* [1991]; 8, *H. J. B. Dick* (unpublished gravity data, 1990).

*HSR, half-spreading rate.

+Avg., average asymmetry; Max., maximum asymmetry; s.d., standard deviation.

‡ Offsets for which asymmetry is calculated over areas <20 km x 20 km.

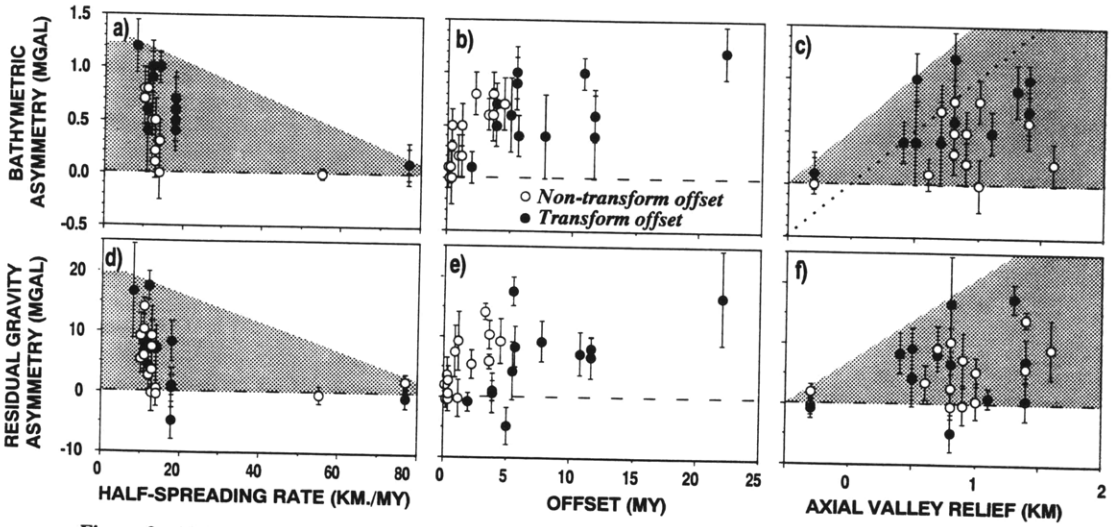

Figure 9. (a)-(c) Average asymmetry in bathymetry and (d)-(f) residual gravity as a function of half-spreading rate (Figures 9a and 9d), age offset (Figures 9b and 9e), and axial valley relief (Figures 9c and 9f). Error bars mark 1σ standard deviation. Dashed lines mark zero asymmetry. The dotted line in Figure 9c shows a linear relationship proposed by *Severinghaus and Macdonald* [1988]. The fan-shaped shaded areas illustrate that variations in asymmetry decrease with decreasing axial valley relief and increasing spreading rate. Open circles: nontransform offsets; closed circles: transform offsets.

can express the proportion of tectonic extension (faulting) to magmatic accretion as the ratio between the horizontal displacement on individual faults (heave) and the spacing between the successive faults. In Figure 12 we present two different multiple-fault models, both with dip angle of 45° and 10% of seafloor spreading by tectonic extension. In case a, faults are spaced 10 km apart with horizontal displacements of 1 km each, whereas in case b, faults are spaced 30 km apart with displacement of 3 km each. These values are comparable to the observed spacings and vertical reliefs on the northern MAR faults (Figure 5). These two cases show clear differences in the gravity anomaly: the peak-to-trough anomaly is practically negligible (~3 mGal) for closely spaced faults with moderate throws (case a), whereas the anomaly is large (~13 mGal) for widely spaced faults with large throws (case b). The peaks in the gravity anomaly (arrows) are located in front of the associated fault scarps, similar to the observed correlation between gravity spikes and fault scarps at the MAR (e.g., profiles 2 and 5 in Figure 5). Small fault scarps not identifiable in Sea Beam can exist [e.g., *Mitchell*, 1991; *Cowie et al.*, 1993] and have not been considered as the anomalies associated with them are too small to be detected on the shipboard gravity data.

Our models reveal that the amplitude and shape of the anomaly is insensitive to crustal thickness. Apart from the

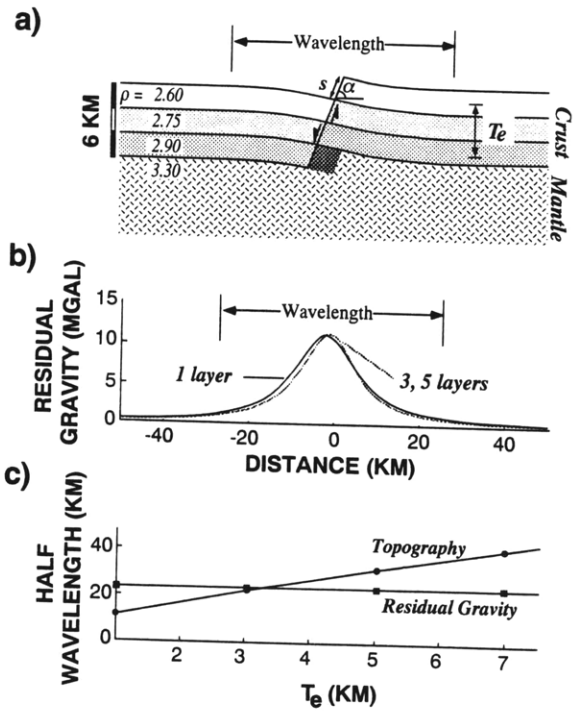

Figure 10. (a) Schematic diagram showing basic parameters used in single-fault models. The crust is divided into three layers with densities of 2600, 2750, and 2900 kg/m^3, respectively. The water and mantle densities assumed are 1030 and 3300 kg/m^3, respectively. For each planar fault, dip angle α and downdip slip s are specified. The darker shading corresponds to the portion of the mantle that is the source of the residual gravity anomaly. (b) Comparison of predicted gravity anomalies for a single fault with one, three, and five assumed crustal sublayers. Note that the three-layer model provides good approximation to the more complex five-layer model. (c) Kernels relating the predicted wavelengths of fault-induced topography and residual anomaly to the effective elastic plate thickness T_e. For all calculations, α = 45°, s=1 km, and the initial crustal thickness is 6 km.

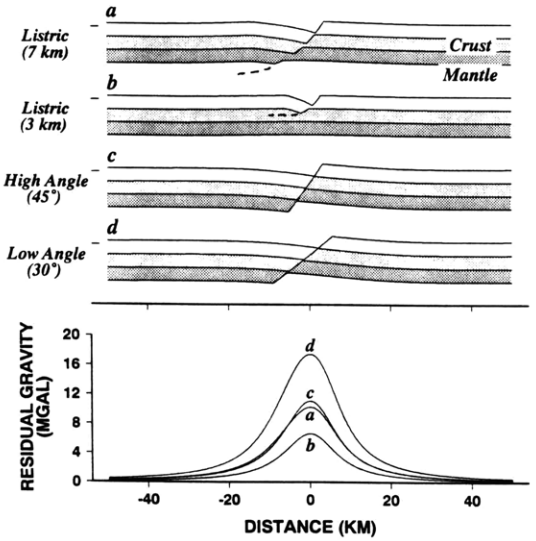

Figure 11. Two-dimensional models of crustal faulting assuming listric (models a and b) and planar geometries (models c and d). In all cases a 2-km vertical fault displacement at the seafloor is assumed. Note that the model of a low-angle fault propagating into the mantle produces the greatest gravity anomaly (model d), while the model of a listric fault restricted to the crust (model b) produces the least anomaly. Models a and c have very similar geometries and similar resultant gravity anomalies.

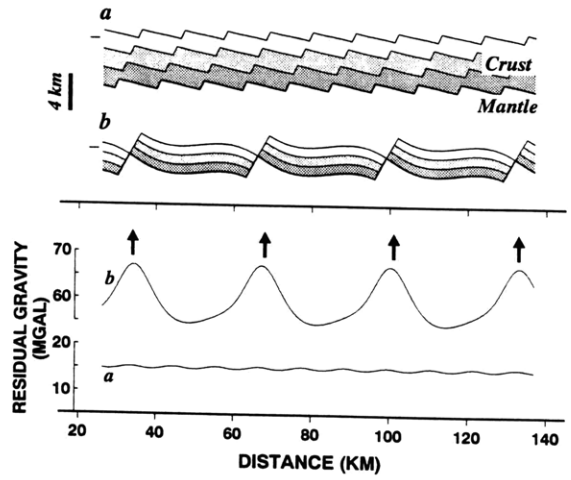

Figure 12. Two multiple-fault models both with 10% tectonic extension (defined as the ratio of horizontal displacement on each fault to fault spacing). Case a is characterized by 10-km fault spacing, 1-km throw, and 6-km initial crustal thickness. Case b has 30 km of fault spacing, 3 km of throw, and 3 km of crustal thickness. Arrows show location of predicted gravity peaks. Note that gravity anomalies produced by small, closely spaced faults are too small to be recognizable in shipboard data with a noise level of 2-5 mGal. Larger and widely spaced faults, on the other hand, can produce significant gravity anomalies (case b). The average level of gravity anomalies is grater in case b because the initial crust thickness is smaller for case b (3 km) than for case a (6 km).

differences in fault spacing and throw, the models in Figure 12 have initial crustal thicknesses of 6 km (case a) and 3 km (case b). A reduction in initial crustal thickness from 6 to 3 km increases the average level of the anomalies from 15 mGal (case a) to 60 mGal (case b) (Figure 12).

Consistent with the results of single-fault calculations (Figure 11), multiple-fault models also predict that lower dip angle and larger throw would result in larger gravity anomalies (Figures 13a and 13b). From simple geometrical arguments, the volume of the mantle material responsible for the calculated residual gravity anomaly high (darker shading in Figure 10) is $V = h\,c\,/\,\sin(\alpha) = s\,c\,/\,\tan(\alpha)$ where h is the fault heave, s the slip, α the angle, and c the crustal thickness. In addition, multiple-fault models predict larger anomalies for more widely spaced faults. The results of Figure 13 thus indicate that, in the case of planar faults propagating into the mantle, only those faults with relatively large throws and relatively large spacings will produce residual gravity anomalies that are recognizable from the observed RMBA data.

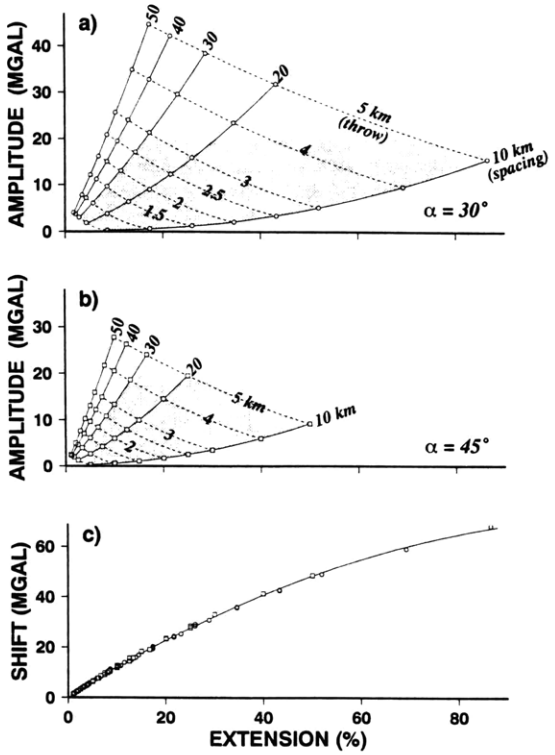

Figure 13. (a) (b) Kernels relating the peak-to-trough amplitude of gravity anomalies and the amount of crustal extension (percent) for different values of fault spacing and throw. (a) Planar faults with dip angles of 30°. (b) Planar faults with dip angles of 45°. The assumed initial crustal thickness is 6 km in all cases. Note that the amplitude of anomalies increases with increasing fault spacing and throw and decreasing dip angle. The shading oulines the area constrained by the measured spacing of gravity peaks (10-30 km, Figure 7) and the amplitude of the measured gravity peaks (<20 mGal, Figure 8). (c) The shift in the average level of gravity anomalies increases with the amount of tectonic extension.

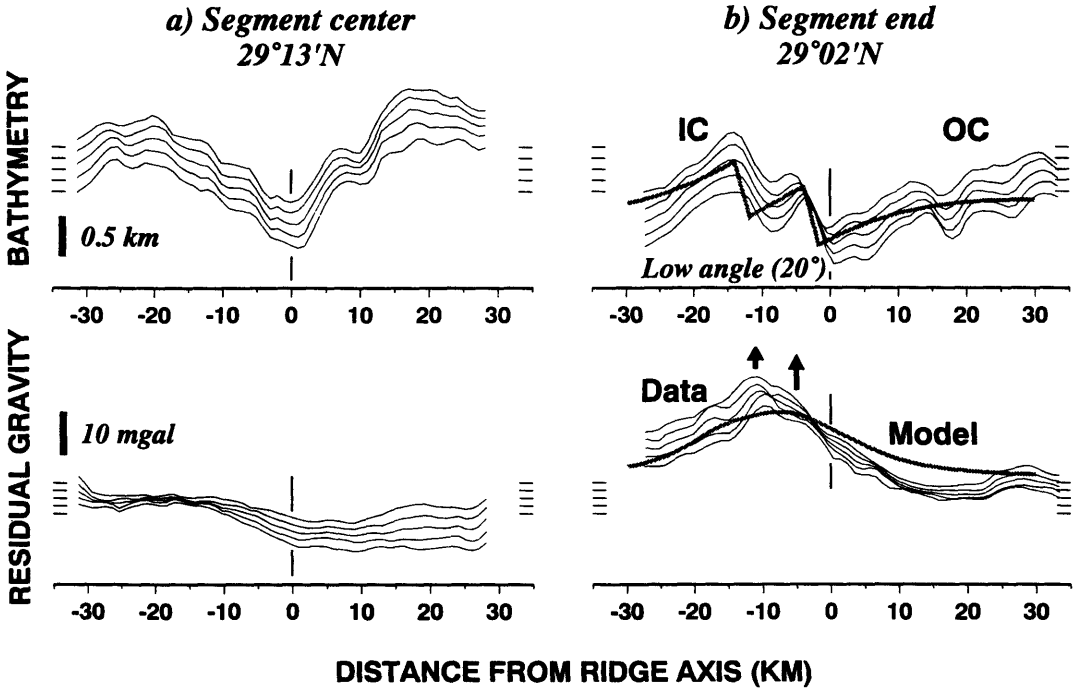

Figure 14. Stacked across-axis profiles in (top) bathymetry and (bottom) residual gravity at the (a) center and (b) the distal end of a MAR segment near 29°N. Short horizontal lines on the left of each plot indicate the reference depths (3 km) and reference RMBA value (15 mGal) for each individual profile. Note that the axial valley is more symmetric and the gravity anomaly is small at the segment center (Figure 14aa). Toward the distal end, however, the rift valley becomes more asymmetrical: its shape suggests that two large faults with large gravity anomalies are located at IC crust. Model calculations (gray lines) show that the gravity anomalies at IC crust can be accounted for by a model of two faults spaced 10 km apart, with throws of 0.8 km each, and a dip angle α of 20°.

Comparison With the MAR Data

Rift valley morphology and residual gravity anomalies vary significantly along slow-spreading ridges as illustrated in across-axis profiles across a MAR spreading segment near 29°N (Figure 14). Near the segment center the rift valley is symmetric, faults have small throws (<0.75 km), and the RMBA profiles are practically flat (Figure 14a). Near the segment end, in contrast, two major fault scarps with large gravity anomalies occur at IC crust (Figure 14b). This along-axis change in rift valley morphology is accompanied by deepening in axial seafloor (by ~0.4 km from a to b) and increase in the RMBA (by ~15 mGal from a to b).

The two faults at IC crust are 10 km apart with throws of ~0.8 km each. Assuming an initial crustal thickness of 4 km and a dip angle of 20°, we predict a gravity anomaly with an amplitude of ~10 mGal and a wavelength of 40 km; this estimation resembles the observed RMBA (Figure 14b). Our calculations also reveal that the smaller (<0.5 km throw) and more closely spaced (<5 km) faults near the segment center and at OC crust would produce RMBA anomalies with amplitudes <3 mGal (Figure 12).

To a first order, the low-angle fault model (30° dip angle) also predicts the trend observed in the gravity peaks associated with individual fault scarps abutting the MAR axis (Figure 8). This low-angle fault model provides an approximate upper bound to the data near transforms (Figure 8a). Some anomalies in Figure 8a are smaller than predicted by this model, and they could be associated with steeper or more closely spaced faults. The remaining scattering in the data may reflect the complex lithologic structure of the lithosphere at slow spreading ridges [*Cannat*, 1993]. Since gravity solutions are non-unique and decay rapidly from source regions, future seismic mapping [e.g., *Mutter and Karson*, 1992] and near-bottom gravity surveys are required to further delineate more detailed structural differences between IC and OC crust.

Discussion

Role of Transform Faults

Transform offsets are characterized by the existence of a strike-slip fault that mechanically decouples the lithospheric plates created at adjacent spreading centers (Plate 1a). Data in Figure 8 show that fault scarps and the associated crustal thinning are systematically greater at IC crust than at OC crust. Such a strong tendency of large low-angle faults to develop at IC crust may be because less work is required to cause finite amplitude extension in IC crust which is decoupled across the transform fault (Figure 15). High elevations of IC crust may thus be the direct consequence of footwall uplifts associated with individual IC low-angle faults. Additional uplift could be produced by three-dimensional isostatic compensation to deep transform valley topography [*Collette*, 1986] and by visco-elastic stresses associated with ridge-transform shearing [*Bercovici et al.*, 1992].

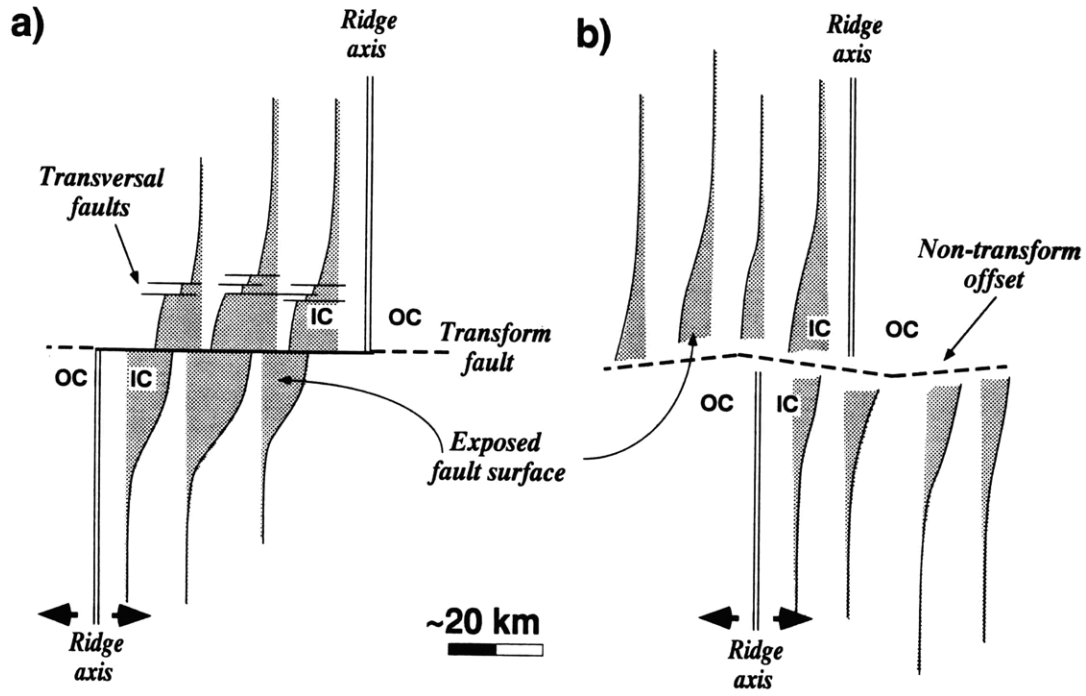

Figure 15. A model of along-axis changes in the structure of low-angle faults near (a) transforms and (b) nontransform offsets. Low-angle fault surfaces allow the exposure of lower crust and/or upper mantle rocks. We postulate that low-angle faults initiate preferentially at IC crust. These faults must die out gradually and may become higher angle toward segment centers. Secondary, axis-perpendicular transversal faults may dissect the low-angle faults and accommodate part of the decrease in fault throw toward segment centers. Toward ridge offsets, low-angle faults may be terminated either by a strike-slip fault along a transform (dashed line in Figure 15a) or an accommodation zone at a nontransform offset (dashed line in Figure 15b). Smaller, higher-angle normal faults at IC crust, OC crust and segment centers were not depicted.

Low-angle faults at IC crust must be finite in its along-axis length, as there is no evidence for exposed lower crust and upper mantle at segment centers or at OC crust [*Tucholke and Lin*, 1994]. Transform faults offer an optimal shear zone in which low-angle faults can terminate laterally toward the end of a segment. Low-angle faults must die out gradually toward the segment center, reducing fault throw and possibly steepening dip angle. This will result in the pinning of the exposed fault surface away from ridge offsets (shaded regions in Figure 15a). Minor transversal faults (thin lines in Figure 15a) could contribute to accommodate some along-axis variations in the strain distribution of low-angle faults [*Dick et al.*, 1991] as earlier studies indicated [*Karson*, 1991; *Cannat et al.*, 1993].

The spacing of the gravity spikes along IC crust near the MAR axis ranges from 10 to 50 km, (Figure 8), similar to the spacing of fossil topographic highs on the transverse ridges bounding the Atlantis II Transform [*Dick et al.*, 1991] and other MAR transverse ridges [*Bonatti and Honnorez*, 1976; *Bonatti et al.*, 1983; *Pockalny et al.*, 1988]. If, as proposed here, the gravity spikes are created by faults, the spacing implies that the formation of individual low-angle faults is a transient process that occurs episodically (every ~2 m.y.). At present, however, there is little data to constrain if the successive low-angle faults at IC crust of the MAR might be active simultaneously [cf. *Shaw and Lin*, 1993].

Role of Nontransform Offsets

Nontransform offsets differ from transform faults in a number of ways. First, instead of being associated with a well-defined strike-slip fault, a nontransform offset is often associated with a relatively wide deformation zone with complex morphology and tectonics [e.g., *Searle and Laughton*, 1977; *Searle*, 1979; *Sempéré et al.*, 1993] (Plate 1b). Second, whereas off-axis traces indicate that transform faults are long-lived and relatively stable, nontransform offsets are commonly characterized by along-axis migrations and have a limited life span [e.g., *Macdonald et al.*, 1991; *Sempéré et al.*, 1993]. Third, the lack of a well-defined decoupling strike-slip fault across some nontransform offsets may require the differential slips between adjacent spreading segments be accommodated by along-axis ridge migration and overlapping normal faults [*Grindlay et al.*, 1991]. Because of these differences between transforms and nontransform offsets, we expect low-angle faults to be smaller and the tendency of low-angle faults to occur at IC crust to be lesser near nontransform offsets (Figure 15b). This is consistent with the slightly smaller anomalies and the more diffuse transition between IC and OC domains in Figure 8. However, as in the case of transform offsets, detachment faults must also pin gradually toward segment centers. Occurrence of gravity spikes along the off-axis traces of some MAR nontransform offsets [*Deplus et al.*, 1992;

Tucholke et al., 1992; *Lin et al.*, 1993; *Rommeveaux et al.*, 1994] suggests that low-angle faults have similar life span near transform and nontransform offsets.

Conclusions

Our systematic analysis of high-resolution bathymetric and gravity data along the Mid-Atlantic Ridge and Southwest Indian Ridge reveals significant differences in crustal structure and tectonic faulting between inside and outside corner crust of these slow spreading ridges. A consistent pattern of positive residual gravity anomalies is found over elevated inside corner crust paralleling transform and nontransform offsets. Individual gravity spikes, which have amplitudes of up to ~20 mGal and across-axis spacings of 10-30 km (Figure 7), often coincide with individual fault scarps and may therefore reflect tectonic thinning of the crust by normal faulting. Theoretical calculations indicate that the amplitude and spacing of such gravity spikes can be adequately explained by the presence of successive, ridge-parallel low-angle faults. The gravity anomaly caused by individual faults is predicted to increase with increasing fault throw and spacing and decreasing dip angle. It is found that fault scarps and crustal thinning (as inferred from gravity anomalies) are consistently larger at inside corner crust than outside corner crust, indicating that tectonic extension near ridge offsets is asymmetric with low-angle faults occurring preferentially at inside corner crust.

Results of the analysis show significantly larger average inside corner versus outside corner asymmetries near transforms than nontransform offsets: the bathymetric asymmetry of individual transforms ranges from 0.4 to 1.0 km with a mean of 0.8 km. In contrast, the corresponding asymmetry of nontransform offsets ranges from 0.0 to 0.8 km with a mean of 0.4 km. Similarly, the gravity asymmetry of individual transforms ranges from 4.4 to 17.6 mGal with a mean of 10 mGal, whereas asymmetry of nontransform offsets ranges from -0.3 to 14.2 mGal with a mean of 5.7 mGal. Such contrasts in the degree of asymmetries may be related to the difference between transforms and nontransform offsets in the extent of lithospheric plate decoupling across the offsets.

The above results on spatial variations in seafloor morphology and gravity anomalies further support a three-dimensional tectonic faulting model at oceanic spreading centers. Low-angle faults may form preferentially at IC crust, where the mantle lithosphere is the strongest and the lithospheric plates are sufficiently decoupled across ridge-axis offsets. Low-angle faults must decrease in throw toward midpoints of long ridge segments, where large low-angle faults may not be sustained by a weak lithosphere. Detail structure of such along-axis changes in fault geometry and their termination toward ridge-offsets are still poorly known at present and await further high-resolution geological, geophysical, and seismological studies.

Acknowledgments. We are grateful to R. Detrick for providing digital bathymetric and gravity data of parts of the MAR and to H. Dick and J. Snow for furnishing unpublished data of the SWIR. We benefited from discussion with C. Ruppel, B. Tucholke, P. Shaw, G. Jaroslow, H. Dick, and C. Wolfe, and editing by L. Pradiero. The manuscript was improved by thoughtful reviews of W. R. Buck, M. Cannat, and N. C. Mitchell. This work was supported by ONR grant N00014-91-J-1433 and NSF grant OCE-9012576. Javier Escartín also benefited from a Fellowship from "Caixa de Pensions La Caixa". Contribution 8751 of Woods Hole Oceanographic Institution.

References

Alexander, R. J., and G. D. Harper, The Josephine Ophiolite: An ancient analog for slow- to intermediate-spreading oceanic ridges, in Ophiolites and their modern oceanic analogues, edited by L. M. Parson, B. J. Murton, and P. Browning, *Geol. Soc. Spec. Publ.*, London, *60*, 3-38, 1992.

Alexander, R. J., G. D. Harper, and J. R. Bowman, Oceanic faulting and fault-controlled subseafloor hydrothermal alteration in the sheeted dike complex of the Josephine Ophiolite, *J. Geophys. Res.*, *98*, 9731-9759, 1993

Barclay, A. H., D. R. Toomey, G. M. Purdy, and S. C. Solomon, FARA microearthquake experiments, III, Results from the Mid-Atlantic Ridge at 35°N (abstract), *Eos Trans. AGU, 74* (43), Fall Meeting Suppl., 601, 1993

Bercovici, D., H. J B. Dick, and T P. Wagner, Nonlinear viscoelasticity and the formation of transverse ridges, *J. Geophys. Res.*, *97*, 14195-14206, 1992.

Blackman, D. K., and D. W Forysth, Axial topographic relief associated with ridge-transform intersections, *Earth Planet. Sci. Lett.*, *95*, 115-129, 1989.

Blackman, D. K., and D. W. Forysth, Isostatic compensation of tectonic features of the Mid-Atlantic Ridge: 25-27°30' S, *J. Geophys. Res.*, *96*, 11,741-11,758, 1991.

Bonatti, E., and J. Honnorez, Non-spreading crustal blocks at the Mid-Atlantic Ridge, *Science*, *174*, 1329-1331, 1976.

Bonatti, E., R. Sartori, and A. Boresma, Vertical crustal movements at the Vema Fracture Zone in the Atlantic: Evidence from dredged limestone, *Tectonophysics*, *91*, 213-223, 1983.

Buck, W. R., Effect of lithospheric thickness on the formation of high- and low-angle normal faults, *Geology*, *21*, 933-936, 1993.

Cannat, M , Emplacement of mantle rocks in the seafloor at mid-ocean ridges, *J. Geophys Res.*, *98*, 4163-4172, 1993.

Cannat, M., et al., Crustal structure and axial segmentation Mid-Atlantic Ridge 21°-24°N (abstract), *Eos Trans. AGU, 74* (43), Fall Meeting Suppl., 664, 1993.

Cochran, J. R., An analysis of isostasy in the world's oceans, 2, Mid-ocean ridges, *J. Geophys. Res.*, *84*, 4713-4730, 1979.

Collette, B. J., Fracture zones in the North Atlantic: Morphology and model, *J. Geol. Soc. London*, *143*, 763-774, 1986.

Cormier, M.-H , K. C. Macdonald, and D. S. Wilson, A three-dimensional gravity analysis of the East Pacific Rise from 18° to 21°30'S, *J. Geophys. Res* , in press, 1995.

Cowie, P A., C. H. Scholz, M. Edwards, and A. Malinverno, Fault strain and seismic coupling on mid-ocean ridges, *J. Geophys. Res* , *98*, 17,911-17,920, 1993.

Crane, K., The spacing of rift axis highs: Dependence upon diapiric processes in the underlying asthenosphere?, *Earth Planet. Sci. Lett.*, *72*, 405-414, 1985.

Deplus, C., M. Maia, D. Aslanian, and P. Gente, Segmentation of the mid-Atlantic ridge south of Kane fracture zone revealed by gravity anomalies (abstract), *Eos Trans. AGU, 73* (43), Fall Meeting Suppl., 368, 1992.

Detrick, R. S., R. S. White, and G. M. Purdy, Crustal structure of North Atlantic fracture zones, *Rev. Geophys.*, *31*, 439-459, 1993.

Detrick, R. S., H. D. Needham, and V. Renard, Gravity anomalies and crustal thickness variations along the Mid-Atlantic Ridge between 33°N and 40°N, *J. Geophys. Res.*, in press, 1995.

Dick, H. J. B., Abyssal peridotites, very slow spreading ridges and ocean ridge magmatism, *Geol. Soc. Spec. Publ. London 42*, 71-105, 1989.

Dick, H. J. B., H. Schouten, P. S. Meyer, D. G. Gallo, H. Bergh, R. Tyce, P. Patriat, K. T. M. Johnson, J. Snow, and A. Fischer, Tectonic evolution of the Atlantis II Fracture Zone, *Proc. Ocean Drill. Program Sci. Results*, *118*, 359-398, 1991.

Dula, W. F., Geometric models of listric normal faults and rollover folds, *AAPG Bull.*, *75*, 1609-1625, 1991.

Escartín, J., and J. Lin, Morfoestructura de la dorsal medio-Atlántica entre 24°N y 30°N (Morphotectonics of the Mid-Atlantic Ridge, 24°N - 30°N), *Acta Geol. Hisp.*, *27*, 33-49, 1992.

Fujita, K., and N. Sleep, Membrane stress near mid-ocean ridge-transform intersections, *Tectonophysics*, *50*, 207-221, 1978.

Gibbs, A. D., Balanced cross-section construction from seismic sections in areas of extensional tectonics, *J. Struct. Geol.*, *5*, 153-160, 1983.

Grindlay, N. R., P. J. Fox, and K. C. Macdonald, Second-order axis discontinuities in the South Atlantic: Morphology, structure, and evolution, *Mar. Geophys. Res.*, *13*, 21-50, 1991.

Harper, G. D., Tectonics of slow-spreading mid-ocean ridges and consequences of a variable depth to the brittle/ductile transition, *Tectonics*, *4*, 395-409, 1985.

Huang, P., and S. C. Solomon, Centroid depths of mid-ocean ridge earthquakes: Dependence on spreading rate, *J. Geophys. Res.*, *93*, 13,445-13,477, 1988.

Karson, J. A., Seafloor spreading on the Mid-Atlantic Ridge: Implications for the structure of ophiolites and oceanic lithosphere produced in slow-spreading environments, in *Proceedings of the Symposium TROODOS 1987*, edited by J Malpas et al., pp. 547-555, Geological Survey Department, Nicosia, Cyprus, 1990.

Karson, J. A., Accommodation zones and transfer faults: Integral components of mid-ocean ridge extensional systems, in *Ophiolite Genesis and Evolution of the Oceanic lLthosphere*, edited by T J. Peters, A. Nicolas, and R. G. Coleman, pp. 21-37, Ministry of Petroleum and Minerals, Sultanate of Oman, Muscat, 1991.

Karson, J. A., and H. J. B. Dick, Tectonics of ridge-transform intersections at the Kane Fracture Zone, *Mar. Geophys. Res.*, *6*, 51-98, 1983.

Karson, J. A., and H. J. B. Dick, Deformed and metamorphosed crust on the Mid-Atlantic Ridge, *Ofioliti*, *9*, 279-302, 1984.

King, G. C., R. S. Stein, and J. B. Rundle, The growth of geological structures by repeated earthquakes, 1, Conceptual framework, *J. Geophys. Res.*, *93*, 13,307-13,318, 1988.

Kuo, B. Y , and D. W. Forsyth, Gravity anomalies of the ridge-transform system in the South Atlantic between 31 and 31°S: Upwelling centers and variations in crustal thickness, *Mar. Geophys. Res.*, *10*, 205-232, 1988.

Kuo, B. Y, J. Phipps Morgan, and D. W. Forsyth, Asymmetry in topography of the crestal mountains near a ridge-transform intersection (abstract), *Eos Trans. AGU*, *65*, 274, 1984.

Lin, J., and E. A. Bergman, Rift grabens, seismicity and volcanic segmentation of the Mid-Atlantic Ridge: Kane to Atlantis Fracture Zones (abstract), *Eos Trans. AGU*, *71*, 1572, 1990.

Lin, J., and E. M. Parmentier, A finite amplitude necking model of rifting in brittle lithosphere, *J. Geophys. Res* , *95*, 4909-4923, 1990.

Lin, J., and J. Phipps Morgan, The spreading rate dependence of three-dimensional mid-ocean ridge gravity structure, *Geophys. Res. Lett* , *19*, 13-15, 1992

Lin, J., G. M. Purdy, H. Schouten, J. C. Sempéré, and C. Zervas, Evidence from gravity data for focused magmatic accretion along the Mid-Atlantic Ridge, *Nature*, *344*, 627-632, 1990.

Lin, J., B. E. Tucholke, and M. C. Kleinrock, Evidence from gravity and morphology for long-term variability in magmatic vs. tectonic extension at the Mid-Atlantic Ridge (abstract), *Eos Trans. AGU*, *74* (16), Spring Meeting Suppl., 303, 1993.

Louden, K. E., and D. W. Forsyth, Crustal structure and isostatic compensation near the Kane fracture zone from topography and gravity measurements, I, Spectral analysis approach, *Geophys. J R. Astron. Soc.*, *68*, 725-750, 1982.

Macdonald, K. C., and B. P. Luyendyk, Deep-tow studies of the structure of the Mid-Atlantic Ridge crest near lat 37°N, *Geol. Soc. Am Bull.*, *88*, 621-636, 1977.

Macdonald, K. C., D. S. Scheirer, and S. M. Carbotte, Mid-ocean ridges: Discontinuities, segments and giant cracks, *Science*, *253*, 986-994, 1991.

Madsen, J. A., R. S. Detrick, J. C. Mutter, P. Buhl, and Orcutt, A two- and three-dimensional analysis of gravity anomalies associated with the East Pacific Rise at 9°N and 13°N, *J. Geophys. Res.*, *95*, 4967-4987, 1990.

McKenzie, D., and C. Bowin, The relationship between bathymetry and gravity in the Atlantic Ocean, *J. Geophys Res.*, *81*, 1903-1915, 1976

Mével, C., M. Cannat, P. Gente, E. Marion, J. M. Auzende, and J. A. Karson, Emplacement of deep crustal and mantle rocks on the west median valley wall of the MARK area (MAR, 23°N), *Tectonophysics*, *190*, 31-53, 1991.

Mitchell, N. C., Distributed extension at the Indian Ocean triple junction, *J. Geophys. Res.*, *96*, 8019-8043, 1991.

Morris, E., and R. S. Detrick, Three-dimensional analysis of gravity anomalies in the MARK area, Mid-Atlantic Ridge 23°N, *J. Geophys. Res.*, *96*, 4355-4366, 1991.

Mutter, J. C., and J. A. Karson, Structural processes at slow-spreading ridges, *Science*, *257*, 627-634, 1992.

Neumann, G. A., and D. W. Forsyth, The paradox of the axial profile: Isostatic compensation along the axis of the Mid-Atlantic Ridge?, *J. Geophys. Res.*, *98*, 17,891-17,910, 1993.

Parker, R. L., The rapid calculation of potential anomalies, *Geophys. J. R. Astron. Soc.*, *31*, 447-455, 1973.

Parmentier, E. M., and J. Phipps Morgan, Spreading rate dependence of three dimensional structure in oceanic spreading centres, *Nature*, *348*, 325-328, 1990.

Phipps Morgan, J., and D. W Forsyth, Three-dimensional flow and temperature perturbations due to a transform offset: Effects on oceanic crustal and upper mantle structure, *J. Geophys. Res.*, *93*, 2955-2966, 1988.

Pockalny, R. A., R. S. Detrick, and P. J. Fox, Morphology and tectonics of the Kane transform from Sea Beam bathymetry data, *J. Geophys. Res.*, *93*, 3179-3193, 1988.

Pollard, D. D., and A. Aydin, Propagation and linkage of oceanic ridge segments, *J. Geophys. Res.*, *89*, 10017-10028, 1984.

Purdy, G. M., J. C. Sempéré, H. Schouten, D. L. Dubois, and R. Goldsmith, Bathymetry of the Mid-Atlantic Ridge, 24°-31°N: A map series, *Mar. Geophys. Res.*, *12*, 247-252, 1990.

Rabinowicz, M., A. Nicolas, and J. L. Vigneresse, A rolling mill effect in asthenosphere beneath oceanic spreading centers, *Earth Planet. Sci. Lett.*, *67*, 97-108, 1984.

Rommeveaux, C., C. Deplus, P. Patriat, and J.-C. Sempéré, Three-dimensional gravity study of the Mid-Atlantic Ridge: Evolution of the segmentation between 28° and 29°N during the last 10 m.y., *J. Geophys. Res.*, *99*, 3015-3029, 1994.

Ruppel, C., and P. Shaw, An elastic plate thickness map of the Mid-Atlantic Ridge between the Kane and Atlantis Fracture Zones, (abstract), *Eos Trans. AGU*, *73* (43), Fall Meeting Suppl., 571, 1992.

Schouten, H., K. D. Klitgord, and J. A. Whitehead, Segmentation of mid-ocean ridges, *Nature*, *317*, 225-229, 1985

Searle, R. C., Side-scan sonar studies of North Atlantic fracture zones, *J. Geol. Soc. London*, *136*, 283-292, 1979.

Searle, R. C., and A. S. Laughton, Sonar studies of the Mid-Atlantic Ridge and Kurchatov Fracture Zone, *J. Geophys. Res.*, *82*, 5313-5328, 1977

Sempéré, J C., J. Lin, H. S. Brown, H. Schouten, and G M. Purdy, Segmentation and morphotectonic variations along a slow-spreading center: The Mid-Atlantic Ridge (24°N - 30°40'N), *Mar. Geophys. Res.*, *15*, 153-200, 1993

Severinghaus, J. P., and K. C. Macdonald, High inside corners at ridge-transform intersections, *Mar. Geophys. Res.*, 9, 353-367, 1988.

Shaw, P R., Ridge segmentation, faulting and crustal thickness in the Atlantic Ocean, *Nature*, *358*, 490-493, 1992.

Shaw, P. R., and J. Lin, Causes and consequences of variations in faulting style at the Mid-Atlantic Ridge, *J. Geophys. Res.*, *98*, 21839-21851, 1993.

Shaw, W. J., and J. Lin, Three-dimensional modeling of thermo-mechanical structure of oceanic spreading centers: Effects of along-axis thickness variations associated with segmentation and hot spots (abstract), *Eos Trans. AGU*, *75* (16), Spring Meeting Suppl., 331, 1994.

Sinha, M. C., and K. E. Louden, The Oceanographer fracture zone, I, Crustal structure from seismic refraction studies, *Geophys. J. R. Astron. Soc.*, *75*, 713-736, 1983.

Solomon, S. C., P. Y. Huang, and L. Meinke, The seismic moment budget of slowly spreading ridges, *Nature*, *334*, 58-60, 1988.

Sparks, D. W., E. M. Parmentier, and J. Phipps Morgan, Three-dimensional convection beneath a segmented spreading segment: Implications for along-axis variations in crustal thickness and gravity, spreading centers, *J. Geophys. Res.*, *98*, 21977-21995, 1993.

Stein, R. S., G. C. King, and J. B. Rundle, The growth of geological structures by repeated earthquakes, 2, Field examples of continental dip-slip faults, *J. Geophys. Res.*, *93*, 13319-13331, 1988.

Tolstoy, M., A. J. Harding, and J. A. Orcutt, Crustal thickness on the Mid-Atlantic Ridge: Bull's eye gravity anomalies and focused accretion, *Science*, *262*, 726-729, 1993.

Tucholke, B. E., Massive submarine rockslide in the rift-valley wall of the Mid-Atlantic Ridge, *Geology*, *20*, 129-132, 1992.

Tucholke, B. E., and J. Lin, A geological model for the structure of ridge segments in slow spreading ocean crust, *J. Geophys. Res.*, *99*, 11,937-11,958, 1994.

Tucholke, B. E., J. Lin, and M. C. Kleinrock, Crustal structure of spreading segments on the western flank of the Mid-Atlantic Ridge at 25°25'N to 27°10'N (abstract), *Eos Trans. AGU, 73* (43), Fall Meeting Suppl., 537, 1992.

Wang, X., and J. R. Cochran, Gravity anomalies, isostasy, and mantle flow at the East Pacific Rise, *J. Geophys. Res.*, *98*, 19,505-19,531, 1993.

Weissel, J. K., and G. D. Karner, Flexural uplift of rift flanks due to mechanical unloading of the lithosphere during extension, *J. Geophys. Res.*, *94*, 13,919-13,950, 1989.

Whitehead, J. A., H. J. B. Dick, and H. Schouten, A mechanism for magmatic accretion under spreading centres, *Nature*, *312*, 146-148, 1984.

J. Escartín and J. Lin, Department of Geology and Geophysics, Woods Hole Oceanographic Institution, Woods Hole, MA 02543 (e-mail: javier@galileo.whoi.edu; jlin@whoi.edu)

(Received June 21, 1994; revised November 29, 1994; accepted December 6, 1994.)

Chapter 3

TECTONIC MODIFICATION OF AXIAL CRUSTAL STRUCTURE: EVIDENCE FROM SPECTRAL ANALYSES OF BATHYMETRY AND GRAVITY FROM THE MID-ATLANTIC RIDGE FLANKS (25.5-27.5°N)

Abstract

Bathymetry and gravity data from the axis of the Mid-Atlantic ridge show a systematic shallowing of the sea floor and thickening of the crust from segment ends towards the center, consistent with focused magmatic accretion at individual ridge segments. Statistical analyses of isochron profiles indicate that this structure is not maintained off-axis. Instead, the most elevated terrain occurs at inside corners of ridge-offset intersections, where the crust tends to be thinnest. Coherence between bathymetry and gravity for the ridge axis is found at wavelengths >20 km, consistent with an effective elastic plate thickness of 1-3 km. However, no significant coherence is observed on isochron profiles at ages of 2.5 Ma and older. These results indicate that the crustal structure that is magmatically formed on axis is strongly modified as the crust is carried off axis. Across-axis profiles display coherence at wavelengths consistent with the typical abyssal hill spacing (5-20 km), and no coherence at wavelengths >~70 km. The estimated effective elastic plate thickness for these profiles is <1/3 km (coherence at wavelengths >~5 km), substantially lower than the 1-3 km inferred for the axial valley floor. Synthetic fault models [*Escartín and Lin*, 1995] results in correlated bathymetry and gravity at wavelengths equal to the fault spacing; the use of flexural models to estimate elastic thickness may yield anomalously low values if the fault spacing is smaller than the wavelength of transition from no coherence to coherence of an unfaulted plate. These results indicate that the crustal structure off-axis is the result of focused magmatic accretion at the ridge axis, and later tectonic extension along the rift valley walls. Along-axis variations in the amount of extension result in the observed changes in bathymetry, gravity and coherence from the ridge axis to the isochron profiles.

1. Introduction

Bathymetry and gravity data from the slow-spreading Mid-Atlantic Ridge (MAR) have revealed that the oceanic crustal structure is strongly controlled by ridge segmentation. The axis of the MAR is divided into ridge segments ~20-80 km in length [e.g., *Schouten et al.*, 1985; *Macdonald et al.*, 1988; *Sempéré et al.*, 1990; 1993]. Within the axial rift valley, the seafloor is systematically shallower and the crust thicker at segment midpoints than at segment ends near ridge discontinuities [e.g., *Kuo and Forsyth*, 1988; *Lin et al.*, 1990; *Detrick et al.*, 1995]. This observation is consistent with models of focused magmatic accretion at the center of these segments [e.g., *Whitehead et al.*, 1984; *Crane*, 1985; *Lin et al.*, 1990].

At the scale of a segment, systematic patterns in seafloor morphology and crustal thickness are also observed off-axis, but differ from those on-axis. Near discontinuities there is a clear asymmetry in seafloor elevation: inside corners (ICs) are typically more elevated and have higher residual gravity anomalies than outside corners (OCs) [*Severinghaus and Macdonald*, 1988; *Tucholke and Lin*, 1994; *Escartín and Lin*, 1995]. Data on the MAR flanks reveal off-axis traces of elevated and thin IC crust, whereas segment centers (SCs) display relatively thick crust [e.g., *Lin et al.*, 1993; in prep.; *Rommeveaux et al.*, 1994; *Pariso et al.*, 1995; *Tucholke et al.*, 1996]. These changes in seafloor morphology and gravity patterns indicate that the off-axis structure of the crust is both the product of magmatic accretion at the ridge axis, and of tectonic faulting in the rift valley walls that extensively modifies the magmatic crustal structure. The extent of crustal modification as well as the processes responsible for it are still poorly understood.

The processes responsible for crustal modification can be studied by examining how the properties of the oceanic lithosphere change from a ridge axis to an off-axis setting. Information on the subsurface processes that modify the crustal structure and estimates of the relative strength of the lithosphere may be obtained from the study of the relationship between bathymetry and gravity. Spectral transfer functions (admittance and coherence) between gravity and bathymetry have been used to estimate the effective elastic thickness (EET) of the oceanic lithosphere. The EET of the ridge valley floor along axial profiles has been estimated to be ~2-4 km [*Neumann and Forsyth*, 1993], and increases to 6-13 km when seafloor adjacent to the ridge axis is included [*McKenzie and Bowin*, 1976; *Cochran*, 1976; *Blackman and Forsyth*, 1991; *Zervas et al.*, 1995]. In addition, although the axial relief appears to be isostatically compensated by crustal thickness variations, the axial valley is probably maintained dynamically and not isostatically [e.g., *Cochran*, 1979; *Parmentier and Forsyth*, 1985; *Neumann and Forsyth*, 1993].

In this paper we test a simple conceptual model for crustal structure and modification off axis at the scale of a single segment, using axial, isochron and across-axis profiles of bathymetry and gravity from the slow-spreading Mid-Atlantic Ridge (MAR). The primary data include a high-resolution data set on the western flank of the MAR near 25.5°-27.5°N extending to 20 Ma old crust, as well as on-axis data. Statistical and coherence analyses suggest that the crust is modified by tectonic extension along the rift valley walls and significant differences in the crustal structure exist between rift valley (0 Ma) and isochron profiles (>2.5 Ma).

2. Conceptual model

The systematic gravity patterns observed along a slow-spreading ridge segment are summarized in Figure 1a. Off-axis zones of gravity highs are marked by the dark shading, while the gravity lows along SCs both on- and off-axis are indicated by the white shading. These areas of relative high or low gravity are continuous but do not have a constant amplitude, as gravity anomalies show a wavy pattern with varying amplitude off-axis; such gravity undulations have been interpreted to reflect the temporal variability of magmatic crustal emplacement [e.g., *Lin et al.*, 1993; in prep.; *Tucholke and Lin*, 1994; *Pariso et al.*, 1995]. From this diagram it is apparent that the structure of the crust off-axis, as indicated by gravity, substantially differs from that formed magmatically on-axis. As illustrated in the along-axis profile in Figure 1b, the thinnest crust and deepest seafloor coincides with ridge discontinuities. This structure, however, is not observed off-axis. The shallowest seafloor is often not located at the center of the segment, but at the ICs instead, and the gravity highs are often displaced from the trace of the discontinuity and centered at ICs (isochron profile in Figure 1c).

It is likely that the change in crustal structure sketched in Figure 1 is caused by tectonic processes along the rift valley walls. It has been proposed that ICs are formed by substantial tectonic uplift through low-angle or detachment faults [e.g., *Dick et al.*, 1981; *Karson and Dick*, 1983] which generate elevated IC seafloor and possibly tectonically thinned crust, as indicated by the associated residual gravity highs. The asymmetry that exists between ICs and OCs [*Severinghaus and Macdonald*, 1988; *Tucholke and Lin*, 1994; *Escartín and Lin*, 1995] indicates either that magmatic emplacement is asymmetric at segment ends or, more likely, that the asymmetry has a tectonic origin. This second interpretation is consistent with the variation in tectonic extension inferred from along-axis

changes in fault patterns and microseismic events. The spacing and throw of faults appear to increase from segment center towards the ends [*Shaw*, 1992; *Shaw and Lin*, 1993]. Also microearthquakes tend to cluster preferentially at ICs of slow-spreading ridges [*Barclay et al.*, 1993; *Wolfe et al.*, 1995]. However, these studies are based primarily on near-axis data, and do not provide good constraints on the resulting crustal structure off-axis. This study will test the model of tectonic modification of a magmatically emplaced crust using both on- and off-axis bathymetry and gravity data.

3. Bathymetry and gravity data reduction

The data used in this study encompass the MAR axis between the Kane and the Atlantis fracture zones (FZs) and extend to 25 Ma crust off-axis on the west flank of the MAR between 25.5°N and 27.5°N (Figure 2). The dataset comprises primarily bathymetry and gravity from along-axis surveys of *Purdy et al.* [1990] and *Lin et al.* [1990], and from the off-axis survey in the ONR Acoustic Reverberations Special Research Program (ARSRP) study area [*Tucholke et al.*, 1996]. We also use data collected in other areas in the same region, including 1) the MAR axis between 24° and 30°N [*Smith et al.*, 1995]; 2) the TAG area [*Rona and Gray*, 1980]; the MAR axis both 3) north [*Fujimoto et al.*, in press] and 4) south of the Kane FZ [*Morris and Detrick*, 1991]. Details on track coverage, navigation system, and the multibeam and gravimeter systems are given in the above references.

Bathymetry and gravity data from the ARSRP area have been rotated, for purposes of presentation and data analysis, into an across- and along-axis coordinate system, as shown in Figures 3a-b. The spreading direction at 26°N predicted by the plate model NUVEL-1 [*DeMets et al.*, 1990] is N100°, and the predicted deviation from this spreading direction is

less than 1° for the MAR between 25.5° and 27.5°N. The magnetic lineations and abyssal hill orientations mark a clear counter-clockwise change in plate motion of approximately 9° at 22-24 Ma [*Tucholke et al.*, 1996], which was also recorded by the Kane FZ [*Tucholke and Schouten*, 1988]. We thus remap the data by rotating crust younger than 20 Ma by 10° towards the west, and crust older than 20 Ma by 19° to account for the change in plate motion. The data is then resampled in the new rotated coordinate system (Figure 3). In this rotated coordinate system the ridge axis, abyssal hills and magnetic lineations are sub-parallel to the y-axis, and the direction of spreading is parallel to the x-axis (Figure 3a). The magnetic data on the MAR at 28°-29°N, immediately north of the study area, show plate motion changes of less than ±10° occurring during the last 10 Ma [*Sloan and Patriat*, 1992]. These changes in spreading direction were relatively small and short-lived, and were not recorded by the abyssal hill orientation in our study area. Consequently, they have not been incorporated in the remapping scheme.

To investigate variations in crustal structure it is necessary to remove the topographic and thermal effects of lithospheric cooling from the free-air gravity anomaly (FAA) in Figure 3b. The reduction of the FAA to obtain mantle-Bouguer (MBA) and residual mantle-Bouguer anomalies (RMBA) followed the procedures of *Prince and Forsyth* [1988] and *Kuo and Forsyth* [1988]. The gravity effects from the water-crust and crust-mantle interfaces were calculated using the upward continuation method of *Parker* [1973] and the thermal cooling effect of the mantle half-space was calculated using the 3-D passive mantle upwelling model of *Phipps Morgan and Forsyth* [1988]. The MBA and RMBA corrections were subtracted from the FAA at each point along ship tracklines, and then gridded to obtain the MBA and RMBA maps in Figures 3c and d, respectively. Values of model parameters used in gravity calculations are summarized in Table 1.

Residual gravity anomalies arise from differences between the modeled and actual densities of the crust and mantle, and from variations in crustal thickness. Mantle density variations associated with thermal anomalies are relatively small and therefore most of the RMBA reflects thickness or density variations of the crust [*Lin and Phipps Morgan*, 1992; *Sparks et al.*, 1993]. The relative crustal thickness is calculated by downward continuation of the RMBA using the method of *Parker and Huestis* [1974]. To ensure convergence of the solution during gravity inversion, a low-pass filter with cosine tapering beginning at 35 km to a cut-off wavelength of 25 km was applied.

As crustal thickness calculations are non-unique and model dependent, we have adopted two alternative density structures. In model A, the crust has a density ρ_c=2700 kg m^{-3}. In model B, a layered structure is assumed in which the upper crust has a constant thickness of 2 km and a density ρ_c=2600 kg m^{-3}, and the lower crust has variable thickness with ρ_c=2800 kg m^{-3}. The calculated relative crustal thickness maps are shown in Figures 3e (Model A) and 3f (Model B). Model B is intended to reflect more accurately recent seismic observations that suggest systematic thinning of the lower crust (layer 3) with the upper crust (layer 2) maintaining a relatively constant thickness [e.g., *Tolstoy et al.*, 1993; *Minshull*, 1996]. Previous gravity analyses including a single layer of constant density underestimate crustal thickness variations with respect to seismic methods [e.g., *Tolstoy et al.*, 1993; *Minshull*, 1996]. However, model B produces substantially larger relative crustal thickness variations (±3.5 km) than model A (±2.0 km) since the density contrast at the Moho is smaller in model B ($\Delta\rho_B$=500 kg m^{-3}) than in model A ($\Delta\rho_A$=600 kg m^{-3}). The use of more realistic layered density models to calculate crustal thickness partly solves the previous discrepancies between estimates of crustal thickness from seismic and gravity methods.

4. Segment-scale variations in bathymetry and gravity structure

The effect of extensional tectonism on crustal structure along the rift valley walls can be best investigated by comparing the gravity and bathymetry along isochrons with those along the ridge axis. The isochron profiles are spaced at 2.5 Ma intervals, from 0 to 25 Ma old crust, as determined from sea floor magnetic anomalies [*Tucholke et al.*, 1996] (Figure 4). Because our primary objective is to quantify the segment-scale variability, we first remove the linear trend in bathymetry and residual gravity anomalies that might be associated with processes at wavelengths longer than the segment length (i.e., regional effect of the Azores hot spot [*Detrick et al.*, 1995]). The detrended curves are then parametrized by segment length (L), amplitude of along-axis bathymetric variation (Δ_B) within a segment, and amplitude of residual gravity anomaly (Δ_{RMBA}) (Figure 5, top). To facilitate comparison among profiles, all the profiles were fit by a cosine shape curve (Figure 5, middle and bottom). The calculated parameters L, Δ_B and Δ_{RMBA} correlation coefficients r_B and r_{RMBA}, correlation between bathymetry and residual gravity $r_{B\text{-}RMBA}$ and confidence level of the fits using a Student's t-test are summarized in Table 2.

The results in Table 2 and Figure 6 indicate that the zero-age crustal structure formed at the ridge axis is modified off-axis. Out of 22 ridge-axis profiles, 15 fit the cosine model with a confidence level equal to or larger than 0.99, and 13 show correlation between bathymetry and gravity at the same confidence level. Off axis, 17 and 18 out of 31 bathymetry and gravity profiles, respectively, are correlated with the cosine model, and only 5 show good correlation between bathymetry and gravity (Table 2). The longer segments on-axis show a more systematic pattern of crustal thickening from the segment ends towards the center than in the case of the off-axis profiles (Figures 6a and 6c). In

addition, differences between the on- and the off-axis profiles are also indicated by the plots of L versus Δ_{RMBA} and Δ_{RMBA} in Figures 6b and 6d, respectively. The amplitude of segment-scale variations in axial bathymetry and gravity increases linearly with segment length, consistent with results from earlier studies [*Lin et al.*, 1990; *Detrick et al.*, 1995]. In contrast, the off-axis data display no correlation of Δ_B and Δ_{RMBA} with L. Values of off-axis Δ_B appear to be somewhat higher than those on-axis, while the values of off-axis Δ_{RMBA} tend to be lower (Figures 6b and 6d, respectively).

5. Coherence analysis

The correlation between the bathymetry and gravity may be estimated in the spectral domain by the coherence (γ^2) function:

$$\gamma^2=\langle G\cdot H^*\rangle^2/\langle G\cdot G^*\rangle\langle H\cdot H^*\rangle$$

where H and G are the Fourier coefficients for the bathymetry and gravity, respectively, and the triangular brackets indicate averaging over individual spectral bands. In the presence of an elastic plate, bathymetry and gravity are expected to be correlated at long wavelengths and therefore have a high coherence. At short wavelengths, however, the topography can be maintained by stresses in the lithosphere and therefore low coherence values are expected. The wavelength of the transition from low to high coherence depends primarily on the effective elastic thickness (EET) of the lithosphere, and is relatively insensitive to the ratio of top to bottom loading (f) of the plate [*Forsyth*, 1985]. Other spectral estimates, such as admittance [e.g., *McKenzie and Bowin*, 1976] are strongly dependent on f and the EET, and may yield anomalously low flexural rigidities depending on the assumed value of f [*Forsyth*, 1985]. Coherence is thus preferred over admittance in

our analysis. The coherence functions were calculated using a section-averaged, multiple-window technique with jackknifed error estimates [*Thomson*, 1977; *Chave et al.*, 1987; *Chave and Thomson*; 1989; *Thomson and Chave*, 1991]. As opposed to band-averaging methods, the multiple window coherence method is not dominated by spectral leakage, and thus yields statistically robust coherence estimations.

To study intra-segment and temporal variability in lithospheric structure, we performed spectral analyses on individual bathymetry and gravity profiles along the ridge axis and off-axis isochrons, as well as on north (N), center (C) and south (S) across-axis profiles for each of the segments (Figure 4). Due to the complex segmentation patterns and the relatively small size of our study area (~500×200 km), 2-D coherence analysis is impractical as it would provide flexural rigidity estimates over a wide range of crustal ages emplaced at different ridge segments. Isochron profiles for a given age from different segments were joined by interpolating over 5 km to obtain a single isochron profile (Figure 7), using a method similar to that of *Neumann and Forsyth* [1993]. Coherence was also calculated on an ~900 km long axial profile extending from south of the Kane FZ (~22°40'N) to north of the Atlantis FZ (30°30'N) (Figure 7). The across axis profiles on N, S, and C crust are located at 25, 50 and 75%, respectively, of the distance between the two offsets bounding each segment (Figure 4). The S and N profiles on segment 1 (Figure 4) corresponds to IC and OC crust, respectively, while the N and S profiles across segments 2 and 3 correspond to both IC and OC crust, due to changes in the polarity of the discontinuities that bound them [*Tucholke et al.*, 1996]. The axial rift valley (within the first 2.5 Ma) was not included in the across-axis profiles, as it is dynamically maintained and the forces sustaining it would result in reduced coherence [e.g., *Neumann and Forsyth*, 1993]. For each across-axis profile, the dependence of bathymetry on the square-root of age was removed to obtain residual bathymetry (Figure 8). Coherence on the

across-axis profiles is calculated using the residual bathymetry and the RMBA; the coherence estimates using actual bathymetry and MBA instead yield essentially identical results.

Axial coherence. The coherence function between bathymetry and MBA along the axis indicates that the effective elastic thickness EET of the axial valley floor varies between 1 and 3 km (Figure 9). The transition from values of coherence of ~0 to ~0.8 occurs between wavelengths of 20-100 km, and is bracketed by the theoretical coherence functions for a 2-D elastic plate [*Forsyth*, 1985] of EET 1-3 km. Coherence decreases somewhat at wavelengths >100 km. We have assumed a top-to-bottom loading ratio, f, of 1. Since the coherence estimates are more sensitive to variations in EET than in f, other f values would yield comparable coherence estimates [*Forsyth*, 1985]. Our result is similar to the EET of ~2 km obtained by *Neumann and Forsyth* [1993] along an axial profile combining several segments from the northern and southern MAR.

To facilitate comparison between the axial and the isochron data we calculated the coherence on four subsets ~240 km long on the axial data. The length of the complete axial profile is ~900 km, considerably longer than the <400 km of each of the isochron profiles. In all cases we obtained an EET of 1-4 km, consistent with the 1-3 km obtained for the complete axial profile. The maximum coherence in all subsections was ~0.6, above the confidence level, but somewhat lower than the ~0.8 value shown in Figure 9 for the complete axial profile.

Isochron coherence. Examination of the coherence functions for all isochron profiles demonstrates that bathymetry and gravity are systematically uncorrelated at all wavelengths. This lack of coherence can be seen clearly by comparing the coherence function for the ridge axis and elastic plate models with those for selected isochrons at crustal ages of 2.5,

10, and 20 Ma (Figure 9). In all profiles, the coherence is lower than the confidence level, except for wavelengths <4 km and ~10 km in the 20 Ma profile. The coherence peaks at wavelengths <4 km can be attributed to noise because wavelengths shorter than the water depth (~4 km) are filtered by upward continuation of the gravity. The coherence peak at wavelengths of ~10 km has large errors, suggesting that these coherence values may not be significant.

Across axis coherence. The observed coherence functions for profiles along flowlines over the crust in the north, center and south of the three segments (Figure 10) also differ substantially from that of the axial profile. The transition from uncorrelated to correlated bathymetry occurs at wavelengths of 7-15 km in average. At wavelengths >20-100 km, bathymetry and gravity become uncorrelated in all across-axis profiles.

6. Discussion

Across-axis coherence and the effect of faulting

The lack of coherence at long wavelengths on the across-axis profiles (Figure 10) is not consistent with flexural models of an elastic plate, which predict high coherence values [*e.g., Forsyth*, 1985]. In addition, the calculated EET for all profiles is <0.3 km, substantially smaller than the 1-3 km determined for the axial valley floor (dashed lines in Figure 10). Furthermore, the EET of the oceanic lithosphere is expected to increase with age [e.g., *McNutt*, 1988]. Therefore, other models must be invoked to explain the observed transition from non-significant to significant coherence at anomalously short wavelengths.

Extensional faulting along axial valley walls can reshape the crust substantially as it is transported off-axis. Fault spacing varies along the length of a ridge segment on the MAR, ranging from ~1-3 km at outside corners and segment centers to ~3-10 km at inside corners [*Shaw*, 1992; *Shaw and Lin*, 1993]. The typical fault spacing estimated from side-scan sonar at the center of segments 1-3 is 0.8-1.5 km [*Goff et al.*; 1995], and the maximum abyssal hill width along the same segments is ~18 km [*Goff et al.*, 1995]. Abyssal hills along the MAR are interpreted to have a tectonic origin [e.g., *Macdonald and Luyendyk*, 1977] , and the abyssal hill width is therefore an indirect measure of the spacing of larger faults responsible for the formation of this topography. The range in fault spacing along each segment is indicated in Figure 10 by the horizontal double arrows, and in all cases overlaps with the transition from no coherence to significant coherence. Thus, the bathymetry is strongly correlated with gravity at wavelengths similar to the abyssal hill spacing, i.e. fault spacing. Results from synthetic models of crustal faulting suggest that faulting can have an expression in both the seafloor topography and the residual gravity [*Escartín and Lin*, 1995], and coherence at the wavelengths similar to the fault spacing is thus expected. Consequently, the use of flexural models to estimate the EET is not appropriate in these models, as the bathymetry and residual gravity are correlated at wavelengths controlled by the fault geometry, and not by the EET of the plate. The coherence on the across-axis profiles at wavelengths of ~5-50 km (Figure 10) may be explained then by tectonic extension. Fault spacing in this area ranges from 1 km (small-scale faults) to ~20 km [*Goff et al.*, 1995] (abyssal-hill forming faults), and coherence should be expected at wavelengths of ~1-20 km. However, the short wavelengths of the gravity signal are filtered by upward continuation from the crust to the sea surface (<4 km approximately). Thus, the observed transition from no coherence to coherence at ~5-10 km may be caused by faulting, and not by a thin (<0.3 km) elastic plate.

The axial coherence reflects the variability in segment lengths (arrow in Figure 9, top), and not the actual elastic plate thickness of the rift valley floor. The axial valley floor is maintained dynamically by stresses in the lithosphere, not isostatically by an elastic plate [*Neumann and Forsyth*, 1993], and therefore the measured coherence the wavelengths of ridge segmentation and not of the EET of the axial valley floor. Consequently, the systematic patterns observed in the bathymetry and gravity reflects mainly focused magmatic accretion at the ridge axis. If that is the case, coherence is expected at wavelengths similar to the length of the segments that form the combined axial profile, between 10 and 100 km approximately (Table 2). These wavelengths correspond to the transition from no coherence to coherence observed on the axial profile, and coincides with that of a flexural model with EET~1-3 km (Figure 9).

The lack of coherence at wavelengths >~50 km in the across-axis profiles is not predicted by the flexural models. Temporal variability in magmatic accretion may result in across-axis variations in crustal thickness at time scales of 2-3 Ma, i.e., 25-40 km [e.g., *Lin et al.*, 1993; in prep.; *Tucholke and Lin*, 1994; *Pariso et al.*, 1995]. In addition to faulting, the magmatic variability may contribute to the observed coherence at these wavelengths (Figure 10). However, there is no identified magmatic or tectonic process that will produce morphologic and crustal thickness variations at longer wavelengths (>100 km or >10 Ma). The lack of power at these long wavelengths in both the bathymetry and the gravity may explain the lack of coherence. In addition, in all cases the coherence at wavelengths longer than ~100 km is poorly constrained, as the across axis profiles are relatively short (<350 km), and the longer wavelengths are not well characterized.

Isochron coherence and the strength of the oceanic lithosphere

Previously published estimates of the effective elastic thickness of the MAR yield values of 2-13 km [*Mackenzie and Bowin*, 1976; *Cochran*, 1979; *Louden and Forsyth*, 1982; *Blackman and Forsyth*, 1991; *Neumann and Forsyth*, 1993; *Zervas et al.*, 1995] that are comparable to the 1-3 km that we obtained for the axial profile. The off-axis coherence functions along isochrons 2.5 Ma and older, however, differ substantially from that at the ridge axis (Figure 10), in that they show no coherence at any wavelengths <300 km. If coherence exists at wavelengths of 200 km or more, greater than the length of the isochron profiles, the predicted elastic plate thickness would be ≥27 km. Such a large elastic thickness would only be expected in areas where the age of the lithosphere at the time of loading is >80 Ma [e.g., *McNutt*, 1984] or in continental zones [e.g., *Zuber et al.*, 1989; *Ebinger et al.*, 1989], but not in young 2.5 Ma oceanic lithosphere. Furthermore, in the study area there is no evidence for off-axis loading. Seamounts are formed on-axis [*Smith and Cann*, 1993], and there is no evidence for large seamounts emplaced off-axis [*Jaroslow et al.*, 1995]. The sediment cover on the area is negligible, although it locally modifies the topography, particularly on basement depressions that act as sedimentary basins [*Jaroslow*, pers. comm.]. Finally, the age offset across the second-order discontinuities is small (0-3.2 Ma). Thermal models do not predict sharp thermal boundary across offsets [e.g., *Phipps Morgan and Forsyth*, 1988], and therefore differential thermal subsidence across discontinuities [e.g., *Parmentier and Haxby*, 1986] is likely negligible. Therefore the expected effective elastic plate thickness recorded on the off-axis profiles should be that of the ridge-axis with modification by near-axis processes. The lack of coherence along isochron profiles may therefore record the role of tectonic processes along the rift valley walls.

The segments in the axial profile (Figure 7) range in length from 12 to 100 km, corresponding to the transition from no coherence to coherence at the axis (Figure 9). Similar to the across-axis profiles, coherence may be caused by systematic patterns in crustal structure related, maybe caused by faulting, and not to a flexural response of the plate. The lack of coherence between gravity and bathymetry on the isochron profiles is attributable to the destruction of this systematic crustal thickness variation (Figures 6b and 6d) by tectonic extension. responsible for the formation of elevated and thin IC crust off-axis. As all isochron profiles from 2.5 to 25 Ma display a similar bathymetry, gravity (Figure 6), and coherence pattern (Figure 9), the transition from axial to off-axis crustal structure must occur between 0 and 2.5 Ma crust. This transition is also indicated by the analyses of individual isochron and axial profiles (Table 2). In particular, there is a marked lack of correlation between segment length and bathymetry and gravity amplitude that is present in the axial profiles (Figures 6b and 6d), and the good correlation between bathymetry and gravity on-axis is lost off-axis (Table 2).

Tectonic extension must vary both temporarily and spatially along-axis to explain the patterns in the bathymetry and gravity profiles, and the calculated coherence. First, numerous off-axis profiles show a pattern similar to those on-axis (Table 2), indicating that the axial crustal structure may be maintained off-axis in some instances. Formation of inside corner terrain may be a discontinuous process, as indicated by the spacing of inside-corner bathymetry and gravity highs off axis [e.g., *Escartín and Lin*, 1995]. It is then possible that some of the along-isochron profiles correspond to crust that has not been substantially tectonized. Second, tectonic extension must vary along axis to result in decorrelation between bathymetry and gravity profiles along isochrons (Figure 9). Variations in elevation and crustal thickness between IC and OC terrain [e.g., *Severinghaus and Macdonald*, 1988; *Escartín and Lin*, 1995] demonstrate that tectonism varies along

axis. In addition, constant tectonic extension would result in homogeneous thinning of the crust in directions parallel to the ridge axis, and the axial crustal structure would be maintained off-axis, which is not observed.

Implications for the structure of segment boundaries

The model proposed in Figure 1 indicates that off-axis RMBA highs do not mark the paleoposition of offsets. Based on off-axis gravity from the MAR at 28°N, *Rommeveaux et al.* [1994] suggested that tectonism reshapes only the upper crust, while the Moho at segment boundaries remains untouched. However, there are two other lines of evidence in addition to our results that suggest that RMBA highs mark the location of extensive tectonic thinning at ICs and not the paleoposition of offsets. First, offsets interpreted from magnetic anomalies (Figures 3 and 4) mark magmatic boundaries between crust accreted at adjacent segments. The offsets correspond to the transition from deep OC crust of one segment to elevated IC crust of the adjacent segment, and consequently the RMBA highs are displaced towards the IC (Figure 2d), away from discontinuities. Second, in the vicinity of fracture zones where the location of the boundary between segments is unequivocal and located within the transform valley, the gravity highs are still located on the IC crust that form the elevated transverse ridges, similar to what is observed at non-transform offsets [*Tucholke and Lin*, 1994; *Escartín et al.*, 1995; *Zervas et al.*, 1995]. Consequently, we conclude that off-axis gravity highs are displaced with respect to the actual position of the discontinuities, as illustrated in Figure 1, instead of indicating the actual trace of the discontinuities.

7. Conclusions

Statistical and spectral analyses of bathymetry and gravity data from the slow-spreading Mid-Atlantic Ridge indicate that the crustal structure at the ridge axis is strongly modified by tectonic extension along the axial valley walls. The on-axis crustal structure, which may reflect focused magmatic accretion, is inferred to be characterized by thick and shallow crust at segment centers and thin crust at segment ends. In contrast, outside of the rift valley walls the elevated terrain and positive RMBA are located at inside corners, while the deepest terrain is typically found at outside corners and the low RMBA values at segment centers. Tectonic extension at inside corners is more profound than at segment centers or outside corners, resulting in what we believe to be thin and elevated crust. This tectonic process results in significant modification of the crustal structure accreted at active spreading centers. Evidence for this tectonic modification can be found from both statistical and spectral analyses of bathymetry and gravity. While the along-axis profile displays high coherence at wavelengths >20 km, which corresponds to an effective elastic plate thickness of 1-3 km, the along-isochron profiles outside the rift valley show no significant coherence at any wavelengths. Furthermore, while there is a marked positive linear correlation between segment length and along-axis bathymetry and gravity signals, such correlation is absent in the off-axis profiles. These results support that tectonism has modified the off-axis crust. The transition from the axial to the off-axis crustal structure occurs between the 0 and 2.5 Ma isochrons, most likely at the zone of active tectonism along the rift valley walls.

Coherence results from synthetic faulting models indicate that faulting can result in correlated bathymetry and gravity at wavelengths corresponding to the fault spacing. The use of flexural models may yield low estimates of the effective elastic thickness if the fault

spacing is smaller than the wavelength of the transition from no coherence to coherence. The elastic thickness of <0.3 km measured in the across-axis profiles, significantly lower than the 1-3 km measured on-axis, is not consistent with a flexural response of a thin elastic plate, but is compatible with faulting along the rift valley walls. The on-axis coherence may also reflect the systematic variations in crustal structure at wavelengths corresponding to the segment lengths, and not to the elastic thickness of the axial valley floor.

Acknowledgments

This study benefited from discussion with and suggestions from Bob Detrick, Greg Hirth, Kip Hodges, Emilie Hooft, Garret Ito, Gary Jaroslow, Dan Lizarralde, Debbie Smith, Maurice Tivey, and Brian Tucholke. Allen Chave is specially acknowledged for providing codes for robust spectral estimations as well as comments and suggestions. The GMT software [*Wessel and Smith*, 1995] was extensively used in this study. This work was supported by NSF grant OCE-9300708, and the ARSRP data were acquired with funding from ONR N00014-90-J-1621. Contribution 9270 of the Woods Hole Oceanographic Institution.

References

Barclay, A. H., D. R. Toomey, G. M. Purdy and S. C. Solomon, FARA microearthquake experiments, III, results from the Mid-Atlantic Ridge at 35°N (abstract), EOS Trans. AGU, 601, 1993.

Blackman, D. K. and D. W. Forsyth, Isostatic compensation of tectonic features of the Mid-Atlantic Ridge: 25-27°30' S, J. Geophys. Res., 96, 11741-11758, 1991.

Chave, A. D., D. J. Thomson and M. E. Ander, On the robust estimation of power spectra, coherences, and transfer functions, J. Geophys. Res., 92, 633-648, 1987.

Chave, A. D. and D. J. Thomson, Some comments on magnetotelluric response function estimation, J. Geophys. Res., 94, 14215-14225, 1989.

Cochran, J. R., An analysis of isostasy in the world's oceans, 2, Midocean ridge crests, J. Geophys. Res., 84, 4713-4730, 1976.

Crane, K., The spacing of rift axis highs: dependence upon diapiric processes in the underlying asthenosphere?, Earth Planet. Sci. Lett., 72, 405-414, 1985.

DeMets, C., R. G. Gordon, D. F. Argus and S. Stein, Current plate motions, Geophys. J. Int., 101, 425-478, 1990.

Detrick, R. S., H. D. Needham and V. Renard, Gravity anomalies and crustal thickness variations along the Mid-Atlantic ridge between 33°N and 40°N, J. Geophys. Res., 100, 3767-3787, 1995.

Dick, H. J. B., W. B. Thompson and W. B. Bryan, Low angle faulting and steady-state emplacement of plutonic rocks at ridge-transform intersections (abstract), EOS Trans. AGU, 62, 406, 1981.

Ebinger, C. J., T. D. Bechtel, D. W. Forsyth and C. O. Bowin, Effective elastic plate thickness beneath the East African and Afar plateaus and dynamic compensation of the uplifts, J. Geophys. Res., 94, 2883-2901, 1989.

Escartín, J. and J. Lin, Ridge offsets, normal faulting, and gravity anomalies of slow-spreading ridges, J. Geophys. Res., 6163-6177, 1995.

Forsyth, D. W., Subsurface loading and estimates of the flexural rigidity of continental lithosphere, J. Geophys. Res., 90, 12623-12632, 1985.

Fujimoto, H., N. Seama, J. Lin, T. Matsumoto, T. Tanaka and K Fujioka, Gravity anomalies of the Mid-Atlantic Ridge north of the Kane transform fault, Geophys. Res. Lett., in press, 1996.

Goff, J. A., B. E. Tucholke, J. Lin, G. E. Jaroslow and M. C. Kleinrock, Quantitative analysis of abyssal hills in the Atlantic Ocean: A correlation between axis crustal thickness and extensional faulting, J. Geophys. Res., 100, 22509-22522, 1995.

Jaroslow, G. E., D. K. Smith and B. E. Tucholke, Production and evolution of seamounts in the ONR Natural laboratory, North Atlantic Ocean, EOS Trans. AGU, 76, 553-554, 1995.

Karson, J. A. and H. J. B. Dick, Tectonics of ridge-transform intersections at the Kane Fracture Zone, Mar. Geophys. Res., 6, 51-98, 1983.

Kuo, B. Y. and D. W. Forsyth, Gravity anomalies of the ridge-transform system in the South Atlantic between 31 and 31°S: Upwelling centers and variations in crustal thickness, Mar. Geophys. Res., 10, 205-232, 1988.

Lin, J. and J. Phipps Morgan, The spreading rate dependence of three-dimensional mid-ocean ridge gravity structure, Geophys. Res. Lett., 19, 13-15, 1992.

Lin, J., G. M. Purdy, H. Schouten, J.-C. Sempéré and C. Zervas, Evidence from gravity data for focused magmatic accretion along the Mid-Atlantic Ridge, Nature, 344, 627-632, 1990.

Lin, J., B. E. Tucholke and M. C. Kleinrock, Evidence from gravity and morphology for long-term variability in magmatic vs. tectonic extension at the Mid-Atlantic Ridge (abstract), EOS Trans. AGU, 74, 303, 1993.

Louden, K. E. and D. W. Forsyth, Crustal structure and isostatic compensation near the Kane fracture zone from topography and gravity measurements, I, spectral analysis approach, Geophys. J. R. Astron. Soc., 68, 725-750, 1982.

Macdonald, K. C. and B. P. Luyendyk, Deep-Tow studies of the structure of the Mid-Atlantic Ridge crest near lat. 37°N, Geol. Soc. Amer. Bull., 88, 621-636, 1977.

Macdonald, K. C., P. J. Fox, L. J. Perram, M. F. Eisen, R. M. Haymon, S. P. Miller, S. M. Carbotte, M.-H. Cormier and A. N. Shor, A new view of the mid-ocean ridge from the behavior of ridge-axis discontinuities, Nature, 335, p. 217-225, 1988.

McKenzie, D. and C. Bowin, The relationship between bathymetry and gravity in the Atlantic Ocean, J. Geophys. Res., 81, 1903-1915, 1976.

McNutt, M., Lithospheric flexure and thermal anomalies, J. Geophys. Res., 89, 11180-11194, 1984.

Minshull, T. A., Along-axis variation in oceanic crustal density and their contribution to gravity anomalies, Geophys. Res. Lett., 23, 849-852, 1996.

Morris, E. and R. S. Detrick, Three-dimensional analysis of gravity anomalies in the MARK area, Mid-Atlantic Ridge 23°N, J. Geophys. Res., 96, 4355-4366, 1991.

Neumann, G. A. and D. W. Forsyth, The paradox of the axial profile: Isostatic compensation along the axis of the Mid-Atlantic Ridge?, J. Geophys. Res., 98, 17891-17910, 1993.

Pariso, J. E., J.-C. Sempéré and C. Rommeveaux, Temporal and spatial variations in crustal accretion along the Mid-Atlantic Ridge (29°-31°30'N) over the last 10 my.:

Implications from a three-dimensional gravity structure, J. Geophys. Res., 100, 17,781-17,794, 1995.

Parker, R. L., The rapid calculation of potential anomalies, Geophys. J. R. Astr. Soc., 31, 447-455, 1973.

Parker, R. L. and S. P. Huestis, The inversion of magnetic anomalies in the presence of topography, J. Geophys. Res., 79, 1587-1593, 1974.

Parmentier, E. M. and D. W. Forsyth, Three-dimensional flow beneath a slow-spreading ridge axis: A dynamic contribution to the deepening of the median valley toward fracture zones, J. Geophys. Res., 90, 678-684, 1985.

Parmentier, E. M. and W. F. Haxby, Thermal stress in the oceanic lithosphere: Evidence from geoid anomalies at fracture zones, J. Geophys. Res., 91, 793-7204, 1986.

Phipps Morgan, J. and D. W. Forsyth, Three-dimensional flow and temperature perturbations due to a transform offset: Effects on oceanic crustal and upper mantle structure, J. Geophys. Res., 93, 2955-2966, 1988.

Prince, R. A. and D. W. Forsyth, Horizontal extent of anomalously thin crust near the Vema Fracture Zone from three-dimensional analysis of gravity anomalies, J. Geophys. Res., 93, 8051-8063, 1988.

Press, W. H., S. A. Teukolsky, W. T. Vetterling and B. P. Flannery, *Numerical recipes in C*, Cambridge University Press, New York, 1992.

Purdy, G. M., J. C. Sempéré, H. Schouten, D. L. Dubois and R. Goldsmith, Bathymetry of the Mid-Atlantic Ridge, 24°-31°N: A map series, Mar. Geophys. Res., 12, 247-252, 1990.

Rommeveaux, C., C. Deplus, P. Patriat and J.-C. Sémpére, Three-dimensional gravity study of the Mid-Atlantic Ridge: Evolution of the segmentation between 28° and 29°N during the last 10 m.y., J. Geophys. Res., 99, 3015-3029, 1994.

Rona, P. A. and D. F. Gray, Structural behavior of fracture zones symmetric and asymmetric about a spreading axis: Mid-Atlantic Ridge (Lat. 23°N to 27°N), Geol. Soc. Amer. Bull., 91, p. 485-494, 1980.

Schouten, H., K. D. Klitgord and J. A. Whitehead, Segmentation of mid-ocean ridges, Nature, 317, 225-229, 1985.

Sempéré, J. C., G. M. Purdy and H. Schouten, Segmentation of the Mid-Atlantic Ridge between 24°N and 30°40'N, Nature, 344, 427-431, 1990.

Sempéré, J. C., J. Lin, H. S. Brown, H. Schouten and G. M. Purdy, Segmentation and morphotectonic variations along a slow-spreading center: the Mid-Atlantic Ridge (24°N-30°40'N), Mar. Geophys. Res., 15, 153-200, 1993.

Severinghaus, J. P. and K. C. Macdonald, High inside corners at ridge-transform intersections, Mar. Geophys. Res., 9, 353-367, 1988.

Shaw, P. R., Ridge segmentation, faulting and crustal thickness in the Atlantic Ocean, Nature, 358, 490-493, 1992.

Shaw, P. R. and J. Lin, Causes and consequences of variations in faulting style at the Mid-Atlantic Ridge, J. Geophys. Res., 98, 21839-21851, 1993.

Sloan, H. and Ph. Patriat, Kinematics of the North American-African plate boundary between 28°N and 29°N during the last 10 Ma: evolution of the axial geometry and spreading rate and direction, Earth Planet. Sci. Lett., 113, 323-341, 1992.

Smith, D. K. and J. R. Can, Hundreds of small volcanoes on the median valley floor of the Mid-Atlantic Ridge at 24-30°N, Nature, 348, 152-155, 1990.

Smith, W. H. F. and D. T. Sandwell, Marine gravity field from declassified Geosat and ERS-1 altimetry, EOS Trans. AGU, 76, 156, 1995.

Smith, D. K., J. R. Cann, M. E. Dougherty, J. Lin, J. Keeton, E. McAllister, C. J. MacLeod and S. Spencer, Mid-Atlantic ridge volcanism from deep-towed side-scan sonar images, 25°-29°N, J. Volc. Geotherm. Res., 67, 233-262, 1995.

Sparks, D. W. and E. M. Parmentier, The structure of three-dimensional convection beneath oceanic spreading centres, Geophys. J. Int., 112, 81-91, 1993.

Thomson, D. J., Spectrum estimation techniques for characterization and development of WT4 waveguide, I, Bell Syst. Tech. J., 56, 1769-1815, 1977.

Thomson, F. J. and A. D. Chave, Jackknifed error estimates for spectral, coherences, and transfer functions, in Advances in Spectrum Analysis and Array Processing, vol. 1, ed. S. Kaykin, pp. 58-113, Prentice-Hall, Englewood Cliffs, N. J., 1991.

Tolstoy, M., A. J. Harding and J. A. Orcutt, Crustal thickness on the Mid-Atlantic ridge: Bull's eye gravity anomalies and focused accretion, Science, 262, 726-729, 1993.

Tucholke, B. E. and H. Schouten, Kane Fracture Zone, Mar. Geophys. Res., 10, 1-39, 1988.

Tucholke, B. E. and J. Lin, A geological model for the structure of ridge segments in slow-spreading ocean crust, J. Geophys. Res., 99, 11937-11958, 1994.

Tucholke, B. E., J. Lin, M. C. Kleinrock, M. A. Tivey, T. Reed, J. Goff and G. Jaroslow, Segmentation and crustal structure of the western Mid-Atlantic ridge flank, 25°30'-27°10'N and 0-29 M.y., J. Geophys. Res., submitted, 1996.

Wessel, P. and W. H. F. Smith, New version of the Generic Mapping Tools released, EOS Trans. AGU, 76, 329, 1995.

Whitehead, J. A., H. J. B. Dick and H. Schouten, A mechanism for magmatic accretion under spreading centres, Nature, 312, 146-148, 1984.

Wolfe, C., G. M. Purdy, D. R. Toomey and S. C. Solomon, Microearthquake characteristics and crustal velocity structure at 29°N of the Mid-Atlantic Ridge: The architecture of a slow-spreading segment, J. Geophys. Res., 100, 24449-24472, 1995.

Zervas, C., J.-C. Sempéré and J. Lin, Morphology and crustal structure of a small transform fault along the Mid-Atlantic Ridge: the Atlantis Fracture Zone, Mar. Geophys. Res., 17, 275-300, 1995.

Zuber, M. T., T. D. Bechtel and D. W. Forsyth, Effective elastic thickness of the lithosphere and mechanisms of isostatic compensation in Australia, J. Geophys. Res., 94, 9353-9367, 1989.

Fig. 1. a) Sketch of systematic variations in residual gravity structure observed at a segment in the north Atlantic. Typically, residual gravity highs extend along IC crust in the vicinity of segment boundaries and are associated with elevated terrain. In contrast, residual gravity lows tend to be found as ribbons that extend off-axis along segment centers. b) Typical along-axis depth cross-section of the crust. Focused magmatic accretion at ridge segments may result in elevated topography and thicker crust at segment centers than near their distal ends. c) As the crust is rafted off-axis, tectonic extension at the rift valley walls may result in tectonic uplift and crustal thinning, particularly at IC crust. Thus rift valley tectonic activity may modify the original crustal structure created at the ridge axis, resulting in ribbons of off-axis residual gravity highs and lows.

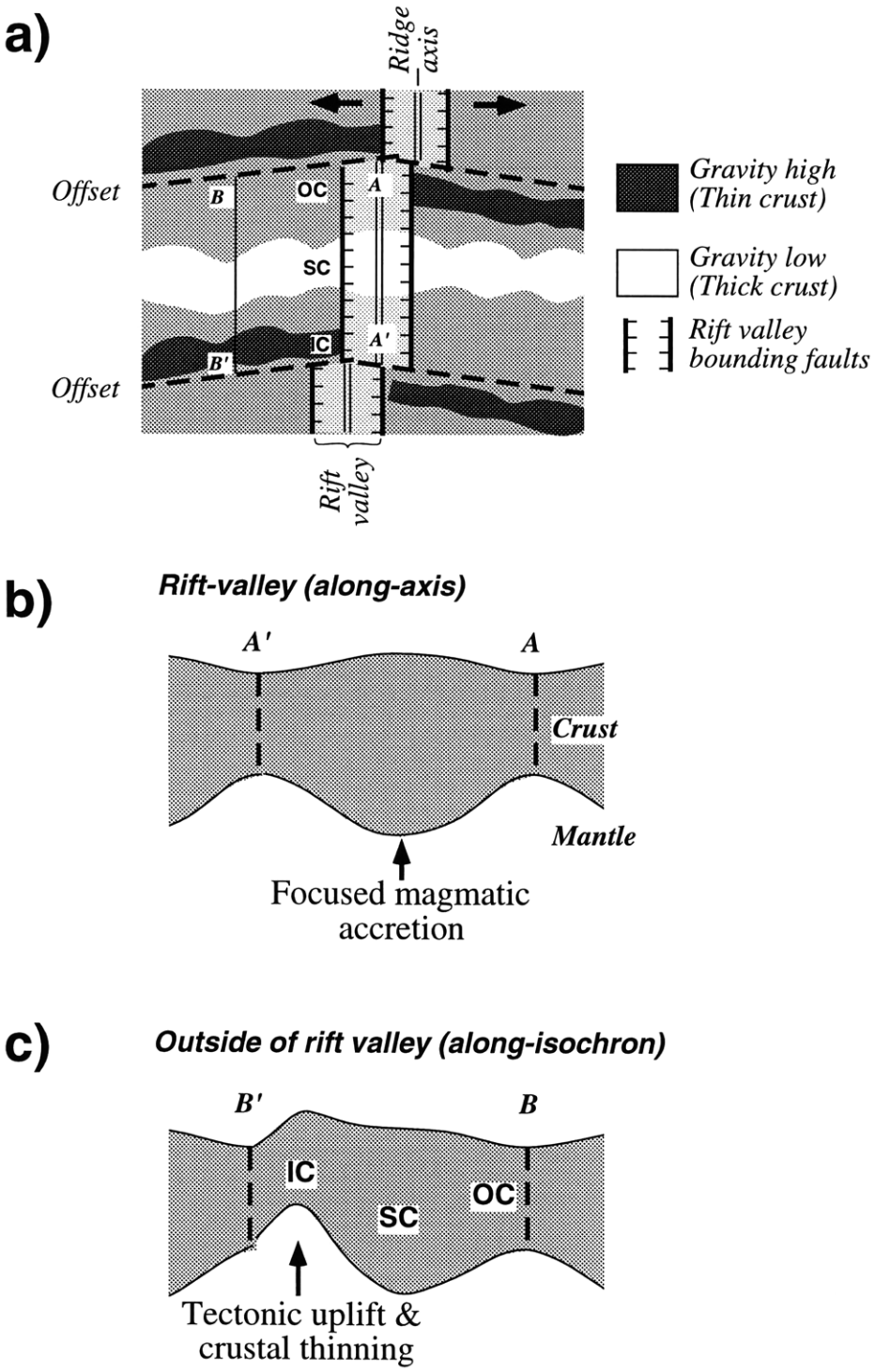

Figure 1, Escartín & Lin

Fig. 2. Location of the study area on the northern Atlantic marked on a free-air gravity anomaly map derived from Geosat and ERS1 satellite altimetry [*Smith and Sandwell*, 1995]. High-resolution shiptrack data encompasses the ridge axis from south of the Kane FZ to north of the Atlantis FZ, and extends off-axis on the western flank between ~25°30'N and ~27°10'N.

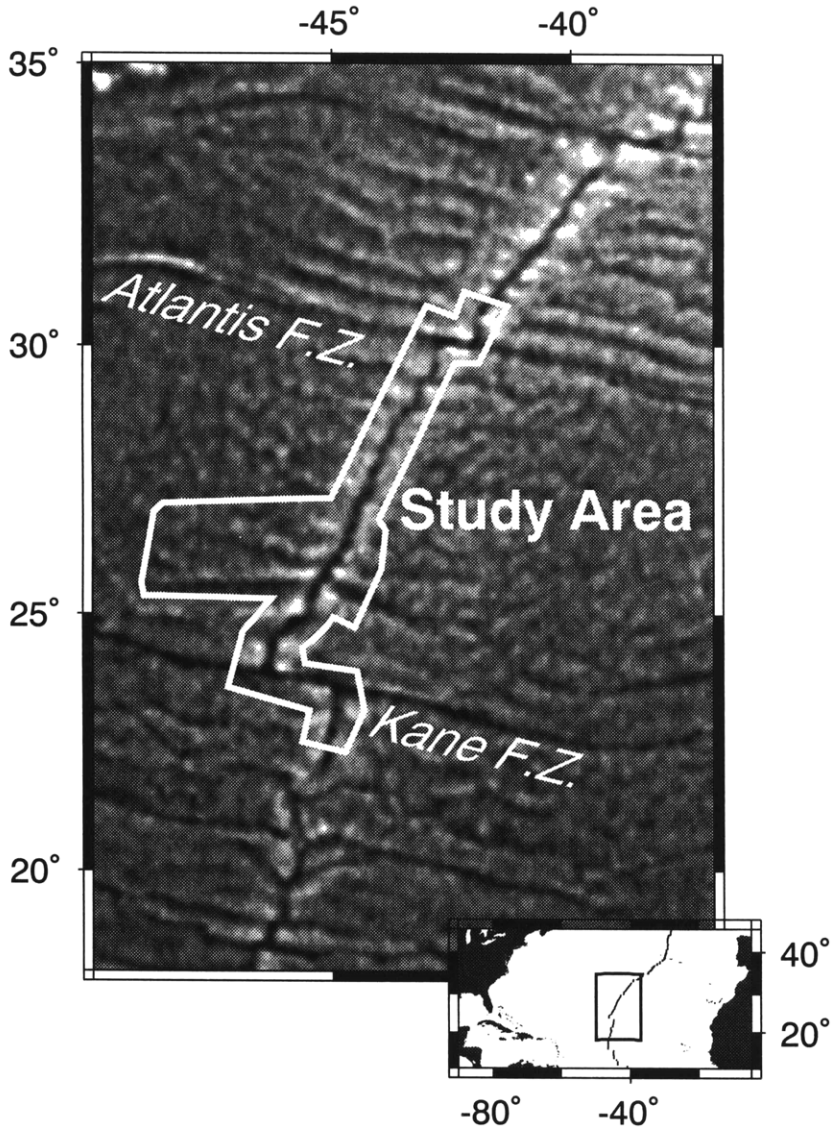

Figure 2, Escartin & Lin

Fig. 3. Rotated grid maps of (a) bathymetry, (b) free-air gravity anomaly (FAA), (c) mantle Bouguer anomaly (MBA), (d) residual MBA (RMBA), and maps of relative crustal thickness calculated from the RMBA data for two different crustal density models (e and f). Model A (e) corresponds to a single crust layer with constant density of 2700 kg m^{-3}, and Model B (f) corresponds to an upper crust of 2-km-thick and density of 2600 kg m^{-3} and a lower crust of variable thickness and a density of 2800 kg m^{-3}. The ridge axis is indicated by the double lines. Segment boundaries identified from magnetic data [*Tucholke et al.*, 1996] are marked by black or white thick lines. See text for details on the rotation of grids, and on calculations of the MBA, RMBA and crustal thickness maps.

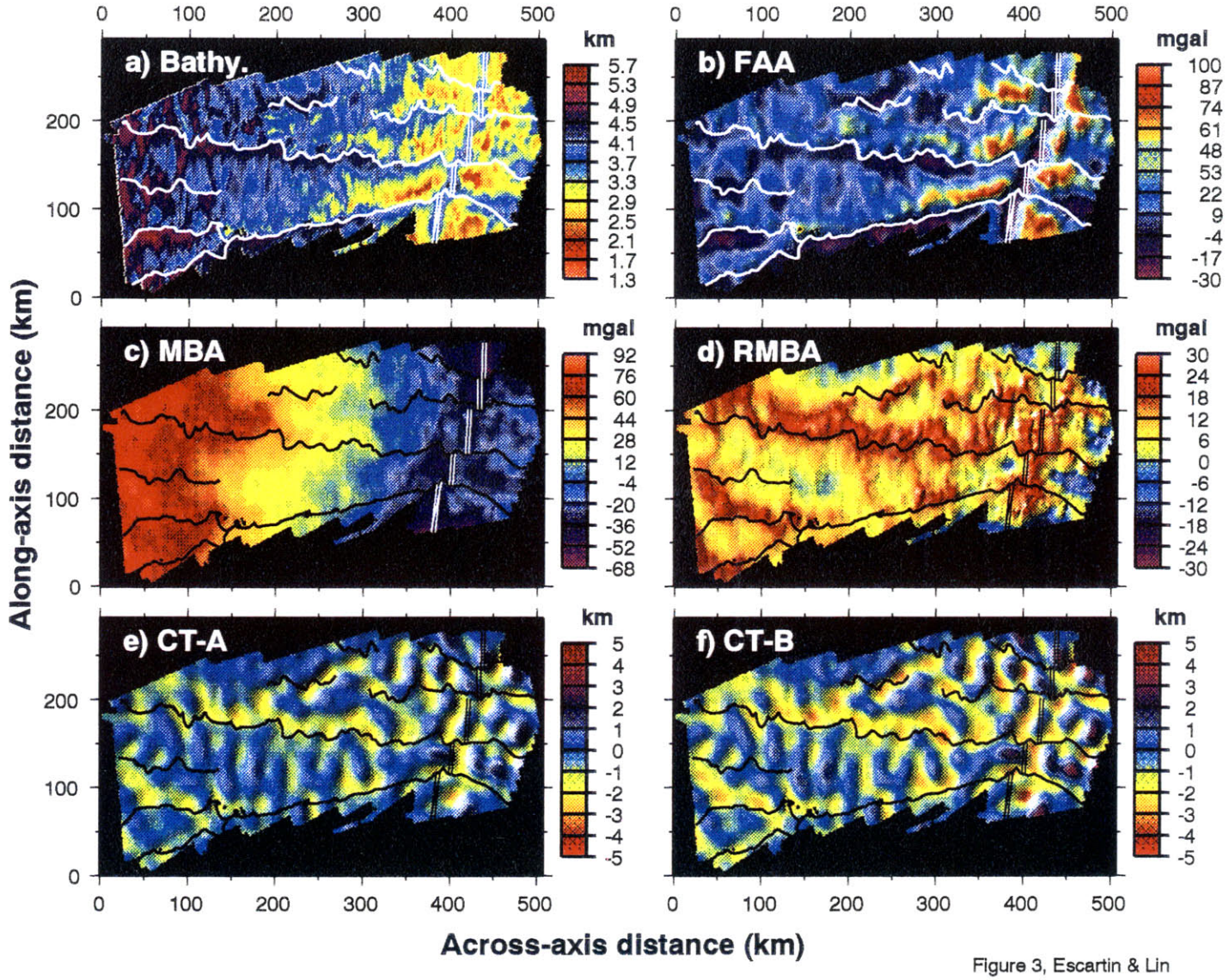

Figure 3, Escartin & Lin

Fig. 4. Location of profiles along the north (N), center (C) and south (S) sections of the segment, and along isochrons. These profiles were used to calculate the coherence between gravity and bathymetry and performing statistical analyses. Segment boundaries are marked by bold lines, and are identified from magnetic anomalies [*Tucholke et al.*, 1996]. Small numbers indicate crustal isochron in Ma, and gray numbers mark different active and extinct segments.

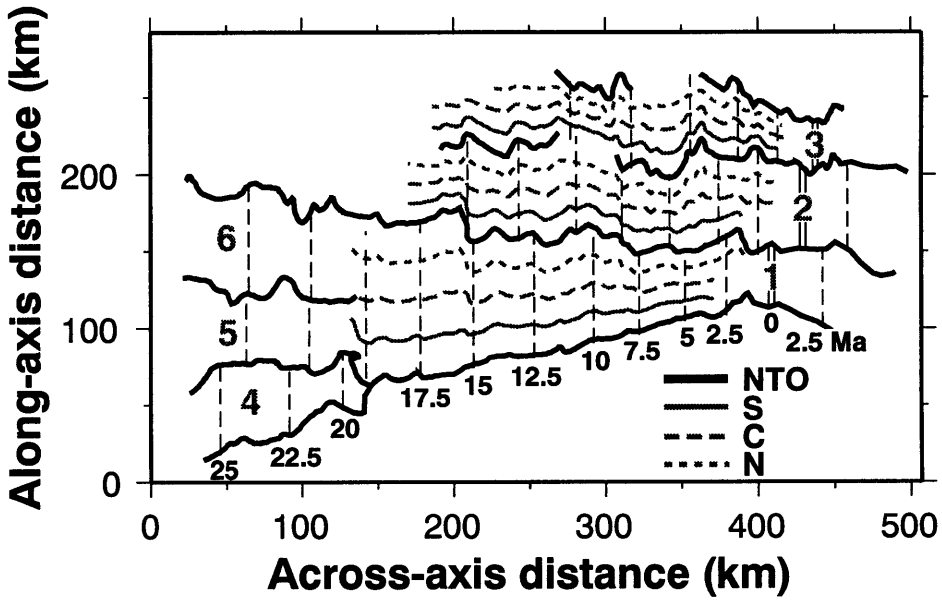

Figure 4, Escartin and Lin

Fig. 5. a) Theoretical cosine function curves used to model the along-axis bathymetry and gravity within a segment. Once linear trends (dashed) are removed, the depth and RMBA curves can be parametrized by cosine functions with the form $y=\pm\Delta/\cos(2\pi x/L)+a+mx$, where a and m correspond to the origin and slope of the linear trend, and Δ characterizes the amplitude of segment-scale variations. b) Example of data and cosine function approximation to the along-axis profile from segment 1. c) Example of data and cosine function approximation to an isochron profile (17.5 Ma, segment 1).

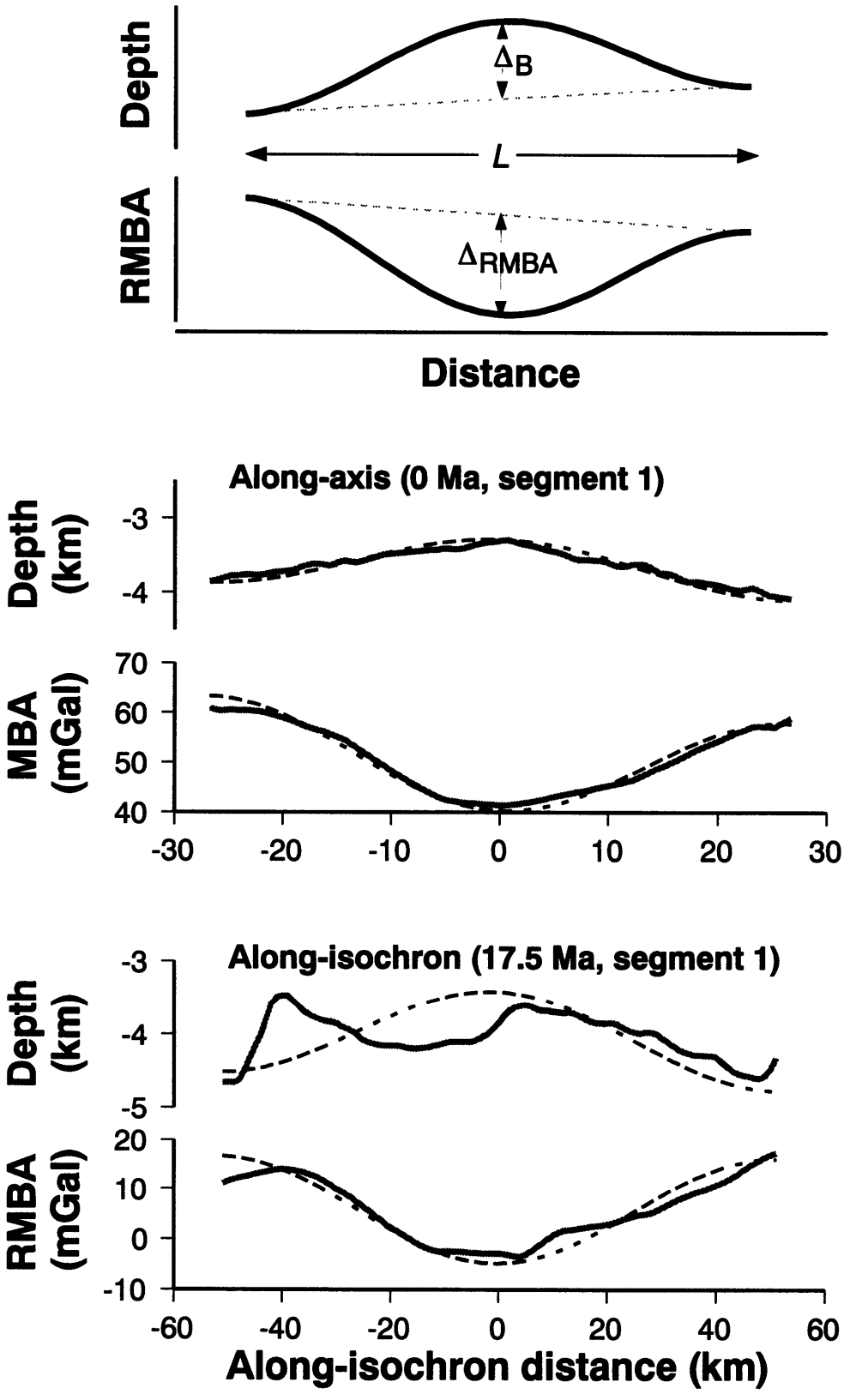

Figure 5, Escartin & Lin

Fig. 6. a) Confidence level of the fit of the bathymetry to the cosine model (see examples of Figure 5) versus segment length for along-axis and along-isochron profiles. b) Measured segment-scale variations in bathymetry (Δ_B) versus segment length L. c) Confidence level of the fit of the residual gravity to the cosine model (see examples of Figure 5) versus segment length. The confidence level in a) and c) corresponds to the Student's t-test of the fit between the model and the data (see *Press et al.* [1992]). d) Measured segment-scale variations in gravity (Δ_{RMBA}) versus segment length L. Note that the along-axis profiles (solid circles) display a linear increase in amplitude with segment length. In contrast, the off-axis along-isochron data (gray diamonds) do not display any clear trends. The lines are the best fit to the data, and the numbers correspond to the correlation coefficient r. The dashed lines correspond to the trends reported by *Lin et al.* [1990] and *Detrick et al.* [1995] for axial segments along the MAR at 28°-30°N and 33°-40°N.

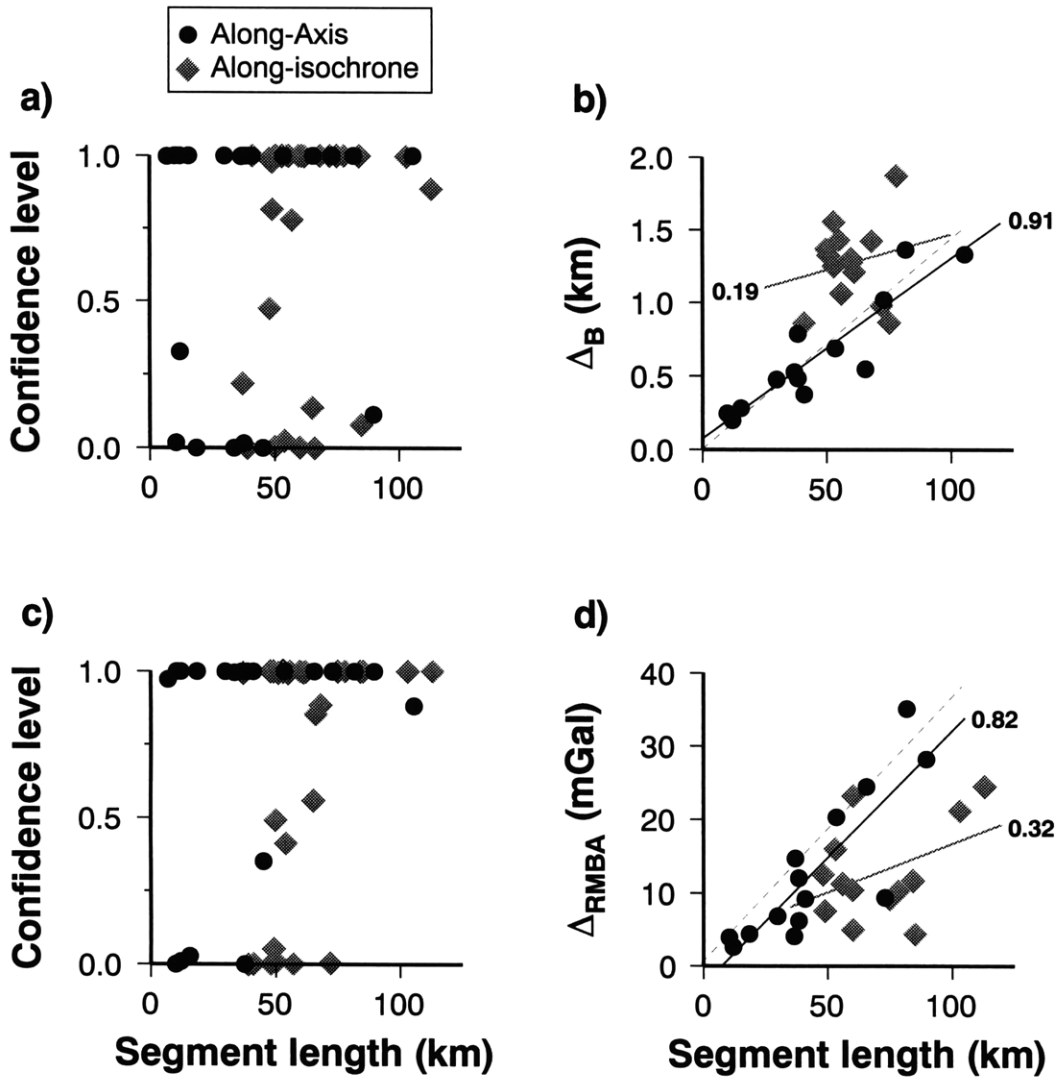

Figure 6, Escartin & Lin

Fig. 7. Selected examples of bathymetry and MBA profiles along the ridge axis, and residual bathymetry and RMBA along isochron profiles. In the axial profile non-transform offsets are marked by thin vertical lines and transform faults by the labeled lines. Numbers on the isochron profiles mark the segment number (Figure 4).

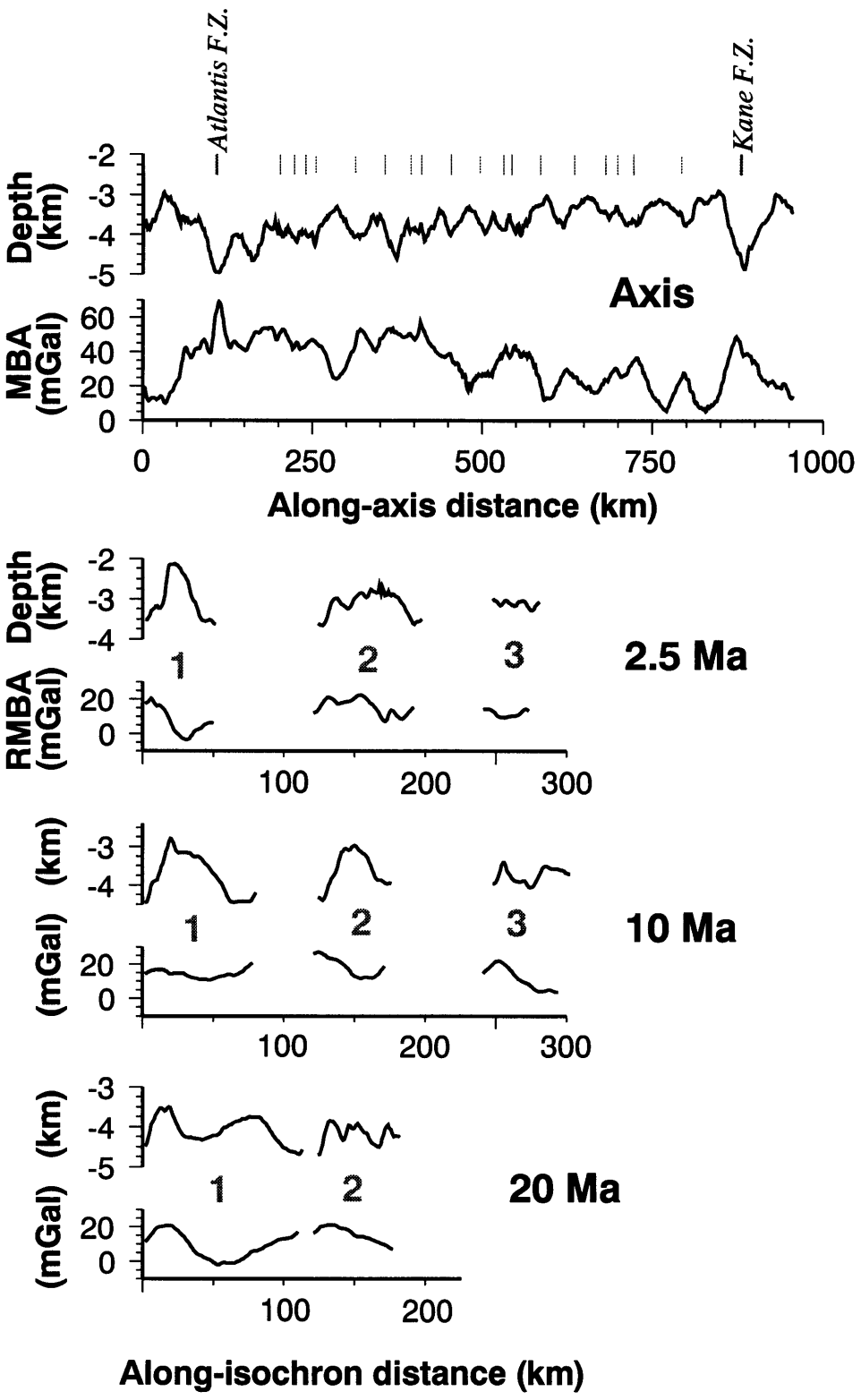

Figure 7, Escartin & Lin

Fig. 8. Across-axis profiles of residual bathymetry and RMBA through the north (N), center (C), and south (S) sections of segments (see Figure 4 for location of profiles).

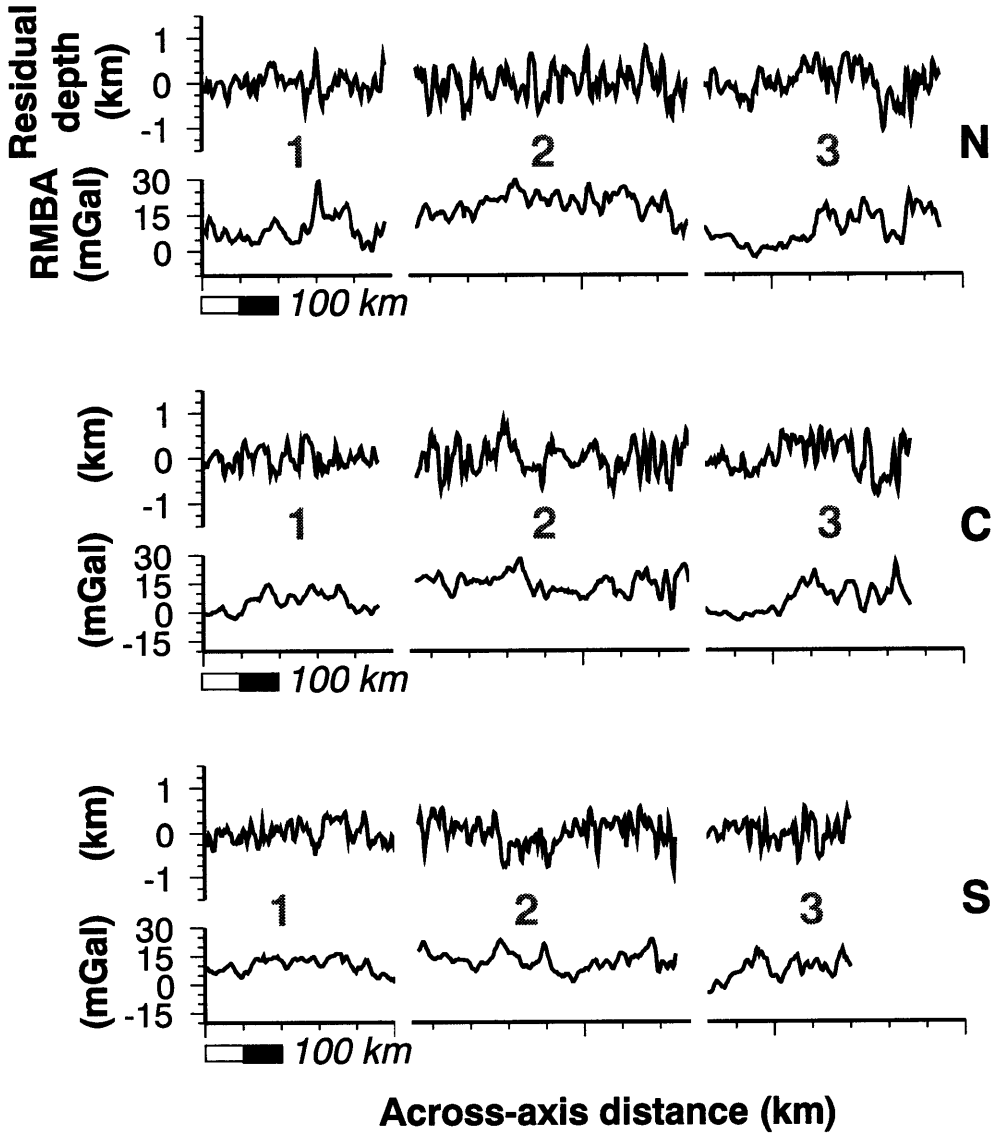

Figure 8, Escartin & Lin

Fig. 9. Computed coherence functions between gravity and bathymetry along the ridge axis and selected crustal isochrons of 2.5, 10, and 20 Ma from Figure 4. Note that off-axis data show no coherence at any wavelengths, indicating that the crustal structure created at the ridge axis is significantly disrupted by tectonic processes within a very short distance from the axis (<2.5 Ma), most likely within rift valley walls. Theoretical coherence functions [*Forsyth*, 1985] for an elastic plate with effective thickness of 1, 3, and 9 km are also shown on the axial profile. Shading corresponds to 1-σ of data uncertainties and the thin horizontal line marks the zero confidence level in the coherence analysis. The double arrow on the axial coherence indicates the range in length of segments on the axial profile.

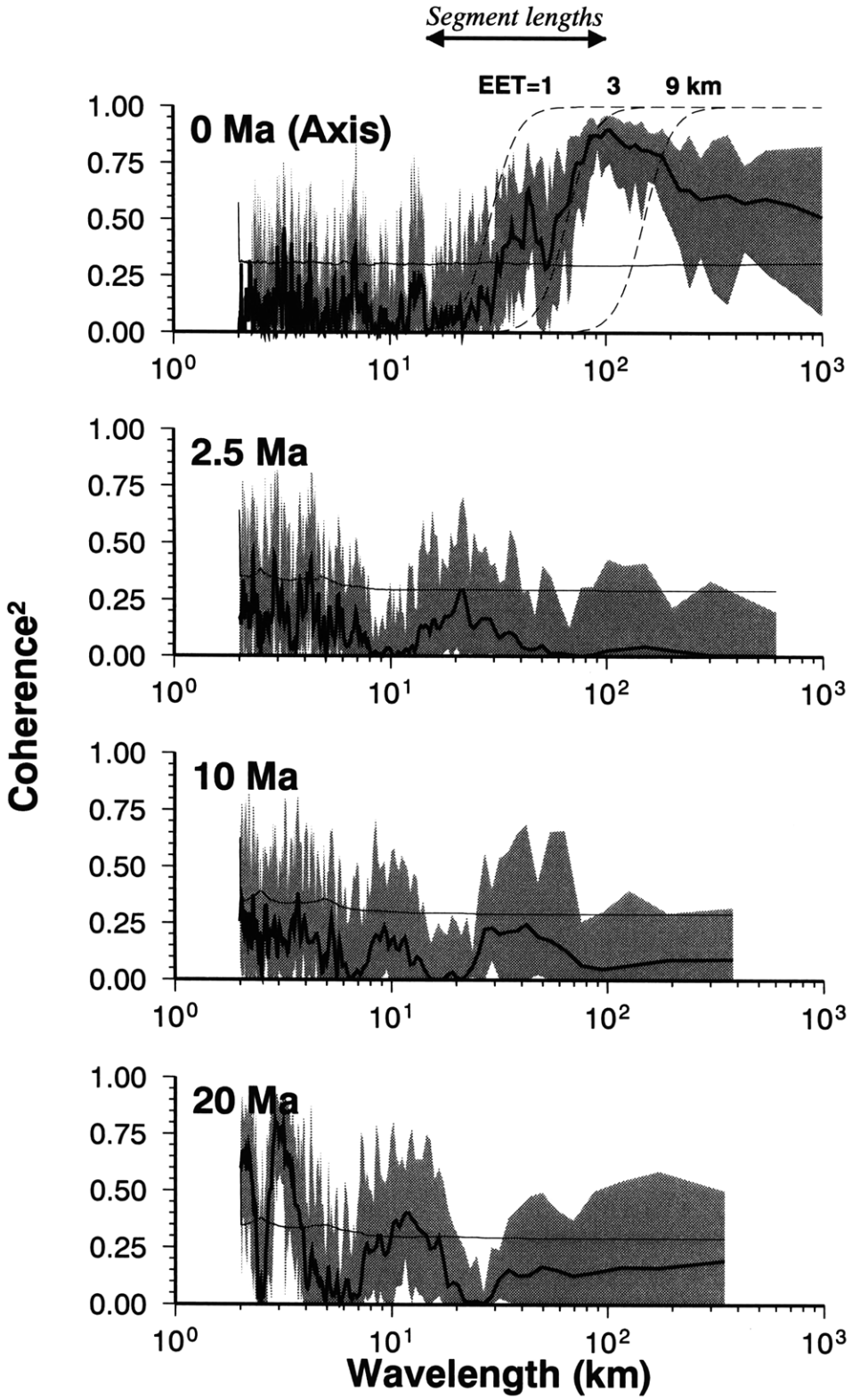

Figure 9, Escartin & Lin

Fig. 10. Across-axis coherence functions for profiles following crust along the north (N), center (C) and south (S) of segments 1, 2, and 3 of Figure 4. The along-axis coherence (dashed) is shown in the top panels for comparison (dashed lines). Theoretical coherence curves for elastic plate thicknesses of 1/3 and 1 km are also shown in the top left panel for comparison. The horizontal double arrows mark the range of fault spacing [*Goff et al.*, 1995] in each of the segments. Other conventions are the same as in Figure 9.

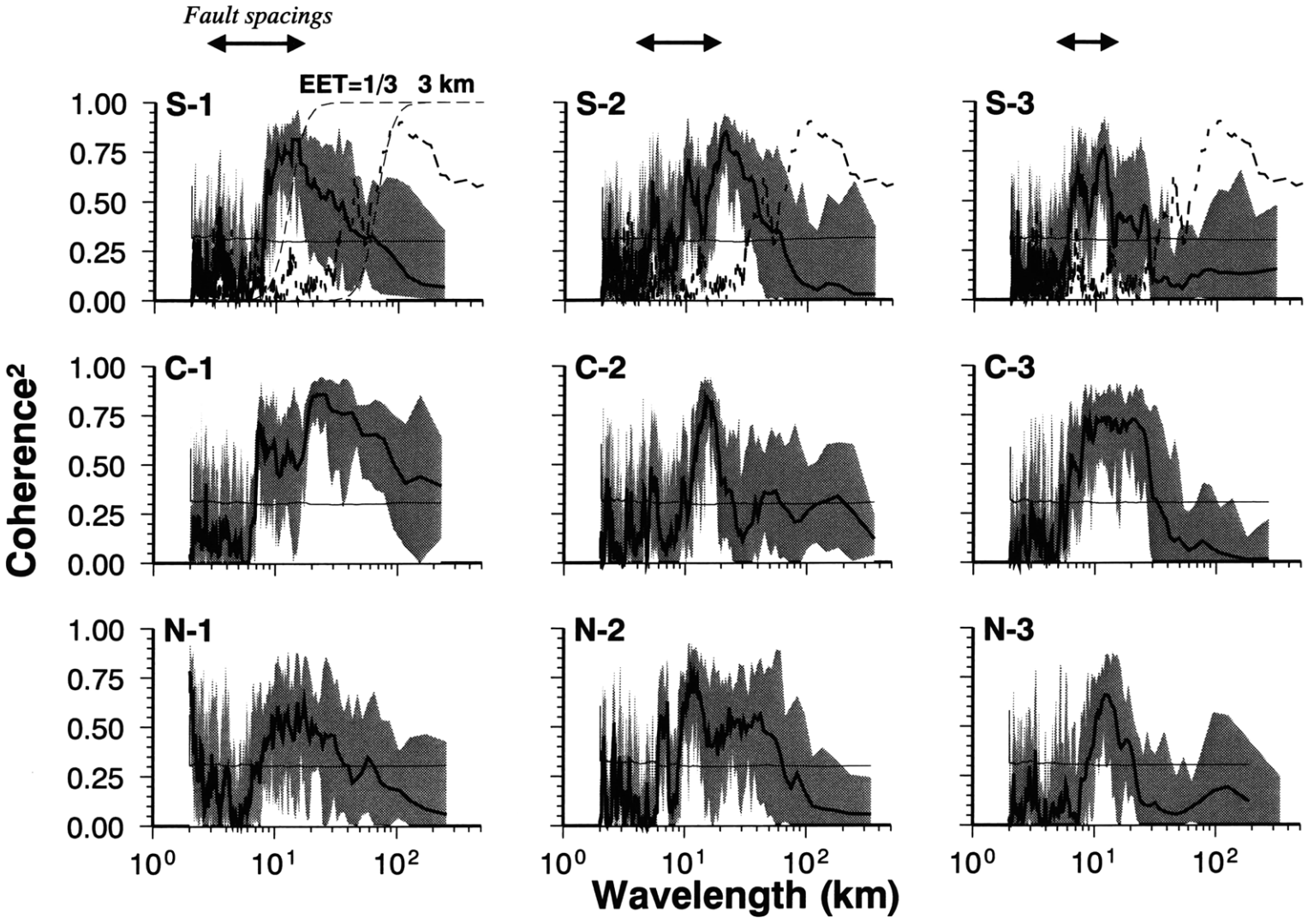

Figure 10, Escartin & Lin

Table 1. Model parameters used in gravity calculations

Parameter	Value
Gravitational constant, $Nm^2 kg^{-2}$	6.6673×10^{-11}
Gravitational acceleration, $m^2 s^{-1}$	9.80
Water density, kg m^{-3}	1030
Crustal density, kg m^{-3}	2700
Mantle density, kg m^{-3}	3300
Crustal thickness, km	6
Half spreading rate, km Ma^{-1}	13
Thermal boundary layer thickness, km	100
Asthenospheric temperature, °C	1350
Coefficient of thermal expansion, $°C^{-1}$	3.2×10^{-5}

Table 2. Results of the statistical analysis

Segment	L (km)	Δ_B (m)	r_B	Conf. level	Δ_{RMBA} (mgal)	r_{RMBA}	Conf. level	$r_{B\text{-}RMBA}$	Conf. level
Present-day axis									
SK-1	53.47	691.74	0.99	1.00	20.28	0.99	1.00	0.98	1.00
KA-1	9.98	245.26	0.97	1.00	1.45	-0.95	0.00	-0.97	0.00
KA-2	11.97	200.03	0.86	1.00	2.62	0.94	1.00	0.82	1.00
KA-3	15.49	282.73	0.96	1.00	1.67	-0.59	0.03	-0.63	0.02
KA-4	89.48	890.55	-0.18	0.11	28.26	0.57	1.00	0.36	0.99
KA-5	105.52	1335.09	0.77	1.00	23.22	0.17	0.88	0.37	1.00
KA-6	37.46	394.18	-0.46	0.02	8.4	-0.68	0.00	-0.10	0.34
KA-7	6.98	269.37	0.88	1.00	2.69	0.76	0.97	0.72	0.96
KA-8	29.93	479.96	0.83	1.00	6.81	0.92	1.00	0.77	1.00
KA-9	36.98	530.25	0.91	1.00	14.69	0.79	1.00	0.89	1.00
KA-10	38.5	787.66	0.85	1.00	6.21	0.90	1.00	0.93	1.00
KA-11	10.5	271.53	-0.71	0.02	3.89	0.85	1.00	-0.81	0.00
KA-12	33.51	794.98	-0.74	0.00	3.69	0.56	1.00	0.01	0.52
KA-13	38.5	485.3	0.65	1.00	11.99	0.79	1.00	0.72	1.00
KA-14	36.51	550.82	0.59	1.00	4.04	0.60	1.00	0.08	0.63
KA-15	72.89	1018.4	0.81	1.00	9.3	0.74	1.00	0.40	0.99
KA-16	81.82	1363.31	0.91	1.00	35.17	0.97	1.00	0.91	1.00
KA-17	65.47	547.75	0.95	1.00	24.51	0.94	1.00	0.92	1.00
KA-18	18.52	241.67	-0.95	0.00	4.36	0.91	1.00	-0.86	0.00
KA-19	12	104.76	-0.18	0.33	1.86	-0.73	0.01	0.38	0.83
KA-20	41.02	375.23	0.96	1.00	9.15	0.79	1.00	0.69	1.00
NA-1	45.03	686.93	-0.87	0.00	11.87	-0.08	0.35	0.47	0.99
Off-axis isochron									
OA-1-2.5	53	1557.19	0.88	1.00	15.98	0.9	1.00	0.77	1.00
OA-1-5.0	48	2163.95	0.57	0.99	12.45	0.85	1.00	0.43	0.94
OA-1-7.5	55	1431.03	0.84	1.00	14.02	0.57	0.99	0.05	0.57
OA-1-10.0	78	1876.59	0.77	1.00	10.23	0.8	1.00	0.35	0.95
OA-1-12.5	84	1509.68	0.56	1.00	11.66	0.84	1.00	0.51	1.00
OA-1-15.0	85	1218.72	-0.3	0.08	4.32	0.87	1.00	-0.47	0.01
OA-1-17.5	103	1224.26	0.47	1.00	21.21	0.97	1.00	0.34	0.97
OA-1-20.0	113	1148.12	0.23	0.89	24.5	0.92	1.00	0.06	0.63
OA-1--2.5	60	1276.95	0.88	1.00	23.24	0.82	1.00	0.60	1.00
OA-2-2.5	72	978.77	0.86	1.00	14.52	-0.55	0.00	-0.46	0.02
OA-2-5.0	60	1303.87	0.73	1.00	10.44	0.77	1.00	0.69	1.00
OA-2-7.5	49	996.59	0.26	0.82	4.87	-0.43	0.05	-0.87	0.00
OA-2-10.0	51	1325.54	0.98	1.00	12.47	0.6	0.99	0.50	0.98
OA-2-12.5	65	937.73	-0.27	0.14	15.82	0.04	0.56	-0.60	0.00
OA-2-15.0	68	1429.89	0.69	1.00	11.75	0.28	0.88	-0.21	0.19
OA-2-17.5	61	1209.21	0.90	1.00	10.02	0.59	1.00	0.29	0.88
OA-2-20.0	57	852.84	0.20	0.78	8.38	-0.63	0.00	-0.51	0.02
OA-2-22.5	48	317.04	-0.02	0.47	7.46	-0.68	0.00	-0.41	0.07
OA-2--2.5	66	1471.64	-0.67	0.00	10.73	0.26	0.85	-0.18	0.24
OA-3-2.5	37	289.42	-0.26	0.22	6.35	0.68	0.99	0.16	0.68
OA-3-5.0	56	1063.74	0.9	1.00	11.22	0.82	1.00	0.70	1.00
OA-3-7.5	53	1250.68	0.69	1.00	9.29	0.63	1.00	0.50	0.98

OA-3-10.0	54	713.44	-0.49	0.02	11.56	-0.06	0.41	-0.04	0.44
OA-3-12.5	39	541.42	-0.79	0.00	9.58	-0.89	0.00	0.50	0.95
OA-4-20.0	41	861.62	0.77	1.00	7.31	-0.91	0.00	-0.73	0.00
OA-4-22.5	49	1346.63	0.53	0.98	7.51	0.8	1.00	0.08	0.60
OA-4-25.0	62	767.97	0.58	1.00	10.39	0.6	1.00	0.75	1.00
OA-5-22.5	50	489.7	-0.64	0.00	11.33	-0.01	0.49	-0.41	0.06
OA-5-25.0	50	1369.6	0.71	1.00	8.24	-0.59	0.01	-0.94	0.00
OA-6-22.5	60	185.83	-0.72	0.00	4.95	0.95	1.00	-0.62	0.00
OA-6-25.0	75	865.38	0.79	1.00	9.15	0.87	1.00	0.86	1.00

Segments: NA, North of Atlantis; KA, Kane-Atlantis, SK, South of Kane, OA, off-axis. Numbers on on-axis profiles are the segment number. Numbers on off-axis profiles are segment number-age in Ma
L: Segment length; Δ_B: Amplitude of bathymetry; r_B: Correlation coefficient of model and bathymetry
Δ_{RMBA}: Amplitude of residual gravity; r_{RMBA}: Correlation coefficient of model and residual gravity
$r_{B\text{-}RMBA}$: Correlation coefficient of bathymetry and residual gravity
Conf. level: Student t-test confidence level of r (see *Press et al.* [1992]).

Chapter 4

RIDGE PROPAGATION AND SEGMENTATION HISTORY IN THE CENTRAL AND NORTHERN ATLANTIC OCEAN BASIN

1. Abstract

Global free-air satellite gravity data provide the most complete view of the history of ridge-segmentation in the central and northern Atlantic basin. Gravity "roughness" or "crenulation", indicated by the amplitude of the gravity variations, changes substantially along the Mid-Atlantic Ridge. Roughness is associated primarily with ridge geometry and secondarily with hot spot effects, and is not sensitive to changes in spreading rate along the length of the ridge axis. Roughness is higher along sections of the ridge that are oblique (>30°) to the spreading direction than along those that are sub-perpendicular. A substantial decrease in gravity roughness is also observed along the Reykjanes Ridge, corresponding to the influence of the Iceland hot spot. Consequently, variations in roughness with spreading rate reflect mainly variations in tectonism rather than three-dimensional mantle upwelling.

The segmentation patterns observed in the Atlantic basin at crustal ages less than 100 Ma suggest that transform offsets are stable and long-lived, while non-transform offsets have shorter life span and either migrate along the ridge axis or remain stable. 75% of the propagating offsets migrate down the regional gradient associated with hot spot swells, particularly Iceland and the Azores. Thus, offset propagation may be driven primarily by regional bathymetric or free-air gravity gradients associated with hot spots. However, the lack of correlation between gradient and rate of propagation, the existence of stable non-transform offsets, and the migration of offsets up regional gradients suggest that other processes in addition to regional gradients also contribute to offset propagation. Variations in lithospheric thickness along the ridge axis can control the rate of propagation, and stress variations associated with plate-motion changes may be important locally to drive segment propagation up regional gradients.

2. Introduction

Shipboard geophysical data from mid-ocean ridges indicate that the structure and morphology of the oceanic crust is strongly linked to ridge segmentation. Slow-spreading ridge segments range in length from ~10 to 100 km and are bounded by either transform or non-transform offsets, characterized by rigid (localized deformation on a transform fault) and non-rigid (distributed deformation) plate boundaries [*Macdonald et al.*, 1988]. Segment-scale variations in crustal thickness [e.g., *Dick*, 1989; *Kuo and Forsyth*, 1988; *Lin et al.*, 1990; *Tolstoy et al.*, 1993; *Detrick et al.*, 1995] and composition [e.g., *Cannat*, 1993] are consistent with models of focused magmatic accretion [e.g., *Whitehead et al.*, 1984; *Crane*, 1985]. Systematic variations in crustal tectonics are also observed at the segment scale. Tectonic extension is more important at segment ends than at segment centers, as indicated by along-axis variations in faulting spacing and displacement [e.g., *Shaw*, 1992; *Shaw and Lin*, 1993]. In addition, the distribution of microearthquake activity [*Rowlett*, 1981; *Barclay et al.*, 1993; *Wolfe et al.*, 1995], and differences in elevation, crustal thickness, and composition between inside- and outside-corners [*Severinghaus and Macdonald*, 1988; *Tucholke and Lin*, 1994; *Escartín and Lin*, 1995] indicate that there is also an asymmetry in tectonic extension across the axis, which results in characteristic elevated inside corner terrain. Consequently, the processes responsible for ridge segmentation ultimately control the structure and morphology of the oceanic crust off-axis.

Available off-axis data from the Mid-Atlantic Ridge (MAR) show a complex history of segmentation, and yet the causes for such spatial and temporal variations are poorly understood. Several models have been proposed to explain the along-axis propagation of ridge segments and abutting offsets, such as concentration of extensional stresses at tips of a propagating rift [*Phipps Morgan and Parmentier*, 1985; *Macdonald et al.*, 1991; *Phipps Morgan and Sandwell*, 1994], mantle upwelling beneath an individual segment [e.g.,

Schouten et al., 1985; *Gente et al.*, 1995], or changes in plate motion [e.g., *Menard and Atwater*, 1968; *Wilson et al.*, 1984]. Some of these models are consistent with geophysical data from individual ridge sections, e.g., 95°W and 85°W propagators of the Galápagos spreading center [*Phipps Morgan and Parmentier*, 1985] and the Mid-Atlantic ridge south of the Kane Fracture Zone (FZ) [*Gente et al.*, 1995]. However, the large differences in segmentation patterns among neighboring sections of a ridge indicate that several processes may control ridge segmentation and propagation on various sections of the ridge system or on different time scales. For example, the ridge segments at the MAR south of the Kane FZ at 20°-24°N are characterized by a complex history of waxing and waning on time scales of 10 Ma or less [*Gente et al.*, 1995], while the segments at 25°-27°N and 28°-31°N appear to have been migrating more gradually during a similar period of ~10 Ma [e.g., *Sempéré et al.*, 1995; *Tucholke et al.*, 1996].

To test the validity and relative importance of each of the proposed causes for propagation and stability of ridge segments and their offsets, it is advantageous to study the systematics of segmentation and its evolution on the scale of a whole oceanic basin. Constraints on basin-wide patterns of segmentation, however, are not available from shipboard marine geophysical surveys, which are limited to a few near-axis areas of the global ridge system. Satellite-derived free-air gravity data, on the other hand, have proven useful to study the distribution of fracture zones and non-transform offsets at the scale of whole ocean basins [e.g., *Müller and Roest*, 1992; *Phipps Morgan and Sandwell*, 1994]. Recently released sea-surface gravity data derived from Geosat and ERS1 altimetry [*Smith and Sandwell*, 1995] have significantly higher resolution and accuracy than any previously available satellite data. Interpretation of tectonic structures from this data set is therefore more reliable than that of earlier studies in the Atlantic that were based only on data along sparsely spaced satellite tracks [i.e., *Shaw*, 1988; *Müller and Roest*, 1992].

In this study we use the latest Geosat and ERS1 gravity dataset [*Smith and Sandwell*, 1995]. We remove the long-wavelength features associated primarily with hot-spots and cooling of oceanic lithosphere with age, to obtain a residual gravity map. This residual gravity allows us to identify the traces of both transform and non-transform offsets throughout the central and northern Atlantic basin. For each segment offset, we measure a set of tectonic variables, including its relative stability, along-axis propagation rate, segment and offset lengths, and long-wavelength regional gravity gradients. These observations are then used to test hypotheses for the causes of ridge segment propagation in slow-spreading oceanic lithosphere.

3. Data Analysis

3.1 Free-air gravity anomalies

The data used in this study are the sea-surface free-air gravity anomaly (FAA) derived from combined Geosat and ERS1 altimetry [*Smith and Sandwell*, 1995] between latitudes 10°S and 72°N and longitudes 70°W and 0° (Figure 1a). The data are gridded every 2 arc minutes (3.7 km at the Equator) and have an accuracy of ~4-7 mGal [*Sandwell and Smith*, 1996]. To first order, the FAA reflects basement relief, as has been shown by *Müller et al.* [1991] along the Kane FZ. The spatial resolution of the FAA data (~4 km) is small enough to resolve morphologic features such as the axial valley, transform valley, and elevated inside-corner crust, allowing the identification of ridge offset traces in off-axis crust, and ridge-axis discontinuities with offset lengths >~10 km; smaller offsets and their traces may not be visible in the satellite data, as the offset length is similar to the resolution of the data.

To highlight "local" features(<100 km in length) associated with ridge segments and their associated offsets we remove the "regional" (>>100 km) features from the FAA map. We filter the sea-surface FAA with a high-pass cosine taper filter at wavelengths of 300-

600 km to obtain a "residual" FAA map (Figure 1b). This map shows little systematic variations with age, the traces of offsets are more clearly identified than in the original FAA map (Figure 1a). The long wavelength "regional" FAA map in Figure 1c was calculated using a low-pass cosine taper filter at wavelengths of 300-600 km. This map reflects the combined effects of lithospheric cooling with age and the presence of numerous hot spot swells on and off the MAR axis (e.g., Azores and Iceland hot spots and Canary islands and Bermuda rise, respectively).

3.2 Mantle-Bouguer and residual gravity anomalies

To investigate the effects of along-axis variations in crustal thickness on the characteristics of ridge segmentation, we also calculated mantle Bouguer gravity anomaly (MBA) and residual Airy anomaly (RAA) at the ocean basin scale. The topographic correction to the satellite FAA was made using the 5 minute gridded ETOPO-5 bathymetry [*National Geophysical Data Center*, 1988]. Although the accuracy of the ETOPO-5 data is limited in areas with sparse ship track coverage [*Smith*, 1993], this data set is useful for basin-wide gravity corrections, but not for segment-scale variations in bathymetry and crustal thickness.

The MBA was computed assuming a constant 6-km thick crust with a constant crustal density of 2700 kg/m^3 and a mantle density of 3300 kg/m^3, ignoring the presence of sediments off-axis. The RAA was computed assuming a crust that is locally compensated (Airy isostasy). To create a map of relative crustal thickness that is consistent with gravity data, it was necessary to determine the "residual topography". In this case the deepening of seafloor with age associated with lithospheric cooling has been removed. This residual topography is calculated assuming that the seafloor depth is proportional to the square root of the crustal age (age$^{1/2}$) for ages <80 Ma. At crustal ages >80 Ma the depth versus age$^{1/2}$

relationship breaks down and no significant deepening is observed [*Parsons and Sclater,* 1977]. The best-fitting depth (ETOPO-5) versus age$^{1/2}$ (ages from *Müller et al.* [1993]) for a section of the Central Atlantic at 0-15°N away from the Azores and Iceland hot spot swells is 290 m/Ma$^{1/2}$, which is close to the values of 342±65 given by *Parsons and Sclater* [1977] an of 280 m/Ma$^{1/2}$ by *Stein and Stein* [1994]. The RAA was calculated by removing the effects of the bathymetry, using the Airy model of isostatically compensated crust from the FAA. The densities assumed for the crust and mantle are the same as those used in the MBA calculations. As we are mainly interested in the MBA and RAA along the ridge axis, the presence of off-axis sediments was neglected, and a constant age/depth was assumed for the whole basin.

3.3 Rigid plate motion models

We calculated synthetic flow lines of plate motion for the central and northern Atlantic using the finite difference stage poles of motion listed in Table 1. Flow-lines for the African-South American (AFR-SAM), African-North American (AFR-NAM), and European-North American (EUR-NAM) plate pairs were initiated on the present day ridge-offset location and then traced back to ~100 Ma (Figure 2). These flow lines provide a reference frame to determine whether individual offsets are stable or migrate along the ridge axis, and to calculate relative along-axis propagation rates. The flow lines are used only to study offset propagation, and not to fully describe the plate kinematics of the central and northern Atlantic Basin.

To calculate the flow lines, we assumed that the opening of the Atlantic during the last ~120 Ma can be described by the relative motion of the African (AFR), North American (NAM), South American (SAM), and European (EUR) plates. The AFR-EUR-NAM triple junction is at present located at 39°N [*McKenzie and Morgan*, 1969; *Searle*, 1980], at the

intersection of the Azores rift with the MAR, and was used in our calculations as the separation point between the EUR-NAM and AFR-NAM flow lines. The AFR-SAM-NAM triple junction is located on the MAR at 15°20', coinciding with the Fifteen-Twenty FZ [*Roest and Collette*, 1986], and corresponds to the separation of the AFR-NAM and AFR-SAM flow lines. No attempt was made to incorporate the possible along-axis migration of these triple junctions through time.

The geometry of the MAR axis between 10°S and 59°N (near Iceland) has been determined from near axis shipboard bathymetry and satellite FAA data. Bathymetry is available only for limited areas in the north Atlantic between 22°N and 39°N [e.g., *Gente et al.*, 1995; *Purdy et al.*, 1990; *Detrick et al.*, 1995; *Sempéré et al.*, 1995] and for the Reykjanes ridge [e.g., *Searle*, unpub. data]. Although some small offsets (<10 km) are not recognized from the satellite data alone, there is good agreement between segmentation patterns identified from shipboard bathymetry and satellite gravity data in Figure 3.

We define transform offsets (TOs) as offsets that are visible in the satellite data as straight and deep valleys, reflecting rigid plate boundaries and localized deformation on a transform fault within the transform valley [*Fox and Gallo*, 1984; *Macdonald et al.*, 1988] (bold black line corresponding to the Atlantis FZ in Figure 2). The transform fault approximately follows a small circle about the pole of plate rotation [*McKenzie and Parker,* 1967]. Non-transform offsets (NTOs) are characterized by jagged and/or shallower valleys, reflecting non-rigid plate boundaries and non-localized deformation [*Macdonald et al.*, 1988] (thin black lines in Figure 3). These zones are characterized by oblique faults with little or no evidence for strain localization on strike-slip faults [i.e., *Searle and Laughton*, 1977; *Grindlay et al.*, 1991; *Sempéré et al.*, 1993]. Although classification of offsets into TOs and NTOs has also been done in terms of offset length, the length at which the transition from TO to NTO occurs is not well defined. For example, the Bight FZ at 56°47'N has an offset of only 17 km but has a well-defined transform fault that is parallel

to the direction of spreading, indicating that it is a TO rather than a NTO [*Applegate and Shor*, 1994]. Other offsets north of the Bight FZ have lengths >30 km, but do not show localized deformation and therefore correspond to NTOs [*Applegate and Shor*, 1994].

4. Results

4.1 Gravity roughness and ridge axis obliquity

There is a strong dependence of seafloor morphology on spreading rate [e.g., *Macdonald et al.*, 1988; *Lin and Phipps Morgan*, 1992], which is also recognizable in satellite-derived gravity data [*Small and Sandwell*, 1989; 1992; *Phipps Morgan and Parmentier*, 1995]. Local variability (roughness) of ridge axis gravity anomalies can be measured by the RMS (root mean square), which changes significantly along the MAR [*Small and Sandwell*, 1992] (shown in Figure 4). The half-spreading rate decrease from ~32 km/Ma at 10°S to ~10 km/Ma at ~55°N near Iceland, and cannot account for this RMS variability long the ridge axis. Instead, we investigate the effects of ridge geometry and magma supply associated with hot spots on gravity roughness. We characterize the segment-scale variability in gravity structure by calculating the RMS of the FAA within small boxes on each flank of the ridge axis (Table 3). These boxes are located on crust < 10 Ma old. The axial valley is not included in any of the sampling boxes because it is a prominent feature that may strongly bias the measured RMS.

Ridge geometry is characterized by the obliquity of the ridge. Obliquity is defined as the angle between the trend of the ridge and the direction perpendicular to the plate spreading direction, as determined from the poles of rotation given in Table 1 (Figure 5); the overall trend of the ridge is defined over an ~300 km section of the ridge axis. Along some sections of the ridge, segment offsets do not step laterally in one direction, and thus

the ridge does not define a clear trend (e.g., immediately south of the Kane FZ, Figure 2). For these areas no obliquity has been measured (Table 3).

A plot of RMS values versus obliquity is shown in Figure 5. There is a weak positive correlation between the RMS values of gravity in the sampling boxes and obliquity of the ridge. The RMS values of the gravity (open circles, Figure 4) is the lowest (5-8 mGal) at the Azores platform, where the ridge is sub-perpendicular (~17°) to the present day spreading direction. The RMS increases to a maximum of 13-19 mGal as the ridge axis becomes more oblique (~55°) in the Equatorial Atlantic, where large offset fracture zones develop. The RMS values on sections of the ridge where obliquity could not be measured, range from ~8-13 mGal (Table 3).

The correlation between gravity variations and ridge axis obliquity is also reflected in the observed change in gravity pattern at 60-70 Ma crust between the Kane and the Atlantis FZs, shown by the gray diamonds in Figure 5. At that time the overall trend of the ridge axis was similar to that at present. However, the spreading direction was rotated ~20° counterclockwise, as recorded by the traces of the Kane [*Tucholke and Schouten*, 1988] and Atlantis FZs (Figure 1b), resulting in a more oblique ridge configuration. The gravity anomalies over the crust generated during this period show more pronounced gravity lineations and higher RMS than near the axis (Figures 1b and 2), suggesting better organized segmentation.

In addition to ridge axis obliquity, magma supply also affects the nature of gravity variations along the MAR. The RMS values for the Reykjanes Ridge are low when compared with other sections of the ridge with similar obliquity (black circles in Figure 5). The morphology of the Reykjanes Ridge differs substantially from that of the rest of the MAR, and is characterized by an axial high instead of an axial valley (Figure 1c). Residual FAA in this area (Figure 1c) reveals several V-shaped ridges emanating from Iceland, probably associated with magmatic plumes or asthenospheric flow of the Iceland plume

[e.g., *Vogt,* 1971; *White et al.*, 1995]. Measured RMS values in this area (5.7-6.2 mGal, Table 3) therefore include variability associated with the V-shaped anomalies; RMS values along the axis of the Reykjanes Ridge (Figure 4) are <5 mGal and are associated with the morphology of the ridge axis.

The RMS values along the Azores platform from the axial profile (Figure 4) are low and relatively similar to those observed along the Reykjanes Ridge, and may be caused by the Azores hot spot. Two lines of evidence, however, suggest that ridge obliquity rather than hot spot effects are the actual cause for the low RMS values at the Azores platform. First, a rift valley is maintained along the Azores Platform (Figure 1b). Second, the shoaling of the ridge axis along the Azores Platform is not as significant as that of the Reykjanes Ridge. These two observations suggest that the Azores plume is smaller or colder than the Iceland plume [e.g., *Vogt*, 1976; *Ito and Lin*, 1995a].

4.2 Ridge segment offsets

We identified and digitized a total of 232 TO and NTO offset traces from the residual FAA map (Figure 2), defining a total of 157 ridge segments on-axis. The length of identified ridge segments ranges from <10 km to ~125 km, with an average length of 49±22 km, consistent with earlier results [e.g., *Macdonald et al.*, 1988]. All the parameters measured for identified offset traces are listed in Table 1. Where possible we also measured the length of offsets, values of regional FAA and its gradient at the mid-point of each offset (from the regional FAA, Figure 1c), the present day spreading direction and rate, the migration rate and direction along the ridge axis, and its life span. The life span of each offset was estimated from the seafloor age map of *Müller et al.* [1993]. The along axis propagation rate (PR) of a migrating offset was calculated from the angle between the offset traces and flow lines, both on the East and West flank of the ridge. All propagation rates are normalized by the half spreading rate (HSR). Small differences in

values of PR/HSR between the East and West flanks may arise from asymmetric spreading or ridge jumps not predicted by the plate model used. The typical uncertainty in the estimation of the angle between offset traces and flow lines is ~5°, and consequently the uncertainty of PR/HSR increases with the measured angle. The PR/HSR errors increase from ~0.08 at stable offsets to ~0.17 when PR/HSR approaches 1. Only one of the identified offsets (AsCh-10b, Table 1) propagates faster than the half-spreading rate, resulting in an angle >45° between the offset trace and flow lines. Due to uncertainties in the age map, the life span and propagation rates have been calculated over 5 Ma age bins; the PR/HSR is given in Table 2 for larger age bins if PR remained constant during that period of time.

The length of TO and NTO offsets show a gamma distribution with an average value $\overline{L_{TO}}$ of ~110 km and $\overline{L_{NTO}}$ of ~17 km. The population of NTOs include those with and without an off-axis trace. The transition from TO to NTO occurs at offset lengths of 20 to 50 km approximately, although some overlap between the two populations exists (Figure 6). There are numerous offsets that are short lived (<5 Ma), leaving no off-axis trace (i.e., segments along the Azores platform between 40° and 50°N). The average life life-span of TOs is 50±30 Ma, while that of stable NTOs with well defined off-axis trace is 27±11 Ma. If all the NTOs with no identifiable off-axis trace are also considered, the average life span drops to ~7 Ma.

The data in Table 2 lists NTOs with offsets >50 km (e.g., offset 27, SPFo-00d), as well as TOs with life spans <20 Ma (e.g., offsets 21 and 22, Saint Paul-b and c). Offset 27, for example, has a length of 65 km, but has no recognizable transform valley connecting the two adjacent rift valleys (Figures 1b and 3, 2.3°N). It has been classified therefore as a NTO. These long NTOs may have originated recently (<10 Ma), and a well-defined strike-slip FZ is not developed yet. Detailed shipboard bathymetry and gravity is

required to determine the actual nature and history of there offsets. The TOs around the Saint Paul's FZ or between Four North and Vema FZs appear to originate after a plate motion change within the last 30 Ma, maybe along the trace of a triple junction. Consequently, their life span is relatively short when compared with the rest of the Atlantic TOs. These offsets are indicated in Figure 7 by gray open and solid circles. The differences between TO and NTOs both in age and length are more clearly marked when, for the reasons given above, these points are not considered in the interpretation of the data.

4.3 Propagation rate of non-transform offsets

While transform offsets are stable, many of the non-transform offsets in the central and northern Atlantic have propagated along the ridge axis. Only 30 out of the 130 identified NTOs (about 23%) remained relatively stable (PR/HSR<0.1), and the majority have migrated along the ridge axis (0.1<PR/HSR<0.2). For comparison, the V-shaped ribbons south of Iceland (Figure 1b) have propagated at rates of 200 km/Ma [*Vogt*, 1971], approximately twenty times the HSR, indicating that the processes driving them differ substantially from those driving segment propagation along the ridge. Examination of the satellite data (Figure 1b) and available bathymetry for areas of the northern MAR between 21°N and 31°N [e.g., *Tucholke et al.*, 1996; *Sempéré et al.*, 1995] (Figure 2) demonstrate that NTO propagation is not a steady process. The traces of NTOs in the bathymetry data (Figure 2b) demonstrate that fast migration (PR/HSR>1) occurs during short periods of time (<1 Ma) in opposite directions; such fast changes in PR/HSR cannot be resolved in the FAA (compare Figure 2a and 2b). These fast changes result in relatively stable PR/HSR values over periods of 5 Ma or longer (Table 2).

5. Discussion

5.1. The origin of gravity roughness

The FAA gravity structure or "roughness" along the MAR reflects to a first order basement topography and, consequently, is related to the expression of ridge segmentation. Gravity and bathymetry data indicate that the seafloor morphology observed off-axis is produced by extensional tectonism along the rift valley walls, in addition to on-axis focused magmatic accretion (Chapter 4) [*Tucholke and Lin*, 1994]. While the on-axis variation in seafloor depth along a segment is typically ~0.5 km [e.g., *Sempéré et al.*, 1993], the difference in elevation between tectonically uplifted inside corner terrain and outside corner terrain is on the order of 1 km or more [*Severinghaus and Macdonald*, 1988; *Escartín and Lin*, 1995]. Consequently, the variations in RMS with ridge obliquity are an indication of the amount of tectonism associated with inside corner uplift along the MAR. With increasing obliquity, the ratio of offset to segment length increases (i.e., greater average offset length). The height of the inside corners increases with increasing offset length [*Escartín and Lin*, 1995]. Consequently, the topography of sections of the ridge with low obliquity (e.g., Azores platform) is less pronounced than that of oblique ridges (e.g., Kane-Atlantis), resulting in lower RMS values (smoother gravity).

The observed transition from smooth to rough gravity structure with decreasing spreading rate thus appears to be related to tectonic segmentation and not to magmatic segmentation as proposed by *Phipps Morgan and Parmentier* [1995]. Inside corners do not form at fast-spreading ridges, and consequently the off-axis traces of NTOs are not easily recognizable in the FAA. At slow-spreading ridges, in contrast, the gravity structure is dominated by elevated IC terrain and deep offset traces of tectonic origin (e.g., the Equatorial Atlantic and sections of the southwest Indian Ridge [*Phipps Morgan and Parmentier*, 1995]). Consequently, the transition in gravity roughness or "crenulation" of

Phipps Morgan and Parmentier [1995] with spreading rate likely reflects mainly faulting, rather than the along-axis variations in zero-age crustal thickness associated with three-dimensional mantle upwelling.

5.2. Factors controlling ridge offset migration

Several models have been proposed to explain the propagation of ridge segments. These models can be broadly separated into "magmatic" (e.g., mantle upwelling, hot spot effects) and "tectonic" hypotheses (e.g., stress concentrations at ridge segment ends). The validity and relative importance of each of these models can be tested using the segmentation patterns and measured offset parameters (Table 3).

Tectonic hypotheses

The along-axis propagation of ridge segments has been modeled as the response of the oceanic lithosphere to changes in local and far field tectonic stresses. Regional tectonic forces may result in a local concentration of stresses at the tip of ridge segments. Propagation of an offset will occur if the difference in stress concentration at the tip of a segment across an offset is sufficient to break the lithosphere across the offset and allow migration of a ridge segment. Differences in stress concentration can be caused by regional gradients in bathymetry [*Phipps Morgan and Parmentier*, 1985; *Phipps Morgan and Sandwell*, 1994], far-field stresses associated with plate spreading [*Macdonald et al.*, 1991], or by plate motion changes [e.g., *Hey et al.*, 1980; 1988].

Our results show that propagation of NTOs in the central and northern MAR is partly caused by regional bathymetric gradients (Figure 8), as suggested by the model of *Phipps Morgan and Parmentier* [1985]. This model predicts that small topographic gradients at regional scales result in a slight imbalance of stresses across an offset that favors its migration down the regional gradient. Of the 128 NTOs identified, 78 (60.9%) do not

have a recognizable trace off-axis, 14 are stable (10.9%) and 36 (28.1%) migrate along the ridge axis. Of the migrating NTOs 72.2% (20.3% of the total number of NTOs) propagate down the regional FAA gradients, while only ~27.8% (7.8% of the total) propagate up the gradient (Figure 8). The use of age bins >5 Ma which can be calculated from Table 2, would result in slight variations in the PR/HSR, and occasionally a change in the spreading direction; however, the results presented in Figure 9 would not vary substantially. A large number of migrating offsets are concentrated on the sections of the ridge between the Fifteen-Twenty FZ to Pico FZ (15°-40°N) and south of Iceland (45°-55°N). These two zones show pronounced bathymetric (Figure 8a) and gravity gradients (Figure 8c) caused by the Azores and Iceland hot spot swells. Other hot spots exist along the Mid-Atlantic Ridge, such as Ascension at 5°S or Sierra Leone at 1.7°N. However, these areas are characterized by an oblique ridge and are associated with large, stable fracture zones. Therefore, no clear correlation between the direction of propagation and gradients is observed in these zones due to the scarce number of NTOs and the small gradients associated with these hot spots (Figures 1c and 8).

Factors other than regional gradients clearly contribute to ridge offset propagation. As seen in Figure 10a, the magnitude and direction of propagation are not directly correlated with the magnitude of the regional gravity gradients. Enhanced stress concentration at the end of segments has been proposed by *Macdonald et al.* [1988] as a mechanism for driving propagation of longer segments at the expense of shorter ones. The central and northern Atlantic data show no correlation between the magnitude and direction of propagation and the difference in the length of segments across each offset (Figure 10b) indicating that this mechanism for offset propagation is not an important driving force for offset propagation in the Atlantic basin. In fact, south of the Kane FZ at 22.75°N several segments appeared ~10 Ma ago. These segments grew from lengths <10 km to ~60 km at the expense of longer adjacent segments [*Gente et al.*, 1995].

Changes in plate motion reorganize the plate boundary geometry both at fast [e.g., *Menard and Atwater*, 1968] and slow spreading ridges [e.g., *Vogt et al.*, 1969; *Tucholke and Schouten*, 1988], and may drive along-axis propagation of ridge segments [e.g., *Hey et al.*, 1988]. Small changes in plate motion have been documented on the northern MAR at time scales of 2 Ma or less [e.g., *Sloan and Patriat*, 1992]. Such plate motion changes may affect locally the propagation of some segment offsets by changing the local stress field and altering the balance of forces across the offsets. This mechanism may drive offset propagation up regional gradients, and result in the lack of correlation between propagation rates and regional gradients (Figure 10a). Further quantification of the effects of small plate motion changes require detailed studies to determine the geometry and history of ridge segmentation.

Variations in the strength of the lithosphere along the MAR axis may also contribute to the lack of correlation between NTO propagation rates and regional bathymetric gradients. The rate of offset propagation along the ridge axis will depend on the difference in stress concentration between adjacent ridge segments, and the strength of the lithosphere. This is consistent with the stability of most of the offsets >50 km, and the migration of those that have offset lengths <25 km (Figure 10c). Variations in lithospheric strength, however, cannot account for the propagation of offsets up the FAA gradient. Consequently, the rate of propagation is controlled primarily by the regional FAA gradient, and other effects such as changes in plate motion and lithospheric strength may result in propagation up the gradients or variations in propagation rates, respectively.

Magmatic hypotheses

Segment propagation has also been explained by mantle diapers that are fixed in the asthenosphere [*Schouten et al.*, 1987] or by temporal variability in mantle upwelling [*Gente et al*, 1995]. The first model of *Schouten et al.* [1987] predicts that traces of ridge offsets

reflect the absolute motion of the plate boundary over fixed mantle diapirs in the asthenosphere. However, offsets have varying propagation rates and directions (e.g., north and south of the Kane FZ, Figure 8), or display abrupt changes in the propagation rate and/or direction that do not correlate with plate motion changes (e.g., NTOs at 10°S-0°, Figures 1b and 2). Alternatively, the initiation of a new mantle plume may explain the birth and growth of short segments at the expense of long ones [*Gente et al.*, 1995]. However, results from numerical experiments only produce segmented mantle upwelling at wavelengths >100 km [e.g., *Sparks and Parmentier*, 1993; *Jha et al.*, 1994; *Magde et al.*, 1996], substantially larger than 49±22 km typical of ridge segments along the MAR. In addition, changes in crustal thickness off-axis at time scales of 2-3 Ma [e.g., *Rommeveaux et al.*, 1994; *Pariso et al.*, 1995; *Sempéré et al.*, 1995; *Tucholke et al.*, 1996] , which are interpreted as magmatic supply variability, do not correlate directly with changes in the rate or direction of offset propagation. These observations suggest that mantle upwelling under individual ridge segments does not substantially contribute to ridge segment propagation.

Hot spots appear to drive segment propagation down the regional gradients associated with the swell (Figure 9). Magmatic effects associated with hot spots appear to be restricted to the Reykjanes Ridge, where an axial high reflects elevated lithospheric temperatures [e.g., *Searle and Laughton*, 1981; *Appelgate and Shor*, 1994], and the V-shaped ridges (Figure 1b) indicate magmatic pulses associated with the hot spot [*Vogt*, 1971; *Smallwood et al*, 1995]. Several other plumes may be present along the MAR, as indicated by the long-wavelength bathymetry and MBA (Figure 8), but their thermal effect is less than that of Iceland, as the ridge axis remains characterized by an axial valley (Figure 1b) instead of an axial high. The RAA is less correlated with bathymetry than the MBA, particularly if 75% of Airy isostasy is assumed, indicating that bathymetry is compensated mostly by crustal thickness variations, consistent with results from the Galápagos hot spot [*Ito and Lin*, 1995b]. Seismic crustal thickness measurements reflect the regional trends,

but variations in crustal thickness at the scale of individual segments cause large scatter in the seismic data (Figure 8). While crustal thickness north and south of 40°N (Azores hot spot) is very similar, the segmentation patterns on both sections of the ridge are substantially different (Figure 1b). As discussed earlier, the style ridge segmentation is controlled mostly by ridge obliquity and secondarily by hot spot effects (Figure 5 and Table 3). The propagation of individual ridge offsets appears to be controlled primarily by FAA gradients (Figure 10), although other factors may also be important.

5.3. Factors affecting ridge offset stability

Transform offsets do not propagate along the ridge axis, while non-transform offsets show both migration and stability. The differences in behavior between TOs and NTOs likely reflect differences in the accommodation of deformation across the offset. Tectonic deformation at TOs is accommodated along a discrete shear zone within the transform valley, rather than on a wide zone of diffuse deformation as in the case of NTOs. This mode of localized deformation tends to be stable in time, and favor the formation of a long-lived transform fault that does not migrate along the ridge axis. The offset length of TOs is also substantially larger than that of NTOs (Figure 6), suggesting that the rifting of old lithosphere by a migrating rift would require substantially more energy than continued slippage along a ridge perpendicular strike-slip fault.

The transition from localized (TO) to distributed (NTO) accommodation of strain across an offset occurs at offset length of 20-40 km on the central and northern MAR (Figure 6) and may be related to the width of the zone of active deformation. Based on the distribution of teleseismic events [*Lin and Bergman*, 1990], microearthquakes [e.g., *Wolfe et al.*, 1995], and the width of the axial rift valley [e.g., *Sempéré et al.*, 1993], the width of axial deformation along the MAR is estimated to be 15-30 km. If the lateral offset of two adjacent ridge segments is shorter than the width of the active deformation zone, tectonic

interaction between adjacent segments may occur through propagation of faults or dikes across the offset, resulting in a diffuse zone of deformation [*Lin*, 1996]. In contrast, if the offset length is shorter than the width of the deformation zone interaction across the offset may be strongly inhibited, due to increased energy required to break stable lithosphere. Shearing along a well-defined strike-slip fault within the transform valley may then become the preferred mechanism to accommodate differential spreading across the offset. The large overlap in offset length between TOs and NTOs (Figure 6) is likely to reflect the variability in mechanical properties and stress state of the oceanic lithosphere along the MAR.

The relatively slow propagation rates of the majority of NTOs (<20% of the HSR) and the stability of numerous NTOs (10.9% of total number of offsets, Table 2, Figures 2 and 8) suggest that the forces driving the propagation of individual segments are close to equilibrium. Therefore, propagation of offsets may reflect small perturbations in this dynamic equilibrium. The relatively stable propagation rates during the periods of >10 Ma of many offsets between the Atlantis and Pico FZs, for example, suggests that the forces driving propagation are relatively constant in time; regional FAA gradients associated with hot spot swells are likely to be persistent and stable during long periods of time.

6. Summary

The free-air satellite gravity from the central and northern Atlantic reveals a pattern of ridge segmentation from which we draw the following conclusions:

(1) Gravity "roughness", as measured by the RMS value of gravity, varies substantially along the ridge axis as a function of ridge geometry primarily and hot spot effect secondarily. Roughness is higher along sections of the ridge that are oblique to the spreading direction than along those that are more orthogonal. A substantial decrease in gravity roughness is also observed along the Reykjanes Ridge, corresponding to the

Iceland hot spot. Gravity roughness is insensitive to changes in spreading rate along the axis.

(2) Segmentation patterns along the MAR during the last 100 Ma suggest that transform offsets are stable, while the majority of non-transform offsets traces (>70%) migrate along the ridge axis. The average length of transform offsets is 110 km, while that of non-transform offsets is 17 km. Transform offsets also have longer life spans (>50±30 Ma) than non-transform offsets (27±11 Ma).

(3) FAA gradients associated with hot spot swells appear to contribute to the propagation of NTOs. Approximately 72% of migrating offsets propagate down regional gradients, and only 28% migrate up the gradient. A lack of correlation between offset propagation rates and the gradients, the presence of stable offsets, and offset propagation up regional gradients suggest that other processes such as plate motion changes may contribute to individual segment propagation. Variations in lithospheric thickness may also control the stability and propagation rate of segments and abutting offsets. Long offsets, such as transforms, remain stable because deformation is localized, and/or because the lithosphere across the offset is too thick to be rifted during segment propagation.

Acknowledgments. This work benefited from discussions and comments from G. Hirth, K. Hodges, E. Hooft, G. Jaroslow, N. Mitchell, H. Schouten, M. Tivey, and B. Tucholke. The GMT software [*Wessel and Smith*, 1991] was extensively used in this study. This work was supported by NSF grant 9300708. Contribution 9207 of the Woods Hole Oceanographic Institution.

References

Abrams, L. J., R. S. Detrick and P. J. Fox, Morphology and crustal structure of the Kane Fracture zone transverse ridge, *J. Geophys. Res.,* 93, 3195-3210.

Appelgate, B. and A. N. Shor, The northern Mid-Atlantic and Reykjanes ridges: Spreading center morphology between 55°50'N and 63°00'N, *J. Geophys. Res.*, 99, 17935-17956, 1994.

Barclay, A. H., D. R. Toomey, G. M. Purdy, and S. C. Solomon, FARA microearthquake experiments, III, results from the Mid-Atlantic Ridge at 35°N (abstract), *EOS Trans. AGU*, 601, 1993.

Bjarnason, I. T., W. Menke, O. G. Flovenz and D. Caress, Tomographic image of the Mid-Atlantic plate boundary in southwestern Iceland, *J. Geophys. Res.,* 98, 6607-6622, 1993.

Bott, M. H. P. and K. Gunnarsson, Crustal structure of the Icealand-Faroe Ridge, *J. Geophys.*, 221-227, 1980.

Bunch, A. W. H. and B. L. N. Kennett, The crustal structure of the Reykjanes Ridge at 59°30'N, *Geophys. J. astron. Soc.*, 61, 141-166, 1980.

Cannat, M., Emplacement of mantle rocks in the seafloor at mid-ocean ridges, *J. Geophys. Res.*, 98, 4163-4172, 1993.

Cormier, M. H., R. S. Detrick and G. M. Purdy, Anomalously thin crust in Oceanic Fracture Zones: New Seismic Constraints from the Kane Fracture Zone, *J. Geophys. Res.,* 89, 10,249-10,266, 1984.

Crane, K., The spacing of rift axis highs: dependence upon diapiric processes in the underlying asthenosphere?, *Earth Planet. Sci. Lett.*, 72, 405-414, 1985.

Detrick, R. S. and G. M. Purdy, The crustal structure of the Kane Fracture Zone from seismic refraction studies, *J. Geophys. Res.,* 85, 3759-3777, 1980.

Detrick, R. S., H. D. Needham and V. Renard, Gravity anomalies and crustal thickness variations along the Mid-Atlantic ridge between 33°N and 40°N, *J. Geophys. Res.*, 100, 3767-3787, 1995.

Dick, H. J. B., Abyssal peridotites, very slow spreading ridges and ocean ridge magmatism, A. D. Saunders and M. J. Norry eds., *Abyssal peridotites, very slow spreading ridges and ocean ridge magmatism*, 71-105, Geological Society Special Publication, 1989

Escartín, J. and J. Lin, Ridge offsets, normal faulting, and gravity anomalies of slow-spreading ridges, *J. Geophys. Res.,* 100, 6163-6177, 1995.

Escartín, J. and J. Lin, Tectonic modification of axial crustal structure: Evidence from spectral analyses of gravity and bathymetry from the Mid-Atlantic Ridge flanks (25.5°-27.5°N), *Earth Planet. Sci. Lett.*, in prep., 1996.

Ewing, J. I. and M. Ewing, Seismic refraction measurements in the Atlantic Ocean Basins, in the Mediterranean Sea, and in the Norwegian sea, *Bull. Geol. Soc. Amer.*, 70, 291-318, 1959.

Fowler, C. M. R., Crustal structure of the Mid-Atlantic ridge, *Geophys. J. astron. Soc.*, 47, 459-491, 1976.

Fowler, C. M. R. and D. H. Mathews, Seismic refraction experiment on the Mid-Atlantic ridge in the FAMOUS area, *Nature*, 249, 752-754, 1974.

Fox, P. J. and D. G. Gallo, A tectonic model for Ridge-transform-Ridge plate boundaries: implications for the structure of oceanic lithosphere, *Tectonophys.*, 104, 205-242, 1984.

Gente, P., R. A. Pockalny, C. Durand, C. Deplus et al., Characteristics and evolution of the segmentation of the Mid-Atlantic Ridge between 20°N and 24°N during the last 10 million years, *Earth Planet. Sci. Lett.*, 129, 55-71, 1995.

Grindlay, N. R., P. J. Fox and K. C. MacDonald, Second-order axis discontinuities in the South Atlantic: Morphology, structure, and evolution, *Mar. Geophys. Res.*, 13, 21-50, 1991.

Hey, R., F. K. Duennebier and W. Jason Morgan, Propagating rifts on Midoecan ridges, *J. Geophys. Res.*, 85, 3647-3658, 1980.

Hey, R. N., H. W. Menard, T. M. Atwater and D. W. Caress, Changes in direction of seafloor spreading revisited, *J. Geophys. Res.*, 93, 2803-2811, 1988.

Ito, G. and J. Lin, Oceanic spreading center - hot spot interactions: constraints from along-isochron bathymetry and gravity anomalies, *Geology*, 23, 657-660, 1995a.

Ito, G. and J. Lin, Mantle temperature anomalies along the present and paleo-axes of the Galápagos spreading center as inferred from gravity analyses, *J. Geophys. Res.*, 100, 3733-3745, 1995b.

Jha, K., E. M. Parmentier and J. Phipps Morgan, The role of mantle-depletion buoyancy in spreading-center segmentation, *Earth Planet. Sci. Lett.*, 125, 221-234, 1994.

Keen, C. and C. Tramontini, A seismic refraction survey of the Mid-Atlantic Ridge, *Geophys. J. astron. Soc.*, 20, 473-491, 1970.

Kuo, B. Y. and D. W. Forysth, Gravity anomalies of the ridge-transform system in the South Atlantic between 30° and 31°S: Upwelling centers and variations in crustal thickness, *Mar. Geophys. Res.*, 10, 205-232, 1988.

Le Pichon, X., R. E. Houtz, C. L. Drake and J. E. Nafe, Crustal structure of the mid-ocean ridges. 1. Seismic refraction measurements, *J. Geophys. Res.*, 70, 319-339, 1965.

Lin, J. and E. A. Bergman, Rift grabens, seismicity and volcanic segmentation of the Mid-Atlantic Ridge: Kane to Atlantis Fracture Zones (abstract), *EOS Trans. AGU*, 71, 1572, 1990.

Lin, J., G. M. Purdy, H. Schouten, J. C. Sempere and C. Zervas, Evidence from gravity data for focused magmatic accretion along the Mid-Atlantic Ridge, *Nature*, 344, 627-632, 1990.

Lin, J. and J. Phipps Morgan, The spreading rate dependence of three-dimensional mid-ocean ridge gravity structure, *Geophys. Res. Lett.*, 19, 13-15, 1992.

Lin, J., On the causes of stable transform and migrating non-transform offsets in slow-spreading oceanic crust (abstract), *EOS Trans. AGU*, 77, 276, 1996.

Louden, K. E., R. S. White, C. G. Potts and D. W. Forsyth, Strucure and seismotectonics of the Vema Fracture Zone, Atlantic Ocean, *J. Geol. Soc. London*, 143, 795-805, 1986.

Macdonald, K. C., P. J. Fox, L. J. Perram, M. F. Eisen, R. M. Haymon, S.P. Miller, S.M. Carbotte, M.-H. Cormier, and A.N. Shor, A new view of the mid-ocean ridge from the behavior of ridge-axis discontinuities, *Nature*, 335, p. 217-225, 1988.

Macdonald, K. C., D. S. Scheirer and S. M. Carbotte, Mid-ocean ridges: Discontinuities, segments and giant cracks, *Science*, 253, 986-994, 1991.

Magde, L. S., D. W. Sparks and R. S. Detrick, The relationship between bouyant mantle flow and the mantle Bouguer anomaly patterns observed along the MAR from 33¡N to 35°N, *Geophys. Res. Lett.*, submitted, 1996.

McKenzie, D. and R. L. Parker, The North Pacific: an example of tectonics on a sphere, *Nature*, 216, 1276-1280, 1967.

McKenzie, D. and W. J. Morgan, Evolution of triple junctions, *Nature*, 125-133, 1969.

Menard, H. W. and T. M. Atwater, Changes in direction of seafloor spreading, *Nature*, 219, 463-467, 1968.

Müller, R. D., D. T. Sandwell, B. E. Tucholke, J. G. Slater and P. R. Shaw, Depth to basement and geoid expression of the Kane Fracture Zone: a comparison, *Mar. Geophys. Res.*, 13, 105-129, 1991.

Müller, R. D. and W. R. Roest, Fracture zones in the north Atlantic from combined Geosat and Seasat data, *J. Geophys. Res.*, 97, 3337-3350, 1992.

Müller, R. D., W. R. Roest, J.-Y. Royer, L. M. Gahagan, and J. G. Sclater, A digital age map in of the ocean floor, *SIO Reference Series*, 93-30, 1993.

National Geophysical Data Center, ETOPO-5 bathymetry/topography data, *Data Announc. 88-MGG-02*, National Oceanic and Atmos. Admin., U.S. Dept. Commer., Boulder, Colo., 1988.

Pariso, J. E., J.-C. Sempéré and C. Rommeveaux, Temporal and spatial variations in crustal accretion along the Mid-Atlantic Ridge (29° - 31°31' N) over the last 10 Ma: Implications from a three-dimensional gravity study, *J. Geophys. Res.*, 100, 17781-17794, 1995.

Parsons, B. and J. G. Sclater, An analysis of the variation of ocean floor bathymetry and heat flow with age, *J. Geophys. Res.*, 82, 803-827, 1977.

Phipps Morgan, J. and E. M. Parmentier, Causes of rate-limiting mechanisms of ridge propagation: A fracture mechanics model, *J. Geophys. Res.*, 90, 8603-8612, 1985.

Phipps Morgan, J. P. and E. M. Parmentier, Crenulated seafloor: Evidence for spreading-rate dependent structure of mantle upwelling, *Earth Planet. Sci. Lett.*, 129, 73-84, 1995.

Phipps Morgan, J. and D. T. Sandwell, Systematics of ridge propagation south of 30°S, *Earth Planet. Sci. Lett.*, 121, 245-258, 1994.

Poehls, K. A., Seismic refraction on the Mid-Atlantic ridge at 37°N, *J. Geophys. Res.*, 79, 3370-3373, 1974.

Purdy, G. M. and R. S. Detrick, Crustal structure of the Mid-Atlantic Ridge at 23°N from seismic refraction studies, *J. Geophys. Res.*, 91, 3739-3762, 1986.

Purdy, G. M., J. C. Sempéré, H. Schouten, D. L. Dubois and R. Goldsmith, Bathymetry of the Mid-Atlantic Ridge, 24°-31°N: A map series, *Mar. Geophys. Res.*, 12, 247-252, 1990.

Ritzert, M. and W. R. Jacoby, On the lithospheric structure of Reykjanes ridge at 62.5°N, *J. Geophys. Res.*, 90, 10117-10128, 1985.

Roest, W. R. and B. J. Collette, The Fifteen Twenty Fracture Zone and the North American-South American plate boundary, *J. Geol. Soc. London*, 143, 833-843, 1986.

Rommeveaux, C., C. Deplus, P. Patriat and J.-C. Sempéré, Three-dimensional gravity study of the Mid-Atlantic Ridge: Evolution of the segmentation between 28° and 29°N during the last 10 m.y., *J. Geophys. Res.*, 99, 3015-3029, 1994.

Rowlett, H., Seismicity at intersections of spreading centers and transform faults, *J. Geophys. Res.*, 86, 3815-3820, 1981.

Sandwell, D. T. and W. H. F. Smith, Marine gravity anomaly from Geosat and ERS-1 satellite altimetry, *J. Geophys. Res.*, submitted, 1996.

Schouten, H., K. D. Klitgord and J. A. Whitehead, Segmentation of mid-ocean ridges, *Nature*, 317, 225-229, 1985.

Schouten, H., H. J. B. Dick and K. D. Klitgord, Migration of mid-ocean ridge volcanic segments, *Nature*, 326, 835-839, 1987.

Searle, R. C., Lithospheric structure of the Azores plateau from Rayleigh-wave dispersion, *Geophys. J. Int.*, 44, 537-546, 1976.

Searle, R., Tectonic pattern of the Azores spreading centre and triple junction, *Earth Planet. Sci. Lett.*, 51, 415-434, 1980.

Searle, R. C. and A. S. Laughton, Sonar studies of the Mid-Atlantic Ridge and Kurchatov Fracture Zone, *J. Geophys. Res.*, 82, 5313-5328, 1977.

Sempéré, J.-C., J. Lin, H. S. Brown, H. Schouten et al., Segmentation and morphotectonic variations along a slow-spreading center: the Mid-Atlantic Ridge (24°N - 30°40'N), *Mar. Geophys. Res.*, 15, 153-200, 1993.

Sempéré, J.-C., P. Blondel, P. Briais, T. Fujiwara, L. Géli, N. Isezaki, J. E. Pariso, P. Parson, P. Patriat and C. Rommevaux, The Mid-Atlantic Ridge between 29°N and 31°30'N in the last 10 Ma, *Earth Planet. Sci. Lett.*, 130, 45-55, 1995.

Severinghaus, J. P. and K. C. MacDonald, High inside corners at ridge-transform intersections, *Mar. Geophys. Res.*, 9, 353-367, 1988.

Shaw, P. R., Investigations of relative plate motions in the South Atlantic using Seasat altimeter data, *J. Geophys. Res.*, 92, 9363-9375, 1987.

Shaw, P. R. and S. C. Cande, High-resolution inversion for South-Atlantic plate kinematics using joint altimeter and magnetic data, *J. Geophys. Res.*, 95, 2625-2644, 1990.

Shaw, P. R., Ridge segmentation, faulting and crustal thickness in the Atlantic Ocean, *Nature*, 358, 490-493, 1992.

Shaw, P. R. and J. Lin, Causes and consequences of variations in faulting style at the Mid-Atlantic Ridge, *J. Geophys. Res.*, 98, 1839-21851, 1993.

Sinha, M. C. and K. E. Louden, The Oceanographer fracture zone. I Crustal structure from seismic refraction studies, *Geophys. J. Int.*, 75, 713-736, 1983.

Sloan, H. and P. Patriat, Kinematics of the North American-African plate boundary between 28° and 29°N during the last 10 Ma: evolution of the axial geometry and spreading rate and direction, *Earth Planet. Sci. Lett.*, 113, 323-341, 1992.

Small, C. and D. T. Sandwell, An abrupt change in ridge axis gravity with spreading rate, *J. Geophys. Res.*, 94, 17383-17392, 1989.

Small, C. and D. T. Sandwell, An analysis of ridge axis gravity roughness and spreading rate, *J. Geophys. Res.*, 97, 3235-3245, 1992.

Smallwood, J. R., R. S. White and T. A. Minshull, Seafloor spreading in the presence of the Iceland plume: the structure of the Reykjanes Ridge at 61°40'N, *J. Geol. Soc. London*, 152, 1023-1029, 1995.

Smith, W. H. F., On the accuracy of digital bathymetric data, *J. Geophys. Res.*, 98, 9591-9603, 1993.

Smith, W. H. F. and D. T. Sandwell, Marine gravity field from declassified Geosat and ERS-1 altimetry (abstract), *EOS Trans. AGU*, 76, 156, 1995.

Sparks, D. W. and E. M. Parmentier, The structure of three-dimensional convection beneath oceanic spreading centres, *Geophys. J. Int.*, 112, 81-91, 1993.

Srivastava, S. P. and C. R. Tapscott, Plate kinematics of the North Atlantic, P. R. Vogt and B. E. Tucholke, *The Western North Atlantic Region*, 379-404, Geological Society of America, Boulder, Co., 1986.

Stein, C. A. and S. Stein, Comparison of plate and asthenospheric flow models for the thermal evolution of the oceanc lithosphere, *Geophysical Research Letters*, 21, 709-712, 1994.

Tolstoy, M., A. J. Harding and J. A. Orcutt, Crustal thickness on the Mid-Atlantic ridge: Bull's eye gravity anomalies and focused accretion, *Science*, 262, 726-729, 1993.

Tucholke, B. E. and H. Schouten, Kane Fracture Zone, *Mar. Geophys. Res.*, 10, 1-39, 1988.

Tucholke, B. E. and J. Lin, A geological model for the structure of ridge segments in slow-spreading ocean crust, *J. Geophys. Res.*, 99, 11937-11958, 1994.

Tucholke, B. T., J. Lin, M. C. Kleinrock, M. A. Tivey, T. Reed, J. Goff, and G. E. Jaroslow, Segmentation and crustal structure of the wetern mid-Atlantic ridge flank, 25°30'-27°10'N and 0-29 My, *J. Geophys. Res.*, submitted, 1996.

Vogt, P. R., O. E. Avery, E. D. Schneider, C. N. Anderson, and D. R. Bracey, Discontinuities in sea-floor spreading, *Tectonophys.*, 8, 285-317, 1969.

Vogt, P. R., Asthenosphere motion recorded by the ocean floor south of Iceland, *Earth Planet. Sci. Lett.*, 13, 153-160, 1971.

Vogt, P. R., Plumes, subaxial pipe flow, and topography along the mid-ocean ridge, *Earth Planet. Sci. Lett.*, 29, 309-325, 1976.

Wessel, P. and W. H. F. Smith, Free software helps map and display data (abstract), *EOS Trans. AGU*, 72, 441, 445-446, 1991.

Wilson, D. S., R. N. Hey and C. Nishimura, Propagation as a mechanism of reorientation of the Jua de Fuca Ridge, *J. Geophys. Res.*, 89, 9215-9225, 1984.

White, R. S., J. W. Bown and J. R. Smallwood, The temperature of the Iceland plume and origin of outward-propagating V-shaped ridges, *J. Geol. Soc. London*, 152, 1039-1045, 1995.

Whitehead, J. A., H. J. B. Dick and H. Schouten, A mechanism for magmatic accretion under spreading centres, *Nature*, 312, 146-148, 1984.

Whitmarsh, R. B., Median valley refraction line, Mid-Atlantic ridge at 37°N, *Nature*, 246, 297-299, 1973.

Whitmarsh, R. B. and A. J. Calvert, Crustal structure of Atlantic Fracture Zones - I. The Charlie-Gibbs Fracture Zone, *Geophys. J. Royal astron. Soc.*, 85, 107-138, 1986.

Wolfe, C., G. M. Purdy, D. R. Toomey and S. C. Solomon, Microearthquake characteristics and crustal velocity structure at 29°N of the Mid-Atlantic Ridge: The architecture of a slow-spreading serment, *J. Geophys. Res.*, 100, 24449-24472, 1995.

Figure 1. a) Satellite-derived free-air gravity anomaly (FAA) for the central and northern Atlantic basin from *Smith and Sandwell* [1995]. b) Short wavelength residual free-air gravity map. This map is obtained by filtering the FAA a high-pass cosine taper filter between 300 and 600 km. The residual anomaly reflects the basement and is dominated mainly by the rift valley and the off-axis traces of ridge segment offsets. c) Long-wavelength regional gravity anomaly of wavelengths >300-600 km. The regional anomaly is dominated the lithospheric cooling with age and the effects hot spots swells, specially of the Azores and Iceland. The double black lines mark the location of individual ridge segments.

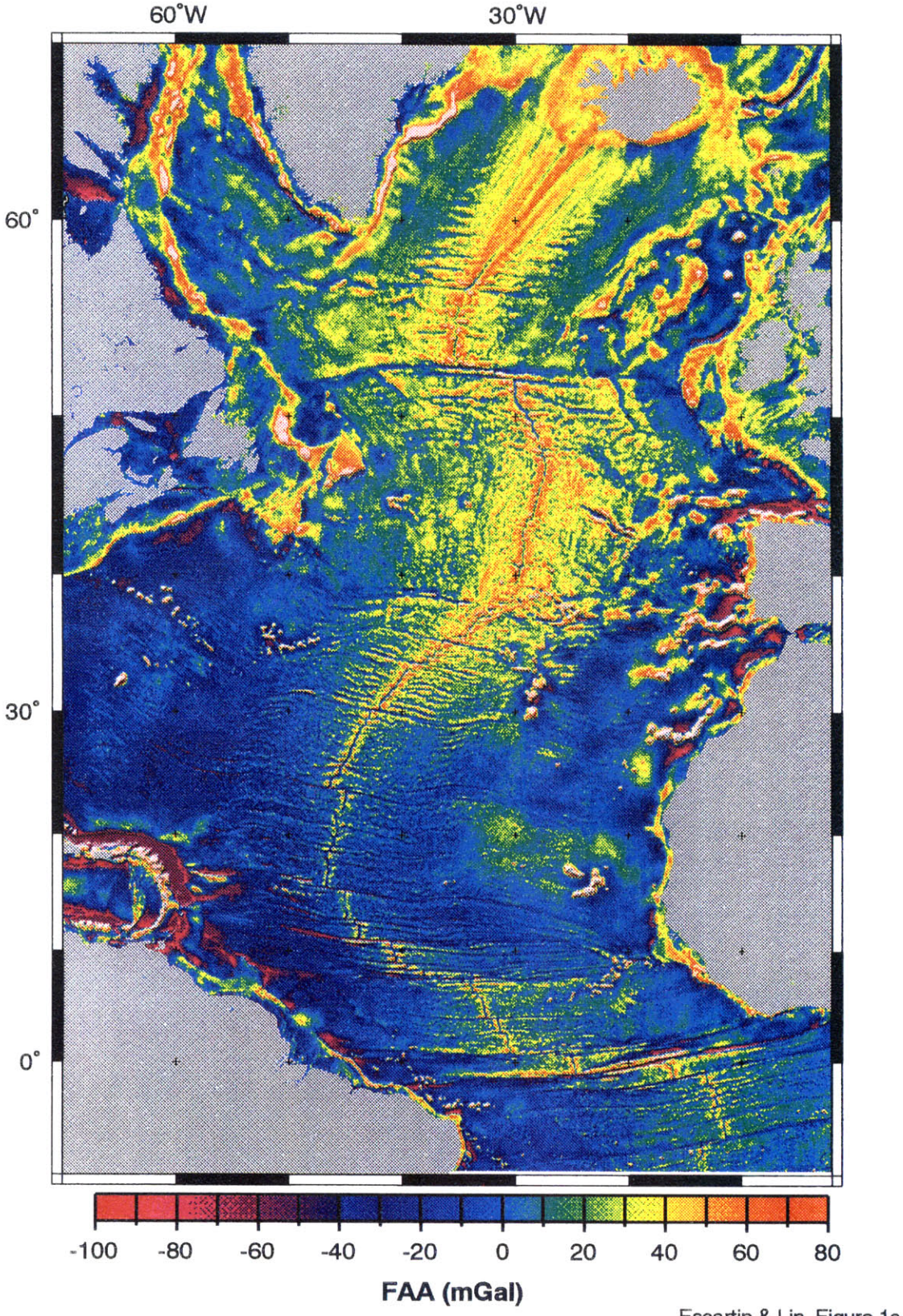

Escartin & Lin, Figure 1a

Figure 1 (cont.)

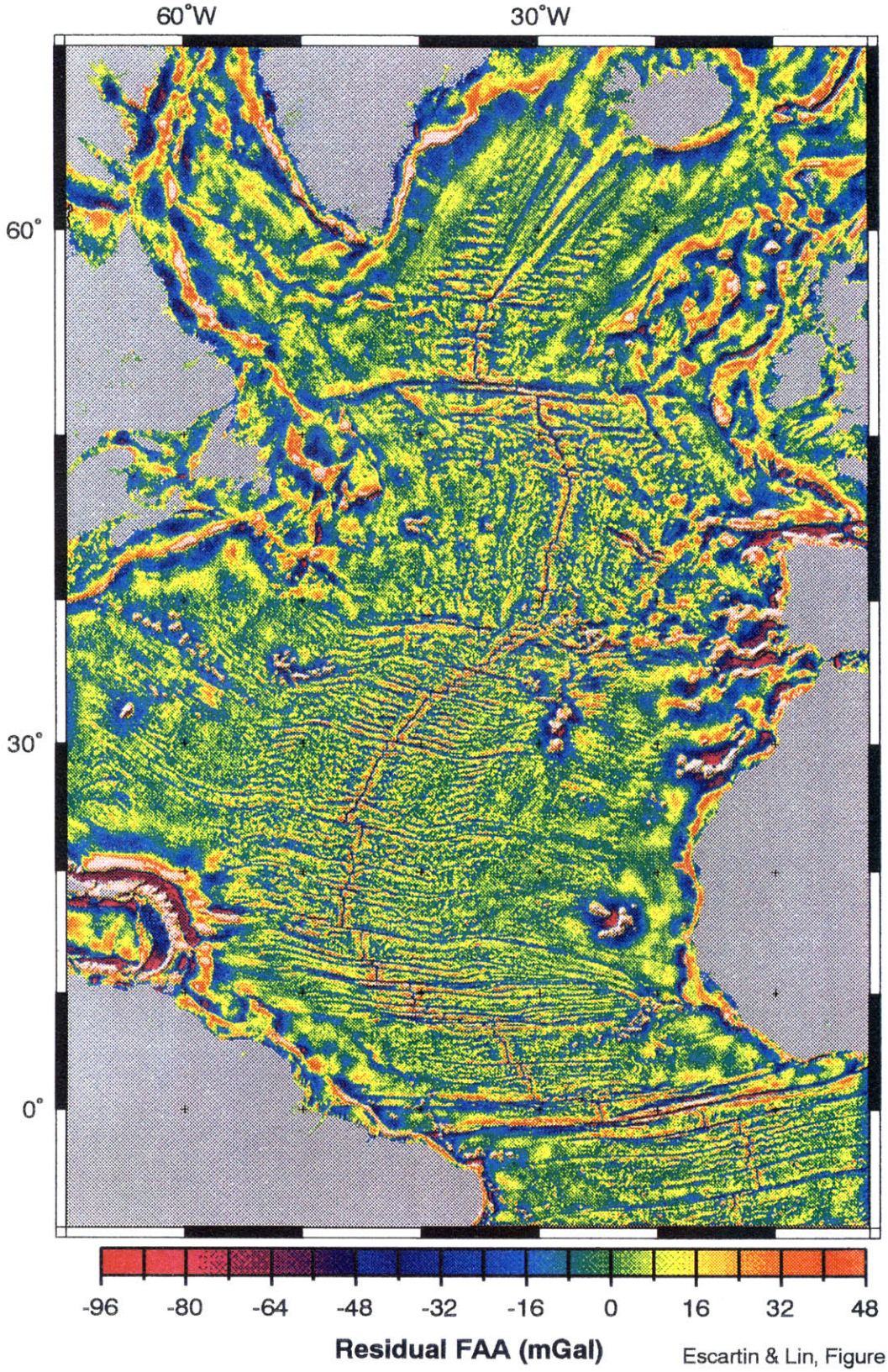

Escartin & Lin, Figure 1b

Figure 1 (cont.)

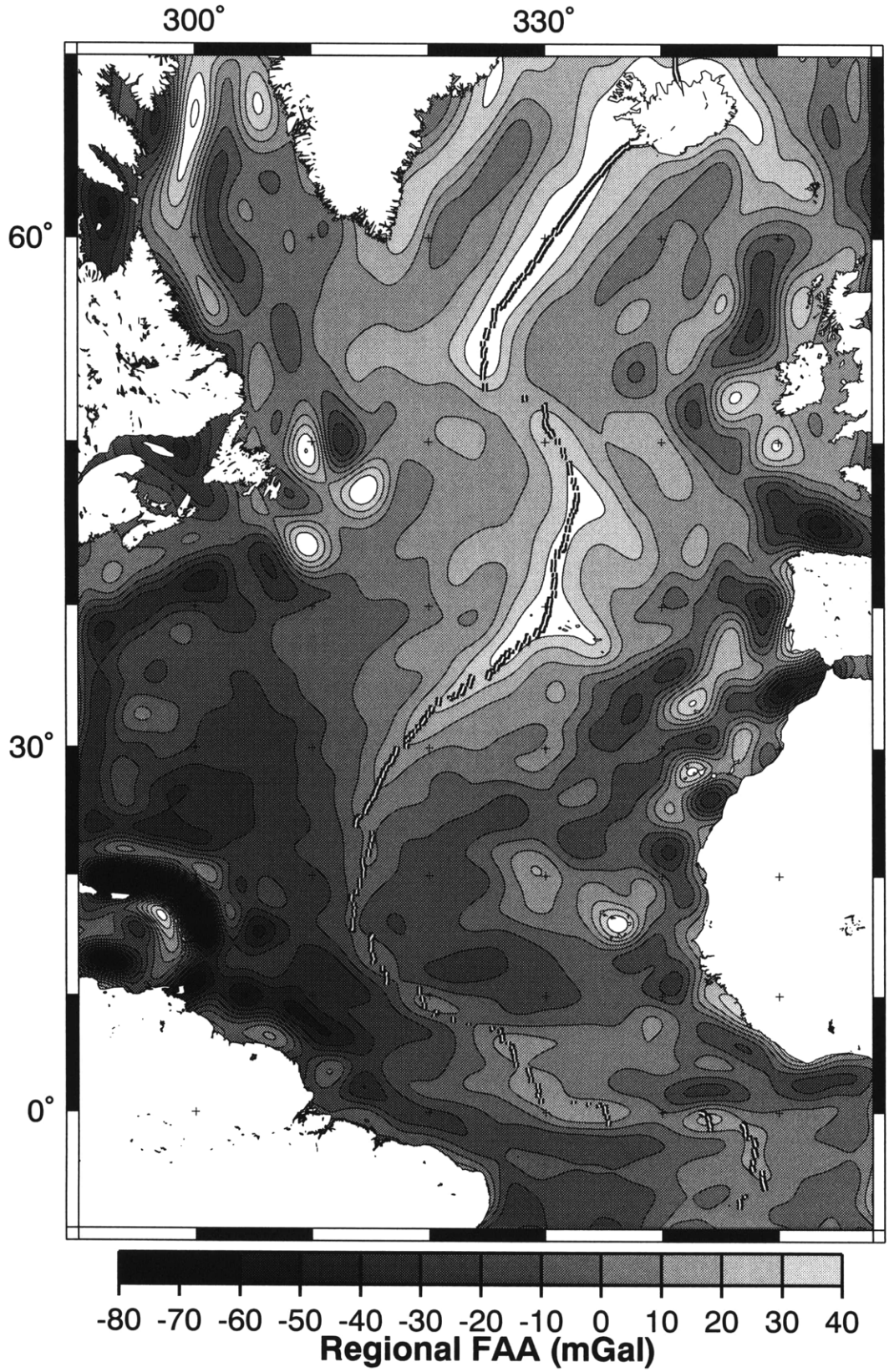

Escartin & Lin, Figure 1c

Figure 2. Map of identified off axis traces of transform offsets (bold lines), non-transform offsets (thin lines), and flow lines (gray lines) calculated from the poles of plate rotation in Table 1. The ridge axis is indicated by double black lines.

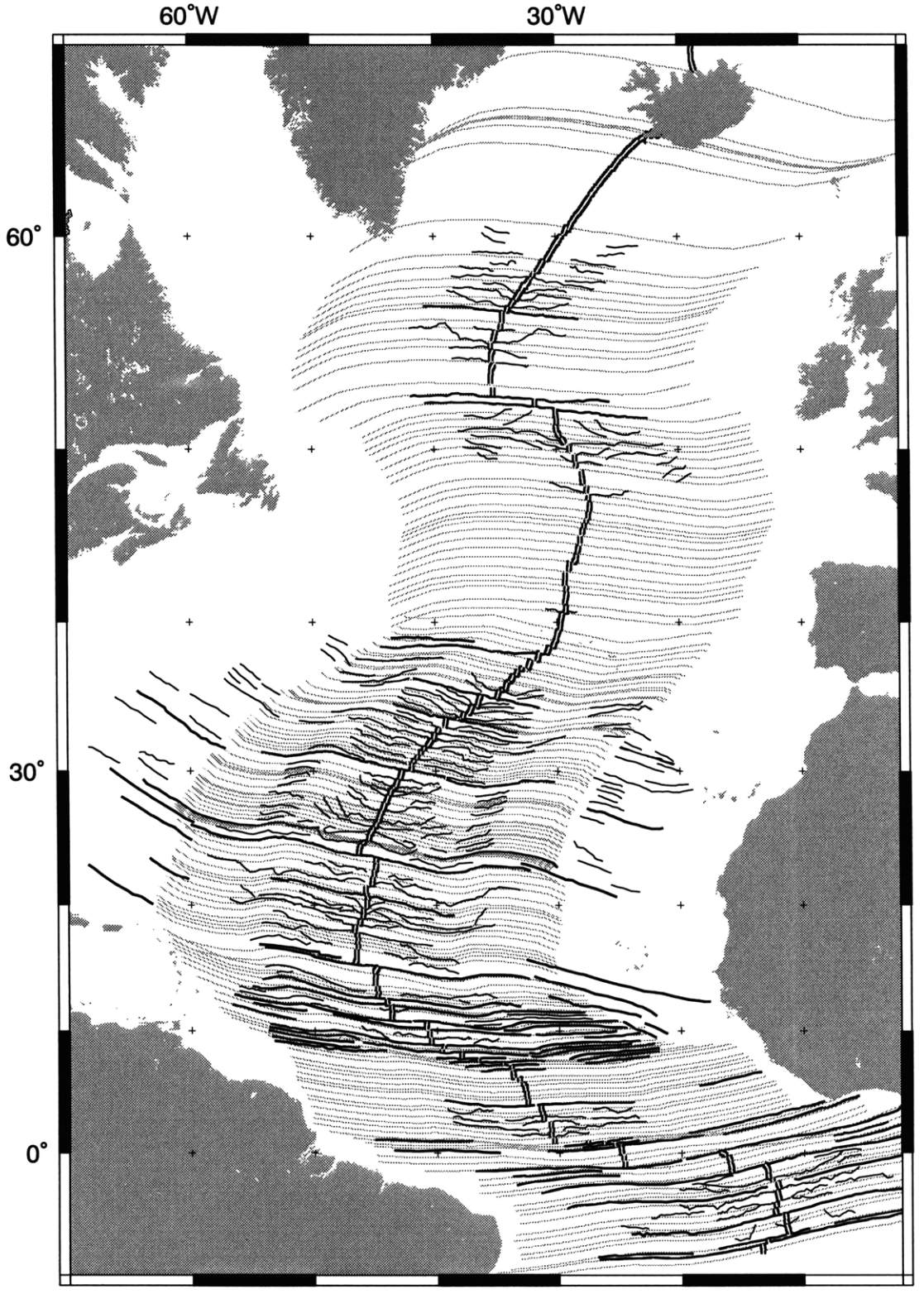

Escartin & Lin, Figure 2

Figure 3. Comparison of satellite FAA data (a) and bathymetry (b) for a section of the MAR around the Atlantis FZ. The digitized traces of offsets are marked in (a) by the black lines, and the ridge axis by the double lines. The Atlantis transform zone (bold line in a) is a transform offset (TO) characterized by a well-defined, linear transform valley. Non-transform offsets (NTO) are characterized by less well defined, wavy valleys.

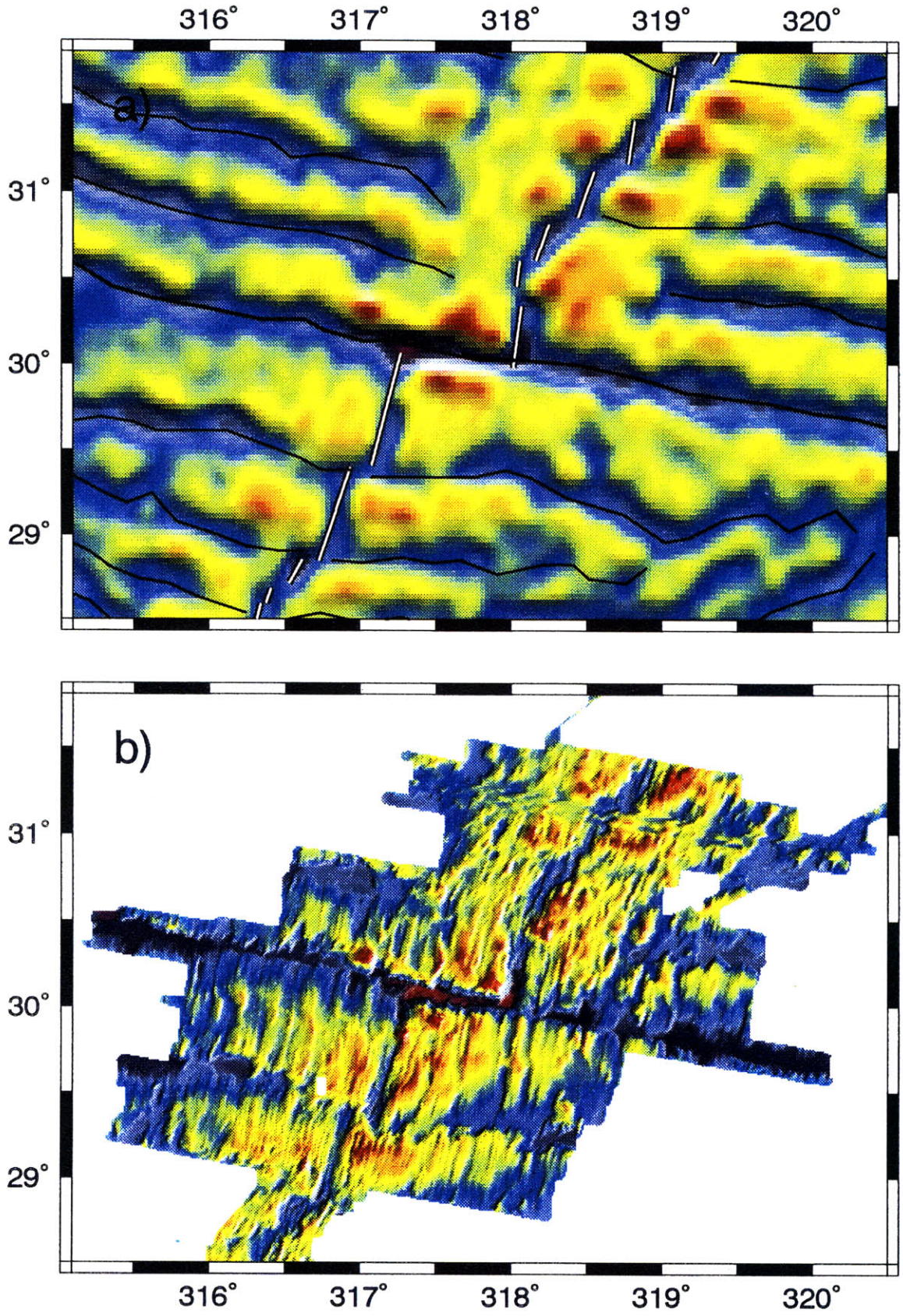

Escartin & Lin, Fig. 3

Figure 4. Variations of RMS along the axial FAA profile. RMS values were calculated using a 500 km running window applied to the axial FAA profile. Note that the RMS values are lowest near Azores platform (40°-50°N) and the Reykjanes Ridge (55-59°N) south of Iceland.

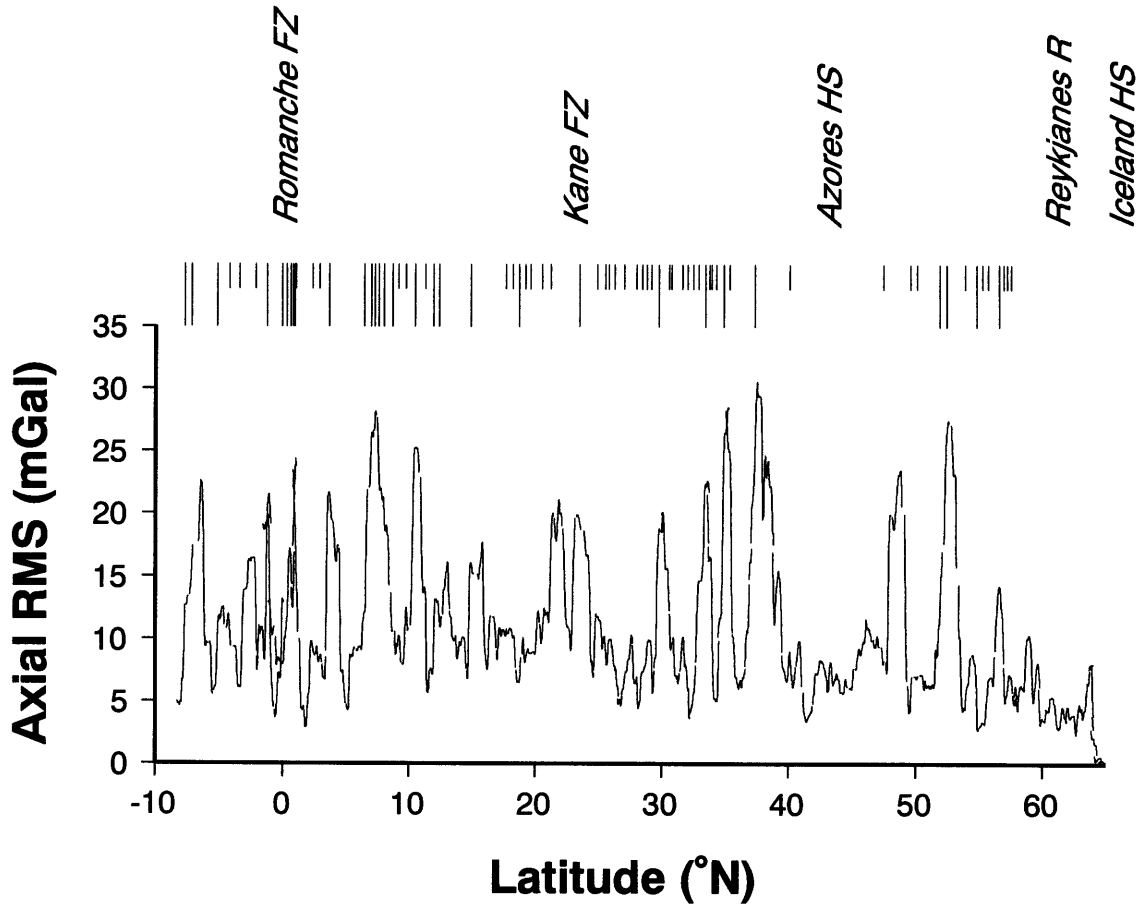

Escartin & Lin, Figure 4

Figure 5. (top) RMS values of local FAA as a function of ridge obliquity. The RMS was calculated within small boxes located at each flank of the rift valley in crust <10 Ma, prior to any major plate motion change. The bounds, RMS and ridge obliquity for each box are given in Table 3. Open circles correspond to those boxes where the ridge obliquity can be measured. Gray diamonds correspond to ~60 Ma crust between Kane and Atlantis FZs (Table 3). Solid circles correspond to data from the Reykjanes Ridge. Error bars mark the standard deviation of the RMS values, and the error in the estimation of the ridge obliquity (5°). The RMS of the FAA tends to increase with increasing obliquity, as indicated by the best-fitting line to the open circles. The RMS values of the Reykjanes Ridge are anomalously low. (bottom) Obliquity is defined as the angle between the ridge trend (discontinuous line) and the direction perpendicular to spreading (thin line). Double bold lines indicate individual ridge segments.

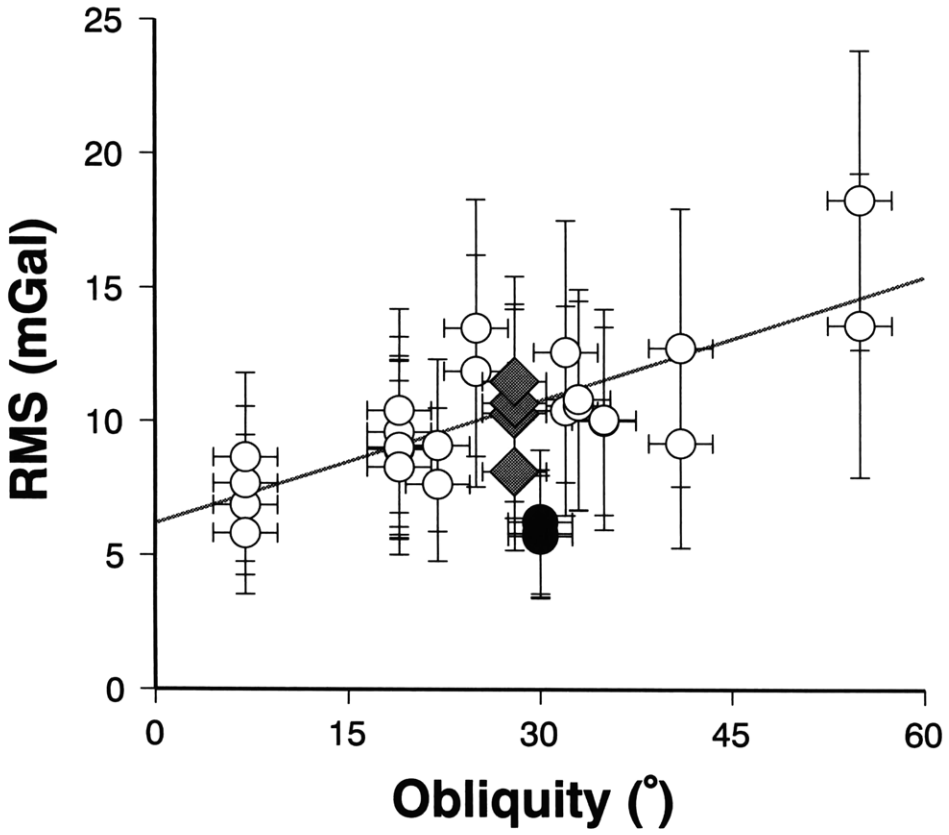

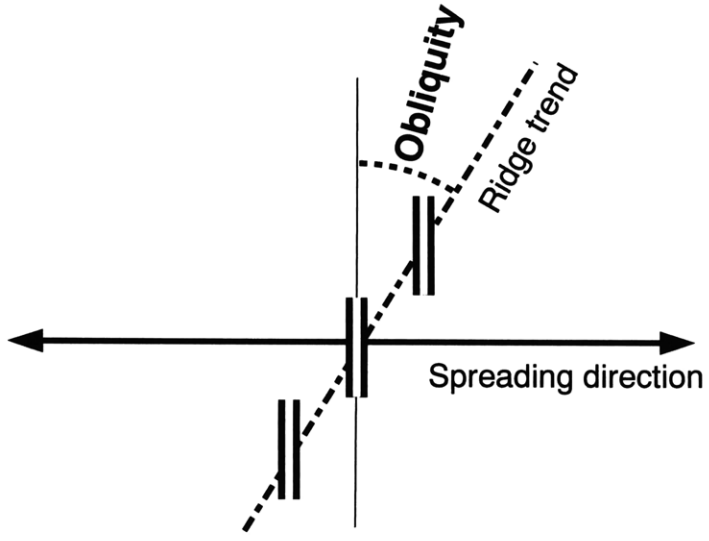

Escartin & Lin, Figure 5

Figure 6. Histograms of offset length showing distinct populations of TOs (black bars) and NTOs (open bars). Offset lengths have a gamma distribution, with mean offset lengths $\overline{L_{TO}}$=110 km for TOs and $\overline{L_{NTO}}$=17 km for NTOs. The transition from TO to NTO occurs at 20-40 km.

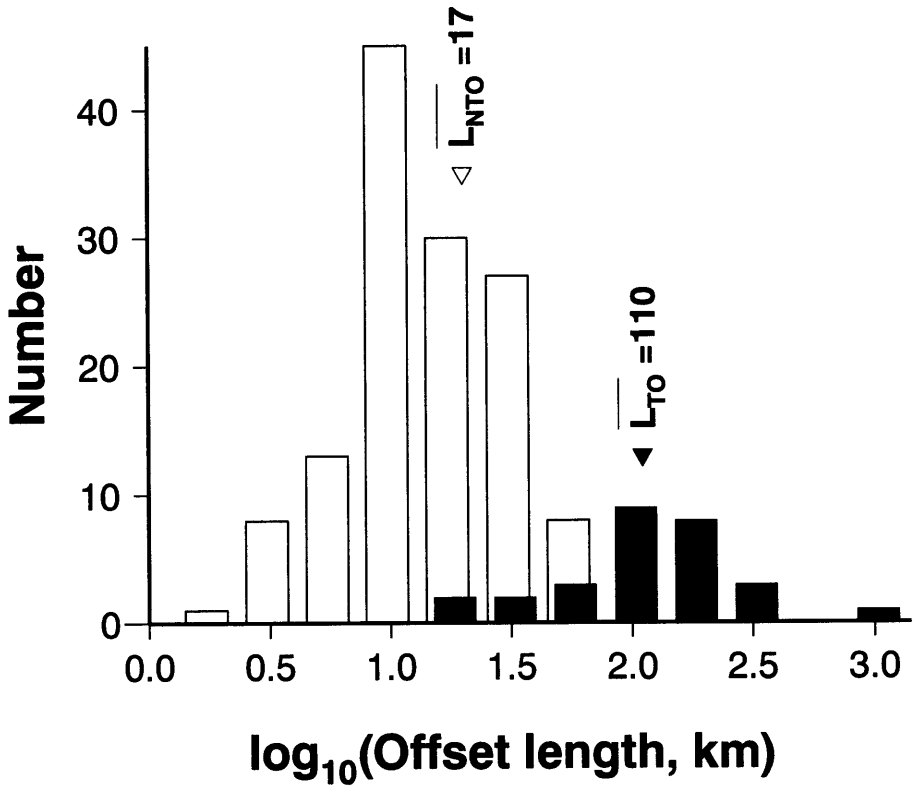

Escartin & Lin, Figure 6

Figure 7. The plot of offset length versus life span. Black and gray circles correspond to TOs, and open circle and circle with a cross to NTOs. Note that long TOs tend to have a longer life span than shorter NTOs. TOs identified along the Equatorial Atlantic were created during the last 30 Ma as a consequence of a plate motion change, and therefore show short life-spans; these offsets are indicated by the gray circles. The NTO marked by a circle with a cross corresponds to a 65 km long offset. It does not have the characteristics of an offset, and may correspond to an incipient TO formed recently and not fully developed (see text for discussion).

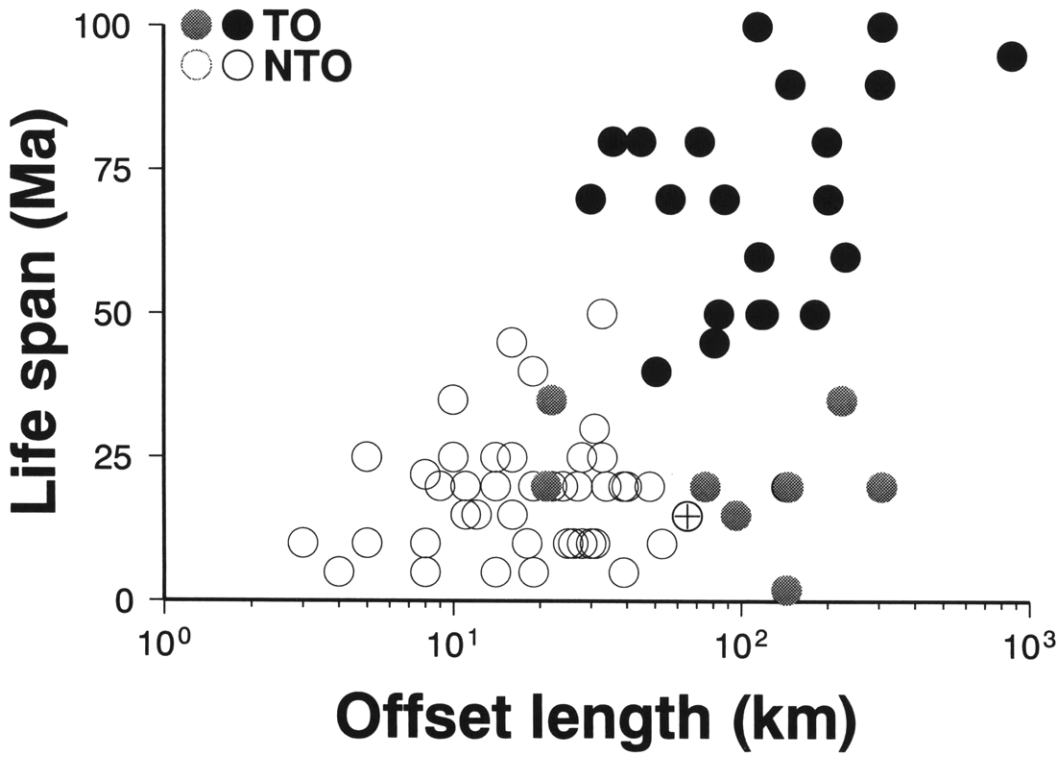

Escartin & Lin, Figure 7

Figure 8. (Top to bottom) Along-axis profiles of seafloor depth, seismic and gravity derived crustal thickness, free-air gravity anomaly, mantle Bouguer anomaly, and residual gravity anomalies. On the top the locations of stable offsets are marked by vertical lines, while the migrating offsets are marked by arrows pointing in the direction of offset propagation. The length of the arrow is proportional to the propagation rate (PR) normalized by the half-spreading rate (HSR). Offsets that migrate north, south or that are stable are separated for clarity. Seafloor depth is from ETOPO-5 combined with shipboard bathymetry data. Crustal thickness was calculated assuming local Airy compensation (solid line) or 75% Airy compensation (gray line). Solid dots are crustal thickness measurements from seismic data (Table 4). See text for details on the gravity calculations for the mantle Bouguer anomaly (MBA) and the residual Airy anomalies (RAA and 75% RAA).

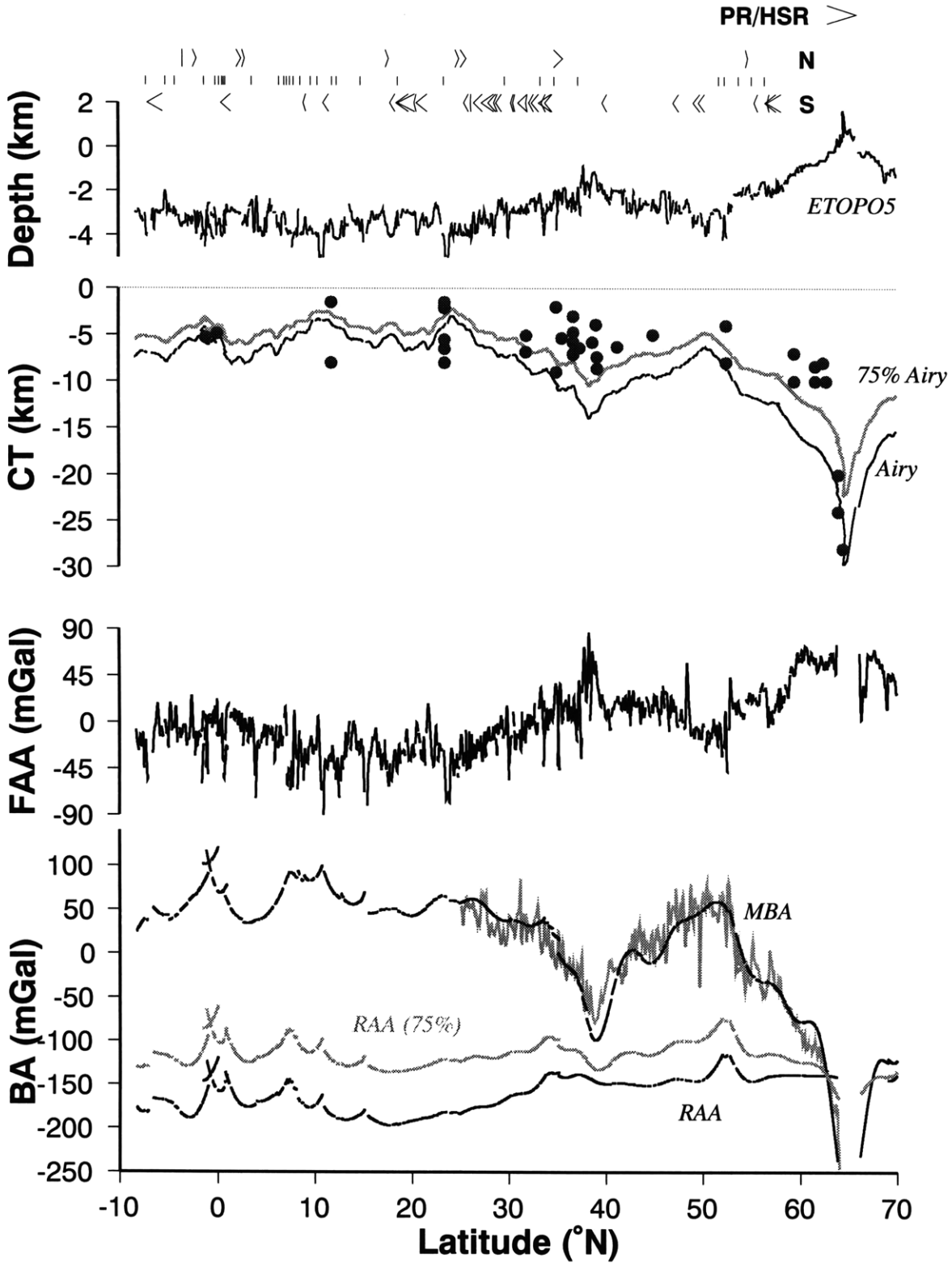

Escartin & Lin, Figure 8

Figure 9. Histogram of the number of transform (TO, solid bar) and non-transform offsets (NTOs, open bar). We differentiate those NTOs that have no off-axis trace, those that are stable, and those that migrate up or down the regional FAA gradients. Approximately 72 % of the migrating NTOs propagate down regional FAA gradients associated primarily with the Azores, Iceland and other smaller hot spots. Regional gradients were calculated from along-axis seafloor and depth and FAA profiles filtered with a low-pass filter at 500 km to remove local variations at the scale of individual segments. A large number of NTOs do not have off-axis traces.

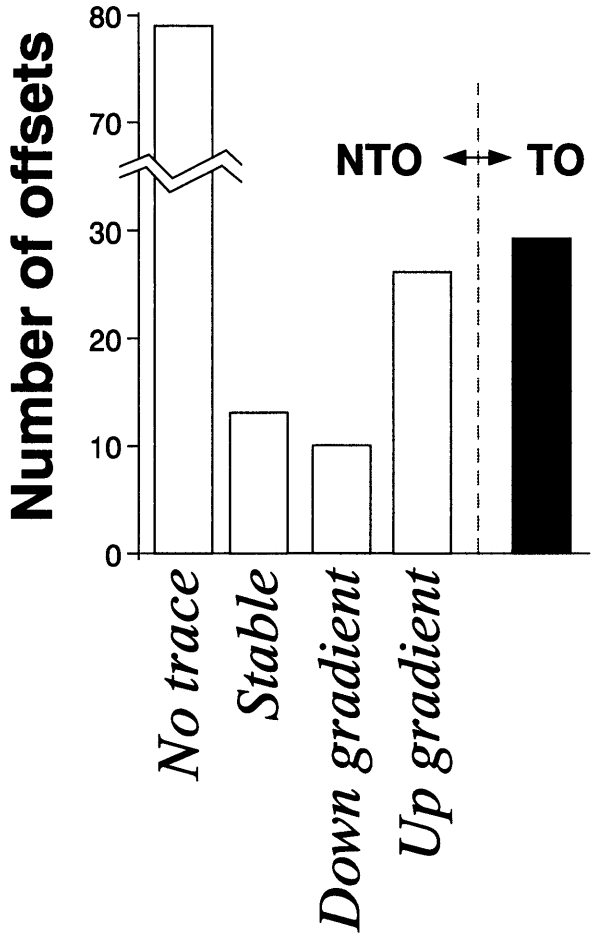

Escartin & Lin, Figure 9

Figure 10. Plots of offset propagation rate (PR) normalized by half-spreading rate (HSR) against a) regional gravity gradient, b) difference in segment length between segments abutting an offset, and c) offset length. Northward offset propagation and gravity gradients are positive. Note that offset propagation rates do not correlate with magnitude of the regional gradients or differences in segment length. Longer offsets tend to be more stable than shorter ones.

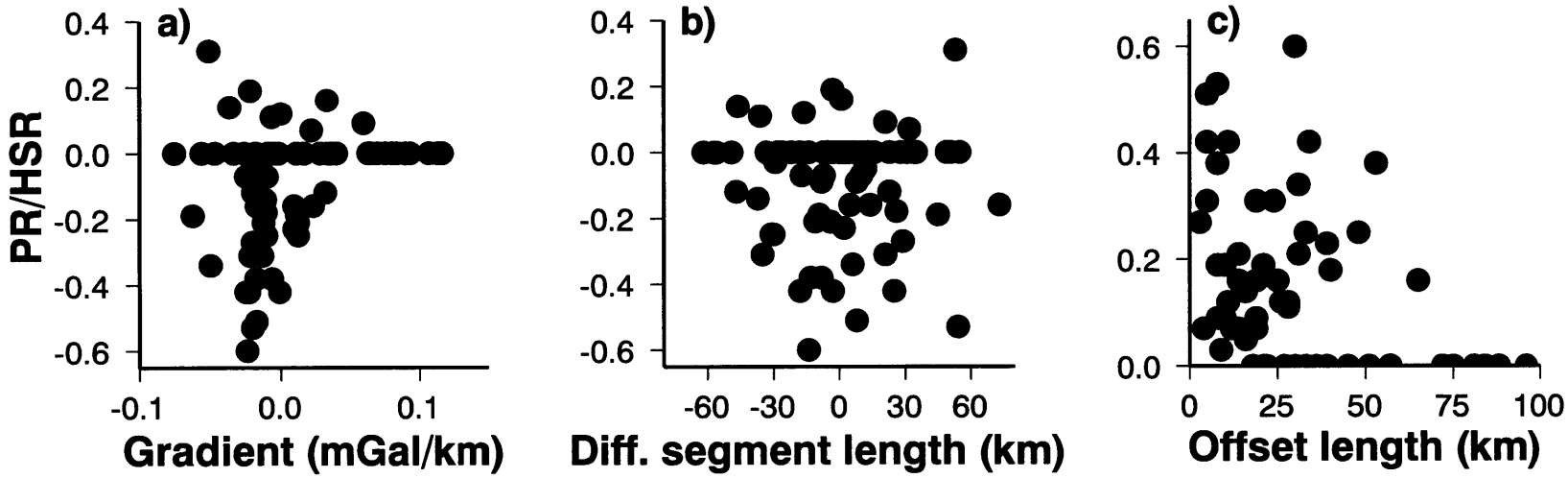

Escartin & Lin, Figure 10

Table 1. Finite difference stage poles of rotation

Stage (Ma)		Lat (°)	Lon (°)	Rot (°)	Lat (°)	Lon (°)	Rot (°)	Reference
		South American Plate				African Plate		Shaw and Cande [1990]
0.0	8.9	59.99	-38.89	1.57	-59.99	141.11	1.57	
8.9	19.4	56.56	-36.18	1.96	-56.49	143.47	1.96	
19.4	26.9	55.08	-30.43	1.47	-54.65	148.85	1.47	
26.9	35.3	55.25	-29.63	1.70	-54.75	149.68	1.70	
35.3	44.7	61.06	-26.49	2.11	-59.99	155.23	2.11	
44.7	51.9	70.99	-32.42	1.28	-70.05	159.42	1.28	
51.9	58.6	76.12	-42.07	1.16	-75.78	162.44	1.16	
58.6	66.7	74.76	-84.30	1.33	-82.49	116.43	1.33	
66.7	74.3	61.36	-35.61	1.58	-61.94	142.83	1.58	
74.3	80.2	60.72	-36.27	1.52	-61.51	141.63	1.52	
80.2	84.0	46.56	-27.41	1.32	-46.47	139.72	1.32	
84.0	100.0	46.55	-27.42	5.53	-46.47	139.71	5.53	
		North American Plate				African Plate		Srivastava and Tappscot [1986]
0.0	10.0	79.00	78.00	0.80	79.00	78.00	-0.80	Müller and Roest [1992]
10.0	12.5	79.00	78.00	0.40	79.00	78.00	-0.40	
12.5	20.0	78.00	5.00	1.22	78.44	3.25	-1.22	
20.0	35.5	67.50	-10.00	0.30	68.09	-13.57	-0.30	
35.5	45.6	67.50	-10.00	3.08	68.09	-13.57	-3.08	
45.6	49.5	75.50	-5.00	1.20	75.70	-3.97	-1.20	
49.5	53.5	72.00	-29.00	0.70	73.80	-31.86	-0.70	
53.5	59.0	72.00	-41.50	0.95	74.58	-45.75	-0.95	
59.0	63.6	55.00	166.00	0.92	53.72	143.52	-0.92	
63.6	67.5	55.00	166.00	0.78	53.72	143.52	-0.78	
67.5	74.3	69.00	-34.00	0.90	70.86	-48.13	-0.90	
74.3	78.8	69.00	-34.00	1.44	70.86	-48.13	-1.44	
78.8	80.2	61.00	-32.00	0.40	62.83	-49.11	-0.40	
80.2	84.0	60.00	-23.00	1.30	61.20	-40.07	-1.30	
84.0	87.2	60.00	-23.00	1.25	61.20	-40.07	-1.25	
87.2	92.1	55.00	-21.50	1.92	56.14	-40.65	-1.92	
92.1	104.3	44.00	-16.20	4.80	44.65	-39.56	-4.80	
104.3	109.7	70.30	5.00	2.15	62.74	-1.16	-2.15	
109.7	118.0	58.00	-5.00	3.25	55.13	-21.84	-3.25	
118.0	120.9	65.80	-0.30	1.12	59.63	-9.30	-1.12	
120.9	126.0	65.64	-0.50	1.10	-59.63	170.34	1.10	
126.0	133.0	75.63		8.39	-63.35	-169.21	0.72	
133.0	141.5	71.46	-9.26	0.84	-65.75	176.77	0.84	
141.5	149.5	66.24	-18.33	1.22	-66.24	161.67	1.22	
149.5	156.5	77.07	53.58	1.49	-55.92	-154.17	1.49	
		North American Plate				European Plate		Srivastava and Tappscot [1986]
0.0	10.0	65.38	133.58	1.22	-65.38	-46.42	1.22	Müller and Roest [1992]
10.0	20.0	72.31	140.42	1.27	-72.18	-38.65	1.27	
20.0	36.0	59.29	138.05	1.28	-59.28	-43.58	1.28	
36.0	56.0	57.41	146.01	2.64	-56.98	-36.07	2.64	
56.0	59.0	71.40	149.11	0.74	-70.24	-25.35	0.74	
59.0	69.0	73.68	158.26	1.39	-71.47	-15.12	1.39	
69.0	84.0	74.25	-168.43	1.44	-68.93	10.91	1.44	
84.0	92.0	67.85	-168.44	0.35	-62.78	6.50	0.35	
92.0	105.0	80.58	-130.37	1.44	-72.82	39.97	1.44	

Table 2. Transform and non-transform offset parameters

Num.	Offset (Name) [Type] *	Off. Len (km)	Lon. (°E)	Lat. (°N)	Dist (km)	SL (km)	DL (km)	FAA reg. (mGal)	FAA grad. (mGal/km)	sr (km/Ma)	sdir (°)	Start (Ma)	End (Ma)	Total (Ma)	PR/SR (East)	PR/SR (West)	PD (N/S)
		1	2	3	4	5	6	7	8	9	10	11	12	13	14	15	16
1	SoAs-00b [NTO]	4	346.61	-8.14	30.0	30	-31	7.38	-0.0371	34.01	77.73	0	-		-	-	-
2	SoAs-00a [TO]	57	346.60	-7.73	91.1	61	35	5.71	-0.0360	33.93	77.61	0	70	70	0	0	-
3	ASCENSION [TO]	203	347.02	-7.19	117.1	26	-62	4.93	-0.0165	33.84	77.12	0	70	70	0	0	-
4	AsCh-00a [NTO]	8	348.65	-6.24	205.2	88	54	8.86	0.0203	33.73	76.74	0	5	5	0.53	0.45	S
5	AsCh-00b [NTO]	13	348.53	-5.65	239.3	34	-16	10.46	0.0122	33.62	76.73	-	-		-	-	-
	AsCh-10b [NTO]									38	78	15	20	10	1.43	1.33	N
										40	78	20	25		0.11	0.07	S
6	AsCh-00c [TO]	81	348.50	-5.18	289.3	50	-4	11.03	0.0027	33.52	76.89	0	45	65	0	0	-
										33	90	45	65		0.05	0.09	N
	AsCh-60c [NTO]											50	60	10	0.12	0.19	S
7	AsCh-00d [NTO]	26	347.67	-4.82	343.4	54	12	10.92	0.0095	33.41	77.01	-	-		-	-	-
8	AsCh-00e [NTO]	39	347.72	-4.24	385.4	42	-49	11.65	0.0038	33.27	76.91	0	5	5	0	0	-
	AsCh-10ea [NTO]									39	78	5	15	20	0.21	0.29	N
										40	78	15	25		0	0	-
	AsCh-10eb [NTO]									38	78	5	15	20	0.11	0.21	S
										40	78	15	25		0.18	0.06	N
	AsCh-30e [NTO]									44	85	30	50	25	0.03	0.05	N
										38	85	50	55		0.36	0.38	N
9	AsCh-00f [NTO]	27	347.87	-3.46	476.5	91	23	11.85	0.0018	33.1	76.81	0	20	45	0	0.05	N
												20	25		0.27	0.11	N
												25	30		0.36	0.27	S
												35	40		0.19	0.19	N
												45	50		0.45	0.4	S
	AsCh-10f (Charcot FZ) [TO]											10	90	80	0	0	-
10	AsCh-00g [NTO]	44	347.90	-2.64	544.6	68	42	12.11	0.0014	32.95	76.85	-	-		-	-	-
	AsCh-20g [NTO]									38	81	20	30	20	0.29	-	S
										44	88	30	40		0	0	-
11	AsCh-00h [NTO]	28	347.40	-2.17	570.7	26	-16	11.63	-0.0001	32.84	76.99	0	10	40	0.12	0.09	N
										36	76	10	30		0.27	0.29	S
										40	80	30	40		-	0	-
12	AsCh-00i [NTO]	11	347.08	-1.87	612.7	42	-41	10.88	0.0052	32.72	77.04	-	-		-	-	-
13	CHAIN [TO]	305	346.94	-1.27	695.7	83	55	11.18	0.0020	32.59	77.69	0	90	90	0	0	-
14	ChRo-00a [NTO]	9	344.09	-1.46	723.7	28	-36	12.96	0.1637	32.49	78.33	-	-		-	-	-
15	ChRo-00b [NTO]	11	344.04	-1.01	787.8	64	19	20.35	0.0541	32.36	78.33	-	-		-	-	-
	ChRo-50b [TO]									45		50	95	45	0	0	-
16	ChRo-00c [NTO]	31	343.92	-0.45	832.9	45	-18	23.58	-0.0854	32.22	78.43	-	-		-	-	-
	ChRo-60c [TO]									45		60	95	35	0	0	-
17	ROMANCHE [TO]	875	343.37	-0.08	895.7	63	13	17.61	-0.1162	32.09	80.47	0	95	95	0	0	-
18	RoSP-00a [NTO]	19	335.38	-0.91	945.8	50	15	8.52	0.1156	31.96	82.43	-	-		-	-	-
19	RoSP-00b [NTO]	27	335.28	-0.38	980.8	35	-36	15.08	0.0492	31.79	82.47	-	-		-	-	-
20	SAINT PAUL-a [TO]	51	335.08	0.29	1051.9	71	49	16.52	-0.0694	31.64	82.61	0	40	40	0	0	-
	SAINT PAUL-50a [TO]									52		50	100	50	0	0	-
21	SAINT PAUL-b [TO]	96	334.58	0.61	1073.9	22	-3	15.28	-0.0750	31.54	82.94	0	15	15	0	0	-
22	SAINT PAUL-c [TO]	146	333.68	0.78	1098.9	25	-3	13.85	-0.0832	31.46	83.49	0	20	20	0	0	-
23	SAINT PAUL-d [TO]	308	332.36	0.91	1126.9	28	-18	12.87	-0.0650	31.38	84.52	0	20	0	0	0	-
24	SPFo-00a [NTO]	31	329.60	1.00	1172.9	46	6	14.15	0.0498	31.25	85.29	0	10	20	0.34	0.25	S
										31.25	85.29	10	20		0.03	0.07	N
25	SPFo-00b [NTO]	10	329.34	1.52	1212.9	40	1	16.89	0.0373	31.11	85.32	-	-		-	-	-
	SPFo-10b [NTO]									32	85	5	45	40	0.07	0.05	S
26	SPFo-00c [NTO]	8	329.40	1.88	1252.0	39	-14	18.30	0.0090	30.99	85.3	-	-		-	-	-
27	SPFo-00d [NTO]	65	329.32	2.32	1305.0	53	1	18.55	-0.0335	30.84	85.46	0	15	15	0.16	0.09	N
	SPFo-20d [NTO]									30.84		25	45	20	0	0	-
28	SPFo-00e [NTO]	8	328.72	2.85	1357.1	52	21	16.62	-0.0597	30.68	85.62	0	22	22	0.09	0.09	N
29	SPFo-00f [NTO]	8	328.62	3.27	1388.1	31	-26	13.98	-0.0585	30.55	85.66	-	-		-	-	-

	SPFo-20f [NTO]									38	93	25	30	20	0.05	0.09	S
										38	93	30	35		0.51	0.45	N
										38	93	35	45		0.21	0.31	S
30	FOUR NORTH [TO]	117	328.51	3.65	1445.2	57	10	11.68	-0.0285	30.4	85.96	0	50	50	0	0	-
31	FoDo-00a [NTO]	12	327.42	4.16	1492.2	47	29	9.90	0.0323	30.24	86.25	-	-		-	-	-
32	FoDo-00b [NTO]	8	327.35	4.54	1510.3	18	-21	11.09	0.0489	30.13	86.27	-	-		-	-	-
33	FoDo-00c [NTO]	8	327.30	4.85	1549.2	39	-8	12.86	0.0590	30.01	86.29	-	-		-	-	-
34	FoDo-00d [NTO]	8	327.21	5.28	1596.3	47	22	15.43	0.0346	29.87	86.34	-	-		-	-	-
35	FoDo-00e [NTO]	34	327.08	5.63	1621.3	25	-4	16.75	0.0060	29.75	86.45	-	-		-	-	-
36	FoDo-00f (S. Leone FZ) [NTO	48	326.75	6.00	1650.4	29	-34	16.13	-0.0364	29.6	86.67	-	-		-	-	-
37	FoDo-00g [TO]	21	326.26	6.46	1713.4	63	33	12.33	-0.0897	29.42	86.83	0	20	20	0	0	-
38	FoDo-00h [TO]	75	326.08	7.02	1743.5	30	3	6.69	-0.1065	29.27	87.05	0	20	20	0	0	-
39	FoDo-00i [TO]	225	325.39	7.28	1770.5	27	4	3.02	-0.0801	29.14	87.81	0	35	35	0	0	-
	FoDo-40i [TO]									40	96	45	90	45	0	0	-
40	FoDo-00j [TO]	144	323.34	7.60	1793.5	23	-26	-1.16	0.0084	29	88.75	0	20	20	0	0	-
	FoDo-40j [TO]									40	96	40	100	60	0	0	-
41	FoDo-00k [TO]	182	322.03	7.98	1842.5	49	28	-3.07	0.0561	28.86	89.58	0	50	50	0	0	-
	FoDo-40k [TO]									40	96	45	90	45	0	0	-
42	FoDo-00l [NTO]	26	320.38	8.34	1863.5	21	-3	-3.58	0.1191	28.73	89.99	-	-		-	-	-
	FoDo-40l [TO]									40	96	45	90	45	0	0	-
43	DOLDRUMS [TO]	115	320.58	8.68	1887.5	24	-33	0.9	0.075235	28.59	90.24	0	100	100	0	0	-
44	DoVe-00a [NTO]	19	319.54	9.13	1944.6	57	8	2.5	0.020377	28.4	90.58	0	20	20	0.09	0.05	S
	DoVe-20a [NTO]									32	100	25	40	15	0.18	0.16	S
	DoVe-70a [TO]									40		70	90	20	0	0	-
45	DoVe-00b [NTO]	33	319.39	9.73	1993.7	49	-22	3.06	-0.0631	27.7	95.94	0	50	50	0	0	-
	DoVe-60b [NTO]									40		60	85	25	0	0	-
46	VEMA [TO]	312	319.15	10.45	2064.8	71	-14	-3.18	-0.1133	27.09	101.3	0	100	100	0	0	-
47	VeFi-00a [NTO]	8	316.32	11.29	2149.9	85	45	-11.60	0.0627	27.05	101.4	0	10	10	0.19	0.34	S
	VeFi-30a [NTO]											35	50	15	0	0	-
	VeFi-40a [NTO]											40	90	50	0	0	-
48	VeFi-00b (Mercurius FZ) [TO]	36	316.31	11.90	2189.9	40	-5	-7.27	0.0472	26.99	101.4	0	80	80	0	0	-
49	VeFi-00c (Marathon FZ) [TO]	88	315.98	12.38	2234.9	45	16	-4.37	0.0336	26.95	101.4	0	70	70	0	0	-
50	VeFi-00d [NTO]	9	315.15	12.82	2264.0	29	2	-3.39	0.0343	26.92	101.5	-	-		-	-	-
	VeFi-40d [NTO]									34	95	45	50	5	0.23	0.23	N
51	VeFi-00e [NTO]	10	315.25	13.10	2291.0	27	-18	-2.18	0.0035	26.88	101.5	-	-		-	-	-
	VeFi-10e [NTO]									30	96	10	45	45	0.11	0.14	S
										34	90	45	55		0.12	0.18	N
52	VeFi-00f [NTO]	20	315.16	13.42	2336.0	45	-51	-2.33	-0.0270	26.83	101.5	-	-		-	-	-
53	VeFi-00g [NTO]	10	314.99	14.11	2432.2	96	31	-5.01	-0.0589	26.74	101.6	-	-		-	-	-
54	FIFTEEN TWENTY [TO]	200	315.06	14.87	2497.2	65	-57	-9.72	-0.0639	26.64	101.6	0	80	80	0	0	-
55	FiKa-00a [NTO]	20	313.40	15.97	2619.2	122	89	-9.25	0.0046	26.53	101.7	-	-		-	-	-
	FiKa-10a [NTO]									34	104	15	25	20	0	0	-
										34	104	25	35		0.34	0.32	S
	FiKa-30a [NTO]									34	104	30	35	20	0.38	0.34	S
												35	50	15	0.05	0.11	N
56	FiKa-00b [NTO]	8	313.60	16.77	2652.3	33	8	-8.87	0.0062	26.45	101.7	-	-		-	-	-
	FiKa-90b [TO]									38		90	170	80	0	0	-
57	FiKa-00c [NTO]	10	313.54	17.07	2677.3	25	-1	-8.67	0.0051	26.41	101.7	-	-		-	-	-
58	FiKa-00d [NTO]	11	313.61	17.35	2703.3	26	-3	-8.46	0.0069	26.37	101.7	-	-		-	-	-
	FiKa-30d [NTO]									45	105	30	40	20	0.47	0.34	N
										44	99	40	50		-	0.07	N
59	FiKa-00e [NTO]	28	313.53	17.64	2732.4	29	-36	-8.33	0.0067	26.31	101.8	0	25	45	0.11	0.11	N
										34	105	25	45		0.19	0.14	S
60	FiKa-00f [NTO]	40	313.32	18.17	2797.4	65	26	-8.57	0.0108	26.23	101.8	0	20	20	0.18	0.14	S
61	FiKa-00g [TO]	30	313.76	18.68	2836.4	39	0	-6.82	0.0181	26.14	101.8	0	70	70	0	0	-
62	FiKa-00h [NTO]	5	314.03	19.16	2875.5	39	-3	-5.43	0.0228	26.06	101.9	0	10	40	0.42	0.58	S
										28	104	10	25		0.11	0.12	N
												25	40		0.16	0.14	S
	FiKa-10h [NTO]									26	100	7	15	8	0.49	0.38	N
	FiKa-20h [NTO]									30	105	20	60	40	0	0	-

	FiKa-60h [NTO]									28	94	60	67	7	0.84	0.93	S
63	FiKa-00i [NTO]	30	314.07	19.57	2917.5	42	-14	-4.36	0.0240	25.98	101.9	0	10	10	0.6	0.7	S
64	FiKa-00j [NTO]	7	314.36	20.09	2973.5	56	21	-2.40	0.0273	25.89	101.9	-	-		-	-	-
65	FiKa-00k [NTO]	4	314.40	20.52	3008.6	35	10	-1.04	0.0181	25.83	102	0	5	5	0.07	0.14	
	[TO]											5	70	65	0	0	-
66	FiKa-00l [NTO]	7	314.33	20.79	3033.6	25	-32	-0.55	0.0163	25.78	102	-	-		-	-	-
										28	105	10	50		0.21	0.14	N
										34	80	50	70		-	0.12	S
												70	80		0	0	-
68	FiKa-00n [NTO]	13	314.80	21.80	3160.6	70	21	1.41	-0.0043	25.56	102.1	-	-		-	-	-
	FiKa-10n [NTO]									30	105	10	20	30	0.42	0.55	N
										38	105	20	30		0.47	0.32	S
										38	105	30	40		0.21	0.12	N
69	FiKa-00o [NTO]	10	314.95	22.41	3209.7	49	-4	1.17	-0.0073	25.45	102.1	-	-		-	-	-
	FiKa-10o [NTO]									30	105	5	25	20	0	0	-
70	FiKa-00p [NTO]	15	315.09	22.91	3262.7	53	17	0.70	-0.0039	25.34	102.2	-	-		-	-	-
71	KANE [TO]	149	315.11	23.44	3298.7	36	-56	0.70	0.0094	25.24	102.3	0	90	90	0	0	-
	KANE N [TO]									20		85	120	45	0	0	-
	NORTHERN [TO]	100								24		35	95	60	0	0	-
72	KaAt-00a [NTO]	14	313.77	24.24	3390.8	92	78	-0.40	0.0415	25.14	102.3	-	-		-	-	-
	KaAt-30a [NTO]											30	40	40	0.07	0.03	N
												40	50		0.07	0.02	N
												50	70		0	0	-
73	KaAt-00b [NTO]	3	314.04	24.70	3404.8	14	5	2.29	0.0391	25.07	102.4	-	-		-	-	-
	KaAt-110b [NTO]									20	100	120	140	20	0.09	0.05	N
74	KaAt-00c [NTO]	16	314.12	24.79	3413.8	9	3	2.88	0.0407	25.05	102.4	-	-		-	-	-
75	KaAt-00d [NTO]	16	314.32	24.85	3419.9	6	-46	3.69	0.0366	25.01	102.4	0	25	30	0.14	0.19	N
										38	100	25	30		0.7	0.73	S
76	KaAt-00e [NTO]	4	314.54	25.12	3471.9	52	17	4.97	0.0255	24.94	102.4	-	-		-	-	-
	KaAt-20e [NTO]									28		25	30	5	0.31	0.25	N
	KaAt-50e [NTO]									36	75	50	65	15	0	0	-
77	KaAt-00f [NTO]	10	314.70	25.50	3506.9	35	-3	6.21	0.0221	24.86	102.4	0	25	25	0.19	0.27	N
	KaAt-20f [NTO]									40	110	30	40	10	0.45	0.38	S
	KaAt-40f [NTO]									36	75	45	65	20	0	0	-
	KaAt-100f [NTO]											102	114	12	0	0	-
78	KaAt-00g [NTO]	14	314.88	25.76	3545.0	38	5	7.01	0.0177	24.79	102.5	0	25	35	0.16	0.12	S
										40	110	25	35		0.62	0.47	S
	KaAt-40g [NTO]									36	75	45	65	20	0.09	0.16	S
79	KaAt-00h [NTO]	3	315.12	26.06	3578.0	33	24	7.82	0.0176	24.74	102.5	-	-		-	-	-
80	KaAt-00i [NTO]	9	315.21	26.24	3587.0	9	-29	8.21	0.0167	24.69	102.5	0	20	30	0.03	0.07	S
												20	30		0.93	1	S
81	KaAt-00j [NTO]	6	315.34	26.43	3625.0	38	2	8.64	0.0173	24.64	102.5	-	-		-	-	-
	KaAt-100j [NTO]											100	110	10	0.31	0.34	N
82	KaAt-00k [NTO]	4	315.44	26.71	3661.0	36	9	9.25	0.0191	24.57	102.6	-	-		-	-	-
	KaAt-40k [NTO]									30	80	45	65	20	0.25	0.21	S
83	KaAt-00l [NTO]	5	315.55	26.98	3688.0	27	21	9.90	0.0219	24.52	102.6	0	25	25	0.31	0.23	S
84	KaAt-00m [NTO]	2	315.65	27.14	3694.1	6	-54	10.37	0.0237	24.46	102.6	-	-		-	-	-
85	KaAt-00n [NTO]	11	315.77	27.44	3754.1	60	-4	11.22	0.0260	24.36	102.7	-	-		-	-	-
	KaAt-10n [NTO]											15	25	10	0.47	0.32	S
	KaAt-40n [NTO]									32	80	50	65	15	0	0	-
86	KaAt-00o [NTO]	11	316.05	27.97	3818.2	64	25	13.00	0.0252	24.24	102.7	0	20	25	0.42	0.27	S
										26	105	20	25		-	0.78	S
	KaAt-40o [NTO]									32	80	50	65	15	0	0	-
87	KaAt-00p [NTO]	3	316.29	28.42	3857.2	39	29	14.51	0.0206	24.15	102.8	0	10	10	0.27	0.19	S
88	KaAt-00q [NTO]	13	316.39	28.64	3867.2	10	-7	15.12	0.0206	24.1	102.8	-	-		-	-	-
89	KaAt-00r [NTO]	11	316.57	28.79	3884.2	17	-47	15.65	0.0202	24.04	102.8	0	15	15	0.12	0.11	S
	KaAt-40r [NTO]									32	80	50	60	10	0	0	-
	KaAt-90r [TO?]											90	135	45	0	0	-
90	KaAt-00s (Tyro FZ) [NTO]	14	316.83	29.12	3948.3	64	-11	16.49	0.0126	23.91	102.9	0	5	20	0.21	0.23	S

												5	15		0.16	0.21	N
												15	20		0.23	0.29	S
	KaAt-40s [NTO]									32	80	47	62	15	0	0	-
91	ATLANTIS [TO]	72	317.17	29.74	4023.4	75	35	17.60	0.0048	23.75	102.9	0	80	80	0	0	-
92	AtHa-00a [NTO]	13	318.04	30.16	4063.4	40	24	19.54	0.0255	23.64	103	-	-		-	-	-
93	AtHa-00b [NTO]	10	318.05	30.53	4079.5	16	-8	20.46	0.0172	23.56	103	0	35	35	0.09	0	S
94	AtHa-00c [NTO]	19	318.21	30.71	4103.5	24	-7	21.23	0.0250	23.5	103.1	0	40	40	0.07	0.11	S
95	AtHa-00d [NTO]	22	318.50	30.99	4134.5	31	4	22.63	0.0261	23.41	103.1	-	-		-	-	-
	AtHa-10e [NTO]									25	105	10	25	30	0.12	0.16	N
										23	###	25	40		0.16	0.19	S
97	AtHa-00f [NTO]	24	319.07	31.59	4189.6	28	-35	25.59	0.0135	23.21	103.2	0	20	40	0.31	-	S
										28	105	20	25		0.36	0.45	N
										23	110	25	40		0.16	0.09	S
98	AtHa-00g [NTO]	16	319.51	31.98	4252.7	63	12	27.43	0.0183	23.07	103.2	0	45	45	0.05	0	S
99	AtHa-00h [NTO]	19	319.90	32.47	4303.7	51	14	28.71	-0.0095	22.94	103.3	0	40	40	0.16	0.11	S
100	AtHa-00i [NTO]	48	320.22	32.86	4340.7	37	-30	29.31	-0.0127	22.79	103.4	0	20	45	0.25	0.14	S
										35	100	20	45		0	0	-
	AtHa-10i [NTO]									25	100	10	50	40	0	0	-
	AtHa-90i [NTO]											90	100	10	0.18	0.16	N
	AtHa-100i [NTO]											105	115	10	0.09	0.14	N
101	HAYES [TO]	84	320.83	33.43	4407.8	67	51	29.93	-0.0398	22.64	103.4	0	50	50	0	0	-
102	HaOc-00a [NTO]	17	321.82	33.65	4423.8	16	7	32.16	0.0084	22.57	103.4	-	-		-	-	-
103	HaOc-00b [NTO]	16	322.05	33.71	4432.8	9	-37	32.41	0.0113	22.52	103.4	0	15	45	0.14	0.09	S
										30	110	15	35		0.34	0.38	S
										30		35	45		0	0	-
	HaOc-20b [NTO]									30	110	20	50	30	0.12	0.16	S
104	HaOc-00c [NTO]	34	322.30	33.90	4478.8	46	-18	32.77	0.0007	22.42	103.5	0	20	45	0.42	0.34	S
										25	110	20	45		0.03	0.09	S
105	HaOc-00d [NTO]	34	322.87	34.27	4542.8	64	-31	33.51	0.0103	22.25	103.5	0	25	25	0.25	0.32	S
	HaOc-10d [NTO]									25	105	5	20	15	0.32	0.23	S
106	OCEANOGRAPHER [TO]	121	323.56	34.87	4637.9	95	31	34.53	0.0058	22.04	103.6	0	50	50	0	0	-
107	OcPi-00a [NTO]	19	325.13	35.31	4701.9	64	53	36.30	0.0511	21.87	103.6	0	5	20	0.31	0.23	N
										22	105	5	20		0.55	0.62	S
	OcPi-10a [NTO]									22	110	10	25	15	0.51	0.42	S
108	OcPi-00b [NTO]	19	325.48	35.62	4712.9	11	-41	38.28	0.0464	21.77	103.7	-	-		-	-	-
109	OcPi-00c [NTO]	10	325.82	35.87	4764.9	52	37	39.78	0.0389	21.67	103.7	-	-		-	-	-
110	OcPi-00d [NTO]	13	326.03	36.17	4779.9	15	-33	41.39	0.0371	21.58	103.7	-	-		-	-	-
111	OcPi-00e [NTO]	22	326.31	36.42	4827.9	48	8	42.32	0.0184	21.47	103.8	-	-		-	-	-
112	OcPi-00f (FZ A) [NTO]	23	326.72	36.76	4867.9	40	21	43.05	0.0082	21.36	103.8	-	-		-	-	-
113	OcPi-00g (FZ B) [NTO]	45	327.08	37.00	4887.0	19	-41	43.08	0.0104	21.25	103.9	-	-		-	-	-
114	PICO [TO]	46	327.73	37.31	4947.0	60	1	42.14	0.0182	21.09	103.9	0	80	80	0	0	-
115	PiCG-00a [NTO]	54	328.46	37.80	5006.0	59	7	41.96	0.0260	20.9	104	-	-		-	-	-
116	PiCG-00b [NTO]	24	329.28	38.21	5058.0	52	0	42.88	0.0397	20.73	104	-	-		-	-	-
117	PiCG-00c [NTO]	7	329.78	38.62	5110.1	52	-35	44.96	0.0255	20.56	104.1	-	-		-	-	-
118	PiCG-00d [NTO]	6	330.04	39.14	5197.1	87	-33	46.34	-0.0102	20.32	104.2	-	-		-	-	-
119	PiCG-00e (Kurchatov FZ) [NT	25	330.35	40.03	5317.2	120	73	44.97	-0.0233	21.93	100.7	0	10	10	0.16	0.18	S
120	PiCG-00f [NTO]	16	330.76	40.83	5364.2	47	-32	42.70	-0.0134	23.66	97.14	-	-		-	-	-
121	PiCG-00g [NTO]	8	330.77	41.52	5443.2	79	48	41.99	-0.0005	23.59	97.17	-	-		-	-	-
122	PiCG-00h [NTO]	15	330.81	42.08	5474.2	31	-3	41.94	0.0013	23.54	97.17	-	-		-	-	-
123	PiCG-00i [NTO]	5	330.67	42.44	5508.2	34	-17	41.95	-0.0022	23.5	97.16	-	-		-	-	-
124	PiCG-00j [NTO]	26	330.73	42.83	5559.3	51	-10	41.88	-0.0069	23.44	97.27	-	-		-	-	-
125	PiCG-00k [NTO]	29	331.04	43.42	5620.3	61	5	41.80	-0.0068	23.37	97.49	-	-		-	-	-
126	PiCG-00l [NTO]	13	331.53	43.92	5676.3	56	11	41.35	0.0007	23.3	97.68	-	-		-	-	-
127	PiCG-00m [NTO]	21	331.77	44.44	5721.3	45	4	41.25	-0.0011	23.23	97.79	-	-		-	-	-
128	PiCG-00n [NTO]	17	331.95	44.99	5762.3	41	0	41.21	-0.0034	23.16	97.9	-	-		-	-	-
129	PiCG-00o [NTO]	8	332.14	45.47	5803.3	41	13	41.45	0.0042	23.1	98	-	-		-	-	-
130	PiCG-00p [NTO]	12	332.28	45.82	5831.3	28	6	41.83	0.0054	23.06	98.09	-	-		-	-	-
131	PiCG-00q [NTO]	12	332.45	46.06	5853.4	22	-21	42.43	0.0074	23.01	98.19	-	-		-	-	-
132	PiCG-00r [NTO]	6	332.61	46.41	5896.4	43	-15	43.12	0.0071	22.95	98.28	-	-		-	-	-
133	PiCG-00s [NTO]	19	332.74	46.88	5954.4	58	30	43.58	-0.0050	22.88	98.31	-	-		-	-	-

134	PiCG-00t (Maxwell FZ) [NTO	21	332.63	47.41	5982.4	28	-9	43.04	-0.0118	22.81	98.27	0	20	20	0.19	0.29	S
135	PiCG-00u [NTO]	27	332.47	47.83	6019.5	37	-45	42.12	-0.0165	22.73	98.18	-	-		-	-	-
136	PiCG-00v [NTO]	41	332.14	48.51	6101.5	82	59	40.39	-0.0171	22.63	98.02	-	-		-	-	-
	PiCG-40v [NTO]									25	96	45	50	5	0.58	0.7	S
137	PiCG-00w [NTO]	13	331.64	49.19	6124.5	23	-13	38.91	-0.0024	22.55	97.9	-	-		-	-	-
	PiCG-40w [NTO]									25	96	45	55	10	0.4	0.62	S
138	PiCG-00x (Faraday FZ) [NTO]	39	331.54	49.54	6160.5	36	2	38.72	-0.0096	22.49	97.79	0	20	20	0.23	0.36	S
	PiCG-10x [NTO]									23	100	15	35	35	0.21	0.31	S
										23	100	35	50		0	0	-
	PiCG-40x [NTO]									25	96	40	50	10	0.25	0.4	S
										25	100	30	50		0	0	-
140	PiCG-00z [NTO]	9	330.57	50.47	6232.5	38	5	37.89	-0.0244	22.36	97.38	-	-		-	-	-
141	PiCG-00aa [NTO]	4	330.23	50.75	6265.5	33	-10	36.90	-0.0390	22.32	97.26	-	-		-	-	-
	PiCG-10aa [NTO]									25	95	10	25	15	0.55	0.45	N
	PiCG-20aa [NTO]									25	95	20	35	30	0.53	0.51	
										27	100	35	45		0.14	0.23	
142	PiCG-00ab [NTO]	7	330.02	51.07	6308.6	43	9	35.28	-0.0616	22.26	97.25	-	-		-	-	-
143	PiCG-00ac [NTO]	5	330.07	51.44	6342.6	34	-13	32.77	-0.0855	22.19	97.26	-	-		-	-	-
144	CHARLIE [TO]	116	329.99	51.83	6389.6	47	7	29.14	-0.0930	22.12	96.84	0	60	0	0	0	-
145	GIBBS [TO]	231	328.28	52.38	6429.6	40	-7	24.07	-0.0337	22.05	95.57	0	60	0	0	0	-
146	CGBi-00a [NTO]	25	324.86	52.96	6476.6	47	-61	32.31	0.1358	21.93	94.7	-	-		-	-	-
147	CGBi-00b [NTO]	22	324.81	53.84	6584.7	108	49	44.10	0.0264	21.76	94.71	0	20	20	0	0	-
148	CGBi-00c [NTO]	14	324.79	54.71	6643.7	59	32	49.30	-0.0221	21.63	94.73	0	20	20	0.07	0.18	N
149	CGBi-00d [NTO]	18	324.70	55.17	6670.7	27	-28	48.63	-0.0370	21.54	94.82	0	10	40	0	0	-
										22	95	10	20		0.62	0.65	S
										18	97	20	40		0.21	0.19	N
150	CGBi-00e [NTO]	26	325.01	55.64	6725.7	55	23	46.76	-0.0319	21.45	95.05	0	10	10	0.12	0.16	S
151	CGBi-00f [NTO]	10	325.52	56.07	6757.7	32	-23	44.96	-0.0101	21.35	95.24	-	-		-	-	-
152	BIGHT [TO]	22	325.66	56.52	6812.7	55	33	44.48	-0.0112	21.27	95.41	0	35	35	0	0	-
153	BiIC-00a [NTO]	12	326.08	56.87	6834.7	22	-17	44.71	0.0101	21.2	95.65	0	15	30	0.07	0.05	S
												15	30		0.34	0.25	S
154	BiIC-00b [NTO]	8	326.47	57.12	6873.7	39	-8	45.17	0.0180	21.13	95.89	0	10	30	0.38	0.31	S
										20	90	10	30		0	0	-
155	BiIC-00c [NTO]	5	326.95	57.46	6920.8	47	8	45.94	0.0177	21.05	96.15	2	10	10	0.51	0.38	S
	BiIC-00c [NTO]									20	95	10	20	10	0	0	-
156	BiIC-00d [NTO]	32	327.36	57.83	6959.8	39	19	46.76	0.0123	21.01	96.27	-	-		-	-	-
	BiIC-10da [NTO]									20	95	0	30	30	0.05	0.09	N
	BiIC-10db [NTO]									20	95	15	35	20	0.11	0.07	S
157	BiIC-00e [NTO]	13	327.34	57.81	6979.8	20	0	46.71	0.0130	21	96.33	-	-		-	-	-
	BiIC-10e [NTO]									20	95	10	25	15	0.12	0.14	S
158	BiIC-00f [NTO]	11	327.58	57.91	6999.8	20	1	46.87	0.0161	20.98	96.42	-	-		-	-	-
	BiIC-10f [NTO]									20	95	10	30	20	0	0	-
159	BiIC-00g [NTO]	10	327.66	57.99	7018.8	19	10	47.00	0.0134	20.97	96.47	-	-		-	-	-
	BiIC-20g [NTO]									20	95	20	30	10	0.32	0.23	S
161	BiIC-00h [NTO]	6	327.80	58.11	7039.8	12	3	47.20	0.0120	20.95	96.57	-	-		-	-	-
	BiIC-20h [NTO]									20	95	20	35	15	0.19	0.16	S

* Names of offsets correspond to the FZs N and S of the offset-age-offset letter. SoAs South of Ascension; As: Ascension; Ch: Chain; Ro: Romanche; SP: Saint Paul Fo: Four North; Do: Dldrum; Ve: Vema; Fi: Fifteen-Twenty; Ka: Kane; At: Atlantis; Ha: Hayes; Oc: Oceanographer; Pi: Pico; CG: Charlie-Gibbs; Bi: Bight; IC: Iceland 1. Off. Len.: Length of the offset; 2. Lon.: Longitude; 4. Dist.: Distance along the axis; 5. SL: Length of segment to the south; 6. Difference in segment length across offset 7. FAA reg.: Regional free-air anomaly; 8. FAA grad.: Regional gradient in the FAA; 9. sr: half spreading rate; 10. sdir: Spreading direction; 11. Start: Start of offset trace; 12. End: End of offset trace; 13. Total: Total life span of offset trace; 14 PR/SR: Propagation rate normalized by spreading rate, East; 15. Same as 14, West flank; 16. PD: Propagation direction of offset

Table 3. Calculated gravity roughness versus ridge geometry

Longitude (°E)		Latitude (°N)		RMS	σ§	α (°)*	Zone¶
Min.	Max.	Min.	Max.	(mGal)			
327.8	331.0	58.8	59.7	5.8	4.8	60	Reykjanes
329.8	331.4	60.8	61.8	5.7	4.5	60	Reykjanes
332.8	334.0	60.2	61.3	6.2	5.4	60	Reykjanes
322.0	325.5	56.7	58.6	12.6	9.8	58	Reykjanes
328.7	332.8	56.3	58.2	10.4	7.9	58	Reykjanes
321.2	323.9	53.1	56.5	9.5	8.0	~	CG-Bi
326.2	328.4	52.9	56.0	9.1	9.4	~	CG-Bi
325.5	328.9	48.6	51.2	10.6	7.8	57	South CG
333.9	337.6	48.9	51.1	10.8	8.3	57	South CG
328.7	330.8	44.4	47.3	6.9	5.2	83	Azores N
323.2	328.1	45.3	47.5	5.8	4.5	83	Azores N
323.1	326.7	39.3	42.3	7.7	5.8	83	Azores S
332.2	335.1	42.0	43.0	8.6	6.3	83	Azores Center
321.2	324.8	35.9	38.0	10.0	7.0	55	Oc-Pi
327.9	331.5	34.7	36.6	10.1	8.3	55	Oc-Pi
318.6	321.9	33.8	35.3	12.8	10.4	49	Ha-Oc
324.4	327.8	33.4	34.7	9.2	7.8	49	Ha-Oc
314.2	318.0	30.8	33.3	13.5	9.6	65	At-Ha
320.4	324.6	30.1	32.5	11.9	8.7	65	At-Ha
312.3	315.7	28.3	30.1	9.6	7.1	71	Ka-At
317.8	320.7	27.5	29.2	9.0	6.6	71	Ka-At
309.0	313.4	25.1	28.0	9.0	6.8	71	Ka-At
316.1	319.4	23.7	25.6	10.4	7.6	71	Ka-At
321.4	324.1	23.6	26.0	10.3	7.8	62	Ka-At off axis
305.7	308.5	26.6	28.0	8.1	5.8	62	Ka-At off axis
323.1	325.4	26.6	28.3	10.7	7.4	62	Ka-At off axis
307.7	309.4	29.1	31.0	11.5	7.9	62	Ka-At off axis
311.1	313.6	21.0	23.4	10.5	7.4	~	South Ka
315.7	318.5	20.6	22.7	10.3	7.6	~	South Ka
310.8	312.8	17.5	19.7	11.2	7.6	~	South Ka
314.7	318.1	17.1	19.1	10.2	8.1	~	South Ka
317.4	318.7	7.6	9.2	18.3	11.2	35	Do
324.0	325.8	7.5	8.8	13.6	11.4	35	Do
324.4	325.8	4.3	6.2	9.1	6.4	68	Fo-Do
328.1	330.0	4.3	6.7	7.6	5.7	68	Fo-Do
326.4	327.9	1.3	3.5	9.0	6.5	71	SP-Fo
330.2	332.1	1.3	3.7	8.3	6.5	71	SP-Fo
343.9	346.7	-6.6	-2.1	8.5	6.6	~	As-Ch
349.3	352.7	-5.5	-0.9	9.0	6.9	~	As-Ch

† RMS: Residual mean squared; § σ: Standard deviation of RMS; *
α: Obliquity, angle between spreading direction and ridge trend. ~ indicates sections of ridge with no clear trend and where obliquity is not calculated. Estimated error is ~5°; ¶ Same convention as Table 2 for naming of FZs.

Table 4. Crustal thickness estimated from seismic data

Area	Lat. (°N)	Thickness (km) Min.	Max.	Reference
Iceland	64.50	28.0	37.0	*Bott and Gunnarson* [1980]
Iceland	64.00	20.0	24.0	*Bjanarsson et al.* [1993]
Reykjanes	62.50	8.0		*Ritzert and Jackoby* [1985]
Reykjanes	62.50	10.0		*Ritzert and Jackoby* [1985]
Reykjanes	61.7	8.4	10.0	*Smallwood et al.* [1995]
Reykjanes	59.50	7.0	10.0	*Bunch and Kennet* [1980]
Charlie-Gibbs	52.50	4.0	8.0	*Whitmarsh and Calvert* [1986]
Charlie-Gibbs	45.00	5.0		*Keen and Tramontini* [1970]
Azores Plateau	41.30	6.3		*Searle* [1976]
Azores Plateau	39.20	7.4	8.6	*Searle* [1976]
Azores Plateau	39.10	3.9		*Ewing and Ewing* [1959]
Azores Plateau	38.75	5.7	8.0	*Ewing and Ewing* [1959]
Azores Plateau	37.40	6.4		*Searle* [1976]
FAMOUS	36.75	5.3		*Fowler and Mathews* [1974]
FAMOUS	36.75	3.0	7.0	*Fowler* [1976]
FAMOUS	36.75	4.7	7.1	*Poehls* [1974]
FAMOUS	36.75	5.8		*Whitmarsh* [1973]
FAMOUS	35.60	5.3		*Ewing and Ewing* [1959]
Oceanographer	35.00	2.0	9.0	*Sinha and Louden* [1983]
Oceanographer	31.90	5.0		*Le Pichon et al.* [1965]
Oceanographer	31.85	6.8		*Le Pichon et al.* [1965]
Kane	23.50	1.5	6.5	*Abrams et al.* [1988]
Kane	23.50	2.1	5.5	*Detrick and Purdy* [1980]
Kane	23.50	2.0	8.0	*Purdy and Detrick* [1986]
Kane	23.50	1.0	6.0	*Cormier et al.* [1984]
Vema	11.80	1.5	8.0	*Louden et al.* [1986]
Central Atl.	00.06	4.8		*Le Pichon et al.* [1965]
Central Atl	-1.10	5.3		*Le Pichon et al.* [1965]

Chapter 5

NON-DILATANT BRITTLE DEFORMATION OF SERPENTINITES: IMPLICATIONS FOR MOHR-COULOMB THEORY AND THE STRENGTH OF FAULTS

Javier Escartín, Greg Hirth and Brian Evans
Accepted by *Journal of Geophysical Research,* April 1996

Abstract

We conducted deformation experiments to investigate the strength, deformation processes, and nature of the brittle-ductile transition of lizardite and antigorite serpentinites. A transition from localized to distributed deformation occurs as confining pressure increases from ~200 MPa to ~400 MPa at room temperature. Deformation in both brittle (localized) and ductile (distributed) regimes is accommodated by shear microcracks, which form preferentially parallel to the (001) cleavage. Axial microcracks (mode I) are infrequently observed. Volumetric strain measurements demonstrate that brittle deformation is mostly non-dilatant, consistent with the shear-dominated microcracking. Three observations indicate that deformation in the ductile regime is accommodated by cataclastic flow: (1) a lack of evidence for crystal plastic deformation, (2) a positive pressure dependence of the maximum differential stress, and (3) abundant evidence for brittle microcracking. The weakness of serpentinites relative to other brittle rocks is explained by a low fracture strength along the (001) cleavage, combined with the low pressure dependence of strength. The transition from brittle to ductile deformation occurs at the cross-over between the strength of intact serpentinite and the friction law unique to each type of serpentinite, rather than the more general Byerlee's law. If brittle deformation regimes are defined based on the mode of microcracking and on the occurrence of crystal plasticity, serpentinites define an end-member style of non-dilatant brittle deformation. This deformation style may result in extremely weak faults in nature, and it may also strongly influence the tectonic evolution of the oceanic lithosphere where serpentinite is present.

Introduction

Serpentine is probably the most abundant alteration phase in ultramafic rocks from the oceanic lithosphere [e.g., *Aumento and Loubat*, 1971; *Bonatti*, 1976]. Such alteration products can influence the rheological properties of shear zones [e.g., *Vernon,* 1977; *Brodie and Rutter*, 1985; *Mével and Cannat*, 1992; *Gillis et al.*, 1993]. However, rheological models [e.g., *Chen and Molnar*, 1983; *Lin and Parmentier*, 1989; *Neumann and Forsyth*, 1993] do not include these phases, owing partly to the scarcity of mechanical data, but also to a lack of information on their distribution and abundance. Instead, lithospheric strength is typically modeled using Byerlee's friction law and experimental plastic flow-laws for unaltered quartzite, diabase, and olivine, [e.g., *Brace and Kohlstedt*, 1980; *Kohlstedt et al.*, 1995].

The importance of serpentine for the tectonics of the oceanic lithosphere has been debated since at least the early 1960's when *Hess* [1962] proposed that oceanic layer 3 is composed mostly of serpentinites. Peridotites dredged or drilled along slow-spreading mid-ocean ridges and fracture zones invariably show a high degree of serpentinization [e.g., *Aumento and Loubat*, 1971; *Bonatti*, 1976; *Dick,* 1989; *Cannat et al.*, 1992], indicating that hydration of peridotite occurs in very young (<1 Ma) oceanic lithosphere. In addition, studies on the Josephine ophiolite have documented oceanic serpentinization of the lithosphere at or near the ridge axis [*Coulton et al.*, 1995]. Consequently, the tectonics of slow-spreading mid-ocean ridges, fracture zones, subduction zones, and obducted ophiolites are likely affected by the presence of serpentinites.

The serpentine group is composed of the polytypes lizardite, chrysotile, and antigorite. Lizardite, the most abundant serpentine mineral, occurs mainly in retrograde metamorphic

assemblages [e.g., *Moody*, 1976; *Wicks and Whittaker*, 1977] and is common along mid-ocean ridges [*Aumento and Loubat*, 1971]. Antigorite is the second most abundant polytype and the main component of prograde serpentinites [e.g., *Coleman*, 1971; *Wicks and Whittaker*, 1977]. Antigorite and lizardite are stable at temperatures <400°-500°C [*Caruso and Chernosky*, 1979; *Janecky and Seyfried*, 1986; *Ulmer and Trommsdorff*, 1995] and lithospheric pressures. Chrysotile, the least abundant polytype, is stable below 300°C [*Caruso and Chernosky*, 1979; *O'Hanley et al.*, 1989] and is a minor component of both prograde and retrograde serpentinites [*Wicks and O'Hanley*, 1988].

Previous experimental work shows that serpentinites are generally weaker than other common lithospheric rocks, and that lizardite is weaker than antigorite. *Raleigh and Paterson* [1965] concluded that intact cores of antigorite had "... an ultimate strength similar to that of granite at room temperature ...". Unfortunately, this assertion has been generalized to all serpentinites, even though those experiments and subsequent work [*Raleigh and Paterson*, 1965; *Murrell and Ismail*, 1976] indicated that lizardite is considerably weaker than both antigorite and granite. The frictional strength of lizardite is also less than that of antigorite [*Dengo and Logan*, 1981; *Reinen et al.*, 1994; *Moore et al.*, 1995]; friction coefficients (μ) of lizardite gouge vary between μ=0.15-0.35 [*Reinen et al.*, 1994] and μ=0.4 [*Moore et al.*, 1995], and increase to μ=0.50-0.56 for polished surfaces [*Dengo and Logan*, 1981]. The coefficient of friction is higher for both antigorite gouge (μ=0.5-0.85 [*Reinen et al.*, 1994], μ=0.47 [*Moore et al.*, 1995]) and polished surfaces (μ=0.77 [*Dengo and Logan,* 1981]). Note that the lizardite used by *Reinen et al.* [1994] may have been mostly chrysotile instead of lizardite [*Reinen et al.*, 1995].

We conducted experiments on lizardite and antigorite to investigate the processes responsible for the transition from localized to distributed deformation, and to determine

why serpentinites are weaker than other lithospheric rocks. We measured volumetric strain, and correlated the mechanical data with deformation microstructures. We observed a new style of mostly non-dilatant brittle deformation. This style of deformation may substantially weaken serpentinite-bearing faults, and thus control the mechanical evolution of the oceanic lithosphere where serpentinites are present.

Experimental details

Samples

Antigorite serpentinite. We used an antigorite serpentinite (VM3) that is ~90% antigorite, with less than 5% Fe oxides, and minor amounts of magnesite along veins; this is the same material studied by *Reinen et al.* [1994]. The rock has a weak macroscopic foliation; bands of elongated antigorite grains (<300 μm in length) with basal planes parallel to the overall foliation (bladed texture [*Maltman*, 1978]) alternate with veins that contain grains (<100 μm) oriented perpendicular to the foliation (Figure 1a). Zones with smaller (<50 μm), randomly oriented grains are sometimes present at the center of veins (Figure 1a). The grains within the bladed zones and veins are primarily oriented parallel and perpendicular to the macroscopic foliation, respectively (Figure 2a). However, the lattice preferred orientation (LPO) of the entire sample is weak (Figure 2b). Scanning and transmission electron microscopy (SEM and TEM, respectively) show little pre-existing porosity, few open microcracks, and a large number of crystal defects (twins and dislocations, Figure 1b). The density of this material (2690 kg/m^3) is slightly higher than that of pure antigorite (of 2600 kg/m^3) [*Deer et al.*, 1966]. Assuming that the excess density is due to the presence of iron oxides (density 5000 kg/m^3), the oxides would comprise 3.4% of the sample volume, consistent with the modal abundance estimated from thin sections.

Lizardite serpentinite. Lizardite samples were cored from serpentinized oceanic peridotites dredged along the central Mid-Atlantic Ridge (samples AII60 9-10, AII60 9-75, and AII60-5 from the WHOI collection) and one of unknown origin (X). All of these rocks are comprised of >80% lizardite, minor amounts of chrysotile, and <10% magnetite and chlorite, as indicated by powder X-ray diffraction patterns, optical microscopy and TEM observations; traces of olivine, enstatite, and other Fe oxides are also found. The microstructure of the lizardite serpentinites is more complex than that of antigorite serpentinites. Lizardite serpentinites have a "mesh texture" matrix (see *O'Hanley* [1996] and references therein) surrounding lizardite pseudomorphs of pyroxenes called bastites [*Hidinger*, 1845; Dungan, 1979], "amorphous" areas (grains <0.01 μm long), and zones with magnetite and other opaque minerals (Figure 1c). The lizardite grains within the mesh-textured zones are <20 μm long. The grain size of lizardite is too small to determine the LPO using optical microscopy. At the TEM scale, the mesh-textured regions show no pre-existing porosity or open microcracks and a high density of crystal defects (dislocations and uncharacterized planar defects, Figure 1d). A small amount of porosity (<5%), is present in some of the amorphous zones. As these zones comprise <10% of the sample volume, we estimate that the porosity of the samples is <0.5%. The density of the lizardite serpentinite (2660 kg/m^3) is higher than that of pure lizardite (2550 kg/m^3), requiring ~4.5% vol. of iron oxides to account for the excess mass.

Westerly granite. Westerly granite was used to compare our volumetric strain measurements with data obtained previously using the same techniques [e.g., *Brace et al.*, 1965]. The characteristics of the particular block of Westerly granite we used are described elsewhere [e.g., *Brace*, 1965; *Wong*, 1982].

Methods

Gas confining medium apparatus. Experiments at confining pressures (P_c) less than 400 MPa were conducted using argon as a confining medium. Cylindrical samples 15.88 mm in diameter and 25.4±2.5 mm in length were jacketed in copper foil, and sealed with copper end-caps. The samples were then pressurized to ~100 MPa, and then returned to ambient conditions, to seat the jacket and to ensure a gas-tight seal. All experiments were conducted at room T, and at displacement rates corresponding to average strain rates from ~3.5×10^{-4} to ~3.8×10^{-6} s^{-1}, at a constant confining pressure. The load and displacement were externally measured and digitally recorded; the load is accurate to 0.3 MPa. Two electrical strain gauges were mounted onto the collapsed copper jacket to measure axial and radial strain. Volumetric strain was calculated using the relationship: $\varepsilon_v = \varepsilon_a + 2 \times \varepsilon_r$, where ε_v, ε_a, and ε_r are the volumetric, axial, and radial engineering strain, respectively (these and other symbols are summarized in Table 1). The calculated volumetric strain is accurate at strains <5%, and/or prior to the localization of deformation on a discrete fault [e.g., *Brace et al.*, 1965; *Brace*, 1978]; strain gauge measurements are precise to strains of 0.001% and accurate to ~0.02% due to electronic noise. The small initial porosity (and therefore small permeability) of both serpentine rocks makes measurement of volume changes by variations in pore volume impractical [e.g., *Brace*, 1978].

Solid confining medium apparatus. Higher-pressure experiments (P_c>300 MPa) were conducted in a modified Griggs-type apparatus using lead as the confining medium. The runs were conducted at room temperature, confining pressures from 300 to 1000 MPa, and constant displacement rates corresponding to average strain rates of ~1.5×10^{-5} and ~1.5×10^{-6} s^{-1}. Axial load and displacement were measured externally; the load is accurate to ~50 MPa. Differential stress versus axial strain curves were calculated assuming that the

samples deformed homogeneously and that the volume remained constant. Cylindrical cores (6.3 mm in diameter, 10 to 14 mm long) were jacketed in a 0.25 mm thick silver tube.

Sample preparation. Samples were cored from as-received materials and ground to obtain flat ends and parallel sides. Samples of antigorite were cored at approximately 0°, 30°, 45°, 60° and 90° to the weak foliation to investigate the effects of textural anisotropy.

Results of deformation experiments

The results of deformation experiments on antigorite, lizardite, and Westerly granite are summarized in Tables 2 and 3.

Stress versus strain curves

Stress-strain curves for antigorite illustrate a transition from unstable faulting or strain weakening to flow at a constant stress with increasing pressure (Figures 3a, b). Unstable faulting was observed at P_c = 60 MPa, while strain weakening was observed at P_c = 150 MPa and 195 MPa. The jackets of these samples showed that deformation localized on a single fault. At P_c = 325 and 345 MPa the flow stress was constant (after an initial strain weakening in the first case); these samples showed a transitional style of deformation with the development of an ~2 mm wide shear zone composed of several anastomosing faults. Slight strain hardening was observed at P_c = 725 and 1000 MPa; these samples deformed homogeneously.

The strength of lizardite is approximately half of that of antigorite, although the macroscopic deformation behavior of both materials is similar (Figure 3). At P_c = 200 MPa the stress-strain curves show strain weakening associated with shear localization on a

fault; the run at P_c = 50 MPa was stopped at the peak stress, prior to strain localization (Figure 3c). Steady-state flow or slight strain hardening was observed at $P_c \geq 300$ MPa (Figures 3c, d). Similar to our observations for antigorite, the jackets of samples deformed at 300 and 400 MPa revealed a transitional style of deformation, while those of samples deformed at 700, 840, and 950 MPa showed no evidence for strain localization.

The elastic portion of the stress-strain curves (i.e., Young's modulus) is similar for experiments on antigorite conducted in both the gas and the solid medium apparatus (Figures 3a, b). In contrast, the Young's modulus of lizardite displays some variability; in Figure 3d the differential stress at 2% strain varies by ~200 MPa. The similarity of the Young's modulus observed for antigorite runs indicates that results from the two apparatus are comparable. Cyclic loading experiments on lizardite demonstrate that deformation in the pre-yield portion of the stress-strain curves is elastic. Results from a cyclic loading experiment are shown in Figure 3c. In run l-54 the sample was successively loaded at P_c=200 MPa to differential stresses of 51, 82, 305 and 424 MPa; permanent strain was only observed after the sample was loaded to 305 MPa, past the yield point (i.e., deviation from an approximately linear loading curve).

Pressure dependence

In both serpentine polytypes, the yield stress (σ_y) and the maximum differential stress (σ_{max}) depend positively on pressure, but the pressure dependence is somewhat lower for lizardite than for antigorite (Figure 4). At a given pressure, the strength of antigorite σ_{max} varies by ~250 MPa, while that of lizardite varies by ~150 MPa (Figure 4b). Part of the scatter in the strength of antigorite can be attributed to mechanical anisotropy. As shown in Figure 5, the strength of antigorite depends on the angle between the macroscopic foliation

and the shortening direction; for any given orientation the strength of antigorite varies by ~150 MPa.

The strength and the pressure dependence of strength are lower for both serpentinites (but most notably for lizardite) than for other rocks deformed in the brittle regime. This observation is illustrated by the Mohr envelopes shown in Figure 6a. These envelopes were calculated using the data listed in Table 2, data for Westerly granite from *Brace et al.* [1965], and data for dunite from *Shimada et al.* [1983]. All of the experiments were conducted at strain rates between 10^{-6} and 10^{-5} s^{-1}. As the strain rate dependence of the maximum stress in the brittle regime is small [e.g., *Sano et al.*, 1981], the failure envelopes for each rock type can be compared directly. The lower strength of serpentinites can be attributed partly to their lower pressure dependence of strength. However, at high pressures the coefficients of internal friction (μ_i) of lizardite, antigorite, and granite are similar (μ_i~0.35-0.45). Thus the differences in strength at normal stresses (σ_n) grater than 1000 MPa must be attributed to other properties of these rocks (e.g., cohesive strength).

The differences in strength and the pressure dependence of strength shown by the Mohr envelopes in Figure 6a may also be correlated with observations made during frictional sliding experiments on serpentinite at lower pressures [e.g., *Dengo and Logan*, 1981; *Reinen et al.*, 1994; *Moore et al.*, 1995]. While the coefficient of friction (μ) for antigorite is somewhat lower than the value of μ~0.85 predicted by "Byerlee's law" [*Byerlee*, 1978] at σ_n<200 MPa, lizardite is substantially weaker than either antigorite or rocks that follow Byerlee's law (Figure 6b).

Volumetric strain

Most crystalline rocks that undergo brittle deformation exhibit significant dilation associated with the opening of axial microcracks [e.g., *Brace et al.*, 1965; *Paterson*, 1978]. However, volumetric strain data indicate that brittle deformation of serpentinites is mostly non-dilatant. Strain gauges were only used on samples deformed in the gas apparatus (13 runs on antigorite, 12 runs on lizardite, and 2 runs on granite, Table 3). Minor amounts of dilatancy (<0.15% $\Delta\varepsilon_V$) were only observed during 3 of 13 experiments on antigorite and 2 of 12 experiments on lizardite. In all other cases deformation resulted in either minor amounts of apparent compaction (<0.2% $\Delta\varepsilon_V$) or no resolvable permanent volume change (Table 3).

Both polytypes show a range of mechanical behavior involving small amounts of apparent dilation, compaction, or no permanent volume change (Figure 7). For antigorite, three examples are shown in Figure 7a, one that resulted in dilation, another in compaction (both at P_c=200 MPa) and a third that showed no resolvable permanent volume change (P_c=50 MPa). Lizardite exhibits similar variability in volumetric strain behavior (Figure 7b). Two of the examples display limited compaction (P_c=50 and 200 MPa), while another for a sample deformed at P_c=200 MPa shows a small amount of dilation.

The variability in the volumetric strain behavior does not appear to correlate with sample-scale textural anisotropy (i.e., the location of strain gauges with respect to the foliation in antigorite). In the case of the lizardite samples there is no recognizable macroscopic foliation. As discussed below, a possible explanation for the variability in the volumetric strain behavior is the development of inhomogeneous strain patterns caused by fault localization under or in the immediate vicinity of strain gauges.

Even when serpentinites dilate, the volume increase is small when compared with that of granite deformed at the same conditions (Figure 7c). Note also that the deviation from elastic behavior (c', the stress at which stress and strain are not linearly related) occurs much later during the loading cycle in both serpentinites than in granite. Values of c'/σ_{max} for serpentinites range from 0.71 to 1 (Table 2), while those for granite range between 0.3 and 0.6 [*Brace et al.*, 1965]. Both the lack of dilatancy and the high values of c'/σ_{max} indicate that serpentinites define an end-member style of brittle deformation. The unique nature of the mechanical behavior of serpentinites is further appreciated when comparisons are extended to other rock types such as aplite, granite and gabbro (Figure 8). Serpentinites are the only one of these rock types that do not show strongly dilatant volumetric strain behavior (Figure 8a). As shown in Figure 8b, the difference in volumetric strain behavior is more apparent when $\Delta\varepsilon_v$ is normalized by the extrapolated elastic strain ε_e [*Brace et al.*, 1965]. The values of c'/σ_{max} for serpentinites are generally >0.7, while the values measured for gabbro, dunite and aplite are always <0.75 and can be as low as 0.25 (Figure 8c).

The volumetric strain measurements also illustrate the elastic nature of deformation prior to yielding. Plots of mean stress ($\sigma_m=[\sigma_1+\sigma_2+\sigma_3]/3$) versus volumetric strain for both antigorite and lizardite show a coincidence of the effective bulk modulus measured during hydrostatic and subsequent triaxial loading (Figure 7d). The effective bulk modulus is given by the slope of the σ_m versus ε_v curve; similar slopes are obtained during both the hydrostatic ($\sigma_1=\sigma_3$) and triaxial ($\sigma_1>\sigma_3$) loading (Figure 7d, dots versus lines), indicating that significant pore collapse did not occur during pressurazation.

Microstructural observations

As the confining pressure increases, the mode of deformation changes from localized (brittle) to distributed (ductile) deformation in both antigorite and lizardite. These observations are summarized on a plot of σ_{max} versus P_c in Figure 4b. Microstructural observations were made on samples deformed in both regimes to determine the processes responsible for the transition in macroscopic deformation behavior.

Localized deformation regime

Optical microscope observations on both serpentine polytypes indicate that deformation localizes on a single fault. In all cases the faults form at high angles (30°-45°) to the shortening direction. Microcracking is generally restricted to the immediate vicinity of the shear zones; the microstructure at distances greater than ~50 μm from the fault zones is indistinguishable from that of the starting material. However, incipient shear zones of limited extent that accommodate small amounts of strain were observed throughout.

In faulted samples of lizardite and antigorite the crystallographic anisotropy of individual grains controls the formation of microcracks and the localization of strain. Faults in antigorite form within the "bladed bands", where the grains are oriented parallel to the foliation. Microcracking is crystallographically controlled, as illustrated by optical micrographs of an antigorite sample that was unloaded immediately after the onset of strain weakening (Figures 9a, b). Two incipient fault zones run along two "bladed bands"; in both cases the (001) cleavage of the grains within the bands is parallel to the faults. A TEM micrograph of one of these incipient faults illustrates that microcracks form almost exclusively along (001) grain boundaries, although some intragranular cracks parallel to the (001) cleavage are also observed (Figure 9c). The microcracks illustrated in Figure 9c are

oriented at high angles (>20°) to the shortening direction, consistent with observations at the optical microscope scale. No axial cracks are observed even at the TEM scale. Figures 9a and 9b also show that the "jog" connecting the two incipient faults is defined by cracks oriented along (001) grain boundaries.

Microcracks in faulted samples of lizardite also form parallel to the (001) cleavage. Fault zones tend to follow the rims of the mesh-textured regions (Figures 9d, e). A TEM micrograph of a fault zone in a lizardite sample deformed at the same conditions as that shown in Figure 9d is shown in Figure 9f. Both grain boundary and intragranular microcracks were observed parallel to the (001) cleavage. Qualitatively, intragranular microcracking is more abundant in lizardite than in antigorite.

Distributed deformation regime

Microstructural observations for samples of both antigorite and lizardite deformed in the distributed ("ductile") deformation regime reveal numerous shear zones of limited lateral extent (0.01-1 mm long) that accommodate small amounts of strain. These shear zones are homogeneously distributed throughout the sample, form at high angles to the shortening direction and are oriented in conjugate directions. Micrographs of samples deformed in this regime demonstrate that the zone of microcracking associated with individual shear zones is wider than that observed in the localized regime (Figure 10). The change from localized to distributed deformation is characterized by a transitional style of deformation at P_c~400 MPa. In the transitional regime strain is accommodated on ~1 mm wide fault zones that are composed of anastomosing and cross-cutting shear zones.

TEM observations demonstrate that the (001) cleavage also controls microcracking in both antigorite and lizardite deformed in the distributed deformation regime. Examples of

both intragranular and grain-boundary microcracks oriented parallel to the (001) cleavage are shown in Figures 10c and 10d. The microcracks form at high angles to the shortening direction, consistent with the orientation of the small-scale shear zones observed optically. Zones of uncracked material are scarce, both at optical and TEM scales, emphasizing the distributed nature of deformation in this regime.

Plastic deformation microstructures

Crystal plastic deformation does not appear to contribute significantly to strain in lizardite and antigorite in either the localized or the distributed deformation regimes. There is no resolvable difference between the density of dislocations or twins in undeformed and deformed samples. However, because the microstructure of the starting materials is complex (Figure 1), we cannot rule out the possibility that some plastic deformation occurred without significantly changing the density of crystal defects. Further evidence for a lack of crystal plasticity is given by a comparison of microstructures in serpentinites to those in biotite schists deformed at similar conditions. Biotite, which has a crystal structure similar to that of serpentine, deforms plastically at room temperature and develops kink bands associated with dislocation glide on the basal plane [*Shea and Kronenberg*, 1992]. Such kink bands were not observed in any of the deformed serpentinite samples.

Microcrack orientations

The orientation of microcracks relative to both the shortening direction and the (001) cleavage was measured optically in antigorite samples deformed in both the localized and distributed regimes. The small grain size of lizardite did not permit similar studies. However, the similarity between the microstructures of antigorite and lizardite at the TEM scale suggests that results obtained from antigorite are representative of processes operating

in lizardite. For each thin section a regular grid with 0.5 mm spacing was defined; at each grid point we a) measured the orientation of the (001) cleavage of the grain, b) determined if the grain was cracked, and c) measured the crack orientation for those grains that were cracked. All orientations are given with respect to the shortening direction. In each sample more than 450 measurements were made (Figure 11).

The strong control that the (001) cleavage of serpentine imparts on the formation of microcracks is illustrated by plots on the right of Figure 11. In all cases the orientation of microcracks coincides with that of the cleavage (r^2>0.98), demonstrating that microcracks form almost exclusively parallel to the (001) cleavage.

Deformation is dominantly accommodated by shear on microcracks as opposed to opening and propagation of axial microcracks at all pressures. Histograms of frequency of cracked grains versus their orientation show that cracked grains are dominantly oriented >20° from σ_1, mostly between 30° and 60° (plots on left side of Figure 11). The weak lattice preferred orientation (LPO) of antigorite may contribute to the distribution of microcracks. However, normalized histograms demonstrate that the perentage of cracked grains in a particular orientation is higher at high angles to the shortening direction (center of Figure 11).

With increasing confining pressure the percentage of cracked grains increases and the anisotropy of crack orientation decreases. Both changes are associated with the transition from localized to distributed deformation. At P_c=50 and 200 MPa less than 20% of the grains are cracked, while at 750 MPa >35% of the grains are cracked, consistent with the transition from localized to distributed deformation shown in Figure 4b. This increase in microcrack density is also accompanied by a marked change in the orientation of the microcracks. In the lower-pressure samples (Figures 11a-c) microcracks are mostly

oriented parallel to the fault. In contrast, in the high-pressure run the microcracks are distributed symmetrically about 0° (Figure 11d).

Discussion

Non-dilatant brittle deformation by shear microcracking

The non-dilatant nature of brittle deformation of serpentinites is consistent with the observation that deformation is accommodated by shear microcracking. It is well documented that dilatant brittle deformation is associated with the opening of mode I (axial) microcracks [e.g., *Wong*, 1982]. However, significant axial microcracking is not observed in serpentinites even at confining pressures as low as 50 MPa (Figure 11). Because creation of void space along a shear crack is restricted to irregularities along the shear plane, this crack geometry is less effective in causing dilatancy than the opening of mode I microcracks.

Although limited dilation or compaction was detected in some runs, several lines of evidence suggest that volumetric strain measurements are influenced by inhomogeneous deformation associated with faulting. Strain measurements during and after localization are representative only of deformation in the vicinity of the strain gauges. Thus, volumetric strain behavior after strain localization is not known as it cannot be measured accurately with strain gauges. In addition, optical inspection of the jackets of 6 deformed samples (l-46, l-47, l-48, l-49, a-57, and l-58) shows that faults localized directly beneath one (l-46, l-47, l-48) or both of the strain gauges (l-49, a-57, l-58). Finally, stress-strain curves also provide evidence for fault-induced inhomogeneous strain. For example, the curve for l-55 (Figure 7b) indicates that apparent dilation is caused by a sudden decrease in radial strain

immediately prior to failure. This abrupt change is not accompanied by a similar change in the axial strain, as would be expected during homogeneous inelastic deformation.

The apparent compaction observed during some experiments on serpentinites cannot be attributed to pore collapse. Rocks with more than ~5% porosity (e.g., sandstones) may display compaction during the initial part of the loading cycle, but ultimately dilate when strain localization occurs [e.g., *Brace*, 1978; *Wong*, 1990]. In contrast, serpentinites show limited compaction or dilation immediately prior to failure. Examination of the starting materials using both optical and TEM microscopy demonstrates that the porosity of undeformed lizardite samples is <0.5%, and that the antigorite serpentinite samples have no resolvable porosity. In addition, deformed samples lack microstructures typical of pore collapse, such as damage zones around pores, or cracks originating at pores [e.g., *Hirth and Tullis*, 1989; *Wong,* 1990; *Zhang et al.*, 1990].

The lack of microstructural evidence for both pore collapse (compaction) and axial microcracking (dilation) indicates that the actual permanent volumetric strain in serpentinites is very small. The high values of c'/σ_{max} suggest that strain localization occurs immediately prior to failure, consistent with studies on granite and sandstone that demonstrate that strain localization occurs near σ_{max} [*Lockner et al.*, 1992; *Wong*, 1982]. Thus, the small amounts of dilatancy and/or compaction in serpentinites may reflect inhomogeneous strains associated with faulting and not volumetric strain associated with shear microcracking.

Brittle deformation regimes and implications for Mohr-Coulomb theory

Brittle deformation regimes can be defined by the operation of different deformation processes. For example, while this study shows that shear microcracking dominates

deformation of serpentinites, granite and quartzite show extensive axial microcracking at confining pressures less than ~750 MPa [e.g., *Wong*, 1982; *Hirth and Tullis*, 1994]. Similarly, while crystal plasticity does not appear to contribute to the deformation of serpentinites, it is an important process during room temperature deformation of calcite marble and mica-schist [e.g., *Fredrich et al.*, 1989; *Shea and Kronenberg*, 1992]. In the case of calcite marble, semi-brittle deformation occurs between P_c~30 MPa and P_c~300 MPa (brittle to semi-brittle and semi-brittle to plastic transitions, respectively). Mica schists show little or no pressure dependence of strength at P_c>200 [*Shea and Kronenberg*, 1992]. Although dislocation glide is the dominant deformation mechanism in mica schists, some brittle deformation microstructures such as voids and cracks associated with kinks are observed in the pressure-insensitive regime (200 MPa <P_c<500 MPa).

These different deformation regimes can be separated by plotting σ_y/σ_{max} versus c'/σ_{max} (Figure 12). The field labeled *Axial cracks* is characteristic of rocks in which deformation is accommodated by axial microcracking with no crystal plasticity (e.g., granite). Experimental data for granite plot at low values of c'/σ_{max} because permanent volumetric strain is achieved well before σ_{max}; in addition, significant yielding (as indicated by deviation of the stress-axial strain curve from linearity) does not occur in the mode I regime until microcracking substantially damages the sample. Thus, the stress-axial strain curves for granite indicate c'/σ_y <1. This observation demonstrates that axial stress-strain curves are not a sensitive indicator of the initiation of permanent deformation [e.g., *Brace et al.*, 1965]. In Figure 12 this situation is reflected by values of $\sigma_y/\sigma_{max} > c'/\sigma_{max}$.

Deformation in the *semi-brittle* regime is characterized by values of c'/σ_y >1 because the initial yielding is accommodated by plastic mechanisms including twinning or dislocation glide. For example, in calcite marble deformed in the semi-brittle regime, c'/σ_y

increases from ~1 to ~2 with increasing confining pressure from 50 to 300 MPa [*Fredrich et al.*, 1989]. As illustrated in Figure 12, semi-brittle deformation of marble is therefore characterized by $c'/\sigma_{max} > \sigma_y/\sigma_{max}$. At these conditions, the brittle component of deformation is accommodated mostly by axial microcracking. Thus, the calcite marble data plot at relatively low values of σ_y/σ_{max}.

The field labeled *shear cracks* in Figure 12 shows the unique behavior exhibited by the serpentinites. Both polytypes of serpentine have high values of c'/σ_{max} because brittle deformation is dominated by shear microcracking. In addition, the apparent lack of crystal plastic deformation is evident from values of $\sigma_y/\sigma_{max} \approx c'/\sigma_{max}$, in contrast to the data for calcite marble that show $c'/\sigma_{max} > \sigma_y/\sigma_{max}$. Consequently, serpentinites tend to plot at higher values of c'/σ_{max} and σ_y/σ_{max} than rocks that deform in the semi-brittle or Mode I (*Axial cracks*) regimes.

The Mohr failure envelopes in Figure 6a demonstrate that the pressure dependence of strength for serpentinite and granite are approximately the same at normal stresses greater than ~1000 MPa. For example, μ_i for granite decreases from ~0.8 to ~0.43 at , reaching a value relatively similar to the μ_i ~0.35 determined for antigorite and lizardite. Such a decrease in the pressure dependence of strength is often related to gradual enhancement of crystal plasticity with increasing pressure [e.g., *Paterson*, 1978]. Alternatively, this decrease may result from the enhancement of shear microcracking because such deformation requires less work against the confining pressure. This interpretation is supported by the lack of crystal plasticity in granite deformed at room temperature [e.g., *Tullis and Yund*, 1977]. In addition, a transition from axial to shear microcracking has previously been identified at P_c>600 MPa in quartz aggregates [*Hirth and Tullis*, 1994] and at P_c~1000 MPa at T<300°C in feldspar aggregates [*Tullis and Yund*, 1992].

The low pressure dependence of strength of serpentinites at $P_c < 200$ MPa (Figure 6a) is consistent with the observation that deformation is accommodated by shear microcracking at these conditions. We conclude that this behavior is primarily a manifestation of the relative ease of cracking on the (001) cleavage. Microstructural observations indicate that rupture and sliding along the (001) cleavage in serpentine grains oriented at high angles to σ_1 is easier than the opening of axial microcracks (Figure 11). These observations indicate that the fracture energy of the (001) cleavage in serpentinites is low compared with the cleavages of other minerals (e.g., feldspars).

The "brittle-ductile" transition

Three observations indicate that the transition from localized to distributed deformation in serpentinites corresponds to a change in deformation mechanism from brittle faulting to cataclastic flow. First, no conclusive evidence for crystal plastic deformation was found in any of the deformed samples. Second, both the maximum and the yield stress of both polytypes depend positively on pressure up to P_c~1 GPa. Third, numerous shear microcracks were present in samples deformed at the highest confining pressures. A transition from faulting to cataclastic flow is observed in feldspar aggregates, at P_c~500 MPa and T~300 °C [*Tullis and Yund*, 1992]. Microstructural observations indicate that cataclastic flow in feldspar is also accommodated by shear microcracks. However, unlike serpentinites, an increase in temperature is required to promote the transition to cataclastic flow.

A transition from localized to distributed deformation is often observed when the strength (σ_{max}) of a material becomes less than Byerlee's friction law [e.g., *Evans et al.*, 1990 and references therein]. The results on serpentinite indicate that, more generally, this criterion should incorporate the friction law derived for each rock type instead of Byerlee's

law. For example, while deformation of lizardite remains localized at stresses below that predicted by Byerlee's law at P_c between 100 and 200 MPa, the transition from faulting to cataclastic flow occurs at the crossover of σ_{max} and the friction law of lizardite (Figure 4c).

It is also commonly accepted and observed that fully plastic deformation occurs when the strength of a rock is less than the confining pressure (Goetze's criterion [e.g., *Evans et al.*, 1990; *Kohlstedt et al.*, 1995]). Although the strength of lizardite at P_c>300 MPa is approximately the same as the confining pressure (Figure 4b), no conclusive evidence for crystal plasticity has been found. The observation that the yield stress of these samples is less than the confining pressure (i.e., $\sigma_y<P_c$) therefore suggests that microcracks nucleated within the regime of assumed plastic deformation ($\sigma_{max}<P_c$). The low fracture strength of the (001) cleavage presumably allows the development of brittle deformation even when the applied differential stress is similar to or less than the confining pressure.

Rheology of shear zones and the tectonic evolution of oceanic lithosphere

The onset of dilatancy is often assumed to impart important controls on the mechanical behavior of fault zones in the presence of fluids [e.g., *Sleep and Blanpied*, 1992; *Lockner and Byerlee,* 1994; *Segall and Rice*, 1995]. In contrast, the lack of significant dilatancy during deformation of serpentinites may result in unique behavior. For example, such behavior would suppress dilatancy hardening. In addition, the geometry of microcracking in serpentinites might favor the confinement of fluids within the shear zone. Natural serpentinite shear zones commonly display a fabric with the (001) cleavage oriented parallel to the fault plane [e.g., *Harding,* 1987; *Norrell et al.*, 1989; *Hoogerduijn Strating and Vissers*, 1994]. Based on our microstructural observations (Figures 9-11) microcracks in such shear zones would be expected to form parallel to the grain boundaries and/or the (001) cleavage, and thus parallel to the fault plane. Although other variables must be

considered (e.g., temperature, high strain deformation and variations in strain rate), such a crack network could limit permeability perpendicular to the fault surface and perhaps increase permeability in directions parallel to the fault plane. Thus, elevated pore fluid pressure may be maintained during brittle deformation, and this, combined with the weak rheology of serpentinites, could significantly reduce the strength of serpentine-bearing faults.

The oceanic lithosphere may be substantially weakened when serpentinization occurs. The amount of weakening resulting from the alteration of stronger peridotite to weaker serpentinite depends on the degree of serpentinization of the mantle lithosphere, the serpentine polytype, and the maximum depth of serpentinization. The maximum strength of partially serpentinized peridotite appears to be comparable to that of serpentinite [*Brace et al.,* 1965]. Consequently, even small amounts of serpentinization of the mantle could substantially weaken the rock. Oceanic serpentinites, which are nearly all composed mostly of lizardite [e.g., *Aumento and Loubat*, 1971], are often dredged in the vicinity of the ridge axis of slow-spreading ridges [e.g., *Aumento and Loubat*, 1971; *Karson et al.*, 1987; *Bonatti and Michael*, 1989; *Dick,* 1989; *Tucholke and Lin*, 1994], indicating that serpentinization can occur in very young (<1 Ma) lithosphere at slow-spreading ridges. Therefore, tectonic processes along the walls of the axial valley and within transform faults may be controlled by the rheology of serpentinized peridotite, particularly in the vicinity of discontinuities at slow-spreading ridges, where the "magmatic" crust is thin, discontinuous or non-existent [e.g., *Lin et al.*, 1990; *Tolstoy et al.*, 1993; *Tucholke and Lin*, 1994; *Cannat et al.*, 1995].

Conclusions

Deformation experiments conducted on intact cores of serpentinite demonstrate that antigorite and particularly lizardite are weaker than other common lithospheric rocks. A transition from localized (faulting) to distributed (ductile) deformation occurs for both polytypes with increasing confining pressure at room temperature. In lizardite, this transition occurs at ~200-400 MPa, while in antigorite it is observed at ~400 MPa. Deformation in the ductile regime is accommodated by cataclastic flow. The transition from localized to distributed deformation in lizardite occurs at the crossover between the strength of intact lizardite and the friction law unique to lizardite. This observation emphasizes that the use of Byerlee's law to define the brittle-ductile transition must be done with caution.

Volumetric strain measurements indicate that brittle deformation of both serpentine polytypes is mostly non-dilatant. Microstructural observations show that microcracks form almost exclusively parallel to the (001) cleavage of individual serpentine grains. In addition, microcracks form dominantly at high angles to the shortening direction indicating that brittle deformation is accommodated mostly by shear microcracking, consistent with the observed lack of dilatancy. The low strength and low pressure dependence of strength of serpentinites can be attributed to this non-dilatant style of brittle deformation and a low fracture strength of the (001) cleavage. Mohr envelopes demonstrate that brittle deformation accommodated by shear microcracking displays a lower pressure dependence than that accommodated by axial microcracking.

The mechanical behavior of serpentinites can result in substantial weakening of fault zones in the oceanic lithosphere. The weak nature of serpentine, lizardite in particular, and the non-dilatant nature of brittle deformation can result in substantial weakening of serpentine-bearing faults relative to the surrounding country rock. In areas such as slow-

spreading ridges, serpentinization of the lithospheric mantle could play a major role on its tectonic evolution.

Acknowledgments. We are grateful to J. Hirst, S. Karner, A. Post, and G. Siddiqi for assistance during the experiments, and especially to H.J.B. Dick, P. Kelemen, N. Shimizu, J. Tullis, and R. Yund for generously allowing us to use their facilities. We thank H.J.B. Dick and T. Tullis for providing rock specimens. In addition, we would like to thank E. Hooft, G. Jaroslow, J. Lin, C. Marone, G. Siddiqi, D. Smith, B. Tucholke, J. Tullis, T. Tullis, and D. Yund for numerous helpful discussions, comments and suggestions. Finally, we thank J. Tullis for comments on the submitted manuscript, and A. Kronenberg, L. Reinen and G. Harper for their thoughtful reviews that helped us clarifying our arguments. The GMT software [*Wessel and Smith*, 1991] was extensively used. This work was supported by NSF grants OCE-9313812 and OCE 9314103. Woods Hole Oceanographic Institution contribution number 9167.

References

Aumento, F. and H. Loubat, The mid-Atlantic ridge near 45°N. Serpentinized ultramafic intrusions, *Can. J. Earth Sci.*, 8, 631-663, 1971.

Bonatti, E., Serpentinite protrusions in the oceanic crust, *Earth Planet. Sci. Lett.*, 32, 107-113, 1976.

Bonatti, E. and P. J. Michael, Mantle peridotites from continental rifts to ocean basins to subduction zones, *Earth Planet. Sci. Lett.*, 91, 297-311, 1989.

Brace, W. F., Some new measurements of linear compressibility of rocks, *J. Geophys. Res.*, 70, 5669-5678, 1965.

Brace, W. F., Volume changes during fracture and frictional sliding: A review, *Pure Appl. Geophys.*, 116, 603-614, 1978.

Brace, W. F. and D. L. Kohlstedt, Limits on lithospheric stress imposed by laboratory experiments, *J. Geophys. Res.*, 85, 6248-6252, 1980.

Brace, W. F., B. W. Paulding and C. Scholz, Dilatancy in the fracture of crystalline rocks, *J. Geophys. Res.*, 71, 3939-3953, 1965.

Brodie, K. H. and E. H. Rutter, On the relationship between deformation and metamorphism, with special reference to the behavior of basic rocks, in *Kinematics, textures and deformation*, eds. A. B. Thompson and D. Rubie, *Adv. Phys. Geochem.*, 4, 138-179, 1985.

Byerlee, J., Friction of rocks, *Pure Appl. Geophys.*, 116, 615-626, 1978.

Cannat, M., D. Bideau and H. Bougault, Serpentinized peridotites and gabbros in the Mid-Atlantic Ridge axial valley at 15°37'N and 16°52'N, *Earth Planet. Sci. Lett.*, 109, 87-106, 1992.

Cannat, M., Emplacement of mantle rocks in the seafloor at mid-ocean ridges, *J. Geophys. Res.*, 98, 4163-4172, 1993.

Cannat, M., C. Mével, M. Maia, C. Deplus, C. Deplus, C. Durand, P. Gente, P. Agrinier, A. Belarouchi, G. Dubuisson, E. Humler and J. Reynolds, Thin crust, ultramafic exposures, and rugged faulting patterns at the Mid-Atlantic Ridge (22°-24°N), *Geology*, 23, 49-52, 1995.

Caruso, L. J. and J. V. Chernosky, The stability of lizardite, *Can. Miner.*, 17, 757-769, 1979.

Chen, W. P. and P. Molnar, Focal depths of intracontinental and intraplate earthquakes and their implications for the thermal structure and mechanical properties of the lithosphere, *J. Geophys. Res.*, 88, 4183-4214, 1983.

Coleman, R. G., Petrological and geophysical nature of serpentinites, *Bull. Geol. Soc. Am.*, 82, 879-918, 1971.

Coulton, A. J., G. D. Harper and D. S. O'Hanley, Oceanic versus emplacement age serpentinization in the Josephine ophiolite: Implications for the nature of the Moho at intermediate and slow-spreading ridges, *J. Geophys. Res.*, 100, 22245-22260, 1995.

Deer, W. A., Howie, R. A. and Zussman, J., *An introduction to the rock-forming minerals*, 528 pp., Longman Group Limited, London, 1966.

Dengo, C. A. and J. M. Logan, Implications of the mechanical and frictional behavior of serpentinite to seismogenic faulting, *J. Geophys. Res.*, 86, 10,771-10,782, 1981.

Dick, H. J. B., Abyssal peridotites, very slow spreading ridges and ocean ridge magmatism, A. D. Saunders and M. J. Norry, *Magmatism in the Ocean Basins*, 71-105, 1989.

Dungan, M. A., Bastite pseudomorphs after orthopyroxene, clinopyroxene and tremolite, *Can. Miner.*, 17, 729-740, 1979.

Evans, B., J. T. Fredrich and T.-f. Wong, The brittle-ductile transition in rocks: Recent experimental and theoretical progress, in *The brittle-ductile transition in rocks, the Herd Volume, Geophys. Monograph Ser.,* vol. 56, edited by A. Duba, W. B. Durham, J. W. Handin, and H. Wang, pp. 1-20, AGU, Washington, D. C., 1990.

Fredrich, J. T., B. Evans and T.-f. Wong, Micromechanics of the brittle to plastic transition in Carrara marble, *J. Geophys. Res.*, 94, 4129-4145, 1989.

Gillis, K. M., G. Thompson and D. S. Kelley, A view of the lower crustal component of hydrothermal systems at the mid-Atlantic ridge, *J. Geophys. Res.*, 98, 19,597-19,619, 1993.

Gleason, G. C. and J. Tullis, A flow law for dislocation creep of quartz aggregates determined with the molten salt cell, *Tectonophys.*, 247, 1-23, 1995.

Haidinger, W, *Naturwissenschaftliche abhandlungen*, vol. 1-4, Wien, 1845.

Harding, D. J., Josephine peridotite tectonites: A record of upper mantle plastic flow, PhD thesis, 334 pp., Cornell University, Ithaca, N.Y., 1987.

Hess, H. H., History of ocean basins, in A. E. J. Engel, H. L. James and B. F. Leonard eds., *Petrological studies: a Volume in honor of A. F. Buddington*, 599-620, Geological Society of America, Boulder, Co., 1962.

Hirth, G., and J. Tullis, The effects of pressure and porosity on the micromechanics of the brittle-ductile transition in quartzite, *J. Geophys. Res.*, 94, 17,825-17,838, 1989.

Hirth, G. and J. Tullis, The brittle-plastic transition in experimentally deformed quartz, *J. Geophys. Res.*, 99, 11731-11747, 1994.

Hoogerduijn Strating, E. H. and R. L. M. Vissers, Structures in natural serpentinite gouges, *J. Struct. Geol.*, 16, 1205-1215, 1994.

Ito, E. and A. T. Anderson Jr., Submarine metamorphism of gabbros from the Mid-Cayman Rise: Petrographic and mineralogic constraints on hydrothermal processes at slow-spreading ridges, *Mineral. Petrol.*, 371-388, 1983.

Janecky, D. R. and W. E. Seyfried, Hydrothermal serpentinization of peridotite within the oceanic crust: Experimental investigations of mineralogy and major element chemistry, *Geochim. Cosmochim. Acta*, 50, 1357-1378, 1986.

Karson, J. A., G. Thompson, S. E. Humphris, J. M. Edmon, W. B. Bryan, J. B. Brown, A. T. Winters, R. A. Pockalny, J. F. Casey, A. C. Campbell, G. P. Klinkhammer, M. R. Palmer, R. J. Kinzler and M. M. Sulanowska, Along-axis variations in seafloor spreading in the MARK Area, *Nature*, 328, 681-685, 1987.

Kohlstedt, D. L., B. Evans and S. J. Mackwell, Strength of the lithosphere: Constraints imposed by laboratory experiments, *J. Geophys. Res.*, 100, 17587-17602, 1995.

Lin, J. and E. M. Parmentier, Mechanisms of lithospheric extension at mid-ocean ridges, *Geophys. J.*, 96, 1-22, 1989.

Lin, J., G. M. Purdy, H. Schouten, J. C. Sempere and C. Zervas, Evidence from gravity data for focused magmatic accretion along the Mid-Atlantic Ridge, *Nature*, 344, 627-632, 1990.

Lockner, D. A., J. D. Byerlee, V. Kuksenko, A. Ponomarev and A. Sidorin, 1992, Observations of quasistatic fault growth from acoustic emissions, in B. Evans and T.-F. Wong eds., *Fault mechanics and transport properties of rocks*, 3-31, Academic Press, San Diego, 1992.

Lockner, D. A. and J. D. Byerlee, Dilatancy in hydraulically isolated faults and the suppression of instability, *Geophys. Res. Lett.*, 21, 2353-2356, 1994.

Maltman, A. J., Serpentinite textures in Anglesey, North Wales, United Kingdom, *Geol. Soc. Amer. Bull.*, 89, 972-980, 1978.

Mares, V. M. and A. K. Kronenberg, Experimental deformation of muscovite, *J. Struct. Geol.*, 15, 1061-1075, 1993.

Mével, C., M. Cannat, P. Gente, E. Marion, J. M. Karson, and J. A. Auzende, Emplacement of deep crustal and mantle rocks on the west median valley wall of the MARK area (MAR, 23°N), *Tectonophys.*, 190, 31-53, 1991.

Mével, C. and M. Cannat, Lithospheric stretching and hydrothermal processes in oceanic gabbros from slow-spreading ridges, in *Ophiolite genesis and evolution of the oceanic lithosphere*, edited by Tj. Peters, A. Nicolas, and P. G. Coleman, pp. 293-312, Kluwer Academic Publishers, Sultanate of Oman, 1992.

Moody, J. B., An experimental study on the serpentinization of iron-bearing olivines, *Can. Miner.*, 14, 462-478, 1976.

Moore, D., D. A. Lockner, M. Shengli, R. Summers and J. D. Byerlee, Strength of serpentinite gouges to 200°C, *EOS Trans. AGU, 76* (46), Fall Meeting Suppl., 632, 1995.

Murrell, S. A. F. and I. A. H. Ismail, The effect of decomposition of hydrous minerals on the mechanical properties of rocks at high pressures and temperatures, *Tectonophys.*, 31, 207-258, 1976.

Neumann, G. A. and D. W. Forsyth, The paradox of the axial profile: Isostatic compensation along the axis of the Mid-Atlantic Ridge?, *J. Geophys. Res.*, 98, 17,891-17,910, 1993.

Norrell, G. T., A. Teixell and G. D. Harper, Microstructure of serpentine mylonites from the Josephine ophiolite and serpentinization in retrogressive shear zones, California, *Geol. Soc. Amer. Bull.*, 101, 673-682, 1989.

O'Hanley, D. S., J. V. Chernosky and F. J. Wicks, The stability of lizardite and chrysotile, *Can. Miner.*, 27, 483-493, 1989.

Paterson, M. S, *Experimental rock deformation. The brittle field*, 254 pp., Springer Verlag, Berlin, 1978.

Raleigh, C. B., and M. B. Paterson, Experimental deformation of serpentinite and its tectonic implications, *J. Geophys. Res.*, 70, p. 3965-3985, 1965.

Reinen, L. A., J. D. Weeks and T. E. Tullis, The frictional behavior of lizardite and antigorite serpentinites: experiments, constitutive models, and implications for natural faults, *Pure Appl. Geophys.*, 143, 318-358, 1994.

Reinen, L. A. and T. E. Tullis, Microstructural evidence of strain localization and distributed strain in serpentinite friction experiments, *EOS Trans. AGU, 76* (46), Fall Meeting Suppl., 560, 1995.

Sano, O., I. Ito and M. Terada, Influence of strain rate on dilatancy and strength of Oshima granite under uniaxial compression, *J. Geophys. Res.*, 86, 9299-9311, 1981.

Segall, P. and J. R. Rice, Dilatancy, compaction, and slip instability of a fluid-infiltrated fault, *J. Geophys. Res.*, 100, 22155-22171, 1995.

Shea, W. T. and A. K. Kronenberg, Rheology and deformation mechanisms of an isotropic mica schist, *J. Geophys. Res.*, 97, 15201-15237, 1992.

Shimada, M., A. Cho and H. Yukutake, Fracture strength of dry silicate rocks at high confining pressures and activity of acoustic emission, *Tectonophys.*, 96, 159-172, 1983.

Shimada, M. and A. Cho, Two types of brittle fracture of silicate rocks under confining pressures and their implications in the Earth's crust, *Tectonophys.*, 175, 221-235, 1990.

Sleep, N. and M. L. Blanpied, Creep, compaction and the weak rheology of major faults, *Nature*, 359, 687-692, 1992.

Tolstoy, M., A. J. Harding and J. A. Orcutt, Crustal thickness on the Mid-Atlantic ridge: Bull's eye gravity anomalies and focused accretion, *Science*, 262, 726-729, 1993.

Toomey, D. R., G. M. Purdy, S. C. Solomon, and M. H. Murray, Microearthquakes beneath the median valley of the Mid-Atlantic ridge near 23°N: hypocenters and focal mechanisms, *J. Geophys. Res.*, 90, 5443-5458, 1985.

Tucholke, B. E. and J. Lin, A geological model for the structure of ridge segments in slow-spreading ocean crust, *J. Geophys. Res.*, 99, 11937-11958, 1994.

Tullis, J. and R. Yund, The brittle-ductile transition in feldspar aggregates: an experimental study, *Fault mechanics and transport properties of rock*, B. Evans and T.-f. Wong eds., 89-117, Academic Press, 1992.

Ulmer, P. and V. Trommsdorff, Serpentine stability to mantle depths and subduction-related magmatism, *Science*, 268, 858-861, 1995.

Vernon, R. H., Relationship between microstructures and metamorphic assemblages, *Tectonophys.* 39, 439-452.

Wessel, P. and W. H. F. Smith, Free software helps map and display data, *Eos Trans. AGU*, 72 (41), 445-446, 1991.

Wicks, F. J. and E. J. W. Whittaker, Serpentine textures and serpentinization, *Can. Miner.*, 15, 459-488, 1977.

Wicks, F. J. and D. S. O'Hanley, Serpentine minerals: structures and petrology, S. W. Bailey, *Hydrous phyllosilicates (exclusive of micas)*, *Rev. Mineral*, 19, 91-167, 1988.

Wong, T.-f., Micromechanics of faulting in Westerly granite, *Int. J. Rock Mech. Min. Sci.*, 19, 49-64, 1982.

Wong, T.-f., Mechanical compaction and the brittle-ductile transition in porous sandstones, in R. J. Knipe and E. H. Rutter eds., *Deformation mechanisms, Rheology and Tectonics*, Geological Soc. Spec. Pub. 54, 111-122, 1990.

Zhang, J., T.-f. Wong and D. M. Davis, Micromechanics of pressure-induced grain crushing in porous rocks, *J. Geophys. Res.*, 95, 345-352, 1990.

Figure 1. Optical (crossed Nicols) and TEM micrographs (bright field) of undeformed antigorite (top) and lizardite (bottom). The foliation in antigorite (marked by arrows in a) is defined by bands of grains oriented parallel and perpendicular (bladed bands and veins, respectively) to the overall foliation. Lizardite is characterized by a mesh texture that surrounds zones of micritic material (c). The TEM micrographs of both serpentine polytypes show elongated grains, closed grain boundaries, no pre-existing open microcracks, and a high density of crystal defects (b and d).

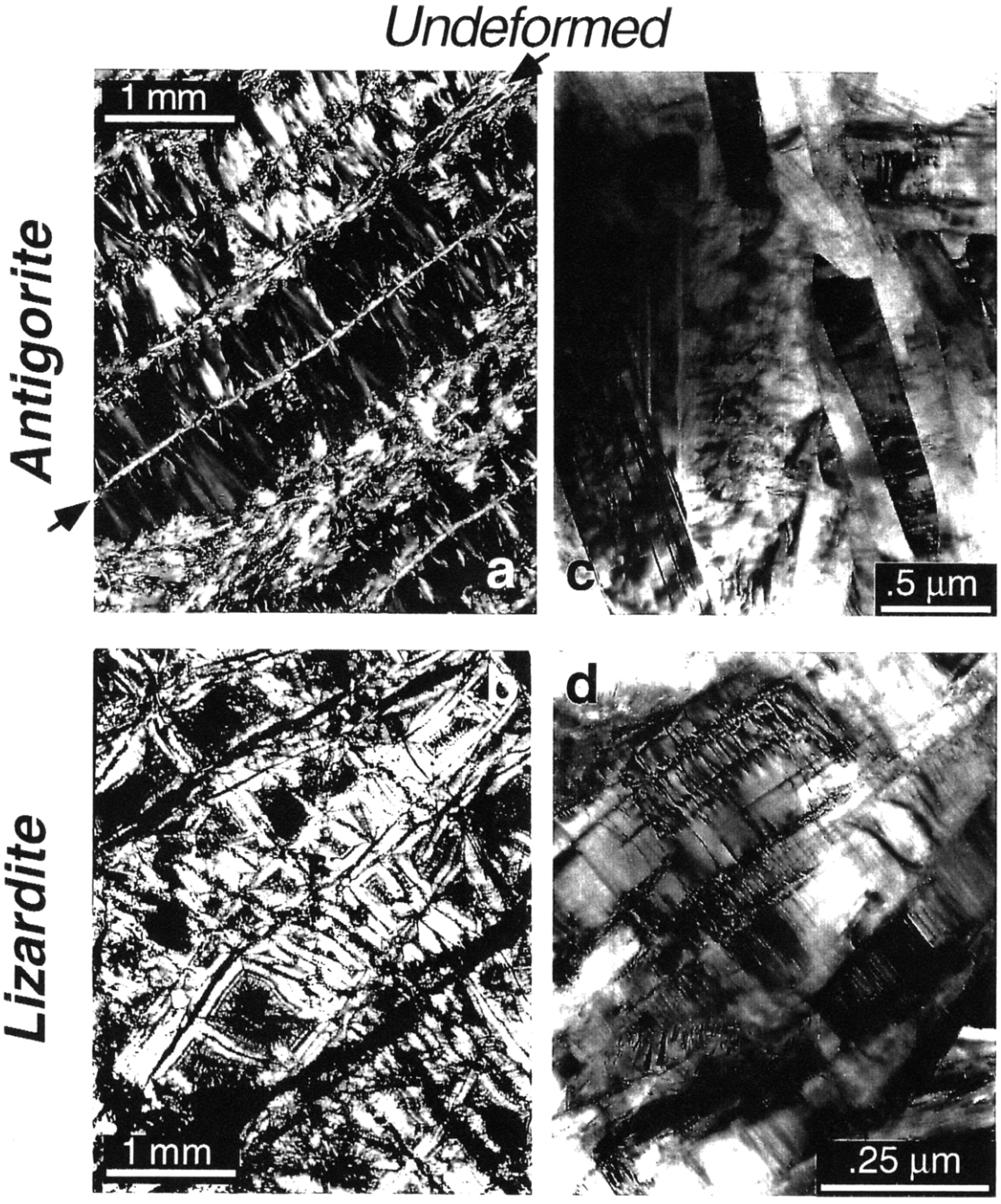

Figure 1, Escartin et al.

Figure 2. Lattice preferred orientation data for antigorite. (a) Histogram of the orientation of the trace of (001) from both the bladed bands (number of measurements n=65) and the veins (n=48) from a plane perpendicular to the foliation. The trace of the macroscopic foliation is shown by the black arrow. (b) A histogram of mineral orientations for the entire sample (n=129) shows that the mineral fabric on the whole is relatively weak. The 0° orientation is arbitrary.

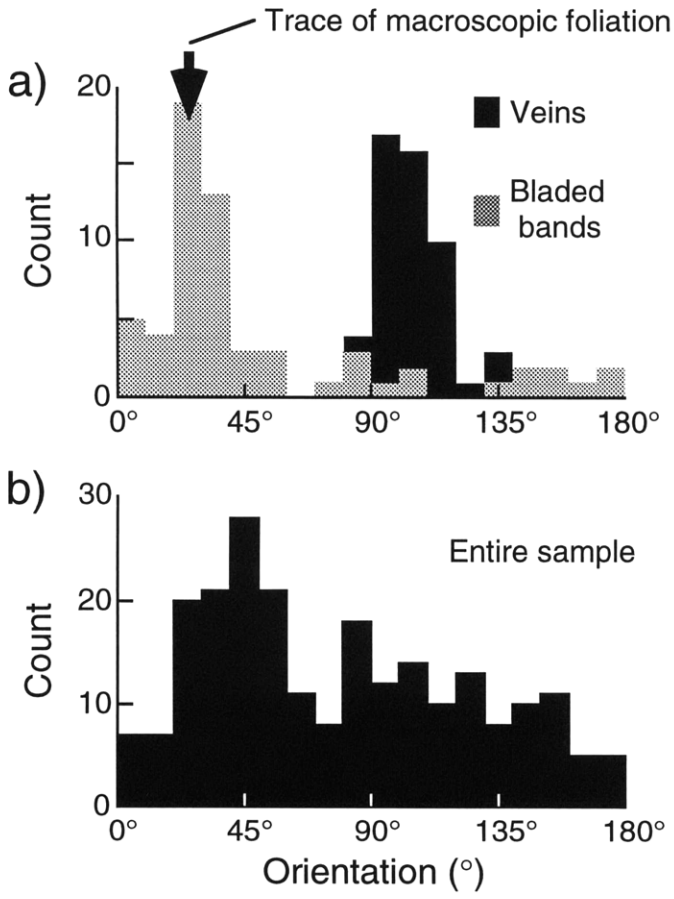

Figure 2, Escartín et al.

Figure 3. Differential stress (σ_1-σ_3) versus axial strain (ε_a) curves for antigorite (left) and lizardite (right) as a function of pressure. Figures (a) and (c) correspond to runs conducted in the gas rig at P_c<400 MPa (thin dots). Figures (b) and (d) correspond to runs conducted in the solid-medium rig at P_c>300 MPa (thick connected dots); a run from the gas rig has also been plotted in both (b) and (d) for comparison (at P_c=345 MPa and P_c=400 MPa, respectively). Both antigorite and lizardite show a positive pressure dependence of the maximum stress. The elastic modulus of antigorite measured from runs in the solid- and gas-confining medium apparatus are the same. The variability in the elastic properties of lizardite is larger than for antigorite, even among runs conducted in the same apparatus. The run at 60 MPa in (a) showed a sudden drop (faulting). The triangle in (c) indicates where confining pressure was increased slightly to maintain P_c~400 MPa. Curves are shown for runs a-24 (1000 MPa), a-25 (725 MPa), a-23 (325 MPa), a-17d (345 MPa), a-4c (195 MPa), a-16c (150 MPa), and a-09 (60 MPa) for antigorite, and from runs l-41 (950), l-53 (840 MPa), l-52 (700 MPa), l-61 (400 MPa), l-51 (300 MPa), l-54 (200 MPa), and l-43 (50 MPa) for lizardite. α is the angle between the shortening direction and the foliation (see Table 1).

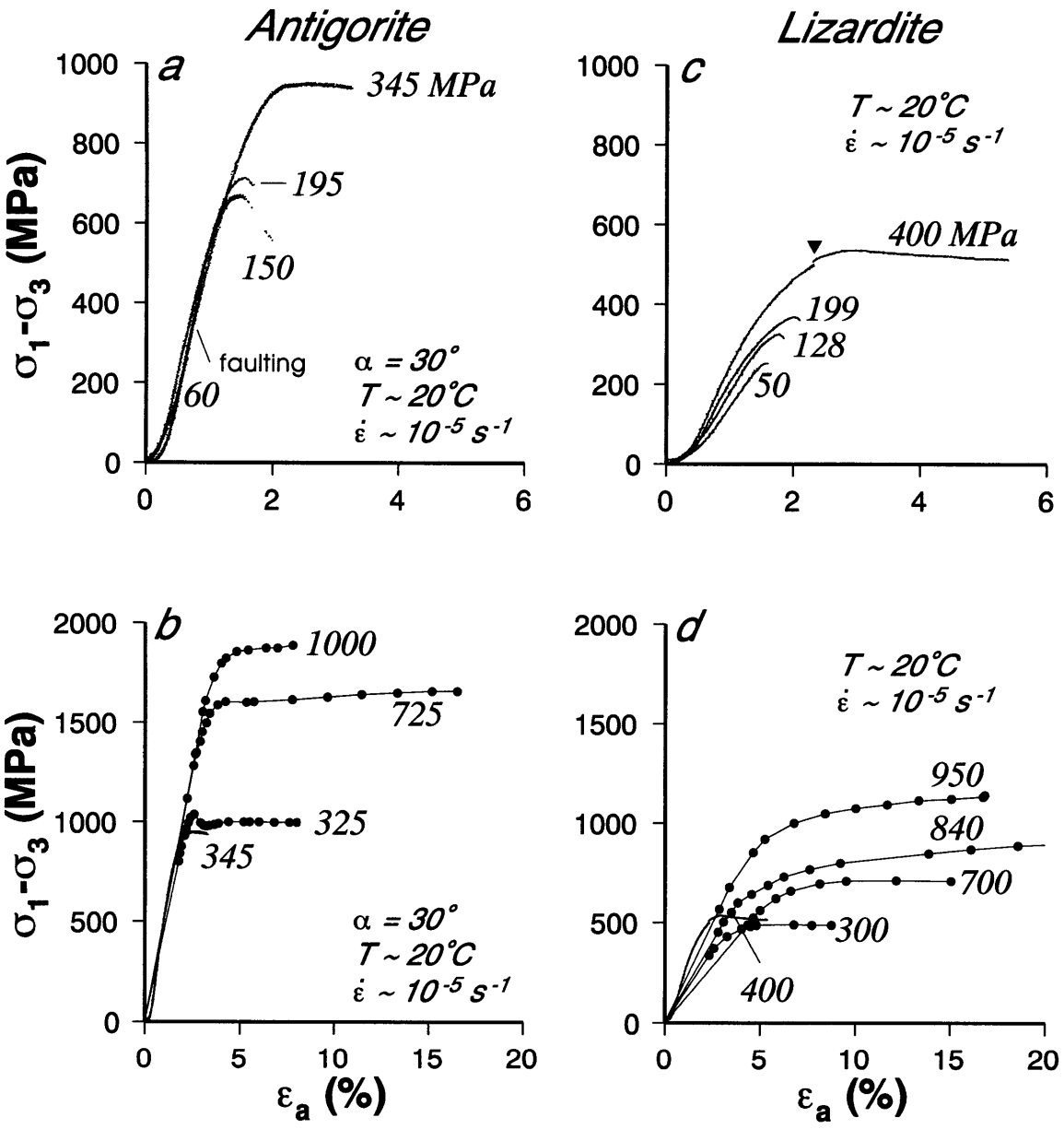

Figure 3, Escartin et al.

Figure 4. The yield stress σ_y (a) and maximum stress σ_{max} (b) in both antigorite and lizardite show positive pressure dependence for P_c up to 1 GPa. Lizardite is approximately a factor of 2 weaker than antigorite and shows a smaller pressure dependence of strength. The gray line in (a) and (b) corresponds to Goetze's criterion (σ_1-σ_3=σ_3). c) The transition from localized to distributed deformation is often observed when the strength of a material becomes less than Byerlee's friction law. However, the results in lizardite indicate that this criterion should incorporate the friction law derived for each rock type instead of Byerlee's law (line labeled BL in b and c). Upper and lower limits of the friction law of lizardite correspond to μ=0.3 [*Reinen et al.*, 1994] and μ=0.5 [*Dengo and Logan*, 1981] for lizardite serpentine gouges and bare surfaces, respectively.

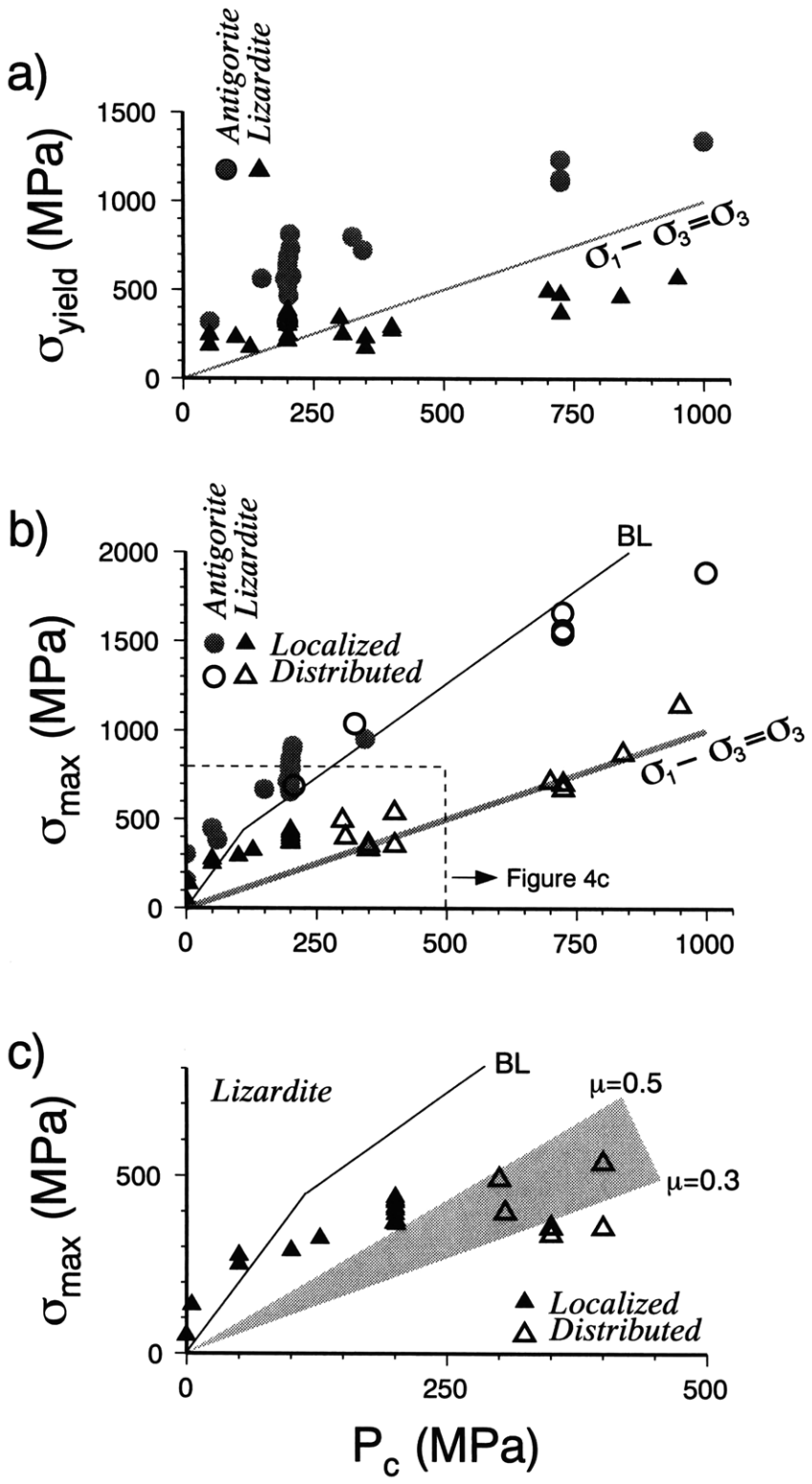

Figure 4, Escartin et al.

Figure 5. Mechanical anisotropy resulting from the macroscopic foliation in antigorite. Both the peak (σ_{max}, denoted as solid circles) and yield stress (σ_y, open circles) depend on the inclination of the foliation (see inset). Both σ_{max} and σ_y are lowest at $\alpha \approx 45°$. The variability in strength at any given orientation is ~150 MPa.

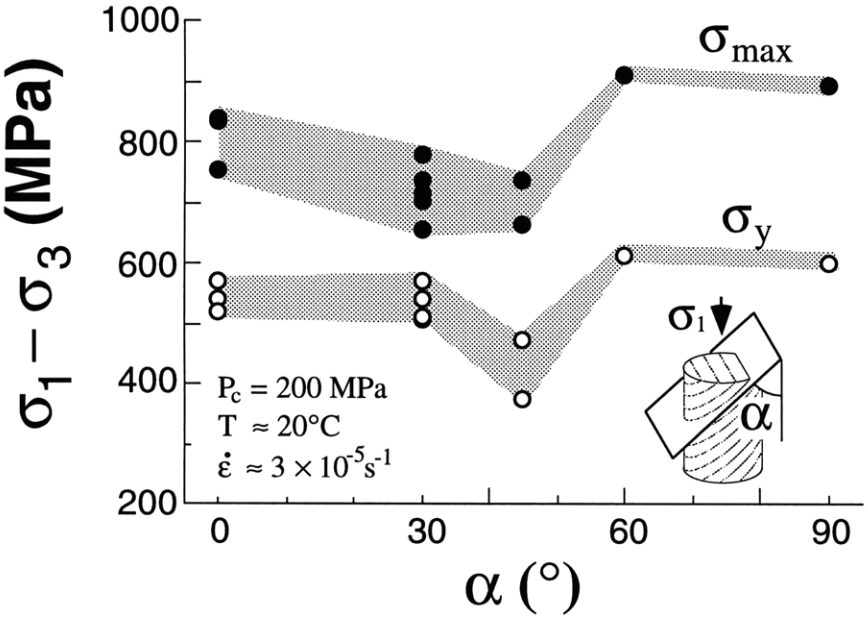

Figure 5, Escartín et al.

Figure 6. Mohr envelopes (a) and friction data (b) for lizardite and antigorite deformed at room temperature. (a) A comparison of Mohr envelopes for antigorite and lizardite serpentinite compared to Mohr envelopes derived from data on granite [*Brace et al.*, 1968] and dunite [*Shimada et al.*, 1983]. The coefficient of internal friction μ_i is given by the slope of the Mohr envelope. (b) Friction data from experiments on bare polished surfaces (open symbols [*Dengo and Logan*, 1981]) and fault gouge (solid symbols [*Reinen et al.*, 1994]) of antigorite and lizardite serpentinites. For comparison, Byerlee's law (BL) and a friction law for serpentinite with μ=0.35, corresponding to the coefficient of internal friction shown in (a), are also plotted.

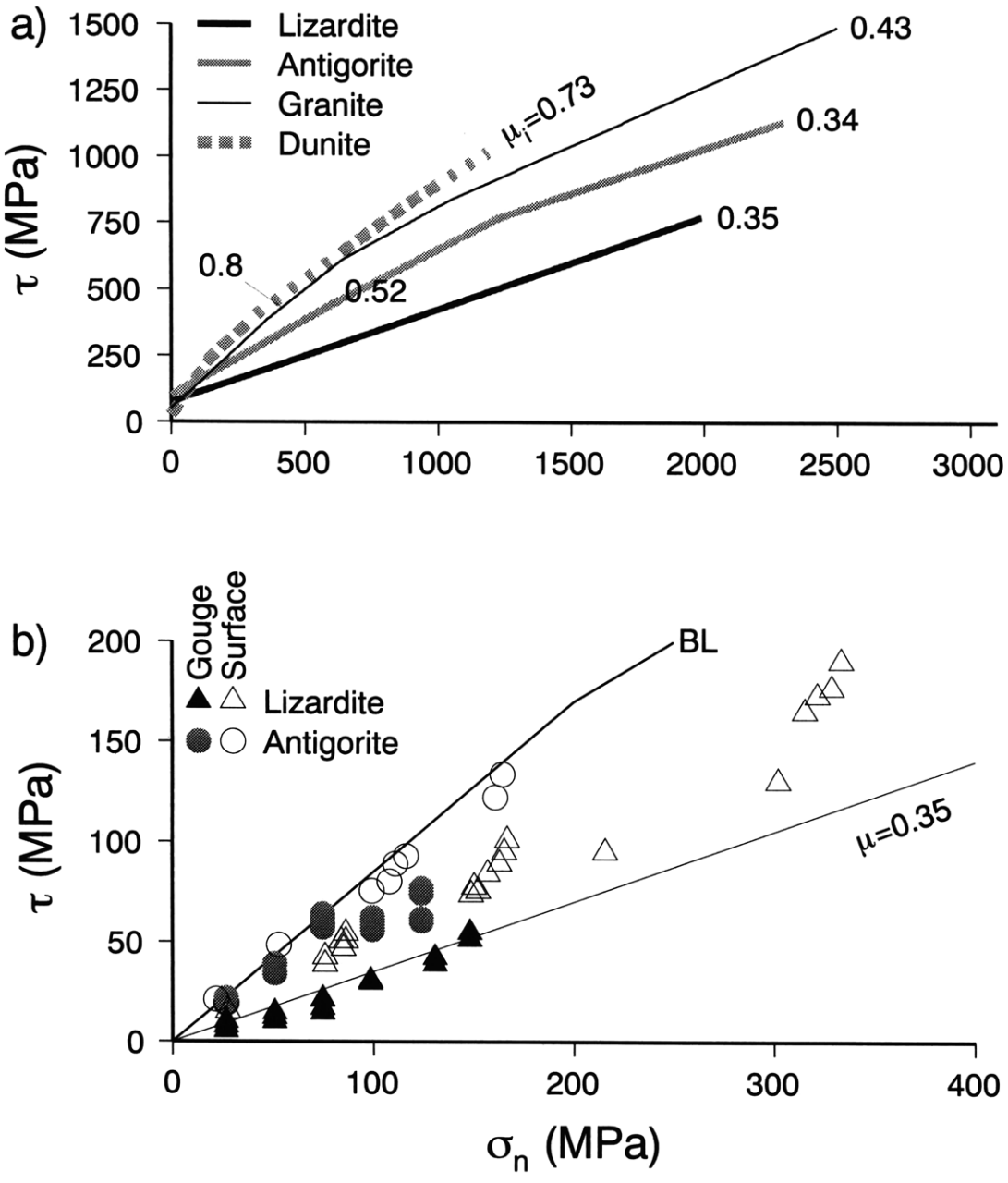

Figure 6, Escartin et al.

Figure 7. Stress versus volumetric strain curves. (a) Curves for experiments on antigorite. The finer connected dots correspond to axial (ε_a, positive) and radial strains (ε_r, negative), and the bold dots are the calculated volumetric strains ($\varepsilon_v=\varepsilon_a+2 \times \varepsilon_r$). The deviation from the linear trend of ε_v corresponds to the onset of dilatancy or compaction (c'). The magnitude of dilatancy or compaction ($\Delta\varepsilon_v$) is the difference between the observed volumetric strain and the elastic strain ε_e extrapolated along a line to σ_{max}. To facilitate comparison, individual curves are displaced laterally, and the calculated volumetric strain curves are plotted together on the right. The variability in the width of the curves is due to electronic noise. Although all experiments resulted in localized brittle deformation, little or no dilatancy was observed prior to failure. Curves are shown for runs a-57 (50 MPa), a-22 and a-38 (200 MPa). (b) Curves for experiments on lizardite; l-58 (50 MPa), l-55 and l-14 (200 MPa). The gray dots on the central curve indicate the end of successive loading and unloading cycles. (c) Comparison of ε_v observed for lizardite and antigorite (l-31 and a-37) to ε_v for Westerly granite (g-18) deformed at the same conditions (P_c=200 MPa, T~20°C). The magnitude of volume change is significantly smaller for serpentinite. In addition, c' for serpentinite (thin lines) occurs much later in the loading history. In this figure the differential stress has been normalized by σ_{max} to facilitate comparison. (d) Mean stress ($\sigma_m=[\sigma_1+\sigma_2+\sigma_3]/3$) versus curves for experiments conducted on lizardite and antigorite at P_c=200 MPa. The ε_v up to σ_m=200 MPa was measured during pressurization. The hydrostatic portion of the curve (large dots, σ_m <200 MPa) yields a bulk modulus similar to that determined during triaxial loading (fine dots, σ_m >200 Mpa).

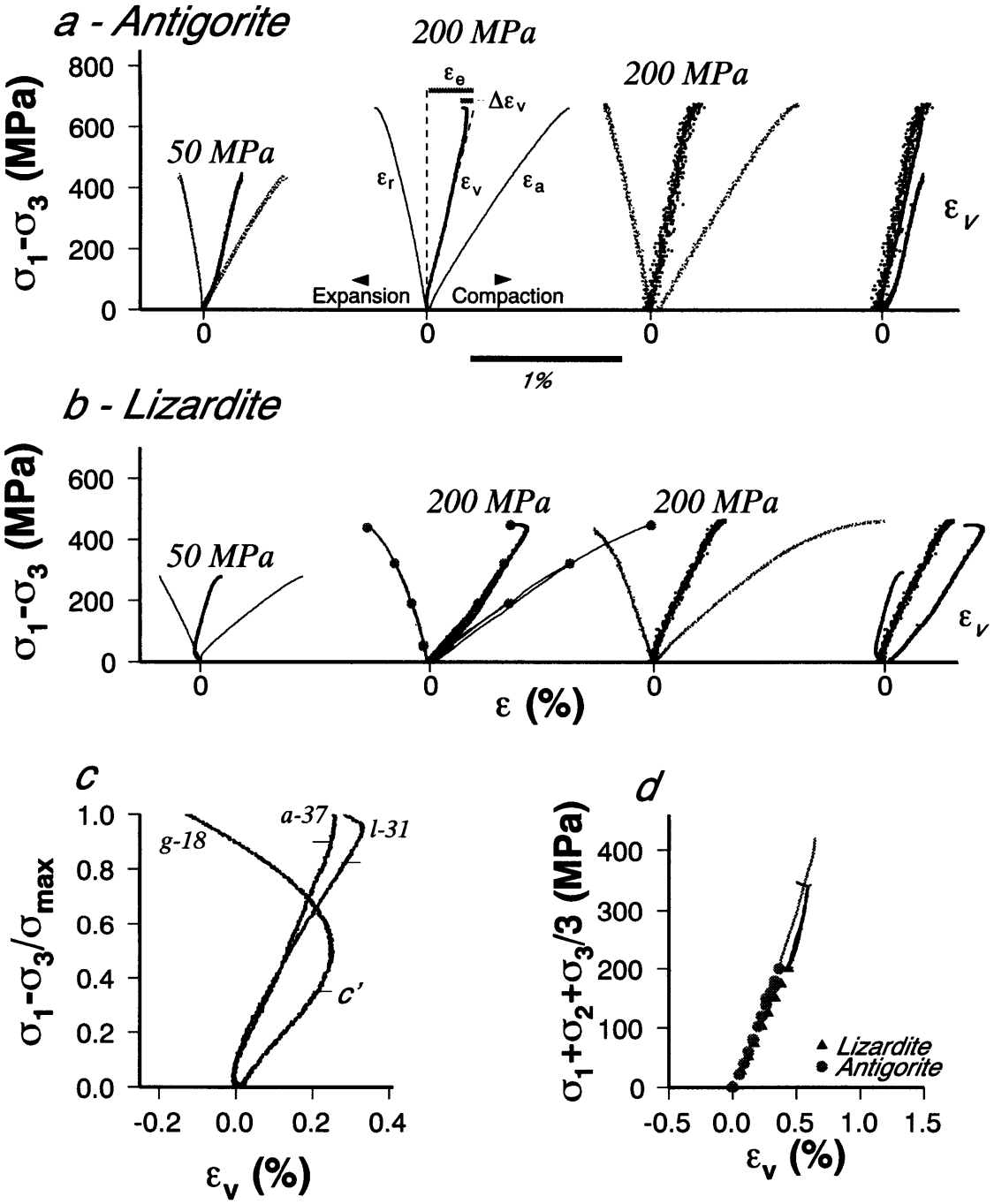

Figure 7, Escartin et al.

Figure 8. Volumetric strain data for serpentinite and other rocks. (a) Both serpentine polytypes display effectively non-dilatant behavior ($|\Delta\varepsilon_v|<0.2\%$), while granite, dunite and gabbro show $\Delta\varepsilon_v$ typically >0.2%. Aplite shows the smallest amount of dilatancy ($0<\Delta\varepsilon_v<0.25\%$) of the other crystalline rocks. Data for granite and aplite are from *Brace et al.* [1966], dunite and gabbro from *Shimada et al.* [1983]. (b) $\Delta\varepsilon_v$ normalized by the extrapolated elastic strain at failure (ε_e). (c) Plot of c'/σ_{max} versus P_c showing that dilation (or apparent compaction) of antigorite initiates very close to failure for both antigorite and lizardite; dilation occurs much earlier in the loading cycle for the other rocks.

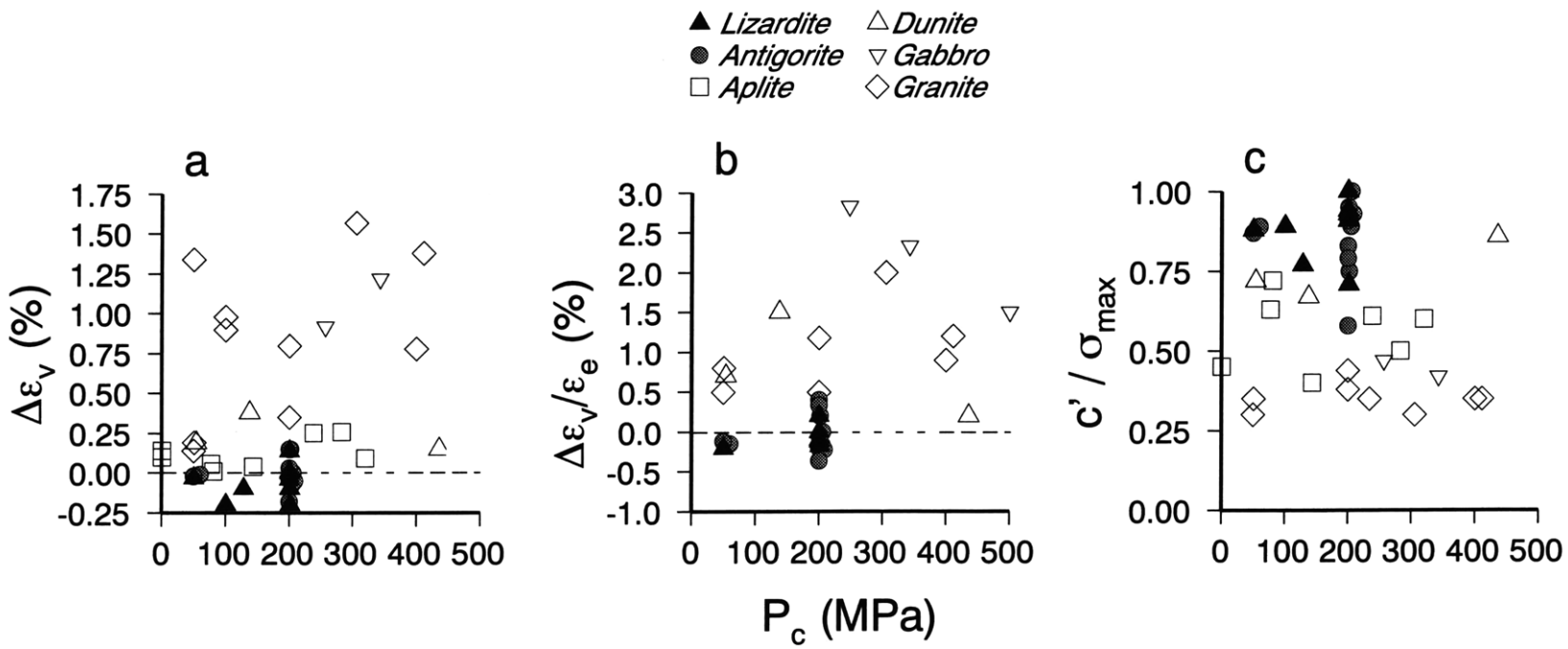

Figure 8, Escartin et al.

Figure 9. Microstructures of faulted samples of antigorite (a-c) and lizardite (d-f) deformed at low confining pressures. In the optical micrographs the same region is shown in both plane light and crossed Nicols. In all cases faults and microcracks follow zones of sub-parallel grains and/or grain boundaries. σ_1 (shortening direction) is vertical for all the optical micrographs. Cracks are at a high angle to σ_1 indicating that they are shear microcracks. TEM micrographs from areas adjacent to faults (c and f) demonstrate that microcracks (open arrows) form parallel to the (001) cleavage, and at high angles to the shortening direction (white arrow by scale bar). The micrographs correspond to samples a-7 (a-c), l-31 (d, e), and l-49 (f).

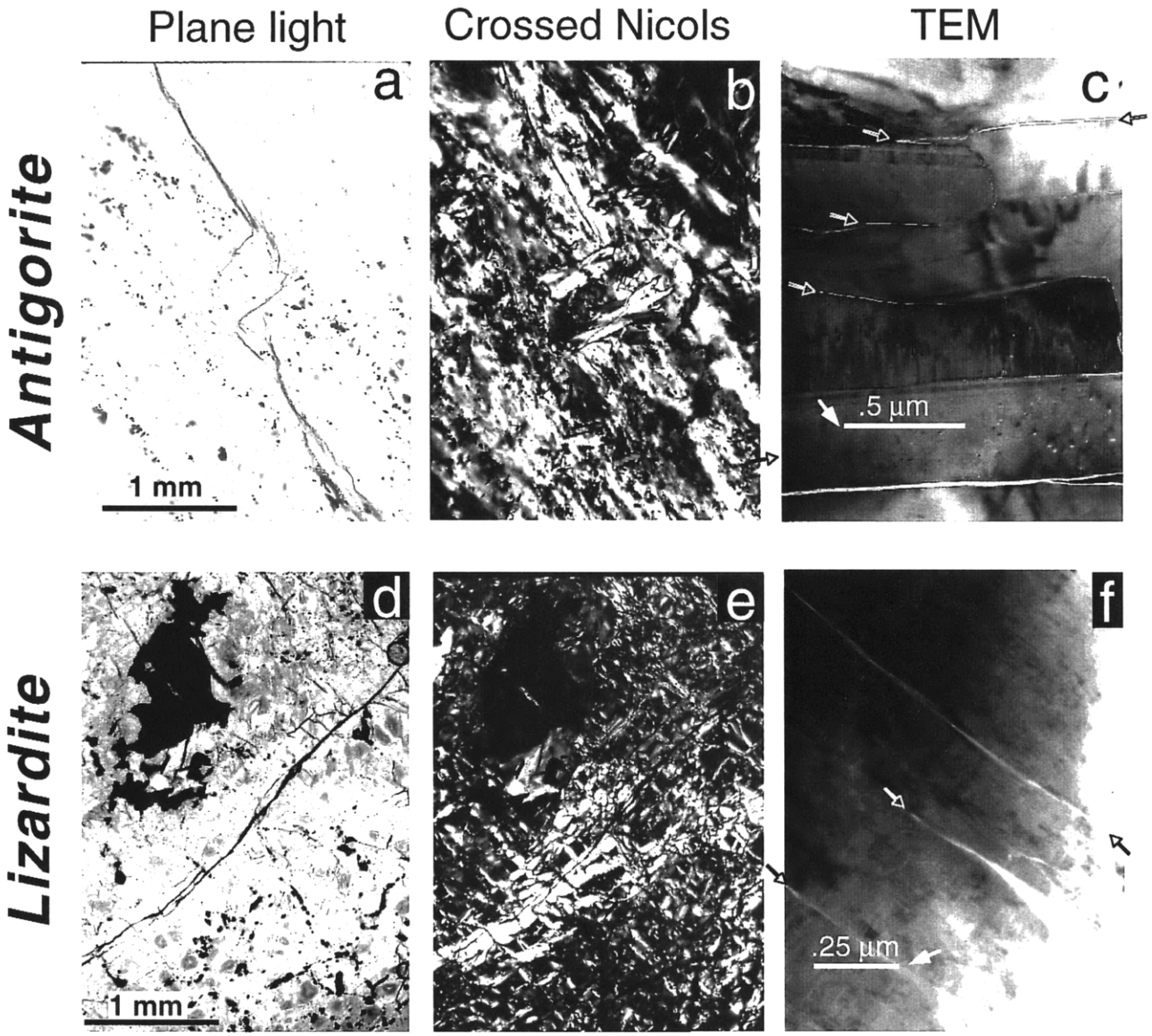

Figure 9, Escartín et al.

Figure 10. Microstructures of "ductile" samples of antigorite (a-c) and lizardite (d) deformed at high pressures. Although deformation was macroscopically ductile, the grain-scale microstructure is dominated by microcracks. Plane light and crossed Nicols optical micrographs of a grain-scale shear zone in antigorite (a and b) display numerous cracks in a zone ~0.2 mm wide. The cracks form parallel to the mineral cleavage, as confirmed by the TEM micrograph (c). Microcracks (open arrows) are at high angles to the shortening direction (white arrow by scale bar). Numerous cracks along grain boundaries and within grains are observed. Lizardite displays similar microstructures at the TEM scale (d); deformation is dominated by intragranular and grain boundary microcracks parallel to (001) cleavage. Microstructural observations did not show evidence for plastic deformation (microkinking, dislocation glide). The micrographs correspond to samples a-25 (a, b), a-24 (c), and l-39 (d). Compression direction in (a) and (b) is vertical.

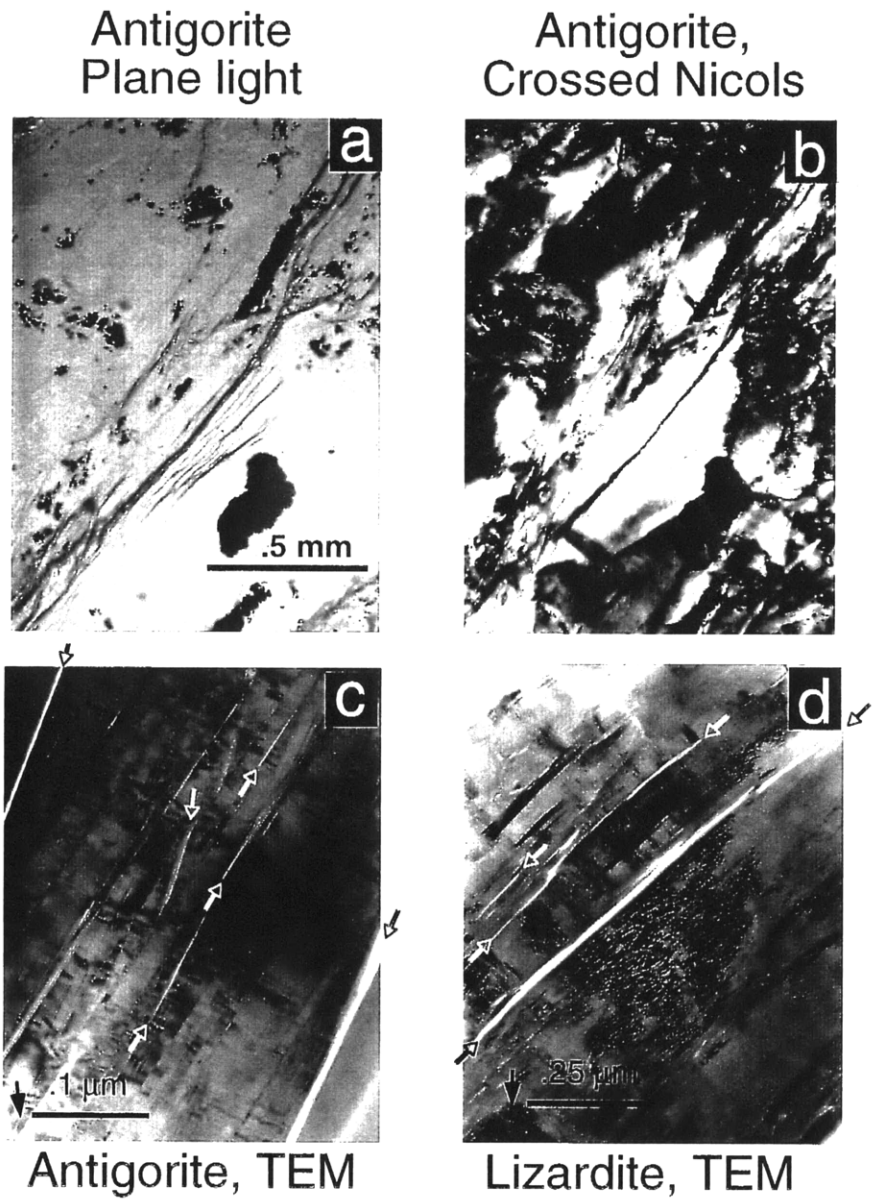

Figure 10, Escartín et al.

Figure 11. Histograms of the orientation of the (001) cleavage and cracks in deformed antigorite. The angle of the (001) cleavage of individual grains with respect to σ_1 is shown on the left (gray shading). The black shaded regions show the number and orientation of grains associated with either an intragranular or grain boundary crack. The percentage of cracked grains for each orientation bin is shown in the center. The orientation of cracks is plotted versus the orientation of the cleavage on the right. These data demonstrate that cracking occurs almost exclusively parallel to the (001) cleavage ($r^2>0.98$ in all cases). In each case the total number of measurements n and the number of cracked grains n_c are indicated. With increasing pressure (a to d) the total percentage of cracked grains increases, and the anisotropy in the orientation of the cracked grains decreases, consistent with a transition from localized to distributed deformation.

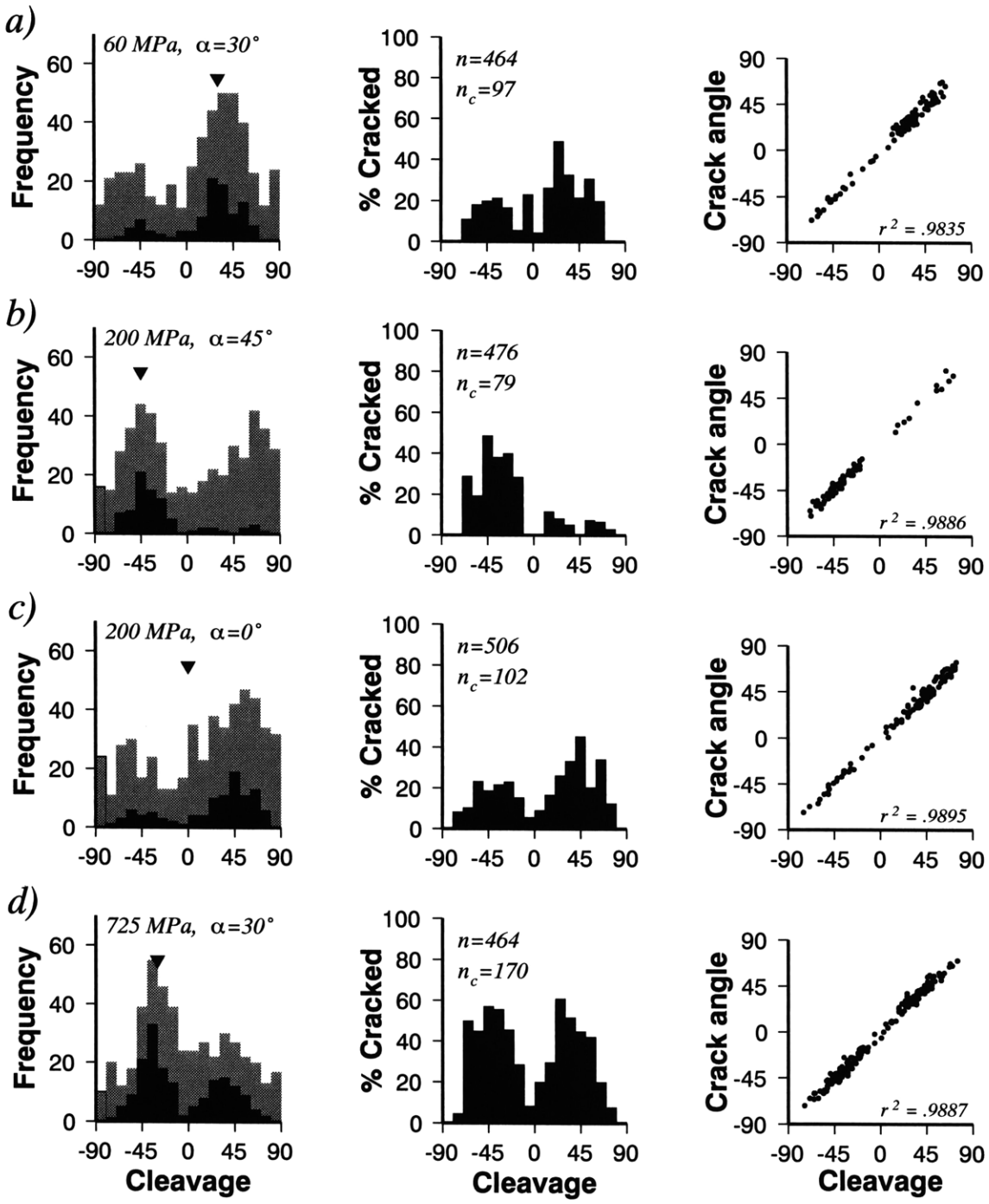

Figure 11, Escartin et al.

Figure 12. Plot of c'/σ_{max} versus σ_y/σ_{max} showing brittle deformation regimes defined by the mechanical response to the style of microcracking, and the activation of crystal plasticity. The field labeled *Axial cracks* is characteristic of rocks in which deformation is accommodated by axial microcracking with no crystal plasticity. Deformation in the *Semi-brittle* regime is characterized by values of $c'/\sigma_{max} > \sigma_y/\sigma_{max}$ because the initial yielding is accommodated by crystal plastic mechanisms. The field labeled *Shear cracks* shows the unique behavior exhibited by the serpentinites. Both polytypes have high values of c'/σ_{max} because brittle deformation is dominated by shear microcracking. In addition, the apparent lack of crystal plastic deformation is indicated by values of $\sigma_y/\sigma_{max} \approx c'/\sigma_{max}$.

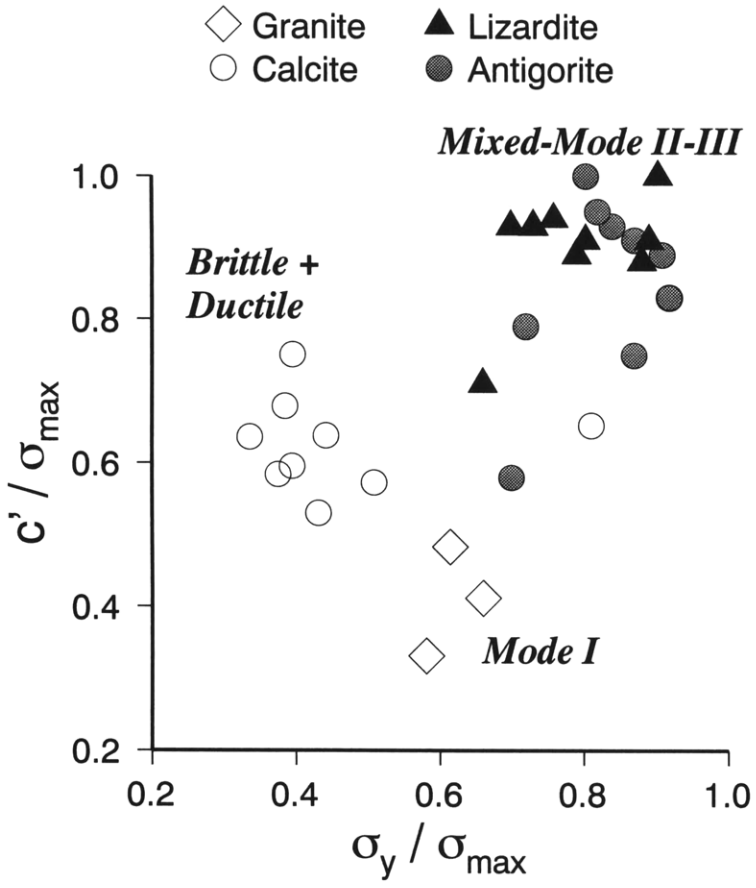

Figure 12, Escartin et al.

Table 1. Summary of symbols used

Symbol (units)	Definition
c' (MPa)	Differential stress at the onset of dilation
P_c (MPa)	Confining pressure
T (°C)	Temperature
α (°)	Angle between foliation and shortening direction
ε_a	Axial strain
ε_r	Radial strain
ε_v	Volumetric strain, $\varepsilon_v=\varepsilon_a+\varepsilon_r$
ε_e	Extrapolated elastic strain at failure
$\Delta\varepsilon_v$	Permanent volumetric strain, $\Delta\varepsilon_v=\varepsilon_v-\varepsilon_e$
μ	Coefficient of friction
μ_i	Coefficient of internal friction
σ_{max} (MPa)	Maximum or peak differential stress ($\sigma_1-\sigma_3$), "strength"
σ_n (MPa)	Normal stress
σ_{mean} (MPa)	Mean stress ($[\sigma_1+\sigma_2+\sigma_3]/3$)
σ_y (MPa)	Differential stress at yield point
τ (MPa)	Shear stress

Table 2. Summary of experimental conditions and results

Run*	P_c, MPa	ε, 10^{-5} s^{-1}¶	σ_{max}, MPa	σ_y, MPa	α, °	Regime, Apparatus§
Antigorite (VM3)						
a-1	200	34.63	335	317	30°	l, g
a-2	0	0.35	155	no yield	30°	a, g
a-3	200	3.77	662	584	30°	l, g
a-4	195	3.46	713	561	30°	l, g
a-5	200	3.46	704	577	30°	l, g
a-6	200	3.46	778	650	30°	l, g
a-7b	200	3.46	736	632	30°	l, g
a-8b	200	3.46	656	603	30°	l, g
a-9	60	3.46	382	*n.m.*	30°	l, g
a-10c	200	3.46	335†	328	30°	l, g
a-16c	150	3.46	670	563	30°	l, g
a-17d	345	3.46	952	724	30°	l, g
a-19	205	3.46	895	814	90°	l, g
a-20	206	3.46	913	734	60°	l, g
a-21d	202	3.46	786	684	45°	l, g
a-22d	208	3.46	688	578	30°	d, s
a-23	325	1.50	1038	799	30°	d, s
a-24	1000	1.50	1888	1341	30°	d, s
a-25	725	1.50	1660	1112	30°	d, s
a-28	725	1.50	1564	1126	30°	d, s
a-29	725	1.50	1541	1233	30°	d, s
a-30	200	3.46	809	566	0°	l, g
a-32c	202	3.46	832	466	0°	l, g
a-33c	201	3.46	838	687	0°	l, g
a-36	0	3.46	304	*n.m.*	0°	a, g
a-37b	200	3.46	656	590	45°	l, g
a-38b	200	3.46	735	529	45°	l, g
a-57	50	3.22	446	320	45°	l, g
Lizardite (AII60 5)						
l-12	200	3.46	393	322	none	l, g
l-14	200	3.46	441	354	none	l, g
l-34	350	1.50	335	231	none	d, s
l-35	350	1.50	356	174	none	d, s
l-39	725	1.50	671	369	none	d, s
l-40	725	1.50	701	477	none	d, s
l-41	950	1.50	1141	571	none	d, s
l-42	199	3.17	368	217	none	l, g
l-43	50	3.34	252	186	none	l, g
l-44	128	3.29	326	176	none	l, g

l-45	306	3.30	398	247	none	l, g
l-50	0	3.46	50	*n.m.*	none	a, g
Lizardite (AII60 9-10)						
l-46	200	3.13	413	211	none	l, g
l-47	201	3.21	375	334	none	l, g
l-51	300	1.50	491	339	none	d, s
l-52	700	1.50	712	491	none	d, s
l-53	840	1.50	871	462	none	d, s
l-55d	200	3.16	406	367	none	d, g
Lizardite (AII60 9-75)						
l-48	200	3.18	432	302	none	l,g
l-49	201	3.31	365	241	none	l, g
l-54d	200	3.26	427	324	none	l, g
l-58	50	3.22	278	245	none	l, g
l-59	100	3.22	291	230	none	l, g
l-60	5	3.26	137	*n.m.*	none	l, g
l-61	400	3.25	537	270	none	d, g
Lizardite (X)						
l-31b	200	3.46	441	384	none	l, g
Westerly Granite						
g-18	200	3.46	1096	638	none	l, g
g-26	0	3.46	124	*n.m.*	none	a, g
g-27	200	3.46	1008	655	none	l, g

* Runs for which volumetric data are available (table 2) are indicated in bold

¶ The bulk of the experiments were conducted at $\varepsilon \sim 10^{-5}\ s^{-1}$

† Run 10c faulted after yielding but prior to attaining the maximum stress

§ Deformation regime: a, axial splitting; l, localized deformation; d, distributed deformation; Apparatus: g, gas confining medium; s, solid confining medium. *n.m.*, not measured.

Table 3. Volumetric Strain Data

Material	Run	P_C (MPa)	c'/σ_{max}	$\Delta \varepsilon_v$ (%)†
Antigorite	a-8b	200	0.83	-0.04
	a-9	60	0.89	-0.10
	a-19	205	0.89	-0.07
	a-20	206	1.00	0.00
	a-21d	202	0.75	0.15
	a-22d	208	0.93	-0.05
	a-30	200	0.58	0.15
	a-33c	201	0.95	-0.04
	a-37b	200	0.91	0.03
	a-38b	200	0.79	-0.18
	a-57	50	0.87	-0.02
Lizardite	l-14	200	0.93	-0.04
	l-31	200	0.91	0.14
	l-46	200	not measured	-0.10
	l-47	201	0.91	-0.10
	l-48	200	0.93	-0.10
	l-49	201	0.71	-0.20
	l-54	200	0.94	0.10
	l-55	200	1.00	0.00
	l-58	50	0.88	-0.03
	l-59	100	0.89	-0.20
Westerly granite	g-18	200	0.38	0.80
	g-27	200	0.44	0.35

† Difference between measured and extrapolated elastic volumetric strain at failure

Chapter 6

CONCLUSIONS

The morphology of the seafloor and the structure of the oceanic crust formed at slow-spreading centers are controlled by tectonic extension along the walls of the rift valley, in addition to magmatic accretion at the ridge axis. The crust at the ridge axis is thicker and shallower at the segment centers than at the ends [*Kuo and Forsyth*, 1988; *Lin et al.*, 1990; *Tolstoy et al.*, 1993; *Detrick et al.*, 1995]. Analyses of bathymetry and gravity data in Chapters 2 and 3 show that this structure is not carried off-axis, and is lost within the first 2.5 Ma, along the walls of the axial rift valley. Off-axis the shallowest seafloor is found at the inside corners of ridge-offset intersections, and coincides with the thinnest crust. The thickest crust remains at the center of segments, which are no longer the shallowest terrain. These patterns result in a marked across-axis asymmetry in gravity between inside- and outside-corner terrain at the end of segments, which is supported by seismic determinations of crustal structure [*Wolfe et al.*, 1995].

The results in Chapters 2 and 3 have two main implications. First, tectonic extension varies substantially along the length of individual ridge segments. Inside corner terrain is more elevated and thinned tectonically than outside corner terrain, suggesting that tectonic extension is largest at inside corners. Inside corners are more seismically active than other sections of a slow-spreading ridge segments [e.g., *Francis et al.*, 1978; *Rowlett*, 1981; *Barclay et al.*, 1993; *Wolfe et al.*, 1995], supporting this interpretation. The asymmetry is larger near transform offsets than in the vicinity non-transform offsets. This observation implies that the amount of tectonic extension at inside corners may be enhanced in the vicinity of well-defined strike-slip faults with respect to zones of more diffuse accommodation of slip motion, such as non-transform offsets. Secondly, the crustal structure magmatically emplaced within the rift valley floor is strongly tectonized, and its overall geometry is modified along the rift valley walls. This implies that the large-scale seafloor morphology off-axis is primarily a record of tectonic extension and uplift of the

crust. The signature of focused magmatic accretion only remains visible in the gravity structure, in the form of thicker crust at the center of segments, and not in the bathymetry.

Off-axis bathymetry data reveal the migration, growth and shortening of ridge segments [e.g., *Schouten et al.*, 1987; *Gente et al.*, 1995; *Tucholke et al.*, 1996]. The traces of transform and non-transform offsets in the bathymetry are marked in the first case by a transform valley, and in the second case by a zone of irregular basins, both flanked by elevated inside-corner terrain. Free-air gravity maps derived from satellite altimetry data [*Smith and Sandwell*, 1995] clearly reflect the topography of the basement, providing a basin-wide view of the history of segmentation. The analysis of these patterns of ridge segmentation in Chapter 4 provides constraints on the processes responsible for the patterns of ridge segmentation, and on the forces driving the propagation of ridge segments. The variability or "roughness" of the gravity data characterizes the pattern of segmentation, and is dominated primarily by the obliquity of the ridge with respect to the direction of plate spreading, and secondarily by the influence of hot spots. Sections of the ridge that are oblique to the direction of spreading, such as the central Atlantic, are rougher than portions of the ridge that are subperpendicular, such as the Azores Platform. A decrease in roughness is also observed along the oblique Reykjanes Ridge as a consequence of the Iceland hot spot. However, this hot spot effect is not observed, along the ridge near the smaller Azores hot spot, or on the central Atlantic hot spots.

The migration of segments along the ridge axis is driven primarily by regional bathymetric gradients associated with hot spot swells. About three-quarters of the offsets that propagate migrate down the bathymetry gradients, as a consequence of stress concentration at the tip of segments. The lack of correlation between gradients and propagation rates, the stability of some segments, and the propagation up gradient of one quarter of the migrating offsets demonstrate that factors other than the regional bathymetric gradient affect segment propagation. Variations in the strength of the lithosphere may

cause the decorrelation between ridge offset propagation rate and regional gradients, and small plate motion changes may drive segment propagation up regional gradients. The important effect of the mechanical properties of the lithosphere on segment propagation is demonstrated by the correlation between offset length, propagation rate, and the life span of offsets. Most non-transform offsets with offset lengths <25 km migrate along the ridge axis, while transform offsets remain stable. Transform offsets live longer (>50±30 Ma) than non-transform offsets (27±11 Ma). The transition from transform to non-transform offsets occurs at 20-40 km.

Both tectonic extension along the length of a ridge segment and propagation of individual ridge segments along the axis are strongly controlled by the strength of the oceanic lithosphere. It is commonly assumed that the strength of the lithosphere can be described using a strength envelope defined by a) Byerlee's friction law in the brittle domain, and b) the flow laws of wet diabase [*Shelton and Tullis*, 1981] and olivine [e.g., *Chopra and Paterson*, 1981] for the plastic crust and mantle, respectively. This lithospheric rheology has been used in numerous numerical models to explain morphology and fault variations along the length of ridge segments [e.g., *Neumann and Forsyth*, 1993; *Shaw and Lin*, 1996]. However, the rheology of the oceanic lithosphere is not so simple, and numerous other rock types such as the alteration products of gabbro, diabase, and peridotite are ubiquitous. In addition, the rheology of dry diabase [*Mackwell et al.*, 1994], which is almost as strong as that of olivine, may be more appropriate to model unaltered crust than that of wet diabase. Chapter 5 provides new mechanical data on the rheology and behavior of serpentinites. Serpentinites are widely found on the seafloor, particularly near discontinuities and over inside-corner terrain (see *Tucholke and Lin* [1994] and references therein). Their presence can strongly result in systematic variations of lithospheric rheology along individual ridge segments, and thus control the style of faulting

along the segment, and the formation of tectonically uplifted inside-corner terrain; it is on these areas where serpentinites are most commonly found.

Serpentinites display a behavior that differs substantially from other rocks. First, serpentinites are substantially weaker than other rock types deformed in the brittle regime. The measured coefficient of internal friction is ~0.3, substantially lower than that measured in granite or dunite. The absolute strength of serpentinites is also approximately half of that of olivine or granite. Second, brittle deformation is non-dilatant, instead of the typical dilatant behavior displayed by other rocks. Third, deformation is accommodated by shear microcracks rather than axial microcracks. This mode of deformation favors the entrapment of fluids on fault planes, and could maintain elevated pore fluid pressures during brittle deformation, thus favoring very low effective confining pressures. The combined mechanical properties of serpentinites, the style of deformation, and the possibly low effective confining pressures (elevated pore fluid pressures) favor the formation of extremely weak faults. These weak faults may localize strain very efficiently, and considerably weaken the oceanic lithosphere in slow-spreading ridges.

The presence of serpentinites may explain the systematic variations in faulting patterns observed along individual ridge segments. Normal faults tend to be more linear at the center of segments than at the ends [*Sempéré et al.*, 1990; 1993; *Shaw*, 1992; *Cannat et al.*, 1995], and their throw and spacing also increases from the center towards the ends [*Shaw*, 1992; *Shaw and Lin*, 1993; *Tucholke and Lin*, 1994]. The presence of serpentinites at the end of segments will favor the formation of weak faults, the localization of strain, and could facilitate displacement along low-angle normal faults. This interpretation is consistent with the large throws observed at segment ends [e.g., *Shaw*, 1992], particularly at inside corners [e.g., *Tucholke and Lin*, 1994], and with the possible presence of low angle normal faults at these locations [e.g., *Dick*, 1981; *Karson and Dick*, 1983], as suggested in Chapter 2 by the fault models and the data. Near the center of segments

serpentinites may not be present, as the crust may be continuous with no peridotite outcrops [*Cannat et al.*, 1995]. At these locations faults may not be as weak as when serpentinites are present, and result in a more distributed deformation along numerous faults with small fault spacing. This interpretation is an alternative to that proposed by *Shaw* [1992] and developed by *Shaw and Lin* [1993]. These authors suggested that along-axis changes in faulting style reflect the strengthening of the lithosphere from segment centers towards discontinuities, due to the combined effect of thinning of weak crust and thickening of strong mantle lithosphere. As has been discussed earlier, the crust may not be as weak as expected, and the presence of other rocks such as serpentinites may strongly control the rheological structure of the lithosphere.

Numerous outstanding questions relevant to the processes associated with ridge segmentation remain to be answered. First, although elevated inside corner terrain appears to be tectonically uplifted, the mechanism responsible for such uplift is not understood. The proximity of these features to both transform and non-transform ridge-offset discontinuities suggests that the processes must be related to the dynamics of ridge-offset intersections, but the details of these interactions require further analysis. Second, it is necessary to determine whether the variations in crustal thickness along the ridge axis are caused by focused mantle upwelling or by focusing of the melt extraction in the asthenosphere or lithosphere. The composition and thermal structure, and therefore the strength of the oceanic lithosphere will the be controlled by these processes of focused magmatic accretion. Third, additional work on the rheology of different rock types and the implementation of more realistic rheological models is required to properly model the oceanic lithosphere and accurately predict its tectonic evolution. A re-evaluation of the simple olivine-wet diabase lithosphere model is then needed. Implementation of these new rheological models cannot be done without new data on the rheology of other common oceanic rock types, such as partially serpentinized peridotites, partially molten gabbro, and

amphibolites. Such models also require better understanding of the relative abundance, distribution, and geometry of the different rock types throughout the oceanic lithosphere.

References

Barclay, A., D. R. Toomey, G. M. Purdy, and S. C. Solomon, FARA microearthquake experiments III: Results fro the Mid-Atlantic Ridge at 35°N (abstract), *EOS Trans. AGU*, 74, 601, 1993.

Cannat, M., C. Mével, M. Maia, C. Deplus et al., Thin crust, ultramafic exposures, and rugged faulting patterns at the Mid-Atlantic Ridge (22°-24°N), *Geology*, 23, 49-52, 1995.

Chopra, P. N., and M. S. Paterson, The experimental deformation of dunite, *Tectonophysics*, 78, 453-473, 1981.

Detrick, R. S., H. D. Needham and V. Renard, Gravity anomalies and crustal thickness variations along the Mid-Atlantic ridge between 33°N and 40°N, *Journal of Geophysical Research*, 100, 3767-3787, 1995.

Dick, H. J. B., W. B. Thompson and W. B. Bryan, Low angle faulting and steady-state emplacement of plutonic rocks at ridge-transform intersections, *EOS Trans. AGU*, 62, 406, 1981.

Francis, T. J. G., I. T. Porter, and R. C. Lilwall, Micoearthquakes near the eastern end of St. Paul's Fracture Zone, *Geophys. J. R. Astron. Soc.*, 53, 201-217, 1978.

Gente, P., R. A. Pockalny, C. Durand, C. Deplus et al., Characteristics and evolution of the segmentation of the Mid-Atlantic Reidge between 20°N and 24°N during the last 10 million years, *Earth and Planetary Science Letters*, 129, 55-71, 1995

Karson, J. A. and H. J. B. Dick, Tectonics of ridge-transform intersections at the Kane Fracture Zone, *Marine Geophysical Researches*, 6, 51-98, 1983.

Kuo, B. Y. and D. W. Forysth, Gravity anomalies of the ridge-transform system in the South Atlantic between 31 and 34°S: Upwelling centers and variations in crustal thickness, *Marine Geophysical Researches*, 10, 205-232, 1988.

Lin, J., G. M. Purdy, H. Schouten, J. C. Sempere, and C. Zervas, Evidence from gravity data for focused magmatic accretion along the Mid-Atlantic Ridge, *Nature*, 344, 627-632, 1990.

Neumann, G. A. and D. W. Forsyth, The paradox of the axial profile: Isostatic compensation along the axis of the Mid-Atlantic Ridge?, *Journal of Geophysical Research*, 98, 17891-17910, 1993.

Rowlett, H., Seismicity at intersections of spreading centers and transform faults, *Journal of Geophysical Research*, 86, 3815-3820, 1981.

Schouten, H., H. J. B. Dick and K. D. Klitgord, Migration of mid-ocean ridge volcanic segments, *Nature*, 326, 835-839, 1987.

Sempere, J. C., G. M. Purdy and H. Schouten, Segmentation of the Mid-Atlantic Ridge between 24°N and 30°40'N, *Nature*, 344, 427-431, 1990.

Sempere, J. C., J. Lin, H. S. Brown, H. Schouten et al., Segmentation and morphotectonic variations along a slow-spreading center: the Mid-Atlantic Ridge (24°N - 30°40'N), *Marine Geophysical Researches*, 15, 153-200, 1993.

Shaw, P. R., Ridge segmentation, faulting and crustal thickness in the Atlantic Ocean, *Nature*, 358, 490-493, 1992.

Shaw, P. R. and J. Lin, Causes and consequences of variations in faulting style at the Mid-Atlantic Ridge, *Journal of Geophysical Research*, 98, 1839-21851, 1993.

Shaw, W. J. and J. Lin, Models of ocean ridge lithospheric deformation: dependence on crustal thickness, spreading rate, and segmentation, *Journal of Geophysical Research*, in press, 1996.

Shelton, G. and J. Tullis, Experimental flow laws for crustal rocks (abstract), *EOS Trans. AGU*, 62, 396, 1981.

Smith, W. H. F. and D. T. Sandwell, Marine gravity field from declassified Geosat and ERS-1 altimetry (abstract), *EOS Trans. AGU,* 76, 156, 1995.

Tolstoy, M., A. J. Harding and J. A. Orcutt, Crustal thickness on the Mid-Atlantic ridge: Bull's eye gravity anomalies and focused accretion, *Science*, 262, 726-729, 1993

Tucholke, B. E. and J. Lin, A geological model for the structure of ridge segments in slow-spreading ocean crust, *Journal of Geophysical Research*, 99, 11937-11958, 1994.

Tucholke, B. E., J. Lin, M. A. Tivey, M. C. Kleinrock, T. B. Reed, J. Goff, and G. Jaroslow, Segmentation and crustal structure of the western Mid-Atantic ridge flank, 25°30'-27°10'N and 0-29 M.y., *Journal of Geophysical Research*, submitted, 1996.

Wolfe, C., G. M. Purdy, D. R. Toomey and S. C. Solomon, Microearthquake characteristics and crustal velocity structure at 29°N of the Mid-Atlantic Ridge: The architecture of a slow-spreading serment, *Journal of Geophysical Research*, 100, 24449-24472, 1995.

ERRATA

Page 24, column 1, line 3 should read "exhume" instead of "exhumate".

Page 25, caption of Figure 8, should read "~1.1 km" instead of "~1.5 km".

Page 27, label in Figure 9a, should read "(km)" instead of "(mGal)".

Page 28, caption of Figure 12, should read "greater" instead of "grater".

Page 30, column 1, line 1, should read "their" instead of "its".

Page 30, column 1, line 2, should read "little evidence" instead of "no evidence".

Page 31, column 1, paragraph 3, line 4, should read "0.4 to 1.2 km" instead of "0.4 to 1.0 km"